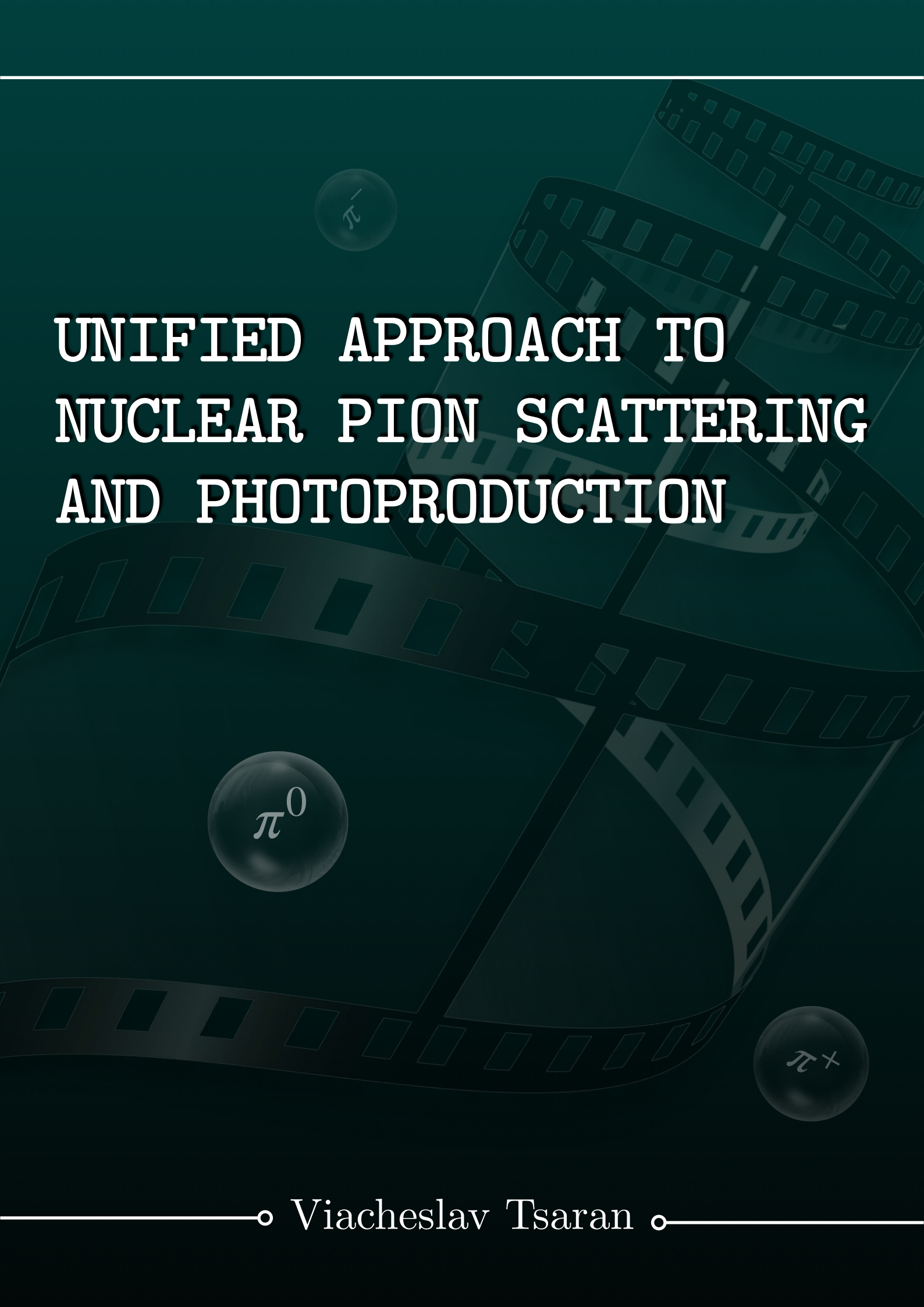

UNIFIED APPROACH TO NUCLEAR PION SCATTERING AND PHOTOPRODUCTION

Viacheslav Tsaran

Unified approach to nuclear pion scattering and photoproduction

Dissertation
zur Erlangung des Grades
„ Doktor der Naturwissenschaften “

am Fachbereich Physik, Mathematik und Informatik
der Johannes Gutenberg-Universität Mainz

vorgelegt von

Viacheslav Tsaran

geboren in Kherson (Ukraine)

Mainz, 2024

Abstract

An improved understanding of the physics governing both atomic nuclei and neutron stars motivates accessing more reliable experimental data on neutron distribution within nuclei.

Coherent nuclear π^0 photoproduction is considered a promising instrument for studying the distribution of neutrons within nuclei. Leveraging this technique, the A2 collaboration meticulously analyzed data from MAMI, extracting a crucial parameter that significantly impacts nuclear models: the neutron skin thickness of ^{208}Pb. However, challenges remain, primarily due to theoretical uncertainties of the nuclear photoproduction model, in particular, stemming from the rough treatment of final-state pion-nucleus interactions. Consequently, the theoretical approach is striving to keep up with the increasing precision of modern experiments. This work aims to address these challenges by developing a unified theoretical framework that encompasses both nuclear pion photoproduction and scattering, thereby laying the groundwork for more accurate theoretical predictions. These developments may also serve as a building block in improving the description of neutrino-induced pion production in view of long-baseline neutrino projects.

We establish our approach by developing an updated model for pion-nucleus scattering in the framework of the distorted wave impulse approximation in momentum space. The scattering amplitude is found from the Lippmann-Schwinger equation for which we construct a novel momentum-space pion-nucleus potential. The developed potential incorporates second-order pion rescattering on intermediate excited nuclear states, in accordance with the Pauli exclusion principle, and involves intermediate pion-nucleon charge exchange and nucleon spin-flip processes. The many-body medium effects are incorporated in the complex effective Δ self-energy, modifying the Δ propagator in the nuclear medium. We estimate three optimal energy-independent parameters of our model by a multienergy fit of the $\pi^{\pm}$-^{12}C total, reaction, and differential elastic cross sections. To demonstrate the predictive power of our approach, we compare its predictions with $\pi^{\pm}$ scattering data on ^{16}O, ^{28}Si, and ^{40}Ca.

Building upon the developed framework for pion-nucleus scattering, we extend our approach to analyze coherent nuclear π^0 photoproduction, incorporating final-state charge exchange and nucleon spin flip. The effective Δ self-energy, modifying the photoproduction amplitude, is directly adopted from the analysis of pion-nucleus scattering. The resulting prediction of our approach for nuclear π^0 photoproduction aligns well with experimental data for ^{12}C and ^{40}Ca without the need to fit the model parameters of the photoproduction amplitude.

Zusammenfassung

Ein besseres Verständnis der Physik, die sowohl Atomkerne als auch Neutronensterne steuert, erfordert den Zugang zu zuverlässigeren experimentellen Daten zur Verteilung von Neutronen in Kernen.

Die kohärente π^0-Photoproduktion am Kern gilt als vielversprechendes Instrument zur Untersuchung der Verteilung von Neutronen in Kernen. Mithilfe dieser Technik hat die A2-Kollaboration die Daten von MAMI sorgfältig analysiert und einen entscheidenden Parameter extrahiert, der die Kernmodelle maßgeblich beeinflusst: die Neutronenhautdicke von ^{208}Pb. Dennoch bestehen weiterhin Herausforderungen, die vor allem auf theoretische Ungenauigkeiten des Kernphotoproduktionsmodells zurückzuführen sind, insbesondere auf die grobe Behandlung von Pion-Kern-Endzustandswechselwirkungen. Folglich bemüht sich der theoretische Ansatz, mit der zunehmenden Präzision der modernen Experimente mitzuhalten. Diese Studie zielt darauf ab, diese Herausforderungen zu bewältigen, indem ein einheitlicher theoretischer Ansatz entwickelt wird, der sowohl die Photoproduktion als auch die Streuung von Pionen am Kern umfasst und damit die Grundlage für genauere theoretische Vorhersagen schafft. Diese Entwicklungen können auch als ein Baustein für Verbesserung der Beschreibung der Neutrino-induzierten Produktion von Pionen im Hinblick auf die Long-Baseline-Neutrino-Projekte dienen.

Wir etablieren unseren Ansatz, indem wir ein aktualisiertes Modell für die Pion-Kern-Streuung im Rahmen der verzerrten Wellen-Impuls-Näherung im Impulsraum entwickeln. Die Streuamplitude wird aus der Lippmann-Schwinger-Gleichung ermittelt, für die wir ein neuartiges Pion-Kern-Potenzial im Impulsraum konstruieren. Das entwickelte Potenzial berücksichtigt die Pion-Rückstreuung zweiter Ordnung an angeregten nuklearen Zwischenzuständen in Übereinstimmung mit dem Paulischen Ausschließungsprinzip und beinhaltet den Pion-Nukleon-Ladungsaustausch im Zwischenzustand und Nukleon-Spin-Flip-Prozesse. Die Vielteilcheneffekte des Mediums sind in der komplexen effektiven Δ-Eigenenergie enthalten und modifizieren den Δ-Propagator im nuklearen Medium. Wir ermitteln drei optimale energieunabhängige Parameter unseres Modells durch eine Multienergie-Anpassung der $\pi^{\pm}$-^{12}C Gesamt-, Reaktions- und differentiellen elastischen Wirkungsquerschnitte. Um die Vorhersagekraft unseres Ansatzes zu demonstrieren, vergleichen wir seine Vorhersagen mit $\pi^{\pm}$-Streuungsdaten an ^{16}O, ^{28}Si, und ^{40}Ca.

Auf der Grundlage des entwickelten Rahmens für die Pion-Kern-Streuung erweitern wir unseren Ansatz auf die Analyse der kohärenten π^0-Photoproduktion am Kern und beziehen dabei den Ladungsaustausch im Endzustand und den Spin-Flip der Nukleonen mit ein. Die effektive Δ-Eigenenergie, die die Photoproduktionsamplitude modifiziert, wird direkt aus der Analyse der Pion-Kern-Streuung übernommen. Die resultierende Vorhersage unseres Ansatzes für die π^0-Photoproduktion am Kern stimmt gut mit experimentellen Daten für ^{12}C und ^{40}Ca überein, ohne dass die Modellparameter der Photoproduktionsamplitude angepasst werden müssen.

List of publications

[1] Viacheslav Tsaran "Coherent pion photoproduction on spin-zero nuclei", EPJ Web Conf. **274** (2022) 07005.

[2] F. Colomer, P. Capel, M. Ferretti, J. Piekarewicz, C. Sfienti, M. Thiel, V. Tsaran, M. Vanderhaeghen "Theoretical analysis of the extraction of neutron skin thickness from coherent π^0 photoproduction off nuclei", Phys. Rev. C **106** (2022) no.4, 044318, arXiv:2204.13395 [hep-ph].

[3] Viacheslav Tsaran and Marc Vanderhaeghen, "Momentum-space second-order pion-nucleus potential including medium effects in the $\Delta(1232)$ region", Phys. Rev. C **108** (2023) no.4, 044608, arXiv:2306.04913 [hep-ph].

[4] Viacheslav Tsaran and Marc Vanderhaeghen, "Nuclear coherent π^0 photoproduction with charge-exchange and spin-flip rescattering", arXiv:2403.08608 [hep-ph].

Contents

1 Introduction **1**
1.1 Pions through the lens of QCD . . . 1
1.2 From nuclei to neutron stars . . . 3
1.3 Theoretical route of pion photoproduction . . . 9
1.4 Pion production in neutrino-nucleus interactions . . . 16
1.5 Outline of the thesis . . . 18

2 Nuclear densities, form factors, and correlation functions **19**
2.1 One- and two-body density matrices . . . 20
2.2 One-body nuclear structure functions . . . 23
2.2.1 Model-independent charge densities from electron scattering . . . 25
2.2.2 The Fermi-gas model . . . 26
2.2.3 The harmonic oscillator shell model . . . 28
2.2.4 Form factors of ^{12}C, ^{16}O, ^{28}Si, and ^{40}Ca . . . 36
2.3 Two-body correlation functions . . . 38
2.4 Summary . . . 42

Appendices **44**
2.A Occupation numbers and probabilities . . . 44

3 Momentum-space second-order pion-nucleus potential **45**
3.1 Multiple-scattering formalism . . . 46
3.2 Pion-nucleon elementary scattering amplitude . . . 49
3.3 Derivation of the pion-nucleus potential . . . 53
3.3.1 The first-order potential . . . 53
3.3.2 The second-order correction . . . 54
3.3.3 Medium modifications . . . 57
3.4 Results and discussion . . . 62
3.4.1 Observables . . . 62
3.4.2 Fit to ^{12}C data . . . 63
3.4.3 Comparison with ^{16}O data . . . 69
3.4.4 Comparison with ^{28}Si and ^{40}Ca data . . . 69
3.4.5 Comparison with ^{4}He data . . . 73
3.5 Conclusion and outlook . . . 77

Appendices **78**
3.A Partial wave decomposition . . . 78

3.B Scattering by nuclear and Coulomb potentials . . . 79
3.C Decomposition of the pion-nucleon scattering amplitude . . . 80
3.D The second-order part of the potential . . . 83

4 Nuclear coherent π^0 photoproduction **87**
4.1 Multiple-scattering formalism . . . 89
4.2 Elementary pion photoproduction amplitude . . . 92
4.2.1 Decomposition of the pion photoproduction amplitude . . . 93
4.2.2 In-medium modification of $M_{1+}^{3/2}$ . . . 95
4.2.3 The effective Δ self-energy . . . 98
4.3 The second-order potential for nuclear pion photoproduction . . . 100
4.4 Results and discussion . . . 103
4.4.1 Comparison with ^{12}C and ^{40}Ca data . . . 103
4.4.2 Preliminary results for ^{208}Pb . . . 110
4.5 Conclusion and outlook . . . 113

Appendices **115**
4.A Pion production on a nucleon . . . 115
4.B In-medium modification of $E_{1+}^{3/2}$ . . . 117
4.C The s-wave part of the pion-^{40}Ca scattering potential . . . 118

5 Summary and outlook **119**

Bibliography **123**

Chapter 1
Introduction

1.1 Pions through the lens of QCD

Quantum Chromodynamics (QCD) is the fundamental theory describing the strong interactions in the the Standard Model. The QCD Lagrangian, which describes the dynamics of spin-1/2 fermions (quarks) and non-Abelian vector gauge bosons (gluons), is given by:

$$\mathcal{L}_{\text{QCD}} = \sum_f \bar{q}_f \left(i\gamma^\mu D_\mu - m_f\right) q_f - \frac{1}{4} G^{(a)}_{\mu\nu} G^{(a)\mu\nu}. \tag{1.1}$$

Here, q_f represents the quark bispinor fields of six flavors $f = \{u, d, s, c, b, t\}$, D_μ is the covariant derivative involving gluon fields $G^{(a)}_\mu$, $G^{(a)}_{\mu\nu}$ is the gluon field strength tensor, and γ^μ are the Dirac matrices. The QCD Lagrangian is invariant under local $SU(3)$ color gauge transformations. In the absence of quark masses, the QCD Lagrangian has no explicit mass scale and is scale-invariant at the classical level. This scale invariance is broken in the non-abelian theory due to quantum loop corrections (trace anomaly), resulting in a running coupling constant and the emergence of a mass scale on the order of $\Lambda_{\text{QCD}} \approx 200\,\text{MeV}$. In the physical world, the u and d quark masses are small compared to Λ_{QCD}, leading to an approximate global chiral symmetry.

The *chiral symmetry* between left- and right-handed components of the quark fields is explicitly broken by the Dirac mass term in the Lagrangian. However, u, d, and s quarks are much lighter than the typical hadronic scale of $1\,\text{GeV}$[1] making the chiral symmetry approximately valid. In the so-called *chiral limit*, the masses of three lightest quarks are assumed to be zero. The corresponding Lagrangian describing massless u, d, and s quarks can be written in the form

$$\mathcal{L}^0_{\text{QCD}} = \sum_{f=u,d,s} (\bar{q}^R_f i\gamma^\mu D_\mu q^R_f + \bar{q}^L_f i\gamma^\mu D_\mu q^L_f) - \frac{1}{4} G^a_{\mu\nu} G^{a\mu\nu}, \tag{1.2}$$

where the left (L) and the right (R) chiral components are explicitly separated and do not interact with each other. The Lagrangian $\mathcal{L}^0_{\text{QCD}}$ has the global symmetry

$$\underbrace{SU(3)_L \times SU(3)_R}_{\text{chiral group}} \times U(1)_V \times U(1)_A,$$

where V and A denote vector and axial groups.[2]

[1] The quark masses are: $m_u \approx 2.2\,\text{MeV}$, $m_d \approx 4.7\,\text{MeV}$, $m_s \approx 93\,\text{MeV}$, $m_c \approx 1.3\,\text{GeV}$, $m_b \approx 4.2\,\text{GeV}$, $m_t \approx 173\,\text{GeV}$ [5]

[2] Under $U(1)_V$ ($U(1)_A$) the left- and right-handed fermions transform with the same (an opposite) global phase: $q^{L,R}_f \to e^{i\phi} q^{L,R}_f$ ($q^{L,R}_f \to e^{\pm i\phi} q^{L,R}_f$).

The QCD vacuum does not respect the exact global $SU(3)_L \times SU(3)_R$ chiral symmetry of $\mathcal{L}^0_{\text{QCD}}$. Instead, the vacuum ground state breaks this symmetry down to the flavor subgroup $SU(3)_L \times SU(3)_R \to SU(3)_V$. According to the *Goldstone theorem*, this spontaneous breaking of continuous symmetry results in the emergence of massless pseudoscalar bosons in the spectrum of vacuum excitations. The number of Goldstone bosons corresponds to the number of broken symmetry generators. The breaking of chiral symmetry produces $3^2 - 1 = 8$ pseudoscalar bosons, forming an octet under the residual $SU(3)_V$ symmetry.

The Goldstone bosons of QCD can be associated with eight light pseudoscalar mesons (bound states of one quark and one antiquark) observed in the hadronic spectrum: π^+, π^-, π^0, K^+, K^-, K^0, $\bar{K}^0$, and η. The nonzero masses of these mesons are due to the small but non-zero masses of the light quarks, which introduce mixing between the left- and right-handed quark fields, explicitly breaking the chiral symmetry of the Lagrangian. This explicit breaking generates small masses for the 8 lightest pseudo-scalar mesons, making them not true Goldstone bosons but so-called *pseudo-Goldstone bosons*. The resulting masses of pseudo-Goldstone particles are given by Gell-Mann-Oakes-Renner relation. For the neutral pion, this relation is:

$$m^2_{\pi^0} = -\frac{1}{f^2_\pi}\frac{m_u + m_d}{2}\langle \bar{u}u + \bar{d}d\rangle, \tag{1.3}$$

where $f_\pi \approx 130\,\text{MeV}$ is the pion decay constant, and $\langle \bar{q}_f q_f\rangle$ is the quark condensate, a measure of spontaneous chiral symmetry breaking. Similar relations hold for the charged pions, kaons, and eta mesons with respect to their quark content. This expression illustrates how the pion mass is directly related to the quark masses and the dynamics of the QCD vacuum.

In the absence of electromagnetic interactions, the Standard Model exhibits *isospin symmetry* if the masses of the two lightest quarks are assumed equal. This additional global symmetry, appearing in the limit $m_u = m_d \ll m_s$, keeps the QCD Lagrangian invariant under the $SU(2)$ transformation of the u and d quark doublet, analogous to the symmetry of spin. With the very small mass difference between the u and d quarks ($m_d - m_u \approx 2.5\,\text{MeV}$), this $SU(2)$ symmetry appears notably more precise than the chiral $SU(3)$ symmetry. The observed deviations from exact isospin symmetry, such as the neutron-proton and charged-neutral pion mass differences, are typically on the order of a few MeV. Although isospin symmetry is broken by the quark mass difference and electromagnetic effects, it remains a powerful and effective approach simplifying the analysis of hadronic interactions.

In the low-energy limit of QCD, the strong force leads to the confinement of quarks within color-neutral hadrons. While the strong interaction in QCD is mediated by massless gluons, pions serve as effective carriers of the strong force between nucleons at low energies. This concept of pions governing nuclear forces finds its roots in the pioneering work of Hideki Yukawa in 1935. The Yukawa potential, characterizing the interaction between two nucleons via pion exchange, is given by

$$V(r) = -\frac{g^2}{4\pi}\frac{e^{-m_\pi r}}{r}, \tag{1.4}$$

where g is the coupling constant, and r is the distance between nucleons. Despite its simplicity, this potential captures the short-range behavior of the nuclear force, rapidly

decreasing beyond distances of the pion Compton wavelength of about 1.4 fm. Although decades have passed from the time of Yukawa's hypothesis to the advent of the Standard Model, Yukawa's original concept remains a valuable and highly effective tool in nuclear physics. It has given rise to modern effective field theories, such as chiral perturbation theory, commonly employed to describe the low-energy dynamics of hadrons.

Pions are pseudo-Goldstone bosons arising from the spontaneous breaking of chiral symmetry in QCD, playing a fundamental role in our understanding of the strong force. The study of pion physics thus provides deep insights into the non-perturbative regime of QCD and the nature of nuclear phenomena. This thesis focuses on investigating the process of nuclear coherent pion photoproduction and scattering. Below in this Chapter, we offer a brief overview of modern research in nuclear structure properties, as well as the theoretical framework employed in analyzing state-of-the-art measurements of nuclear π^0 photoproduction at the Mainz Microtron (MAMI). Additionally, we explore the relevance of pion scattering and photoproduction studies to modern measurements of neutrino properties through neutrino oscillations in long-baseline facilities.

1.2 From nuclei to neutron stars

Studying the structure of atomic nuclei has remained one of the central interests in physics since the groundbreaking Geiger–Marsden experiments, which revealed the divisible nature of the atom at the dawn of the 20th century. As early as 1956, elastic electron scattering enabled accurate probing of the charge distribution within nuclei [6]. Achieving this was made possible by a straightforward yet accurate theoretical model describing this process. According to this model, the differential cross section for elastic scattering of non-polarized electrons off a spinless nucleus can be expressed as

$$\frac{\mathrm{d}\sigma}{\mathrm{d}\Omega}(eA \to eA) = \rho_{\mathrm{ch}}^2(q) \left[\frac{\mathrm{d}\sigma}{\mathrm{d}\Omega}\right]_{\mathrm{Mott}}, \tag{1.5}$$

where A denotes the nucleus in its ground state, q is the momentum transfer, $[\mathrm{d}\sigma/\,\mathrm{d}\Omega]_{\mathrm{Mott}}$ is Mott's differential cross section describing the elastic scattering of relativistic electrons on a point-like charge, and $\rho_{\mathrm{ch}}(q)$ is the elastic form factor accounting for the charge distribution within the nucleus. The form factor is related to the corresponding density distribution by the Fourier transform. In the case of symmetric nuclei, $\rho_{\mathrm{ch}}(q)$ solely depends on the absolute value of the momentum transfer, q, leading to the relationship

$$\rho_{\mathrm{ch}}(q) = 4\pi \int_0^\infty r^2\,\mathrm{d}r \frac{\sin qr}{qr} \rho_{\mathrm{ch}}(r), \tag{1.6}$$

where $\rho_{\mathrm{ch}}(r)$ is the charge density distribution.[3] Over subsequent years, further advancements in experimental techniques for electron scattering, muonic spectroscopy, and optical isotope shifts facilitated highly accurate determination of the charge distribution and the corresponding root-mean-square (rms) radius [7, 8]. For instance, the

[3] In this work, we use notations $\rho(q)$ and $\rho(r)$ for form factors and density distributions, respectively. This choice reflects that these quantities are momentum- and coordinate-space representations of the same density operator $\hat{\rho}$.

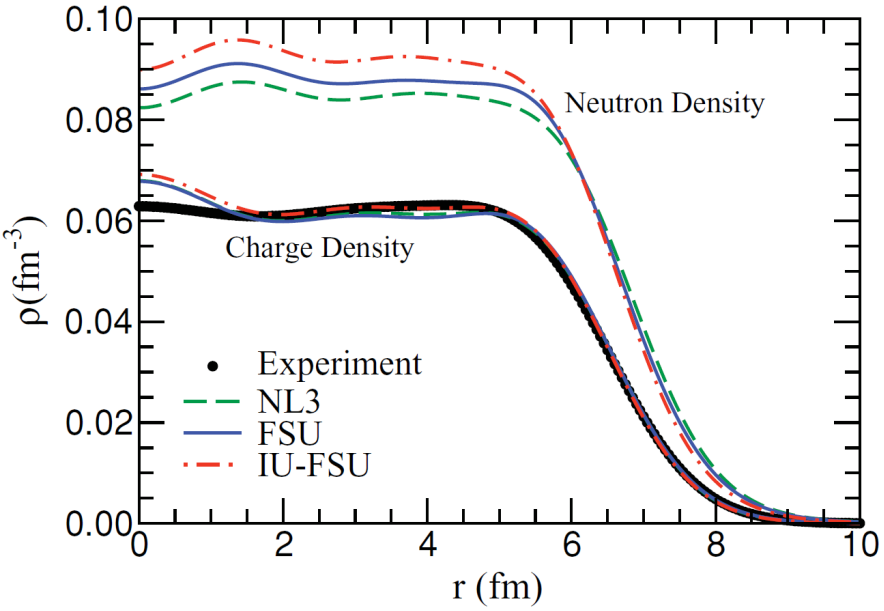

Figure 1.1: Model predictions for the charge and neutron densities of ^{208}Pb from Ref. [14]. Three models considered for comparison are NL3 [15], FSUGold (FSU) [16], and IU-FSU [14]. The experimental charge density data is from Ref. [7].

rms radius of ^{208}Pb is determined to be 5.5012(13) fm [9], indicating an exceptional level of accuracy of approximately 0.02%.

The distribution of protons within the nuclei is well determined, owing to the remarkable results of measuring the charge density across the nuclear chart.[4] On the contrary, the realm of neutrons remains veiled in complexity and vast uncertainties. The techniques that have provided exceptional charge density results are not applicable to neutral particles. Consequently, efforts to access the neutron densities commonly rely on hadronic experiments, e.g., heavy ion collisions [10], antiproton [11] and proton [12] elastic scattering, accompanied by uncontrollable uncertainties from theoretical models for the strongly interacting probes (for example, see Ref. [13]).

The challenges involved in extracting the neutron density lead to notable discrepancies among predictions from theoretical models describing nuclear matter, which still need to be solved. Fig. 1.1 from Ref. [14] illustrates these inconsistencies among the models. The plot compares predictions for charge and neutron densities of ^{208}Pb from three parametrizations of the interacting Lagrangian density [17, 18] within relativistic mean field theory: NL3 [15], FSUGold [16], and IU-FSU [14]. As seen from Fig. 1.1, while the models exhibit good agreement on the charge distribution, significant differences emerge in the predictions for the elusive neutron density. These discrepancies are observed both deep inside the nucleus and on its surface region. In recent years, there has been a notable surge of interest surrounding the neutron distribution on the surface area of nuclei, specifically to the parameter known as the *neutron skin thickness* [19, 20].

In heavy nuclei with a neutron excess, the neutron distribution extends beyond that of

[4] Although neutrons having zero charge, their contribution to the overall charge density is non-zero, albeit small. The corresponding details are discussed in Sec. 2.2.

Table 1.1: Ground-state properties of ^{48}Ca and ^{208}Pb [14]. The theoretical models taken for the comparison are the same as those used in Fig. 1.1. Here, B/A denotes the binding energy per nucleon, $R_{\rm ch}$ is the charge rms radius, and $r_{np} = R_n - R_p$ is the neutron skin thickness. The experimental values of r_{np} for ^{48}Ca and ^{208}Pb are taken from CREX [21] and PREX [22] measurements, respectively.

Nucleus	Observable	Exp	NL3	FSU	IU-FSU
^{48}Ca	B/A [MeV]	8.67	8.64	8.58	8.55
	$R_{\rm ch}$ [fm]	3.45	3.46	3.45	3.44
	r_{np} [fm]	0.121(35)	0.23	0.20	0.17
^{208}Pb	B/A [MeV]	7.87	7.88	7.89	7.89
	$R_{\rm ch}$ [fm]	5.50	5.51	5.52	5.48
	r_{np} [fm]	0.283(71)	0.28	0.21	0.16

protons, forming the outermost neutron-rich layer of the nucleus, as depicted in Fig. 1.1. This difference between the two distributions is quantified by the neutron skin thickness, which is defined as the difference in the rms radius of the neutron density relative to that of protons, denoted as $r_{np} = R_n - R_p$. The experimental determination of the neutron skin thickness serves as a powerful tool for testing nuclear models. Table 1.1 [14] summarizes the theoretical predictions of the models illustrated in Fig. 1.1 for ground-state properties of ^{48}Ca and ^{208}Pb. Experimental values for the neutron skin thickness are taken from the state-of-the-art model-independent measurements of ^{208}Pb and ^{48}Ca Radius Experiments (PREX [22] and CREX [21], respectively) using parity-violating elastic electron scattering [23–25].[5] As depicted in the table, while theoretical predictions for the binding energies and the charge radii align well with experimental values, the situation regarding the neutron skin is much more complex. Each model provides substantially different predictions for r_{np}. For instance, while the NL3 parametrization accurately predicts the neutron skin thickness for ^{208}Pb, it yields the result for ^{48}Ca twice as large as the experimental value. This trend is illustrated in Fig. 1.2 from Ref. [21], which compares predictions from coupled cluster [26], dispersive optical [27], and diverse density functional models[6] for the neutron skin thickness of ^{48}Ca and ^{208}Pb with the CREX and PREX results. As shown, none of the considered models agree well with the experimental values, consistently underestimating the neutron skin of ^{208}Pb and/or overestimating that for ^{48}Ca. Accurate determination of the neutron skin across a spectrum of nuclei will offer critical insights that refine and constrain parameters of models describing nuclear matter, particularly the symmetry energy of the nuclear equation of state (EoS).

The EoS relates energy, temperature, density, and neutron-proton asymmetry of nu-

[5] Parity-violating experiments measure the difference in the cross section between right- and left-handed longitudinally polarized electrons. The asymmetry arises from the exchange of the weak-neutral Z^0 vector boson. Since the weak charge of the neutron is much larger than that of the proton, this process enables a purely electroweak determination of the neutron distribution.

[6] For the list of the density functional models, see the supplemental material of Ref. [21] at http://link.aps.org/supplemental/10.1103/PhysRevLett.129.042501

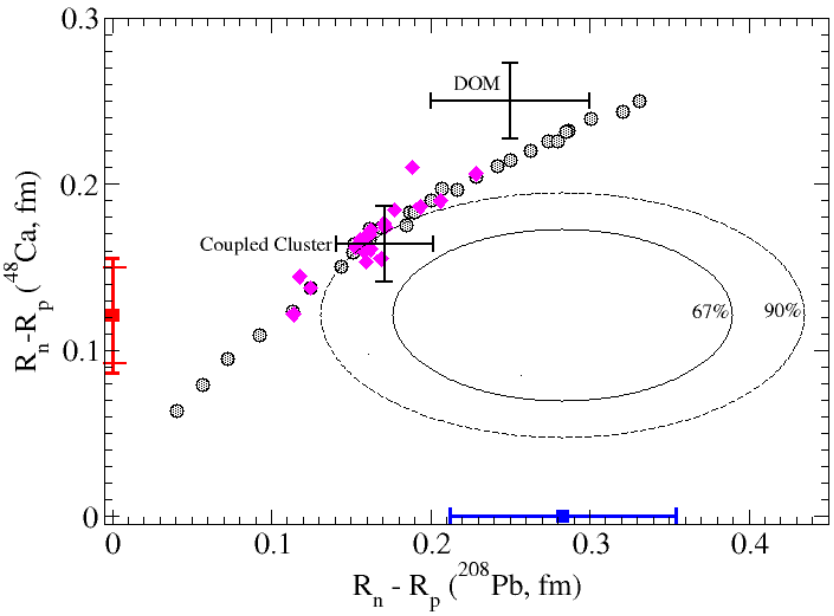

Figure 1.2: The neutron skin thickness of ^{48}Ca versus that for ^{208}Pb from Ref. [21]. The PREX [22] and CREX [21] experimental results are shown as blue and red square markers, respectively. The ellipses represent joint PREX and CREX 67% and 90% probability contours. The magenta diamonds (gray circles) depict predictions from a range of (non)relativistic density functional models. The black error bars correspond to the coupled cluster [26] and dispersive optical model (DOM) [27].

clear matter. At zero temperature and in the thermodynamic limit, the binding energy per nucleon depends on the conserved baryon density $\rho = \rho_p + \rho_n$ and the relative neutron-proton asymmetry parameter $\alpha = (\rho_n - \rho_p)/(\rho_n + \rho_p)$. The EoS for asymmetric infinite nuclear matter can be expressed as power expansion of the energy per particle across the symmetric limit, giving

$$\mathcal{E}(\rho, \alpha) = \mathcal{E}(\rho, 0) + \mathcal{S}(\rho)\alpha^2 + \mathcal{O}(\alpha^4), \tag{1.7}$$

where even powers of α do not contribute due to the assumed isospin symmetry of the nuclear forces, a consequence of neglecting the electroweak interaction. The leading term, $\mathcal{E}(\rho, 0)$, represents the energy per nucleon of the isospin-symmetric nuclear matter and $\mathcal{S}(\rho)$ is the symmetry energy, which characterizes the cost of converting part of the protons in symmetric nuclear matter at density ρ to excess neutrons. The boundary values of the asymmetry parameter, $\alpha = 0$ and $\alpha = 1$, correspond to symmetric nuclear and pure neutron matter, respectively. Due to the significant dominance of the second term in Eq. (1.7) over the $\mathcal{O}(\alpha^4)$ correction for all allowed α values, the symmetry energy with high accuracy is given by

$$\mathcal{S}(\rho) \approx \mathcal{E}(\rho, 1) - \mathcal{E}(\rho, 0), \tag{1.8}$$

which is the energy required to convert symmetric nuclear matter into pure neutron matter.

A distinctive feature of symmetric infinite nuclear matter is its saturation, which implies that at the saturation density $\rho_0 \simeq 0.16\,\mathrm{fm}^{-3}$, the pressure $P = \rho^2 \partial \mathcal{E}(\rho, 0)/\partial\rho$

vanishes. Correspondingly, the expansion of the EoS around the saturation density up to the first order[7] yields

$$\mathcal{E}(\rho,\alpha) = \mathcal{E}(\rho_0,0) + \mathcal{S}(\rho_0)\alpha^2 + Lx\alpha^2 + \cdots , \tag{1.9}$$

where the dimensionless parameter $x \equiv (\rho-\rho_0)/3\rho_0$ characterizes the deviations of the density from its saturation value and L is the slope of the symmetry energy at saturation density. In contrast to the zero pressure of symmetric nuclear matter, the pressure of pure neutron matter at ρ_0 is proportional to the slope of the symmetry energy:

$$P \approx \rho_0 L/3. \tag{1.10}$$

The first two terms on the right-hand side of Eq. (1.9) describe incompressible nuclear matter similar to Gamow's liquid drop model [29]. These terms, coinciding with the thermodynamic limit of the semi-empirical Bethe-Weizsäcker formula [30, 31], provide a reasonably accurate depiction of the binding energy of stable nuclei. However, they do not capture the properties of the neutron-rich surface of heavy nuclei. The third term in Eq. (1.9) introduces the first-order response to density fluctuations, generating the non-zero symmetry pressure, Eq. (1.10). This pressure drives the formation of the neutron skin, pushing excess neutrons toward the surface of a heavy nucleus where the symmetry energy is substantially lower than in the core. Consequently, the neutron skin thickness, r_{np}, in neutron-rich nuclei is strongly sensitive to the slope of the symmetry energy, L [19, 32, 33]. The interplay between r_{np} and L is illustrated in the upper panel of Fig. 1.3 from Ref. [34]. The plot demonstrates predictions from various models for ^{48}Ca and ^{208}Pb alongside constraints derived from CREX and PREX measurements. The symmetry pressure, which drives the formation of the neutron skin, also impacts the size of objects that are a staggering 10^{55} times heavier than neutron-rich nuclei.

The scope of modern nuclear physics extends far beyond studying the structural properties of atomic nuclei and encompasses the densest known objects — neutron stars. These stellar remnants, born from core-collapsed supernovas, exhibit enormous densities several times greater than that of saturated nuclear matter.[8] Remarkably, they are governed by the same physics as heavy nuclei, which are described by the EoS. While the mass of a neutron star is defined by the EoS at its highly dense core, its radius, as well as the neutron skin of nuclei, is described by the EoS in the vicinity of the nuclear saturation density [43]. Consequently, the neutron star radius correlates with the slope of symmetry energy L at saturation density [18, 44, 45]. The lower panel of Fig. 1.3 from Ref. [34] illustrates theoretical predictions for L versus the radius of the 1.4 solar mass neutron star, alongside constraints provided by the neutron skin measurements. As seen from Fig. 1.3, there is a strong correlation between the radius of a neutron star

[7] While a comprehensive analysis requires the inclusion of terms beyond the first order (see Ref. [28] for details), for the current brief discussion on neutron skin thickness, such terms are irrelevant and thus have been omitted.

[8] The detected neutron stars with masses of 1.44 [40, 41] and 2.08 [42] solar masses are estimated to have radii of $R_{1.44} \approx 12.45\,\text{km}$ and $R_{2.08} \approx 12.35\,\text{km}$, respectively [42]. These measurements show that the average mass densities of the corresponding neutron stars are $\rho_{1.44} \approx 3.5\times10^{14}\text{g/m}^3$ and $\rho_{2.08} \approx 5.3\times10^{14}\text{g/m}^3$, which exceed the nuclear saturation mass density of approximately $2.7\times10^{14}\text{g/m}^3$.

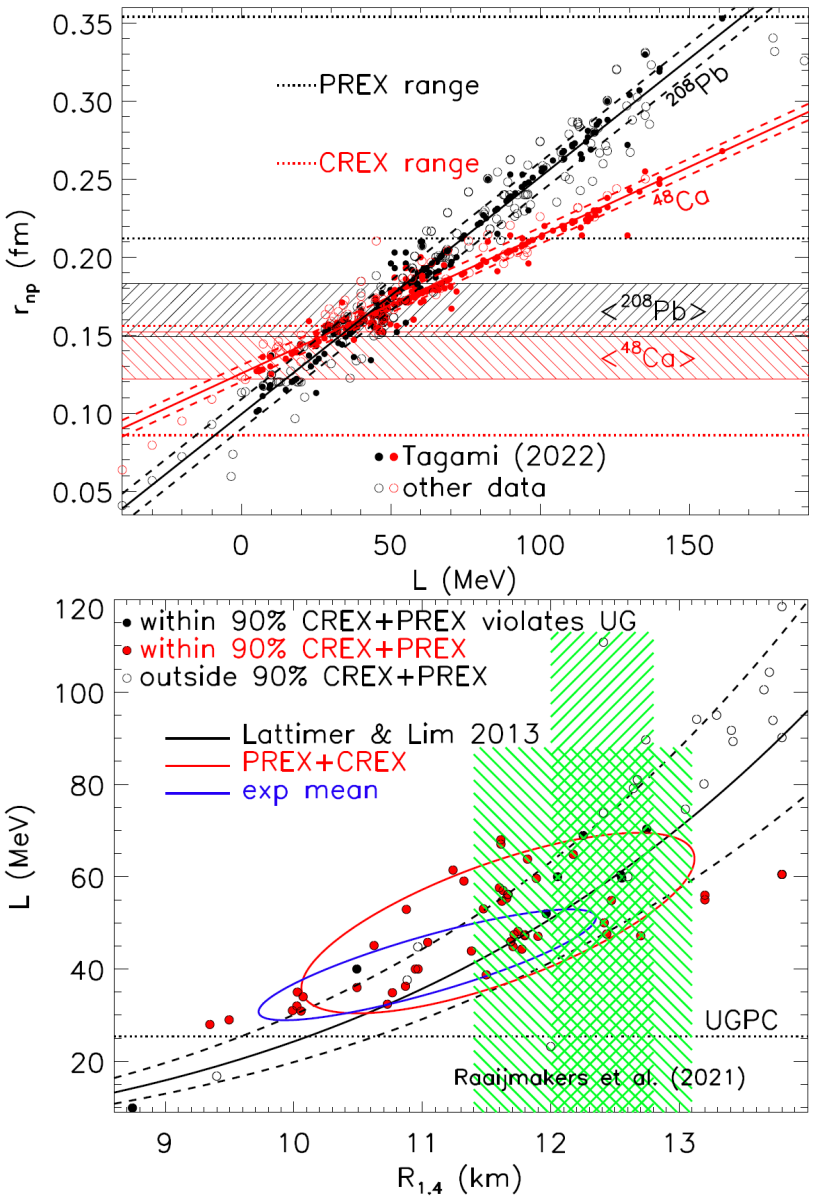

Figure 1.3: **Upper panel:** Neutron skin thicknesses of ^{48}Ca (red) and ^{208}Pb (black) versus the slope of the symmetry energy [34]. The model predictions are provided by Ref. [35] (filled circles) and Refs. [21, 36–38] (open circles). The solid and dashed lines represent the linear fits of all references and the corresponding 1σ deviations, respectively. The horizontal shaded bands indicate the 1σ deviation ranges of the averaged experimental results. The horizontal dotted black (red) lines indicate the 1σ deviation range from PREX [22] (CREX [21]). **Lower panel:** The slope of the symmetry energy versus the radius of the 1.4 solar mass neutron star [34]. The model predictions are sourced from the same references as in the upper panel, along with Ref. [35]. The solid and dashed lines represent the fits from each reference and the corresponding 1σ deviations, respectively (see Ref. [34] for details). Red (blue) ellipses represent constraints provided by parity-violating (average experimental) measurements for ^{48}Ca and ^{208}Pb. The shaded green bands are 68% and 95% confidence intervals from astrophysical measurements of tidal deformability [39].

and the neutron skin in neutron-rich nuclei, arising from their mutual relationship with L [16, 46–48].

At present, achieving an accurate determination of the density dependence of the symmetry energy remains elusive [49].[9] As demonstrated in Fig. 1.3, a precise determination of neutron skin thickness across the periodic table would provide critical constraints on the slope of the symmetry energy, which governs the structure and cooling mechanisms of neutron stars [16, 18, 53–55]. Moreover, this information would help determine the poorly known three-nucleon forces of the chiral effective field theory that significantly affect the symmetry energy [56–58]. Also exploring the nature of the neutron skin is important for searches for physics beyond the Standard Model [59, 60], as well as for describing collective nuclear excitations [33, 52, 61, 62] and flows in heavy-ion collisions [63, 64]. Thus, our limited understanding of the neutron density distribution hinders the development of efficient nuclear models capable of describing the dynamics of both atomic nuclei and neutron stars within a unified framework.

Parity-violating electron scattering measurements of the neutron skin [21, 22] benefit from an accurate theoretical background, making them one of the cleanest experimental techniques available. However, they are exceptionally challenging to execute, demanding the detection of parts-per-million parity-violating asymmetries. In contrast, experiments utilizing strongly interacting probes are comparatively simpler to carry out but suffer from uncontrolled uncertainties arising from the limited precision of models describing hadron dynamics [20]. It turns out that the simpler the experiment, the more challenging the accompanying theoretical description required. Therefore, the concurrent implementation of parity-violating and other indirect techniques would offer an efficient means of determining the neutron skin of nuclei across the nuclear chart.

Nuclear coherent π^0 photoproduction ($\gamma + A \to \pi^0 + A$) offers a powerful and elegant tool for probing the nucleon distribution within nuclei and, consequently, investigating the neutron skin [65]. The advantage of using a photon probe to explore neutron distribution is the absence of Coulomb interaction effects, which can shadow the interaction of the probe with neutrons. The neutral pions produced in this reaction are efficiently detected through their dominant 2γ decay channel. This technique has been successfully employed since the late 1950s [66, 67] and improved significantly with a modern large solid-angle photon detector, the Crystal Ball/TAPS setup at the MAMI [68]. However, discussions [2, 69, 70] following the extraction of the neutron skin of ^{208}Pb with this approach [65] suggest that a more sophisticated theoretical model for coherent pion photoproduction is required, the development of which forms a central focus of this work.

1.3 Theoretical route of pion photoproduction

In the nuclear photoproduction reaction, a pion is emitted as a result of the interaction of a high-energy photon with an atomic nucleus. While charged pion photoproduction is inherently incoherent, implying that the final-state of the nucleus differs from the initial

[9] In recent years, however, constraints on the density dependence of the symmetry energy have significantly improved due to advancements in various experimental techniques. These include the measurements of the tidal polarizability [50] and radii [40–42] of neutron stars, neutron skin thickness of ^{48}Ca [21] and ^{208}Pb [22], and dipole polarizabilities of nuclei [51, 52].

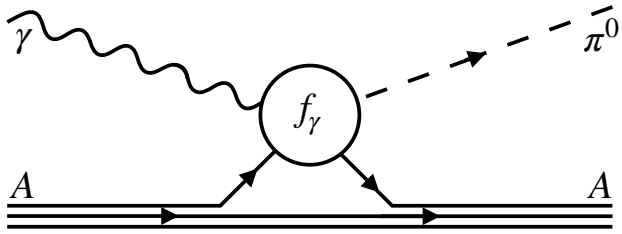

Figure 1.4: Diagrammatic representation of the coherent nuclear π^0 photoproduction within the PWIA. The amplitude f_γ describes π^0 photoproduction on a free nucleon and A denotes the nucleus in its ground state.

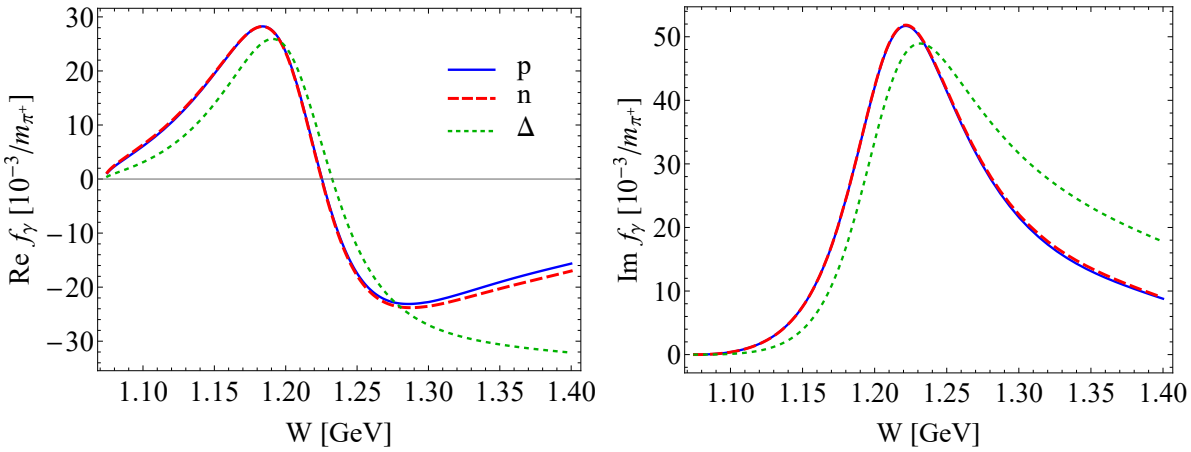

Figure 1.5: Real (**left panel**) and imaginary (**right panel**) parts of the spin-independent part of the elementary π^0 photoproduction amplitude as functions of the reaction energy. The blue solid (red dashed) curves correspond to photoproduction on the proton (neutron), and the green dotted curves represent the Δ-resonance contribution equal for both nucleons. The numerical values are taken from MAID2007 [73].

one, π^0 photoproduction can occur coherently, preserving the target nucleus in its ground state. In the simplest plane wave impulse approximation (PWIA), the total amplitude for the coherent process is given by the coherent sum of the production amplitudes on all nucleons within the nucleus [71], which corresponds to the diagram in Fig. 1.4. A distinctive feature of π^0 photoproduction is that both protons and neutrons contribute equally after applying spin averaging, as shown in Fig. 1.5. As a result, the differential cross section for coherent π^0 photoproduction on spin-zero nuclei can be expressed as [71, 72]

$$\frac{\mathrm{d}\sigma^{\mathrm{PWIA}}}{\mathrm{d}\Omega}(\gamma A \to \pi^0 A) = \mathscr{W}^2 \rho^2(q) \frac{\mathrm{d}\sigma}{\mathrm{d}\Omega}(\gamma N \to \pi^0 N), \tag{1.11}$$

where $\mathscr{W}$ is the kinematic factor, $\mathrm{d}\sigma/\mathrm{d}\Omega(\gamma N \to \pi^0 N)$ represents the spin-independent elementary π^0 photoproduction cross section, and $\rho(q)$ is the nuclear mass form factor. The PWIA cross section, Eq. (1.11), shares the same form as Eq. (1.5), which enables the determination of the charge distribution from elastic electron scattering measurement.

The coherent π^0 photoproduction process exhibits sensitivity to the total baryon den-

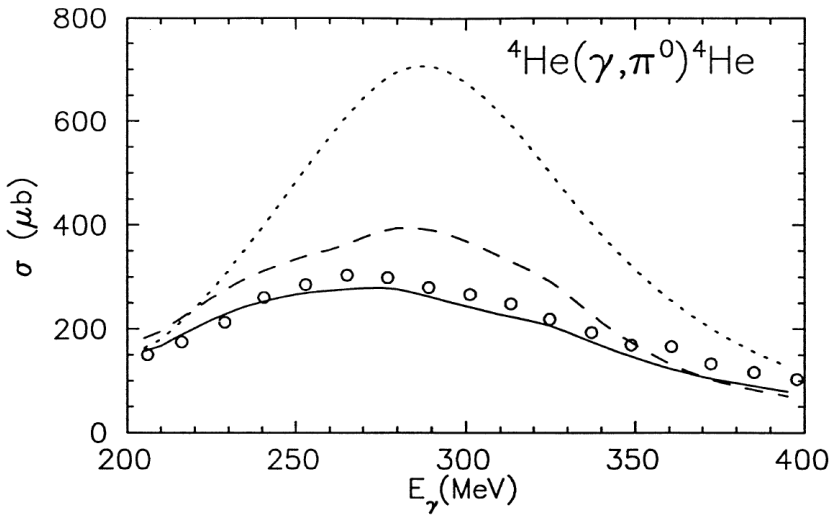

Figure 1.6: The total cross section for the coherent π^0 photoproduction on ^{4}He as a function of the photon laboratory energy from Ref. [75]. The short- and long-dashed curves are the results of PWIA and DWIA, respectively. The solid curve is obtained from the DWIA after fitting the Δ self-energy Σ_Δ. The experimental data are from Ref. [80].

sity. As follows from Eq. (1.11), the differential cross section for this process is directly proportional to the squared form factor $\rho(q)$, which is related to the nucleon density distribution $\rho(r)$ by the same Fourier transform as given by Eq. (1.6). Consequently, coherent π^0 photoproduction provides valuable insights into nucleon distribution and mass rms radii of atomic nuclei [74]. Employing the well-established proton density $\rho_p(r)$, the analysis of this reaction can focus on extracting the neutron density: $\rho_n(r) = \rho(r) - \rho_p(r)$.

Unfortunately, the seemingly straightforward route to neutron distribution suggested by the PWIA falls short when its predictions are compared with experimental data, as illustrated in Fig. 1.6 from Ref. [75]. In the plot, the total cross section for coherent π^0 photoproduction on ^{4}He within the PWIA is represented by the short-dashed curve, significantly overestimating the experimental data. This discrepancy arises due to the substantial influence of nuclear medium effects on the nuclear photoproduction process. While the electromagnetic photon-nucleus interaction does not require consideration of initial state iterations, the produced pion undergoes strong interactions with the surrounding nucleons. Consequently, it becomes necessary to incorporate final-state interaction, which modifies the pion propagator within the nuclear medium [76, 77]. The distorted wave impulse approximation (DWIA) accounts for the π^0 rescattering of the nucleus in its ground state [71, 78, 79], as depicted by the diagram in Fig. 1.7. The prediction of the DWIA is shown in Fig. 1.6 by the long-dashed curve, which, however, still fails to match the experimental data.

The residual deviation between the DWIA prediction and the data in Fig. 1.6 is attributed to the modification of the $\Delta(1232)$- resonance characteristics within the nuclear medium. The Δ is the first excited state of the nucleon with spin and isospin 3/2, playing a dominant role in pion-production processes [81, 82] (as depicted by the green short-dashed curves in Fig. 1.5), as 99.4% of its decays produce the pion-nucleon

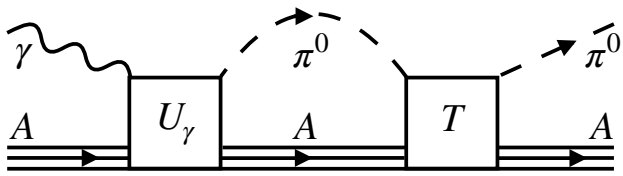

Figure 1.7: Diagrammatic representation of the final-state interaction in the coherent nuclear π^0 photoproduction reaction within the DWIA. The photoproduction potential U_γ within the PWIA is given by the diagram in Fig. 1.4, and T is the pion-nucleus scattering amplitude.

pair, $\Delta \to \pi N$ [5]. The resonant nature of the photoproduction process is also evident from Fig. 1.6, where the peak in the cross sections at about 300 MeV corresponds to the resonance position. With a relatively long lifetime on the nuclear scale and a mean free path within a nucleus of approximately 1 fm, the Δ can be regarded as a nuclear quasiparticle, effectively treated as a distinct baryonic species without delving into the intrinsic quark dynamics. Strong scalar and vector fields impact the propagation of the Δ-isobar within the nucleus.[10] These medium effects can be encapsulated in the effective Δ self-energy Σ_Δ, which shifts the mass and width of the resonance, thus modifying the very production amplitude.

In Reference [75], the complex energy-dependent self-energy Σ_Δ was fitted to the experimental differential cross sections for coherent π^0 photoproduction on ^{4}He from Ref. [80]. The resulting best fit, depicted by the solid curve in Fig. 1.6, demonstrates satisfactory agreement with the experimental data. Assuming the extracted Σ_Δ is already saturated for ^{4}He and remains appropriate for heavier nuclei, the elegant and efficient framework of Ref. [75], hereafter referred to as the Drechsel-Tiator-Kamalov-Yang (DTKY) model, successfully describes π^0 photoproduction measurements on ^{12}C, ^{40}Ca, ^{93}Nb, and ^{208}Pb within the Δ-resonance energy region [72, 95].

Achieving the most comprehensive and consistent description of nuclear photoproduction involves employing the DWIA in momentum space representation [71, 78, 96], demanding a precise momentum-space approach to pion-nucleus scattering. In the multiple-scattering formalism [97, 98], the scattering amplitude T is determined as a solution of the Lippmann-Schwinger equation [99] with a complex optical potential. This potential effectively characterizes the interaction between the pion and the nucleus as a whole [100–102], with its imaginary part accounting for pion flux lost to various inelastic channels [103]. While initially introduced in coordinate space [100, 101], the optical potential formalism was later adapted for use in momentum space [104–106].[11] The DTKY framework employs the second-order momentum-space potential of Ref. [108]:

$$U(B_0, C_0) = \mathscr{W}_1 \langle \boldsymbol{k}' | \hat{f} | \boldsymbol{k} \rangle \rho(q) + \mathscr{W}_2 \left[B_0 + C_0 \, \boldsymbol{k}' \cdot \boldsymbol{k} \right] \rho_2(q), \tag{1.12}$$

[10] The properties of the Δ isobar in the nuclear medium have been the subject of numerous investigations [75, 83–86], especially in the framework of the Δ-hole model [87–94], covering both pion scattering and photoproduction.

[11] A coordinate-space pion-nucleus potential, e.g., from Ref. [107], can also be effectively utilized within the momentum space DWIA after properly Fourier transformed, as demonstrated in Ref. [2].

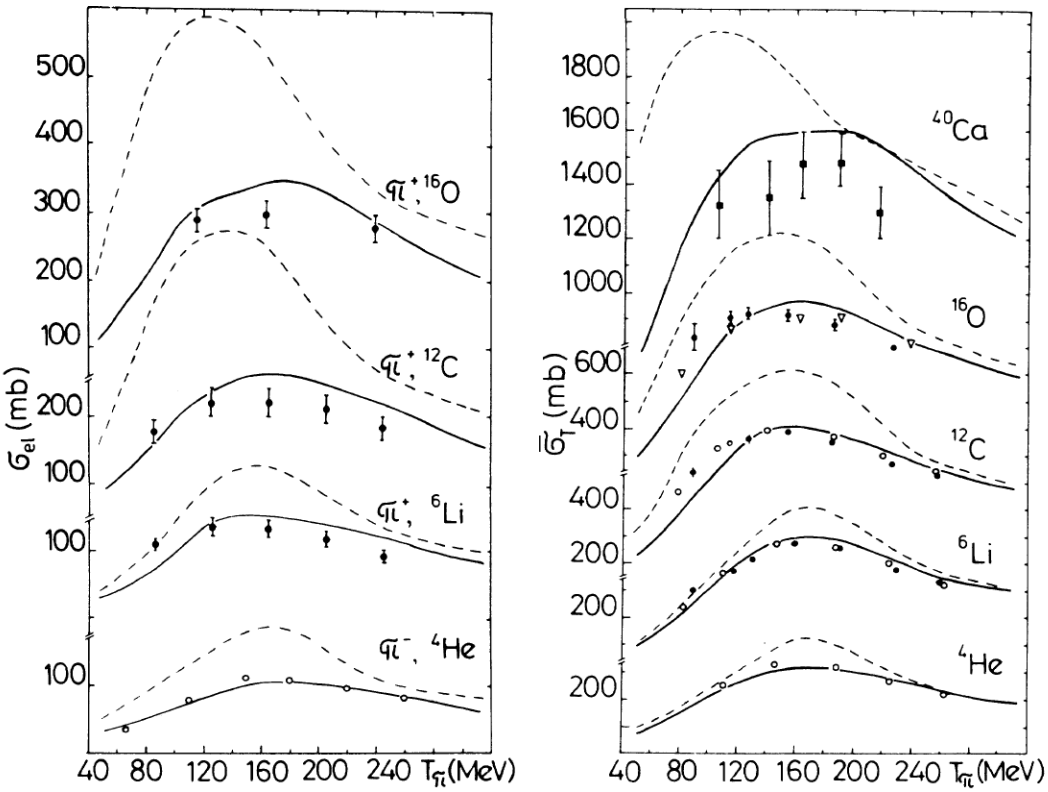

Figure 1.8: Integrated elastic (**left panel**) and total (**right panel**) cross sections for π^+ and charge-averaged scattering, respectively, as functions on the pion laboratory kinetic energy from Ref. [108]. The dashed and solid curves are obtained with the first- and second-order scattering potentials, respectively. The experimental data are from Refs. [109–115].

where $\boldsymbol{k}$ ($\boldsymbol{k}'$) is the initial (final) pion momentum, $\mathscr{W}_{1,2}$ are kinematic factors, $\hat{f}$ is the pion-nucleon scattering amplitude, and $\rho_2(\boldsymbol{q})$ is the Fourier transform of the squared nucleon density $\rho^2(r)$. Here B_0 and C_0 are phenomenological complex model parameters.

The first term in Eq. (1.12) represents the first-order optical potential, composed of the matrix element of the pion-nucleon scattering amplitude $\hat{f}$ and the nuclear mass form factor. This first-order part corresponds to the same diagram as depicted in Fig. 1.4, with the photon line replaced by the pion one. In the approach of Ref. [108], this term is parameter-free, relying on the elementary amplitude $\hat{f}$ derived from phase-shift analysis of pion-nucleon scattering. Since pion-nucleon scattering in the Δ-resonance energy region is described accurately by only two first partial waves, the isospin-averaged scattering amplitude can be expressed as $\langle \boldsymbol{k}'|\hat{f}|\boldsymbol{k}\rangle \approx b_0 + c_0\, \boldsymbol{k}' \cdot \boldsymbol{k}$, where b_0 and c_0 are energy-dependent complex s- and p-wave coefficients, respectively. The dashed curves in Fig. 1.8 represent integrated elastic and total cross sections obtained with the first-order potential for isospin-zero nuclei with $A = 4$–40. As in the case of nuclear pion photoproduction, the basic first-order model overestimates the experimental data significantly, especially for heavier nuclei, highlighting the critical need for including the higher-order correction.

The second-order part of the potential, given by the second term in Eq. (1.12), is in-

troduced phenomenologically to account for the modification of $\hat{f}$ and true pion absorption in nuclear matter. This second-order part adopts a similar form as the first-order term and presumes the dominance of the two-nucleon mechanism in nuclear-medium corrections.[12] The complex energy-dependent s- and p-wave parameters, B_0 and C_0, respectively, were determined in Ref. [108] from the best fit to $\pi^{\pm}$-^{12}C scattering data and assumed to be universally applicable across the nuclear chart. The solid curves in Fig. 1.8 represent this fit and corresponding predictions for other nuclei, illustrating the applicability of the model across light and medium-heavy isospin-zero nuclei.

A flow chart displayed in Fig. 1.9 summarizes all the essential theoretical steps within the DTKY framework employed in Ref. [65] to extract the neutron skin of ^{208}Pb. The description of nuclear pion photoproduction relies on two key components: the photoproduction potential $U_\gamma(\Sigma_\Delta)$ (where $U_\gamma(0)$ corresponds to the PWIA photoproduction amplitude, represented by the diagram in Fig. 1.4) and the pion-nucleus scattering potential $U(B_0, C_0)$ (used to compute the scattering amplitude $T(B_0, C_0)$ for the DWIA correction illustrated in Fig. 1.7). The model involves six energy-dependent real parameters: the real and imaginary parts of Σ_Δ, B_0, and C_0, determined from two distinct fitting procedures. The phenomenological scattering parameters B_0 and C_0 were adjusted to $\pi^{\pm}$-^{12}C scattering data, while the Δ self-energy Σ_Δ was determined by fitting measured differential cross sections for π^0 photoproduction on ^{4}He.

The DTKY framework utilizes substantially different approaches to scattering and photoproduction. The common features end in the resemblance between the first-order part of the scattering potential, $U(B_0 = 0, C_0 = 0)$, and the unmodified photoproduction potential, $U_\gamma(\Sigma_\Delta = 0)$. However, subsequent implementation of in-medium corrections for these two processes takes separate ways. While the scattering part employs the phenomenological second-order part of the potential, properties of the Δ resonance are modified to adjust the photoproduction amplitude. However, both reactions exhibit resonance behavior, visible in Figs. 1.6 and 1.8, indicating their reliance on similar underlying physics. Indeed, the excitation of the Δ resonance in the spin-isospin-3/2 channel is the dominant contribution to the elementary pion-nucleon scattering amplitude f, as for single-nucleon photoproduction amplitude f_γ in Fig. 1.5 [119]. The duality in the approach to two resembling processes serves as a telltale of potentially increased theoretical uncertainties in the model. In addition, a significant shared aspect of both scattering and photoproduction, overlooked in the DTKY model, is final-state charge-exchange interaction [101, 120–125], e.g., the contribution from $\gamma p \to \pi^+ n \to \pi^0 p$ channel to π^0 photoproduction.

Employing the DTKY model, the A2 collaboration reported the neutron skin thickness of ^{208}Pb to be $0.15 \pm 0.03\,(\text{stat.})^{+0.02}_{-0.03}\,(\text{sys.})$ fm based on high-precision coherent π^0 photoproduction measurements [65]. This value notably contrasts with the PREX result of 0.283 ± 0.071 fm derived from parity-violation electron scattering experiments [22]. It was argued that while the measured cross section and corresponding experimental error may be realistic, the influence of intermediate charge exchange could significantly increase the extracted value of the neutron skin thickness and the associated theoretical error [69, 70]. Furthermore, there are other uncertainties associated with the

[12] The three-nucleon absorption mechanism, however, is known to provide a significant fraction of the total absorption in the Δ-resonance energy region [116–118].

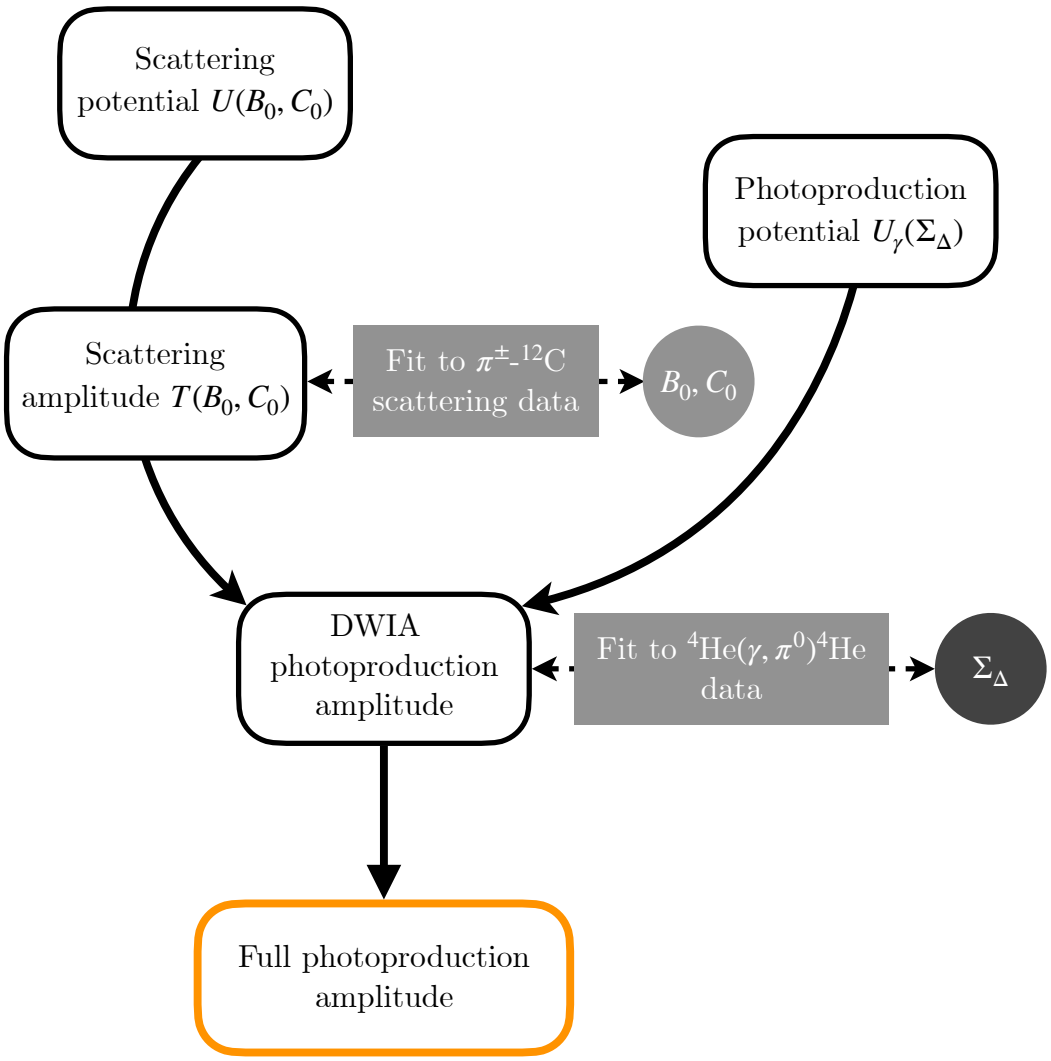

Figure 1.9: Flow chart illustrating the computational steps behind the DTKY model [75] for nuclear coherent π^0 photoproduction, which was applied for extracting the neutron skin thickness of ^{208}Pb [65].

pion-nucleus final-state interaction, particularly concerning the pion-nucleus optical potential of Ref. [108]. A more advanced model of both scattering and photoproduction is needed to comprehensively investigate the suitability of the π^0 photoproduction process for extracting neutron skin thickness.

In this work, our objective is to develop a unified approach to nuclear pion scattering and photoproduction. Our framework, illustrated in Fig. 1.10, incorporates the in-medium effects within the effective Δ self-energy Σ_Δ, while explicitly accounting for the final-state charge exchange and intermediate nucleon spin flip. Correspondingly, our route to describing nuclear π^0 photoproduction will begin with studying pion-nucleus scattering.

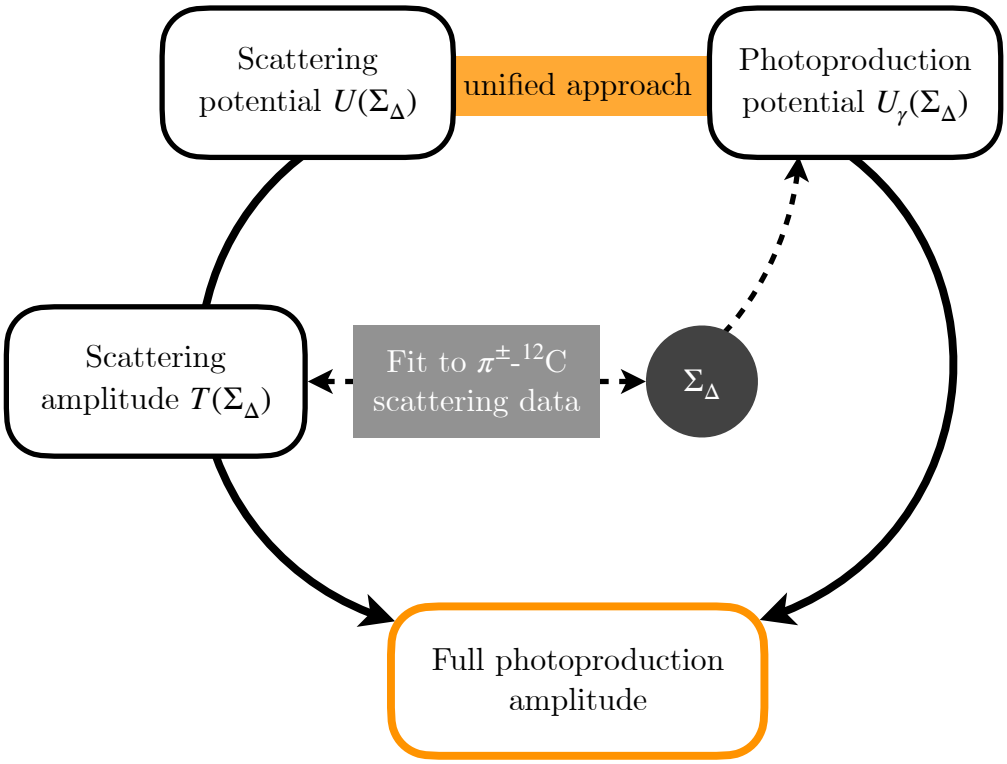

Figure 1.10: Flow chart illustrating the computational steps for nuclear coherent π^0 photoproduction within the developed approach presented in this thesis.

1.4 Pion production in neutrino-nucleus interactions

Photoproduction is just one instance of pion production in the inelastic interaction of high-energy particles with atomic nuclei. As discussed above, the emitted pions undergo considerable rescattering within the nuclear medium before being measured by a detector. Consequently, investigating pion-nucleus interactions remains relevant across various nuclear reactions. The process of pion production in neutrino-nucleus scattering, essential for extracting neutrino mixing matrix properties from neutrino oscillations, is no exception.

Current and upcoming neutrino oscillation experiments explore with ever-increasing precision a wide neutrino energy range from 0.1 to 10 GeV [126–131]. In the 1–5 GeV range, resonant interactions become dominant, as demonstrated in the left panel of Fig. 1.11, where the struck nucleon can be excited to one of many nucleon resonances, subsequently decaying into various meson and baryon states, including single- and multi-pion configurations. Neutrino energy reconstruction relies on the accurate detection of outgoing particles and the determination of their kinematics from the cross sections. However, uncertainties in treating pion final-state rescattering could bias the inferred neutrino energy. The selection of quasi-elastic events with no pion in the final state, as performed in T2K [132] and future Hyper-Kamiokande [133] analyses, also requires

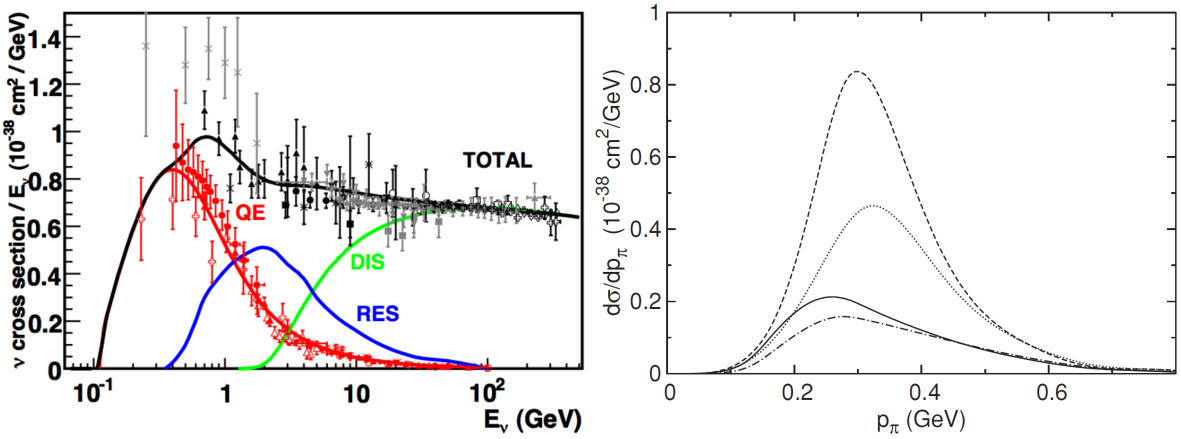

Figure 1.11: **Left panel**: Total muon neutrino per nucleon charge-current cross sections divided by neutrino energy for spin-zero nuclei as functions of energy from Refs. [134, 135]. The black curve and markers denote measurements and predictions for the total cross section, while the red represents quasielastic (QE) scattering, blue represents resonance production (RES), and green represents deep inelastic scattering (DIS). **Right panel**: Pion momentum distribution for $\nu_\mu + {}^{12}\mathrm{C} \to \mu^- + \pi^+ + {}^{12}\mathrm{C}$ reaction at 1 GeV as a function of the pion laboratory momentum from Ref. [136]. The dashed curve corresponds to the PWIA, the dotted was obtained incorporation the Δ self-energy, derived from the analysis to coherent π^0 photoproduction. The solid curve represents the full calculation: the DWIA with the Δ self-energy correction. The dash-dotted curve represents the scenario where the pion production operator includes only the Δ mechanism.

precise treatment of pion-nucleus interaction to properly separate final-state pion absorption contributions.

At neutrino energies below approximately 1.5 GeV relevant to, e.g., MicroBooNE [137], T2K/Hyper-Kamiokande [138], and DUNE [139] experiments, single pion production through excitation of the $\Delta(1232)$ is the dominant resonant process. Neutrino-nucleus scattering allows for coherent production of both charged (charged-current interaction $\nu_l + A \to l^- + \pi^+ + A$) and neutral (neutral-current interaction $\nu_l + A \to \nu_l + \pi^0 + A$) pions.[13] Despite their much smaller cross sections compared to incoherent processes, coherent reactions hold particular significance in modern neutrino physics. In the energy range around 1 GeV, coherent $\pi^\pm$ and π^0 production generates important background contributions with a large uncertainty to neutrino disappearance ($\nu_\mu + n \to \mu^- + p$, quasielastic) and $\nu_\mu \to \nu_e$ oscillation measurements, respectively [148]. In addition, neutrino-induced coherent pion production serves as a test of Adler's partially conserved axial vector current (PCAC) theorem [149, 150], which establishes a relationship between forward neutrino scattering and pion-nucleon cross sections [151].

Incorporating the medium modification of the Δ-resonance properties and pion rescattering within nuclear matter is equally essential for both neutrino- and photo-induced

[13] While older measurements failed to detect evidence for coherent $\pi^\pm$ production [140, 141], modern high-precision MINERvA [142, 143] and T2K [144, 145] experiments have successfully extracted nonzero cross sections for this process. The MINOS [146] and NOvA [147] Collaborations have also conducted recent measurements on coherent neutral-current pion production.

pion production. Moreover, the vector parts of the elementary amplitudes are similar for both processes [152]. However, the neutrino-induced production additionally involves the axial-vector part. These similarities suggest that coherent π^0 photoproduction could be employed to validate a model for coherent pion production in neutrino-nucleus scattering. Following this idea, a unified approach to nuclear neutrino- and photo-induced pion production was developed in Ref. [136] to predict differential cross section for $\nu_\mu + {}^{12}\mathrm{C} \to \mu^- + \pi^+ + {}^{12}\mathrm{C}$ process shown in the right panel of Fig. 1.11. The plot explicitly demonstrates the importance of the final-state interaction and the Δ self-energy incorporation, analogous to Fig. 1.6. Correspondingly, just as coherent pion production in neutrino-nucleus collisions facilitates the investigation of neutrino oscillations, nuclear coherent π^0 photoproduction could help study the process of coherent neutrino-induced pion production itself.

Given the relevance of both pion scattering and photoproduction in neutrino physics, a possible further extension of our unified model describing these two processes is coherent pion production in neutrino-nucleus collisions.

1.5 Outline of the thesis

In this thesis, we develop the second-order momentum-space potentials for nuclear pion scattering and π^0 photoproduction in a combined approach. The second-order parts of both potentials describe pion rescattering on intermediate excited nuclear states, encompassing final-state charge exchange and intermediate nucleon spin flip. This is achieved by employing the more realistic two-body nuclear correlation functions compared to those used in previous studies.

The thesis is organized as follows: In Chapter 2, we discuss briefly one- and two-nucleon densities, providing details on the form factors employed in our calculations, and derive the correlation function functions. Chapter 3, based on the work published in Ref. [3], is focused on pion-nucleus scattering. We derive the potential starting from the basic multiple-scattering formalism and introduce in-medium modifications to the resonant spin-isospin-3/2 channel as well as to the s-wave part of the potential. Finally, we demonstrate the best fit of our model to $\pi^{\pm}$-${}^{12}\mathrm{C}$ scattering data and our predictions for pion scattering on ${}^{4}\mathrm{He}$, ${}^{16}\mathrm{O}$, ${}^{28}\mathrm{Si}$, and ${}^{40}\mathrm{Ca}$. In Chapter 4, based on the work published in Ref. [4], we build the second-order potential for π^0 photoproduction following the framework developed for pion scattering. Without any additional fitting involved, we demonstrate our prediction for ${}^{12}\mathrm{C}$ and ${}^{40}\mathrm{Ca}$. Finally, in Chapter 5 we give a summary and outlook.

Chapter 2

Nuclear densities, form factors, and correlation functions

Theoretical models of nuclear pion scattering and photoproduction heavily depend on understanding the structural properties of nuclei. In the first-order approximation for these two processes, the projectile interacts with an individual nucleon, which requires a reliable nuclear density form factor for an accurate description. Similarly, the Coulomb interaction of a charged pion with a nucleus relies on the employed charge form factor. In addition, a comprehensive description of pion-nucleus rescattering involves considering nucleon correlations [153–155], particularly due to the Pauli principle originating from the antisymmetry of the nuclear wave function.

Charge form factors are directly obtained from elastic electron scattering experiments. For isospin-zero nuclei considered in this thesis, comparing these charge form factors alongside well-established electric form factors of nucleons [156] offers a reasonable estimate of the nucleon distribution form factors. In contrast, correlation functions are model-dependent and not directly measurable. Previous derivations of beyond-first-order correction to the pion-nucleus optical potential have predominately employed the Fermi gas model assumption [101, 107, 124] or treated these corrections phenomenologically [108]. In this chapter, we derive two-body correlation functions within the harmonic oscillator (HO) nuclear shell model, which will be used in constructing the second-order parts of the pion scattering and photoproduction potentials. Since our approach explicitly incorporates the spin-isospin structure of the elementary amplitudes, we introduce two types of correlation functions in accordance with the Pauli principle. One correlation function applies to the scenario where two nucleons preserve their spin-isospin states during the rescattering process, while the other accounts for nucleons that exchange their spin and/or isospin quantum numbers.

This chapter provides a detailed description of the nuclear structure functions, which will be utilized in developing the nuclear pion scattering and photoproduction potentials. The derived HO two-body correlation functions have been presented and used in Ref. [3]. The chapter is organized as follows:

- Section 2.1 introduces the general definitions of the one- and two-body density matrices and discusses their properties.
- Section 2.2 focuses on one-body nuclear structure quantities in both coordinate- and momentum-space representations, namely charge and nucleon density distributions and their corresponding form factors. This section discusses and compares the model-independent approach with the Fermi gas and HO shell model approximations. Additionally, it explicitly presents the employed form factors for ^{12}C,

^{16}O, ^{28}Si, and ^{40}Ca nuclei.

- In Section 2.3, we apply the approach described in the previous section to derive the two-body correlation functions for ^{12}C, ^{16}O, ^{28}Si, and ^{40}Ca.
- Finally, Section 2.4 summarizes with a discussion.

2.1 One- and two-body density matrices

Density matrices offer a powerful framework for describing and analyzing many-body quantum mechanical systems, particularly atomic nuclei, covering the structural properties and correlations of nucleons within a nucleus [157]. In this Section, we focus on one- and two-body density matrices of a system of A nucleons in a nucleus. In coordinate space, the ground state of this system is described by a normalized antisymmetric A-body wave function $\Psi_0(x_1, \ldots, x_A)$, where $x_i = \{\boldsymbol{r}_i, s_i, \tau_i\}$ encompasses the position ($\boldsymbol{r}_i$), spin (s_i), and isospin (τ_i) degrees of freedom of the i-th particle. The one-body and two-body density matrices associated with the wave function $\Psi_0(x_1, \ldots, x_A)$ are defined in coordinate space as[1]

$$\rho_1(x_1; x_1') \equiv A \int \left\{ \prod_{i=2}^{A} \mathrm{d}x_i \right\} \Psi_0^\dagger(x_1, x_2, \ldots, x_A) \Psi_0(x_1', x_2, \ldots, x_A), \tag{2.1a}$$

$$\rho_2(x_1, x_2; x_1', x_2') \equiv A(A-1) \int \left\{ \prod_{i=3}^{A} \mathrm{d}x_i \right\} \Psi_0^\dagger(x_1, \ldots, x_A) \Psi_0(x_1', x_2', x_3, \ldots, x_A), \tag{2.1b}$$

respectively. The integration over x_i in these equations and hereafter implies an integral over the corresponding spatial coordinates and a sum over the spin and isospin degrees of freedom:

$$\int \mathrm{d}x_i \ \ldots = \sum_{s_i} \sum_{\tau_i} \int \mathrm{d}\boldsymbol{r}_i \ \ldots . \tag{2.2}$$

Similarly, an arbitrary n-body density matrix is defined through an integral over the degrees of freedom of $A - n$ nucleons.

The density matrix formalism allows for straightforward derivation of the expectation values of any physical quantity Q associated with a many-body system. In its most general form, the operator $\hat{Q}$ includes all possible interactions, from single particles to all particles interacting simultaneously, which can be represented as

$$\hat{Q} = \sum_i \hat{Q}_i^{(1)} + \sum_{i<j} \hat{Q}_{ij}^{(2)} + \sum_{i<j<k} \hat{Q}_{ijk}^{(3)} + \cdots , \tag{2.3}$$

where $\hat{Q}_i^{(n)}$ are operators acting on n particles. The expectation value of $\hat{Q}$ can be expressed in terms of the density matrices as follows:

$$\begin{aligned} \langle \Psi_0 | \hat{Q} | \Psi_0 \rangle = & \int \mathrm{d}x_1 \, \rho_1(x_1; x_1') \left\langle x_1' \middle| \hat{Q}^{(1)} \middle| x_1 \right\rangle \\ & + \int \mathrm{d}x_1 \, \mathrm{d}x_2 \, \rho_2(x_1, x_2; x_1', x_2') \left\langle x_1', x_2' \middle| \hat{Q}^{(2)} \middle| x_1, x_2 \right\rangle + \cdots , \end{aligned} \tag{2.4}$$

[1] Note that the factor $A(A-1)$ in Eq. (2.1b) is twice as large as that in another commonly used definition.

where the pattern continues similarly for higher-order terms involving more interacting particles. Thus, the density matrices defined by Eqs. (2.1) encapsulate the correlations and statistical properties of the nucleus, providing a way to compute the expectation values of nuclear one- and two-body operators. In this regard, they play a key role in deriving the potentials describing nuclear pion scattering and photoproduction.

As follows from their definitions, the density matrices are Hermitian:

$$\begin{aligned} \rho_1(x;x') &= \rho_1^*(x';x), \\ \rho_2(x_1,x_2;x_1',x_2') &= \rho_2^*(x_1',x_2';x_1,x_2). \end{aligned} \tag{2.5}$$

They are related by the formula

$$\int \mathrm{d}x_2\, \rho_2(x_1,x_2;x_1',x_2) = (A-1)\rho_1(x_1;x_1'). \tag{2.6}$$

The one-body density matrix in momentum space is obtained using the double Fourier transform:

$$\rho_1(\boldsymbol{p},s,\tau;\boldsymbol{p}',s',\tau') = \int \mathrm{d}\boldsymbol{r}\,\mathrm{d}\boldsymbol{r}'\, e^{i(\boldsymbol{p}\cdot\boldsymbol{r}-\boldsymbol{p}'\cdot\boldsymbol{r}')}\rho_1(x;x'). \tag{2.7}$$

A similar relation holds for the momentum-space two-body density matrix.

The diagonal elements of the density matrices,

$$\rho_1(x) \equiv \rho_1(x;x), \tag{2.8a}$$

$$\rho_2(x_1,x_2) \equiv \rho_2(x_1,x_2;x_1,x_2), \tag{2.8b}$$

referred to as "densities" or "density distributions", are of special importance because they represent the probability densities of finding particles in specific states and positions. For an infinitesimal volume $\mathrm{d}V_1$, $\mathrm{d}V_1\rho_1(x_1)/A$ provides the probability of finding a nucleon with spin s_1 and isospin τ_1 in the volume $\mathrm{d}V_1$ around the coordinate $\boldsymbol{r}_1$ when other nucleons have arbitrary positions, spins, and isospins. Similarly, $\rho_2(x_1,x_2)/A(A-1)$ gives the probability density for finding two nucleons with coordinates, spins, and isospins specified by x_1 and x_2. The density distributions, Eqs. (2.8), are positive definite, and ρ_2 is symmetric in its coordinates: $\rho_2(x_1,x_2) = \rho_2(x_2,x_1)$. The normalization conditions for the densities are

$$\int \mathrm{d}x\, \rho_1(x) = A, \tag{2.9a}$$

$$\int \mathrm{d}x_1\,\mathrm{d}x_2\, \rho_2(x_1,x_2) = A(A-1). \tag{2.9b}$$

Since nucleons obey Fermi-Dirac statistics, the total wave function of the nuclear system, $\Psi_0(x_1,\ldots,x_A)$, is antisymmetric with respect to the exchange of any two nucleons. This antisymmetry applies also to the density matrices:

$$\rho_2(x_1,x_2;x_1',x_2') = -\rho_2(x_2,x_1;x_1',x_2') = -\rho_2(x_1,x_2;x_2',x_1'). \tag{2.10}$$

The simplest approach to impose the required antisymmetry property of a system of fermions is to employ the A-body Slater determinant form for the total wave function:

$$\Psi_0^{\mathrm{SD}}(x_1,\cdots,x_A) \equiv \frac{1}{\sqrt{A!}}\det\{\phi_{\alpha_i}(x_j)\}, \tag{2.11}$$

with the determinant taken over the matrix of single-nucleon wave functions forming an orthonormal basis:

$$\phi_{\alpha_i}(x_j) = \varphi_{\alpha_i}(\boldsymbol{r}_j)\chi_i(s_j)\eta_i(\tau_j), \tag{2.12}$$

where $\varphi_{\alpha_i}(\boldsymbol{r})$ is the spatial part of the wave function, while $\chi_i(s)$ and $\eta_i(\tau)$ are the spinor and isospinor, respectively, of the i-th nucleon. The multi-index $\alpha \equiv \{n, l, j, m, m_j\}$ encapsulates all the quantum numbers fully specifying the state of a nucleon. The Slater determinant form of the total nuclear wave function is based on the *independent particle assumption*. Besides explicitly accounting for the Pauli correlations, this approach allows for incorporating nucleon interactions forming the nuclear mean field, which affects the single-particle states $\phi_\alpha(x)$.

Substituting the Slater determinant wave function into Eqs. (2.1) yields the following correlation matrices:

$$\rho_1^{\mathrm{SD}}(x; x') = \sum_{i=1}^{A} \phi^\dagger_{\alpha_i}(x)\phi_{\alpha_i}(x'), \tag{2.13a}$$

$$\begin{aligned}\rho_2^{\mathrm{SD}}(x_1, x_2; x_1', x_2') = \sum_{i,j=1}^{A} \Big[&\phi^\dagger_{\alpha_i}(x_1)\phi^\dagger_{\alpha_j}(x_2)\phi_{\alpha_i}(x_1')\phi_{\alpha_j}(x_2') \\ &- \phi^\dagger_{\alpha_i}(x_1)\phi^\dagger_{\alpha_j}(x_2)\phi_{\alpha_i}(x_2')\phi_{\alpha_j}(x_1')\Big].\end{aligned} \tag{2.13b}$$

Hence, the two-body density matrix within the Slater determinant assumption can be expressed solely in terms of the one-body density matrix as

$$\rho_2^{\mathrm{SD}}(x_1, x_2; x_1', x_2') = \rho_1^{\mathrm{SD}}(x_1; x_1')\rho_1^{\mathrm{SD}}(x_2; x_2') - \rho_1^{\mathrm{SD}}(x_1; x_2')\rho_1^{\mathrm{SD}}(x_2; x_1'). \tag{2.14}$$

By substituting the explicit structure of the single-nucleon wave functions from Eq. (2.12) into Eq. (2.13a), we find that only the one-body density matrices that are diagonal in spin and isospin are nonzero: $\rho_1^{\mathrm{SD}}(x; x') \propto \delta_{ss'}\delta_{\tau\tau'}$. Employing the Slater determinant total wave function incorporates the Pauli exclusion principle in the two-body correlation function, Eq. (2.14), resulting in $\rho_2(x, x) = 0$, where the two-body density is defined by Eq. (2.8b).

The spin-isospin-independent density matrices defined as

$$\rho_1(\boldsymbol{r}; \boldsymbol{r}') \equiv \sum_{s,\tau} \rho_1(\boldsymbol{r}, s, \tau; \boldsymbol{r}', s, \tau), \tag{2.15a}$$

$$\rho_2(\boldsymbol{r}_1, \boldsymbol{r}_2; \boldsymbol{r}_1', \boldsymbol{r}_2') \equiv \sum_{s_1,s_2} \sum_{\tau_1,\tau_2} \rho_2(\boldsymbol{r}_1, s_1, \tau_1, \boldsymbol{r}_2, s_2, \tau_2, ; \boldsymbol{r}_1', s_1, \tau_1, \boldsymbol{r}_2', s_2, \tau_2), \tag{2.15b}$$

can be further simplified for spin-zero nuclei with an equal number of protons and neutrons considered in this thesis. In this case, by neglecting the Coulomb interaction and assuming isospin invariance, the resulting single-nucleon basis includes $A/4$ spatial wave functions. As result, the spin-isospin-independent one-body correlation matrix allows for trivial summation over spin and isospin:

$$\rho_1^{\mathrm{SD}}(\boldsymbol{r}; \boldsymbol{r}') = 4\sum_{i=1}^{A/4} \varphi^*_{\alpha_i}(\boldsymbol{r})\varphi_{\alpha_i}(\boldsymbol{r}'), \tag{2.16}$$

where the factor 4 results from the spin and isospin degeneracy of the single-nucleon basis. Similarly, the spin-isospin-independent two-body correlation matrix for spin-isospin-zero nuclei becomes

$$\begin{aligned}\rho_2^{\mathrm{SD}}(\boldsymbol{r}_1,\boldsymbol{r}_2;\boldsymbol{r}_1',\boldsymbol{r}_2') \\ = \sum_{i,j=1}^{A/4}\Big[16\,\varphi^*_{\alpha_i}(\boldsymbol{r}_1)\varphi^*_{\alpha_j}(\boldsymbol{r}_2)\varphi_{\alpha_i}(\boldsymbol{r}_1')\varphi_{\alpha_j}(\boldsymbol{r}_2') - 4\,\varphi^*_{\alpha_i}(\boldsymbol{r}_1)\varphi^*_{\alpha_j}(\boldsymbol{r}_2)\varphi_{\alpha_i}(\boldsymbol{r}_2')\varphi_{\alpha_j}(\boldsymbol{r}_1')\Big] \\ = \rho_1^{\mathrm{SD}}(\boldsymbol{r}_1;\boldsymbol{r}_1')\rho^{\mathrm{SD}}(\boldsymbol{r}_2;\boldsymbol{r}_2') - \frac{1}{4}\rho_1^{\mathrm{SD}}(\boldsymbol{r}_1;\boldsymbol{r}_2')\rho_1^{\mathrm{SD}}(\boldsymbol{r}_2;\boldsymbol{r}_1'). \quad (2.17)\end{aligned}$$

Correspondingly, the spin-isospin-independent two-body density for the Slater determinant wave function takes the form

$$\rho_2^{\mathrm{SD}}(\boldsymbol{r}_1,\boldsymbol{r}_2) = \rho_1^{\mathrm{SD}}(\boldsymbol{r}_1)\rho_1^{\mathrm{SD}}(\boldsymbol{r}_2) - \frac{1}{4}|\rho_1^{\mathrm{SD}}(\boldsymbol{r}_1;\boldsymbol{r}_2)|^2. \quad (2.18)$$

The obtained result does not fulfill the basic property $\rho_2(\boldsymbol{r},\boldsymbol{r}) = 0$, which forbids two nucleons from occupying the same point in space. While the Slater determinant wave function automatically satisfies the Pauli exclusion principle for nucleons with the same spin and isospin, it fails to account for short-range repulsion between nucleons in different spin-isospin states, leading to $\rho_2(\boldsymbol{r},\boldsymbol{r}) \neq 0$. To solve this problem, a more sophisticated structure for the nuclear wave function is required.[2] Despite its limitations in short-range behavior, the mean-field approach utilizing the Slater determinant approximation is effective and useful for describing nuclear structure functions, as will be demonstrated in the next Section. We will return to discussing the influence of short-range correlations in the context of nuclear pion scattering and photoproduction in Sec. 2.4.

2.2 One-body nuclear structure functions

In the study of nuclear physics, one-body nuclear structure functions play a crucial role in understanding the properties of individual nucleons within a nucleus. Key quantities of interest include the proton and neutron density distributions, which are derived from the spin summation of diagonal elements of the corresponding one-body density matrices:

$$\rho^{(N)}(\boldsymbol{r}) = \sum_{s=\downarrow,\uparrow}\rho_1(\boldsymbol{r},s,\tau_N), \quad (2.19)$$

where the superscript N stands for protons (p) and neutrons (n). The nucleon density, characterizing the nucleon distribution within a nucleus, is defined as

$$\rho(\boldsymbol{r}) = \rho^{(p)}(\boldsymbol{r}) + \rho^{(n)}(\boldsymbol{r}) = \sum_{s,\tau}\rho_1(\boldsymbol{r},s,\tau). \quad (2.20)$$

[2] A common approach for including short-range correlations is employing a Jastrow-type wave function [158], modifying the simple Slater determinant by incorporating factors that accounts for the interactions between nucleon pairs. For example, see Ref. [159], where the Jastrow correlation method is allied using HO single-particle wave functions and a state-independent gaussian-like correlation function.

This nucleon density distribution corresponds to the ground-state expectation value of the local density operator

$$\hat{\rho} = \sum_{i=1}^{A} \delta(\boldsymbol{r} - \hat{\boldsymbol{r}}_i), \tag{2.21}$$

where $\hat{\boldsymbol{r}}_i$ represents the position operator of the i-th nucleon.

Since nucleons are not elementary particles, the charge density distribution of a nucleus, $\rho_{\rm ch}(\boldsymbol{r})$, differs from the protons density distribution $\rho^{(p)}(\boldsymbol{r})$. The charge distribution in an individual proton is not point-like and is characterized by the density function $\rho_{\rm ch}^{(1p)}(\boldsymbol{r})$. Consequently, the charge distribution produced by protons within the nucleus is given by the convolution

$$\rho_{\rm ch}^{(p)}(\boldsymbol{r}) = \int \mathrm{d}\boldsymbol{r}'\, \rho^{(p)}(\boldsymbol{r}')\rho_{\rm ch}^{(1p)}(\boldsymbol{r} - \boldsymbol{r}'). \tag{2.22}$$

While $\rho_{\rm ch}^{(p)}(\boldsymbol{r})$ provides the dominant part of the charge distribution in nuclei, the overall nuclear charge density consists of both proton and neutron contributions:

$$\rho_{\rm ch}(\boldsymbol{r}) = \rho_{\rm ch}^{(p)}(\boldsymbol{r}) + \rho_{\rm ch}^{(n)}(\boldsymbol{r}), \tag{2.23}$$

where nonzero $\rho_{\rm ch}^{(n)}(\boldsymbol{r})$ arises due to the nontrivial internal structure of the neutron.

The mean-square radius serves as a key characteristic of symmetric density distributions. For instance, investigating the charge mean-square radius of nuclei, defined as

$$\langle r_{\rm ch}^2 \rangle = \frac{4\pi}{Z} \int_0^\infty \mathrm{d}r\, r^4 \rho_{\rm ch}(r), \tag{2.24}$$

with the number of protons Z, played an important role in highlighting the importance of neutron contribution $\rho_{\rm ch}^{(n)}(\boldsymbol{r})$ to the overall nuclear charge distribution, Eq. (2.23). Electron scattering [160] and muonic X-ray [161] experiments investigating the isotope shifts have revealed a decrease in the charge rms radii for ^{40}Ca and ^{48}Ca. This anomalous narrowing of the charge distribution, as demonstrated in Ref. [162], is attributed to the non-negligible negative contribution from the skin formed by eight $f_{7/2}$ neutrons. Despite being electrically neutral, neutrons possess a charge distribution with a negative mean-square radius of about $-0.116\,\mathrm{fm}^2$ [5], which is not negligible compared to the mean-square radius of the proton, $0.707\,\mathrm{fm}^2$.

Although the density distributions are defined in coordinate space, their momentum-space representations are of special importance, as shown in the previous Chapter. The Fourier transform of the nucleon density distribution yields the nucleon density form factor:

$$\rho(\boldsymbol{q}) = \int \mathrm{d}\boldsymbol{r}\, e^{i\,\boldsymbol{q}\cdot\boldsymbol{r}} \rho(\boldsymbol{r}). \tag{2.25}$$

A similar definition applies to the charge form factor, resulting in Eq. (1.5) for symmetric nuclei. It follows from the normalization condition for $\rho(\boldsymbol{r})$, Eq. (2.9a), that $\rho(\boldsymbol{q} = 0) = A$ and $\rho_{\rm ch}(\boldsymbol{q} = 0) = Z$.

As a result of the properties of the Fourier transform, Eqs. (2.22) and (2.23) yield the following relation between charge and nucleon distribution form factors for isospin-zero nuclei

$$\rho(q) = \frac{2\rho_{\rm ch}(q)}{\rho_{\rm ch}^{(1p)}(q) + \rho_{\rm ch}^{(1n)}(q)}, \tag{2.26}$$

where $\rho_{\rm ch}^{(1p)}(q)$ and $\rho_{\rm ch}^{(1n)}(q)$ are the charge form factors of the individual proton and neutron, respectively, and the isospin symmetry is assumed.

2.2.1 Model-independent charge densities from electron scattering

Determining the nuclear charge density $\rho_{\rm ch}(r)$ provides crucial insights into the nucleon distribution within nuclei and serves as a fundamental test for nuclear structure models. Electron-nucleus elastic scattering offers an exceptionally precise method for measuring this quantity. With accurate experimental data, model-independent methods have been developed to analyze measured electron scattering cross sections and extract nuclear charge densities [163–165].

The model-independent approach is based on the general and plausible assumption that the density function can be expanded in a complete set of orthogonal functions $P_n(r)$:

$$\rho_{\rm ch}(r) = \sum_{n=1}^{\infty} A_n P_n(r). \tag{2.27}$$

The expansion coefficients A_n are determined by fitting the experimental elastic electron scattering cross section using Eq. (1.5).

The Fourier-Bessel (FB) basis, first applied in Ref. [164], has been widely used to analyze both elastic [166, 167] and inelastic [168] electron scattering data for spherical or near-spherical nuclei [169]. The orthogonality relation for the spherical Bessel functions of the first kind in a finite interval $[0, R_c]$ is given by

$$\int_0^{R_c} {\rm d}r\, r^2 j_l(q_n^l r) j_l(q_m^l r) = \frac{1}{2}\delta_{n,m} R_c^3 \left[j_{l+1}(q_n^l R_c)\right]^2, \tag{2.28}$$

where $q_n^l R_c$ is the n-th zero of the l-order Bessel function $j_l(x)$, defined from $j_l(q_n^l R_c) = 0$.

As follows from Eq. (2.28), employing the FB basis involves truncating the density at the cutoff radius R_c. For the elastic process, zeroth-order spherical Bessel functions $j_0(x) = \sin x/x$ are commonly used, resulting in the expansion of the charge density function as

$$\rho_{\rm ch}^{\rm FB}(r) = \theta(R_c - r) \sum_{n=1}^{n_{\rm max}} a_n j_0\left(q_n r\right), \tag{2.29}$$

where $\theta(x)$ is the Heaviside step function and

$$q_n = q_n^0 = \frac{n\pi}{R_c}. \tag{2.30}$$

The corresponding series in momentum space, obtained by the Fourier transform, Eq. (1.6), provides the charge form factor expressed as

$$\rho_{\rm ch}^{\rm FB}(q) = 4\pi \frac{\sin(qR_c)}{q} \sum_{n=1}^{n_{\rm max}} a_n \frac{(-1)^n}{q^2 - q_n^2}. \tag{2.31}$$

The normalization condition $\rho_{\text{ch}}(0) = Z$ imposes the constraint on the expansion coefficients

$$Z = 4\pi R_c \sum_{n=1}^{n_{\max}} a_n \frac{(-1)^{n+1}}{q_n^2}. \tag{2.32}$$

The expansions given by Eqs. (2.29) and (2.31) actually exhibit some degree of model dependence. Truncating the density at R_c produces a discontinuity in the density function, resulting in a nonphysical contribution to the form factor. Since electron scattering data are available only up to a finite momentum transfer $q_{\max}$, the optimal value of R_c is chosen to minimize the unphysical contribution within the momentum range defined by the experiment (see Ref. [166] for details). Because the contribution of the n-th expansion term in Eq. (2.31) to the form factor is localized around the q_n, the optimal number of expansion coefficients is determined by the maximal experimentally measured momentum $q_{\max}$ as

$$n_{\max} = \frac{1}{\pi} q_{\max} R_c. \tag{2.33}$$

The charge densities derived from the FB approach are significantly more robust than those obtained from model-dependent fits. An additional advantage of the FB expansion method is that it enables the separate determination of uncertainties in the charge distribution arising from experimental errors and from the lack of knowledge about the behavior at large q. Notably, another widely used model-independent approach is expansion in the sum of Gaussians, first introduced in Ref. [165]. Both methods provide nearly identical results for the same analyzed data set. However, due to the strong correlation between the expansion coefficients, calculating the uncertainties in the charge distribution requires the full correlation matrix, which is unfortunately never published [7].

2.2.2 The Fermi-gas model

While nuclear physics is governed by strong forces between nucleons, a simplified framework can aid in exploring fundamental aspects of the nuclear ground state. The Fermi-gas assumption offers the simplest approach, treating nucleons within nuclei as a gas of non-interacting fermions at zero temperature. The Pauli exclusion principle keeps fermions separated and moving even at zero temperature, forcing them to occupy quantum states up to a maximum energy level called the Fermi energy. Below this energy, all states are gradually filled, forming the so-called Fermi sea. Given that the mean free path of a nucleon within the nuclear medium is comparable with the size of the nucleus, it is reasonable to expect that these crude assumptions can adequately capture the fundamental properties of nuclei [170, 171].

Since any interaction besides the Pauli correlations is neglected, the single-particle wave functions within the Fermi-gas model are the plane waves:

$$\varphi_n^{\text{FG}}(\boldsymbol{r}) = \frac{1}{\sqrt{V}} e^{i\,\boldsymbol{k}_n \cdot \boldsymbol{r}}, \tag{2.34}$$

where V is the nuclear volume and k_n is the momentum the n-th nucleon. Consequently,

the one-body density matrix, Eq. (2.16), becomes

$$\rho_1^{\mathrm{FG}}(\boldsymbol{r};\boldsymbol{r}') = \frac{4}{V}\sum_{k_n\le k_F} e^{-i\,\boldsymbol{k}_n\cdot\boldsymbol{r}'}e^{i\,\boldsymbol{k}_n\cdot\boldsymbol{r}}, \tag{2.35}$$

where the summation over A states is presented as the summation over all momenta below the Fermi momentum k_F. In the thermodynamic limit, the summation is replaced by an integral over the momenta within the Fermi sea:

$$\frac{1}{V}\sum_{k_n\le k_F} \longrightarrow \int_0^{k_F}\frac{\mathrm{d}\boldsymbol{k}}{(2\pi)^3}. \tag{2.36}$$

Performing the integration yields the one-body density matrix in the form

$$\rho_1^{\mathrm{FG}}(\boldsymbol{r};\boldsymbol{r}') = 3\rho_0\frac{j_1(k_F|\boldsymbol{r}'-\boldsymbol{r}|)}{k_F|\boldsymbol{r}'-\boldsymbol{r}|}, \tag{2.37}$$

where $j_1(x) = \sin(x)/x^2 - \cos(x)/x$ is the first-order spherical Bessel function and

$$\rho_0 \equiv \frac{2k_F^3}{3\pi^2}. \tag{2.38}$$

Given that $\rho(\boldsymbol{r}) \equiv \rho_1(\boldsymbol{r};\boldsymbol{r})$ and $j_1(x)/x \to 1/3$ as $x \to 0$, it follows from Eq. (2.37) that ρ_0 represents the density of the Fermi gas: $\rho^{\mathrm{FG}}(\boldsymbol{r}) = \rho_0$. Correspondingly, the momentum of the highest occupied state depends solely on the density ρ_0, as indicated by Eq. (2.38). Apart from the global factor of 4 in Eq. (2.35), which accounts for spin and isospin degeneracy, the obtained equations are general and apply to any system of non-interacting fermions.

In the context of nuclear physics, the Fermi-gas model suggests the existence of a saturation density that is independent of the nuclear mass, as a consequence of the Pauli principle. However, this framework cannot predict the value of ρ_0 itself. Assuming that the Fermi-gas density coincides with that of saturated nuclear matter, $\rho_0 \approx 0.16\,\mathrm{fm}^{-3}$, the corresponding Fermi momentum is $k_F = 1.33\,\mathrm{fm}^{-1}$. To account for the finite size of a real nucleus, we can assume that all its mass is contained within the radius R, with the density distribution modeled as a step-like function:

$$\rho^{\mathrm{FG}}(r) = \rho_0\,\theta(R-r). \tag{2.39}$$

Consequently, the normalization condition Eq. (2.9a) for the Fermi-gas model becomes

$$A = \int \mathrm{d}\boldsymbol{r}\,\rho_0\,\theta(R-r) = \frac{4}{3}\pi R^3\rho_0. \tag{2.40}$$

As a result, the nuclear radius is defined as $R = r_0A^{1/3}$ with $r_0 = 3^{1/3}/(4\pi\rho_0)^{1/3} \approx 1.14\,\mathrm{fm}$. Finally, the nucleon density form factor within the Fermi-gas model is given by

$$\rho^{\mathrm{FG}}(q) = 3A\,\frac{j_1(Rq)}{Rq}. \tag{2.41}$$

The Fermi-gas model provides a largely simplified yet valuable framework demonstrating how certain nuclear properties follow directly from the Pauli exclusion principle. However, it falls short in explaining several key phenomena observed in atomic nuclei, notably the existence of specific *magic numbers* of protons or neutrons that make nuclei exceptionally stable. Even in terms of symmetry, translation-invariant plane waves cannot fully describe a finite nucleus, which is only invariant under translations of its center of mass. Thus, a more realistic description of nuclear structure requires incorporating the interactions between nucleons. In the next Section, we will compare the predictions of the Fermi-gas model with those of other more reliable approaches.

2.2.3 The harmonic oscillator shell model

Despite the significant limitations of the Fermi-gas model, this approach has demonstrated the effectiveness of the independent-particle assumption in describing nuclear structure. Consequently, a natural step in improving the nuclear model is to incorporate nucleon-nucleon interactions through an effective potential that acts on individual nucleons.

In a more realistic framework, the nucleus is considered as a non-relativistic quantum-mechanical system described by the many-body Hamiltonian

$$\hat{H} = -\frac{\hbar^2}{2m}\sum_{i=1}^{A}\Delta_i + \frac{1}{2}\sum_{i\neq j}^{A} v(\boldsymbol{r}_i, \boldsymbol{r}_j) + \cdots , \tag{2.42}$$

where the potential $v(\boldsymbol{r}_i, \boldsymbol{r}_j)$ describes the two-nucleon interaction and spin-isospin dependence is omitted for simplicity. In general, the full Hamiltonian also includes terms accounting for three-body and other many-body forces. In practice, however, even accounting for just two-body interactions within the many-body framework makes calculations extremely complicated as the number of particles increases.

The mean-field approximation is employed to simplify the problem, assuming that the interaction of each particle with the rest of the system can be effectively reduced to a self-consistent field. Thus, instead of considering the detailed interactions between every pair of particles, nucleons are treated as bound in a central one-particle potential $U(\boldsymbol{r})$. Consequently, the nuclear many-body Hamiltonian is approximated by a sum of one-body Hamiltonians describing the motion of A independent nucleons:

$$\hat{H} \approx \sum_{i=1}^{A}\left[-\frac{\hbar^2}{2m}\Delta_i + U(\boldsymbol{r}_i)\right]. \tag{2.43}$$

The spectral equation with the Hamiltonian given by Eq. (2.43) is factorizable, and the single-particle wave functions $\phi_\alpha(\boldsymbol{r})$ are solutions of the one-particle Schrödinger equation

$$\left[-\frac{\hbar^2}{2m}\Delta + U(\boldsymbol{r})\right]\phi_\alpha(\boldsymbol{r}) = \varepsilon_\alpha\phi_\alpha(\boldsymbol{r}). \tag{2.44}$$

The ground state wave function of the system is given by the Slater determinant, Eq. (2.11), while the total system energy is a sum of single-particle energies: $E = \sum_i \varepsilon_{\alpha_i}$. Similar to the formation of the Fermi sea governed by the Pauli principle, nucleons within the potential $U(\boldsymbol{r})$ fill the lowest available energy states up to the Fermi energy.

The simplicity gained by reducing the complex many-body problem to a one-body problem comes with the challenge of determining the single-particle potential $U(\boldsymbol{r})$. The Hartree-Fock approach provides a method for deriving $U(\boldsymbol{r})$ from the two-body nucleon-nucleon interaction $\sum_{i\neq j} v(\boldsymbol{r}_i, \boldsymbol{r}_j)$ (see Ref. [172] for details). However, this method still has limitations associated with the Slater determinant form of the total wave function and approximate modeling of nucleon interactions. Therefore, employing a phenomenological potential is a common and effective approach for describing of nuclear structure. The parameters of the phenomenological potential are individual for each nucleus and are determined by fitting experimental data on charge form factor, charge rms radius, or the energy spectrum.

In the simplest approximation, the single-particle potential can be represented by the isotropic harmonic oscillator potential:

$$U^{\mathrm{HO}}(r) = -U_0 + \frac{1}{2} m\omega^2 r^2. \tag{2.45}$$

Solving the spherically symmetric Schrödinger equation allows for the variable separation, resulting in the HO eigenfunctions of the form

$$\varphi^{\mathrm{HO}}_{nlm}(\boldsymbol{r}) = R^{\mathrm{HO}}_{nl}(r/a) Y_{lm}(\Omega_{\boldsymbol{r}}), \tag{2.46}$$

with the HO parameter $a^2 \equiv \hbar/(m\omega)$ and the spherical harmonics $Y_{lm}(\Omega)$. The radial part of the HO wave function is given by

$$R^{\mathrm{HO}}_{nl}(\rho) = \frac{1}{a^{3/2}} \sqrt{\frac{2 \cdot n!}{\Gamma(n + l + 3/2)}} \rho^l e^{-\rho^2/2} L_n^{l+\frac{1}{2}}(\rho^2), \tag{2.47}$$

where $L_n^{\alpha}(x)$ are the generalized Laguerre polynomials, and $\Gamma(x)$ is the gamma function. The energy eigenvalues corresponding to these eigenfunctions are

$$E_N = \hbar\omega \left(N + \frac{3}{2} \right) - U_0, \tag{2.48}$$

with the principal quantum number $N = 2n + l$. The HO spectrum exhibits degeneracy, with each energy level N corresponding to $(N+1)(N+2)/2$ combinations of the radial (n), orbital (l) and magnetic (m) quantum numbers. Furthermore, there is an additional factor of 2 due to spin degeneracy. Thus, the HO single-nucleon states group together in sets that share the same energy E_N, where each group contains $(N+1)(N+2)$ proton or neutron states.

Just as the atomic shell model arranges electrons in discrete energy shells within the Coulomb field of the nucleus, nucleons fill energy levels in the single-nucleon potential $U(\boldsymbol{r})$. Due to the significant degeneracy of nuclear orbitals, the highest nuclear binding energy is achieved when the outermost energy shell is completely filled. According to the nuclear shell model utilizing the HO potential, closed shells are predicted to form with $2, 8, 20, 40, 70, \cdots$ nucleons, whether protons or neutrons.[3] However, experimental observations reveal a different set of magic numbers: $2, 8, 20, 28, 50, 82, \cdots$, as depicted

[3] Nuclei in which both the proton and neutron numbers correspond to the magic ones, e.g, ^{4}He, ^{16}O, ^{40}Ca, ^{48}Ca, and ^{208}Pb, are referred to as "double magic".

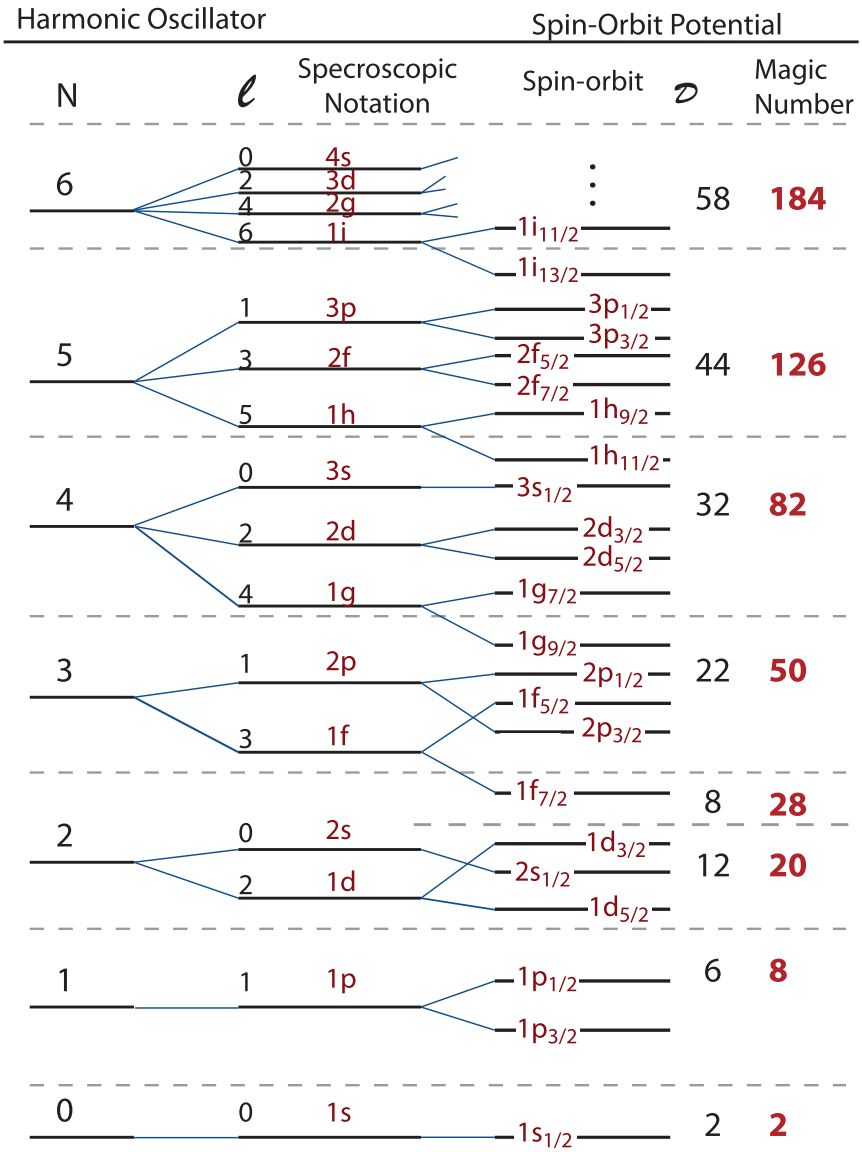

Figure 2.1: The nuclear energy spectrum from Ref. [173]. The horizontal dashed lines represent the separation between different shells. On the left, shell model energy levels are depicted, derived using the HO potential with the principal quantum number $N = 2n + l$. In the middle, degeneracy in the orbital angular momentum l is removed, as in the spectrum of the Woods–Saxon potential, yet the shells remain consistent with the HO potential. On the right, realistic energy levels are shown, obtained with a potential that incorporates the spin-orbit interaction, separating states with different total angular momentum $j = l \pm 1/2$. The second-to-last and the last columns provide the number of nucleons within a closed shell ($\mathcal{D}$) of the realistic potential and the corresponding magic numbers, respectively.

in Fig. 2.1. As shown in the plot, accurately describing the energy spectrum requires removing degeneracy not only in the orbital angular momentum l, but also in the total angular momentum $j = l \pm 1/2$. To properly separate the energy levels of heavy nuclei, a more realistic nuclear potential that incorporates spin-orbit interaction is necessary [174]. Consequently, the HO potential lose its efficiency for heavy nuclei. Nevertheless, since the heaviest nucleus under consideration in this thesis is ^{40}Ca, employing the HO shell model is considered a reasonable choice.

A prominent characteristic of nuclei with fully closed shells is their spherical symmetry.[4] This symmetry allows for the explicit simplification of the sum over m states in the one-body density matrix, Eq. (2.16). Using the addition theorem for the spherical harmonics:

$$\sum_{m=-l}^{l} Y_{lm}^{*}(\Omega_{\boldsymbol{r}'}) Y_{lm}(\Omega_{\boldsymbol{r}}) = \frac{2l+1}{4\pi} P_l(\cos\theta_{\boldsymbol{r}\boldsymbol{r}'}), \tag{2.49}$$

where $\theta_{\boldsymbol{r}\boldsymbol{r}'}$ is the angle between $\boldsymbol{r}$ and $\boldsymbol{r}'$ vectors, the one-body density matrix takes the form

$$\rho_1(\boldsymbol{r}, \boldsymbol{r}') = \frac{1}{4\pi} \sum_{nl} 4(2l+1)\eta_{nl} R_{nl}^{\mathrm{HO}}(r) R_{nl}^{\mathrm{HO}}(r') P_l(\cos\theta_{\boldsymbol{r}\boldsymbol{r}'}). \tag{2.50}$$

Here, the factor of 4 is due to the summation over spin and isospin, and we explicitly introduce the occupation probability η_{nl} of the nl orbital. Within the employed individual-nucleon assumption, this probability equals 1 for filled states in closed-shell nuclei.

In addition to nuclei with completely closed shells, those with closed subshells also exhibit spherical symmetry. A "subshell" refers to a group of atomic orbitals that share the same n, l, and j quantum numbers, e.g., the $1p$ shell consists of the $1p_{3/2}$ and $1p_{1/2}$ subshells. Examples of such nuclei include ^{12}C, with a closed $1p_{3/2}$ subshell, and ^{28}Si, with a closed $1d_{5/2}$ subshell (see Fig. 2.1). Within the individual-nucleon assumption in the shell model, the occupation probabilities for closed subshells are expressed through Clebsch–Gordan coefficients, taking values $0 < \eta_{nl} < 1$. Further discussion and comparison of these occupation probabilities with experimental data are given in Appendix 2.A.

One advantage of the HO potential is that it produces relatively simple nucleon wave functions, allowing the entire computation to be handled analytically. Substituting the HO radial wave functions, Eq. (2.47), into Eq. (2.50) yields

$$\rho_1^{\mathrm{HO}}(\boldsymbol{r}'; \boldsymbol{r}) = \frac{4}{\pi^{3/2} a^3} Q(\boldsymbol{r}', \boldsymbol{r}) \exp\left[-\frac{(\boldsymbol{r}^2 + \boldsymbol{r}'^2)}{2a^2}\right], \tag{2.51}$$

[4] This follows from Unsöld's theorem [175], which states that summing over all magnetic quantum number m states for a shell of hydrogen-like orbitals yields a spherically symmetric function.

where

$$Q(\boldsymbol{r}', \boldsymbol{r}) = \begin{cases} 1 & \text{for } {}^{4}\text{He}, \\ 1 + \frac{4}{3}\frac{\boldsymbol{r}\cdot\boldsymbol{r}'}{a^2} & \text{for } {}^{12}\text{C}, \\ 1 + 2\frac{\boldsymbol{r}\cdot\boldsymbol{r}'}{a^2} & \text{for } {}^{16}\text{O}, \\ 1 + 2\frac{\boldsymbol{r}\cdot\boldsymbol{r}'}{a^2} + \frac{6\,(\boldsymbol{r}\cdot\boldsymbol{r}')^2 - 2r^2r'^2}{5a^4} & \text{for } {}^{28}\text{Si}, \\ \frac{5}{2} - \frac{(\boldsymbol{r}-\boldsymbol{r}')^2}{a^2} + 2\frac{(\boldsymbol{r}\cdot\boldsymbol{r}')^4}{a^4} & \text{for } {}^{40}\text{Ca}. \end{cases} \tag{2.52}$$

The corresponding nucleon density distributions, $\rho^{\text{HO}}(r)$, are directly obtained by substituting $\boldsymbol{r}' = \boldsymbol{r}$, and the form factors are given by the Fourier transform of $\rho^{\text{HO}}(r)$. In the following discussion of the HO shell model approach, we will focus on p-shell nuclei for simplicity. The corresponding nucleon density distribution and form factor in this case can be expressed as:

$$\rho^{\text{HO}}(r) = \frac{4}{\pi^{3/2}a^3}\left(1 + \alpha\frac{r^2}{a^2}\right)\exp\left[-\frac{r^2}{a^2}\right], \tag{2.53a}$$

$$\rho^{\text{HO}}(q) = \left(A - \alpha a^2 q^2\right)\exp\left[-a^2q^2/4\right], \tag{2.53b}$$

where $\alpha \equiv (A-4)/6$ is the number of nucleons in the p shell.

Center-of-mass motion

The wave function describing a real nucleus should be an eigenfunction of the total momentum operator, thus being proportional to $\exp(i\boldsymbol{q}\cdot\boldsymbol{R})$, where $\boldsymbol{R} = \sum_i \boldsymbol{r}_i/A$ is the coordinate of the center of mass (c.m.). The residual part of the wave function then depends on $A-1$ "internal" coordinates, e.g., Galilean-invariant Jacobi coordinates $\boldsymbol{\xi}_i$. Consequently, the total wave function, satisfying translation symmetry, can be written as

$$\Psi_0(\boldsymbol{r}_1, \cdots, \boldsymbol{r}_A) = e^{i\boldsymbol{q}\cdot\boldsymbol{R}}\,\overline{\Psi}_0(\boldsymbol{\xi}_1, \ldots, \boldsymbol{\xi}_{A-1}). \tag{2.54}$$

This explicit separation of the internal coordinate space from the c.m. motion allows the form factor to be expressed as [176, 177]

$$\rho(\boldsymbol{q}) = A\int\left(\prod_{i=1}^{A-1}\mathrm{d}\boldsymbol{\xi}_i\right)e^{i\frac{A-1}{A}\boldsymbol{q}\cdot\boldsymbol{\xi}_{A-1}}|\overline{\Psi}_0(\boldsymbol{\xi}_1, \ldots, \boldsymbol{\xi}_{A-1})|^2. \tag{2.55}$$

Employing Eqs. (2.54) and (2.55) allows for proper treatment of nucleus recoil in the description of projectile interactions with the nucleus [177, 178]. However, for deriving the nuclear structure functions, the shell model and Hartree-Fock approaches cannot provide the total wave functions in the form of Eq. (2.54).

Despite the similarities between nuclear and atomic shell models, the systems they describe differ significantly regarding translations of the coordinate system. Electrons are bound within the central Coulomb potential generated by a static nucleus. In contrast, a system of interacting nucleons is invariant under translation of its mass center. However, employing the shell model with a central potential $U(r)$ violates the translation invariance. As a result, the c.m. of the nucleus oscillates around the origin of $U(r)$,

with neither the amplitude nor the kinetic energy of these fluctuations being negligible, especially for light nuclei. These fluctuations are absent in the rest frame of real nuclei, so their effect must be removed. Otherwise, they give rise to spurious contributions.

Another advantage of the HO shell model is that it allows for an unambiguous and straightforward separation of the c.m. motion. Introducing the relative coordinates $\bar{\boldsymbol{r}}_i = \boldsymbol{r}_i - \boldsymbol{R}$, the total wave function of the system, constructed with the HO eigenfunctions Eq. (2.47), can be written as [179]

$$\Psi_0^{\mathrm{HO}}(\boldsymbol{r}_1, \cdots, \boldsymbol{r}_A) = \Psi_0^{\mathrm{HO}}(\bar{\boldsymbol{r}}_1, \cdots, \bar{\boldsymbol{r}}_A) e^{-\frac{1}{2}A\boldsymbol{R}^2/a^2}. \tag{2.56}$$

Consequently, the HO density distribution corrected for the c.m. motion is obtained through the following convolution [179]:

$$\rho^{\mathrm{HOcm}}(\boldsymbol{r}) = \left(\frac{A}{\pi a^2}\right)^{3/2} \int \mathrm{d}\bar{\boldsymbol{r}}\ \rho^{\mathrm{HO}}(\boldsymbol{r} - \bar{\boldsymbol{r}}) \exp\left[A\bar{\boldsymbol{r}}^2/a^2\right], \tag{2.57}$$

which results in the Tassie-Barker correction factor [180] to the form factor:

$$\rho^{\mathrm{HOcm}}(\boldsymbol{q}) = e^{\frac{a^2q^2}{4A}} \rho^{\mathrm{HO}}(\boldsymbol{q}). \tag{2.58}$$

Applying these transformations to the HO density and form factor given by Eqs. (2.53) yields their c.m.-corrected forms:

$$\rho^{\mathrm{HOcm}}(r) = \frac{1}{\pi^{3/2}\bar{a}^3} \frac{2A}{3\bar{\alpha}+2} \left(1 + \bar{\alpha}\frac{r^2}{\bar{a}^2}\right) \exp\left[-\frac{r^2}{\bar{a}^2}\right], \tag{2.59a}$$

$$\rho^{\mathrm{HOcm}}(q) = \left(A - \alpha a^2 q^2\right) \exp\left[-\bar{a}^2 q^2/4\right], \tag{2.59b}$$

with

$$\bar{\alpha} \equiv \alpha \frac{a^2}{\bar{a}^2 + 3/2\alpha(\bar{a}^2 - a^2)} \quad \text{and} \quad \bar{a}^2 \equiv \frac{A-1}{A} a^2. \tag{2.60}$$

While the removal of the c.m. motion in a nuclear many-body system is highly complicated and lacks a unique solution [181, 182], the HO shell model approach allowed for an elegant and exact solution to this problem. For this reason, the HO transformations given by Eqs. (2.57) and (2.58) are commonly applied for other more realistic shell-model potentials [183, 184]. The impact of the c.m. motion correction on the HO shell model for ^{12}C is illustrated in Fig. 2.2.

The charge distribution

Utilizing Eq. (2.26) allows for the derivation of the charge form factor from the HO shell model results given by Eqs. (2.59). However, further application of the analytical approach requires incorporating an additional approximation on the charge distribution within individual nucleons. A common assumption is to omit the neutron density and employ the Gaussian form of the proton's internal charge density:

$$\rho_{\mathrm{ch}}^{(1p)}(\boldsymbol{r}) \approx \left(\frac{1}{\pi a_p^2}\right)^{3/2} \exp\left[-\frac{r^2}{a_p^2}\right], \tag{2.61}$$

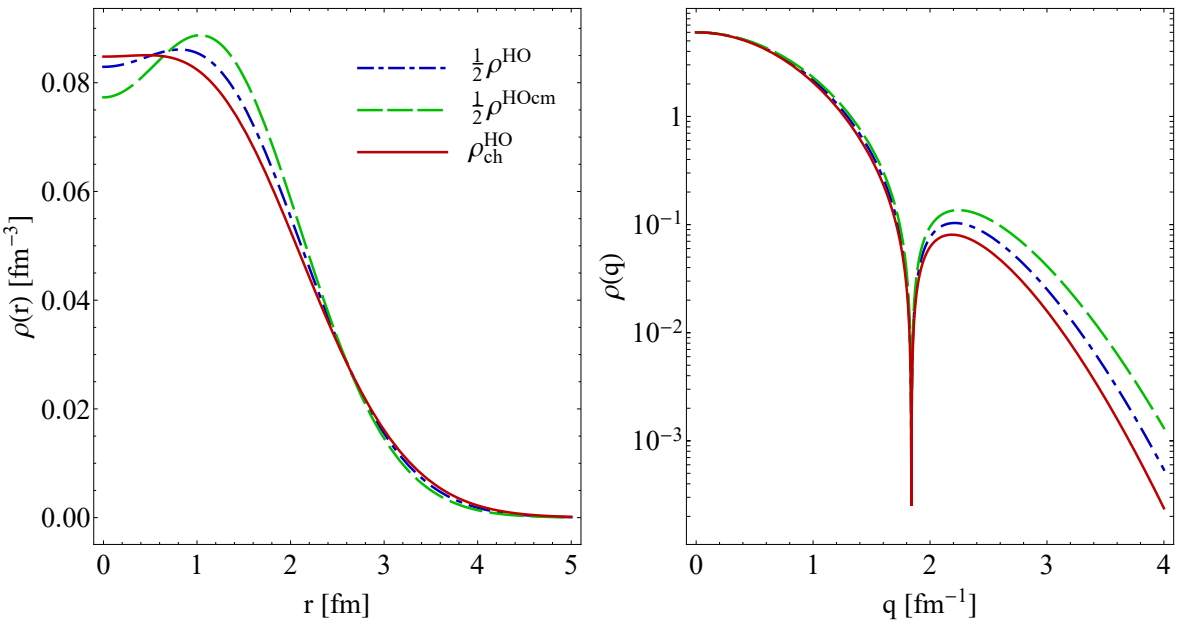

Figure 2.2: Density distributions (**left panel**) and form factors (**right panel**) of ^{12}C within the HO shell model. The dot-dashed blues curves represent the direct HO shell model results for the distribution of protons, given by Eqs. (2.53) divided by 2. The dashed green curves, given by Eqs. (2.59) divided by 2, include the c.m. motion correction. The solid red curves describe the charge distribution, Eqs. (2.62).

with $a_p^2 = 2\langle \bar{r}^2_{\mathrm{ch},1p}\rangle/3$. Here, $\langle \bar{r}^2_{\mathrm{ch},1p}\rangle^{1/2} \approx 0.8\,\mathrm{fm}$ is the effective rms charge radius of the proton within nuclear matter. This value of $\langle \bar{r}^2_{\mathrm{ch},1p}\rangle^{1/2}$ is smaller than that of a free proton $\langle r^2_{\mathrm{ch},1p}\rangle^{1/2} \approx 0.84\,\mathrm{fm}$. This difference can be understood as effectively incorporating the internal charge distribution on the neutron, having a negative mean-square charge radius.

Finally, utilizing Eqs. (2.22) and (2.26), the HO charge density and form factor can be expressed as

$$\rho^{\mathrm{HO}}_{\mathrm{ch}}(r) = \frac{1}{\pi^{3/2}\tilde{a}^3}\frac{2Z}{3\tilde{\alpha}+2}\left(1+\tilde{\alpha}\frac{r^2}{\tilde{a}^2}\right)\exp\left[-\frac{r^2}{\tilde{a}^2}\right], \tag{2.62a}$$

$$\rho^{\mathrm{HO}}_{\mathrm{ch}}(q) = \left(Z - \frac{Z-2}{6}a^2q^2\right)\exp\left[-\tilde{a}^2q^2/4\right], \tag{2.62b}$$

where $Z = A/2$ is the number of protons,

$$\tilde{\alpha} \equiv \alpha\frac{a^2}{\tilde{a}^2 + 3/2\alpha(\tilde{a}^2 - a^2)} \quad \text{and} \quad \tilde{a}^2 \equiv \frac{A-1}{A}a^2 + a_p^2. \tag{2.63}$$

The corresponding mean-square charge radius defined by Eq. (2.24) is expressed as

$$\langle r^2_{\mathrm{ch,HO}}\rangle = \frac{3}{2}\frac{2+5\tilde{\alpha}}{2+3\tilde{\alpha}}\tilde{a}^2. \tag{2.64}$$

Figure 2.64 compares the densities and form factors obtained within the HO shell model, Eqs. (2.53), (2.59), and (2.62). The plot demonstrates that both the internal

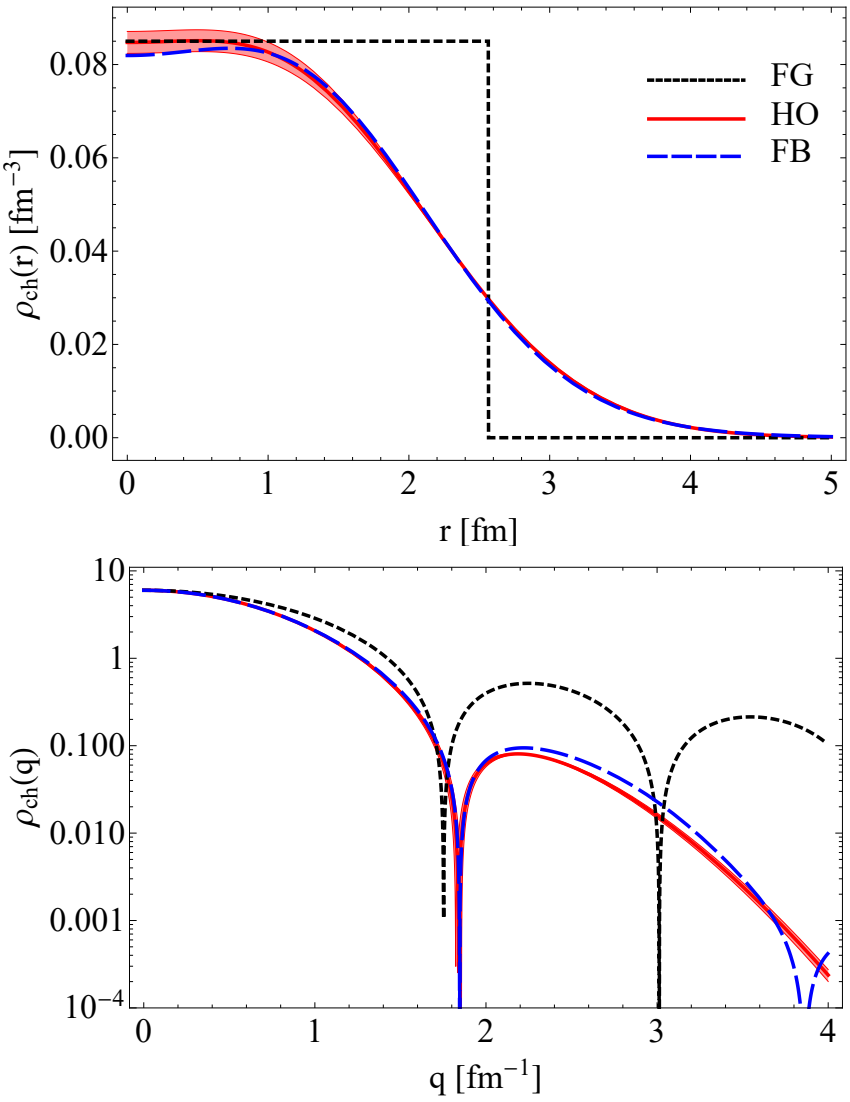

Figure 2.3: Charge density distribution (**upper panel**) and charge form factor (**lower panel**) of ^{12}C. The solid red curves represent results from the HO shell model, while the dashed blue curves show the Fourier-Bessel analysis results [185] The red bands correspond to 1σ variation of the HO parameter $a = 1.63 \pm 0.15\,\text{fm}$, extracted from Ref. [186], although this error band is barely visible in the lower panel. The short-dashed black curves represent the Fermi-gas model predictions, Eqs. (2.39) and (2.41) divided by 2.

charge distribution within the proton and the c.m. motion are non-negligible. The most prominent differences between the structure functions appear at small distances and large momenta, but discrepancies are also present across all regions. Therefore, a precise extraction of the HO parameter a from model-independent analysis or experimental data on charge distribution must account for both c.m. motion and the internal charge distribution within nucleons.

Figure 2.3 illustrates the charge density and form factor of ^{12}C as provided by the HO shell model, the Fermi-gas models, and the model-independent FB analysis. The

Table 2.1: Comparison of the HO parameter a and rms charge radius for ^{12}C, ^{16}O, ^{28}Si, and ^{40}Ca. The value of $\langle r^2_{\mathrm{ch,FB}}\rangle^{1/2}$ ($\langle r^2_{\mathrm{ch,HO}}\rangle^{1/2}$) represents the rms charge radius calculated using the FB (HO) charge density. The experimental values from Ref. [9] are provided by $\langle r^2_{\mathrm{ch,exp}}\rangle^{1/2}$.

	^{12}C	^{16}O	^{28}Si	^{40}Ca
a [fm]	1.63	1.76	1.80	1.98
$\langle r^2_{\mathrm{ch,FB}}\rangle^{1/2}$ [fm]	2.47	2.74	3.09	3.45
$\langle r^2_{\mathrm{ch,HO}}\rangle^{1/2}$ [fm]	2.46	2.71	3.08	3.47
$\langle r^2_{\mathrm{ch,exp}}\rangle^{1/2}$ [fm]	2.47	2.70	3.12	3.48

plot clearly shows that, unlike the Fermi-gas model, the HO shell model's charge distribution and form factor align well with the FB results. The lower panel indicates that only at momentum transfers greater than $2\,\mathrm{fm}^{-1}$, discrepancies between the HO and FB approaches exceed the HO error bars, which are barely visible in the plot. This discrepancy arises from the limitations of the HO shell model and occurs outside the range of data used to fit the HO parameter a. Despite its simplicity, the HO shell model is capable of providing a satisfactory depiction of the charge distribution.

2.2.4 Form factors of ^{12}C, ^{16}O, ^{28}Si, and ^{40}Ca

The successful application of the HO shell model in describing the charge form factor of ^{12}C suggests the potential applicability of this approach to heavier nuclei. Building upon the procedure used to derive the form factors of isospin-zero nuclei with closed p-(sub)shell (^{12}C and ^{16}O), providing Eq. (2.59b) for the form factor, we extend the HO approach to isospin-zero nuclei with closed d-(sub)shell. Performing a similar calculation while considering the additional closed $1d_{5/2}$ subshell, we derive the nucleon distribution form factor of ^{28}Si:

$$\rho^{\mathrm{HOcm}}(q) = \left(28 - 6a^2q^2 + \frac{1}{5}a^4q^4\right)\exp\left[-\frac{1}{4}\frac{A-1}{A}a^2q^2\right]. \tag{2.65}$$

Accounting for the fully closed d shell yields the form factor of ^{40}Ca:

$$\rho^{\mathrm{HOcm}}(q) = \left(40 - 10a^2q^2 + \frac{1}{2}a^4q^4\right)\exp\left[-\frac{1}{4}\frac{A-1}{A}a^2q^2\right]. \tag{2.66}$$

Although the influence of the residual c.m. motion on medium-heavy nuclei like ^{40}Ca is less pronounced compared to ^{12}C, this correction is still included in Eqs. (2.65) and (2.66) due to its straightforward incorporation method.

The HO nucleon density form factors defined by Eqs. (2.59b), (2.65), and (2.66), enable us to determine the corresponding values of the HO model parameters a, which are listed in Table 2.1. This table also provides a comparison of the rms charge radius for HO and FB analyses with experimental values from Ref. [9]. The utilized FB expansion coefficients are taken from Refs. [185] (^{12}C) and [7] (^{16}O, ^{28}Si, and ^{40}Ca). For each nucleus, the FB cutoff radius is $R_c = 8\,\mathrm{fm}$.

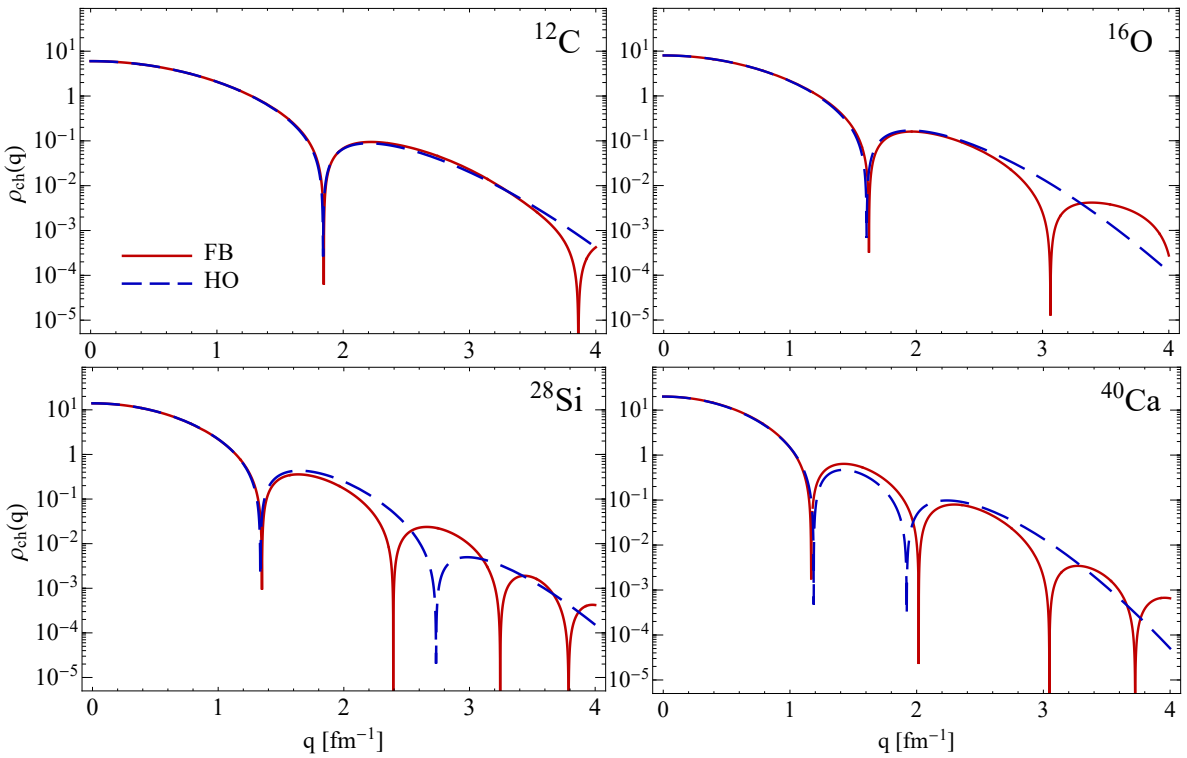

Figure 2.4: The charge form factors of ^{12}C, ^{16}O, ^{28}Si, and ^{40}Ca as functions of momentum. The solid red curves represent the results of the model-independent FB analysis, while the dashed blue curves are provided by the HO shell model. The FB expansion coefficients are taken from Refs. [185] (for ^{12}C) and [7] (for ^{16}O, ^{28}Si, and ^{40}Ca). The values of the HO parameter a are listed in Table 2.1.

In Figure 2.4, we compare charge form factors of ^{12}C, ^{16}O, ^{28}Si, and ^{40}Ca provided by the HO shell model and the model-independent FB approach. The plot reveals a good agreement between the approaches up to $2\,\mathrm{fm}^{-1}$ for ^{12}C and ^{16}O, and up to $1.5\,\mathrm{fm}^{-1}$ for ^{28}Si and ^{40}Ca. Notably, the HO potential efficiently reproduces the first zero of the form factors and captures their overall slope. However, it fails to capture additional zeros (occurring for $q > 1.5\,\mathrm{fm}^{-1}$), leading to increased discrepancies for heavier nuclei.[5] Nonetheless, this range of validity of the HO shell model is satisfactory for the present computations, as discussed in Sec. 2.4.

In conclusion, the HO shell model not only effectively captures fundamental aspects of nuclear structure but also provides a satisfactory depiction of charge distribution within nuclei. Given its ability to accurately describe charge distribution without the need for invoking short-range correlations, it follows that this framework also offers a reasonable description of nucleon distribution as well. Consequently, the shell-model wave functions generated within the HO potential can be applied to derive a reasonable

[5] An accurate description of the form factor of ^{40}Ca at larger momenta can be achieved by employing the Woods-Saxon potential, which includes spin-orbit interaction. The parameters of this potential are typically fitted to the separation energy and the spin-orbit splitting for each state independently [184]. However, this approach, besides not allowing for an analytical solution, poses additional difficulties associated with the orthonormalization of single-nucleon wave functions.

two-body density matrix for ^{12}C, ^{16}O, ^{28}Si, and ^{40}Ca, along with correlation functions.

2.3 Two-body correlation functions

Similarly to the nucleon density distribution given by Eq. (2.20), the spin-isospin-independent two-body density is defined as

$$\rho_2(\boldsymbol{r}_1, \boldsymbol{r}_2) \equiv \sum_{s_1 s_2} \sum_{\tau_1 \tau_2} \rho_2(x_1, x_2). \tag{2.67}$$

As follows from the definition of the two-body density matrix, Eq. (2.1b), the density $\rho_2(\boldsymbol{r}_1, \boldsymbol{r}_2)$ corresponds to the ground-state expectation value of the two-body local density operator

$$\hat{\rho}_2 = \sum_{i=1}^{A} \sum_{j \neq i}^{A} \delta(\boldsymbol{r}_1 - \hat{\boldsymbol{r}}_i) \delta(\boldsymbol{r}_2 - \hat{\boldsymbol{r}}_j). \tag{2.68}$$

Correspondingly, the two-body nucleon density in momentum space is given by the double Fourier transform:

$$\rho_2(\boldsymbol{q}_1, \boldsymbol{q}_2) = \int \mathrm{d}\boldsymbol{r}_1 \, \mathrm{d}\boldsymbol{r}_2 \, e^{i(\boldsymbol{q}_1 \cdot \boldsymbol{r}_1 + \boldsymbol{q}_2 \cdot \boldsymbol{r}_2)} \rho_2(\boldsymbol{r}_1, \boldsymbol{r}_2). \tag{2.69}$$

As follows from Eq. (2.13b), the two-body density of a system described by the Slater determinant total wave function can be expressed as

$$\rho_2^{\mathrm{SD}}(\boldsymbol{r}_1, \boldsymbol{r}_2) = \rho^{\mathrm{SD}}(\boldsymbol{r}_1) \rho^{\mathrm{SD}}(\boldsymbol{r}_2) - C_{\mathrm{ex}}^{\mathrm{SD}}(\boldsymbol{r}_1, \boldsymbol{r}_2), \tag{2.70}$$

with the exchange sum given by

$$C_{\mathrm{ex}}^{\mathrm{SD}}(\boldsymbol{r}_1, \boldsymbol{r}_2) = \sum_{s_1 s_2} \sum_{\tau_1 \tau_2} \sum_{i,j=1}^{A} \phi_{\alpha_i}^{\dagger}(x_1) \phi_{\alpha_j}^{\dagger}(x_2) \phi_{\alpha_i}(x_2) \phi_{\alpha_j}(x_1). \tag{2.71}$$

The second term in Eq. (2.70) arises solely from the antisymmetry of the total wave function and describes the Pauli correlations in a system of fermions. It characterizes how the probability of finding one particle at position $\boldsymbol{r}_1$ and another at position $\boldsymbol{r}_2$ differs from the product of the probability densities for finding each particle independently at these positions.

For a system of independent identical bosons, characterized by a symmetric total wave function, the one-body density matrix would coincide with that of fermions. However, the bosonic two-body density is given by

$$\rho_2^{\mathrm{boson}}(\boldsymbol{r}_1, \boldsymbol{r}_2) = \frac{A-1}{A} \rho^{\mathrm{boson}}(\boldsymbol{r}_1) \rho^{\mathrm{boson}}(\boldsymbol{r}_2) \tag{2.72}$$

where we assume that all bosons occupy the lowest energy state. In this system, the absence of Pauli correlations results in

$$C_0^{\mathrm{boson}}(\boldsymbol{r}_1, \boldsymbol{r}_2) \equiv \frac{A-1}{A} \rho^{\mathrm{boson}}(\boldsymbol{r}_1) \rho_2^{\mathrm{boson}}(\boldsymbol{r}_1, \boldsymbol{r}_2) - \rho_2^{\mathrm{boson}}(\boldsymbol{r}_1, \boldsymbol{r}_2) = 0. \tag{2.73}$$

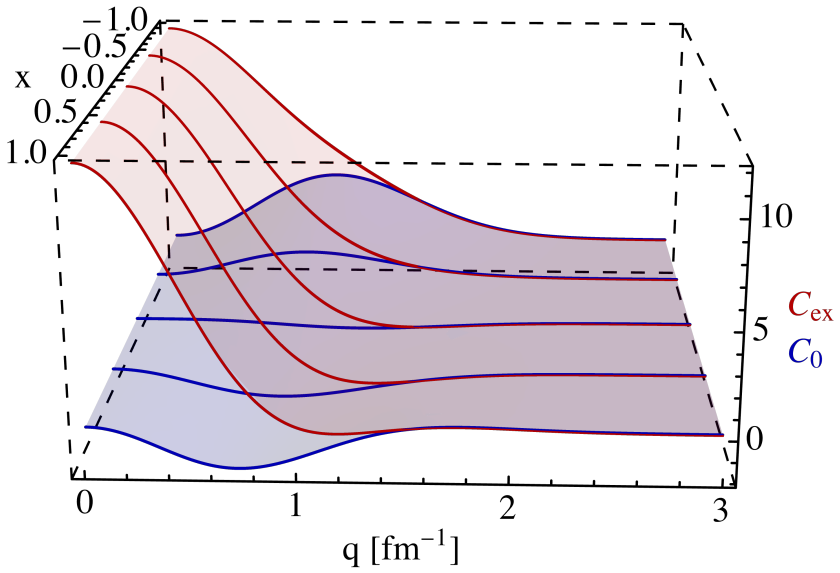

Figure 2.5: The correlation functions $C_{ex}(\boldsymbol{q}_1, \boldsymbol{q}_2)$ and $C_0(\boldsymbol{q}_1, \boldsymbol{q}_2)$ for ^{12}C in momentum space, obtained with the HO shell model, as functions of the momentum magnitude $|\boldsymbol{q}_1| = |\boldsymbol{q}_2| = q$ and $x = \boldsymbol{q}_1 \cdot \boldsymbol{q}_2/(q_1 q_2)$. The red upper curves correspond to C_{ex}, while the blue lower ones correspond to C_0.

Correspondingly, two types of two-body correlation functions can be defined in terms of one- and two-body nucleon densities [187, 188][6]:

$$C_{ex}(\boldsymbol{r}_1, \boldsymbol{r}_2) \equiv \rho(\boldsymbol{r}_1)\rho(\boldsymbol{r}_2) - \rho_2(\boldsymbol{r}_1, \boldsymbol{r}_2), \tag{2.74a}$$

$$C_0(\boldsymbol{r}_1, \boldsymbol{r}_2) \equiv C_{ex}(\boldsymbol{r}_1, \boldsymbol{r}_2) - \frac{1}{A}\rho(\boldsymbol{r}_1)\rho(\boldsymbol{r}_2). \tag{2.74b}$$

Both correlation functions are employed in our calculations, as we do not neglect terms of order A^{-1} appearing in the calculation. The function $C_{ex}(\boldsymbol{r}_1, \boldsymbol{r}_2)$ can be referred to as the "exchange correlation function" because, as demonstrated in the next Chapter, it accounts for the spin- and isospin-exchange contributions to pion-nucleus scattering. The two-body correlation functions in momentum space are then obtained by the same Fourier transform as given by Eq. (2.69).

Finally, as neither of the two-body correlation functions is directly measurable, we rely on Eq. (2.71) and single-nucleon wave functions provided by the HO nuclear shell model. The resulting momentum-space correlation functions depend on the magnitudes of the momenta $\boldsymbol{q}_{1,2}$ and the cosine of the angle between them, $x = \boldsymbol{q}_1 \cdot \boldsymbol{q}_2/(q_1 q_2)$. Thus, they can be expressed in the form $C_{ex,0}(\boldsymbol{q}_1, \boldsymbol{q}_2) \equiv C_{ex,0}(q_1, q_2, x)$. The derived two-body HO correlation functions are presented in Figs. 2.5–2.7, and they can be expressed in the form

$$C_{ex,0}(q_1, q_2, x) = \widetilde{C}_{ex,0}(q_1, q_2, x) \exp\left[-\frac{1}{4}\frac{A-1}{A}a^2\left(q_1^2 + q_2^2\right)\right], \tag{2.75}$$

Here, the factor $(A-1)/A$ in the exponential is introduced for consistency with Eq. (2.59b), taking into account the c.m. motion correction. The values of the HO parameter a used

[6] Note that different normalizations are used in this thesis compared to Refs. [187] and [188].

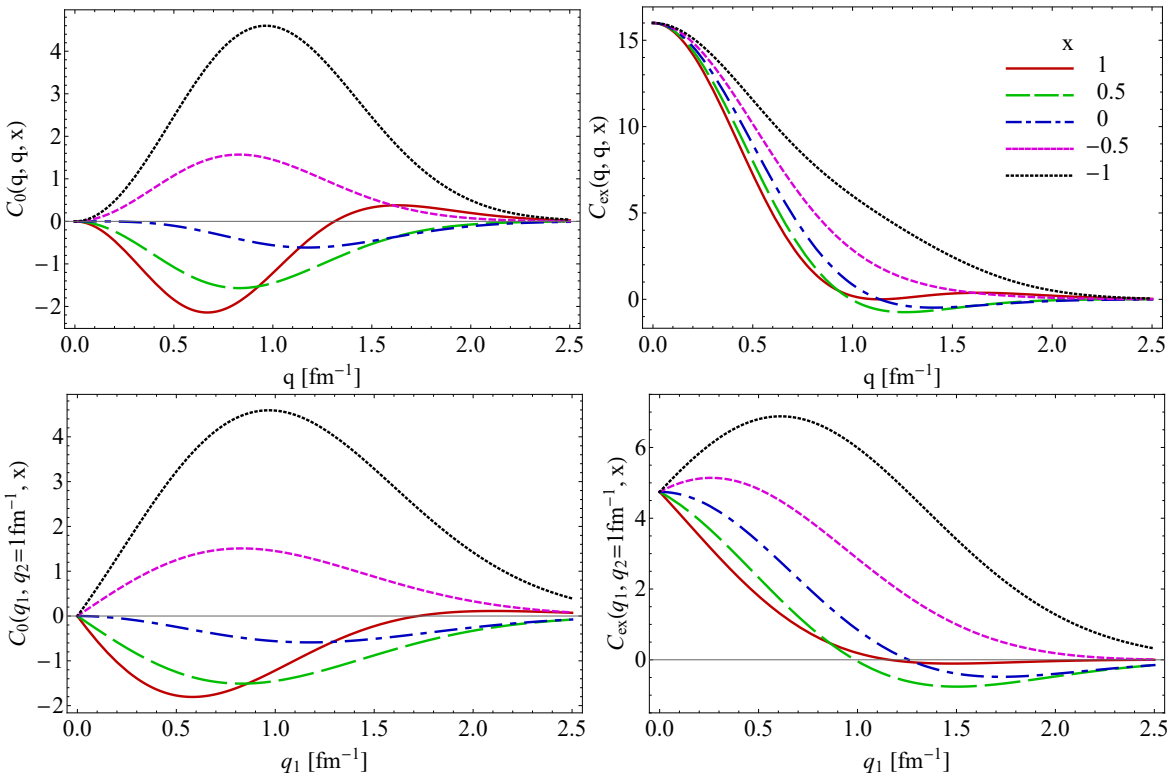

Figure 2.6: The HO correlation functions C_0 (left panels) and C_{ex} (right panels) for ^{16}O in momentum space. In the upper panels, $C_{0,\text{ex}}(q, q, x)$ are plotted as functions of the momentum magnitude $|\boldsymbol{q}_1| = |\boldsymbol{q}_2| = q$ for various $x = (\boldsymbol{q}_1 \cdot \boldsymbol{q}_2)/(q_1 q_2)$. Similarly, on the lower panels, $C_{0,\text{ex}}(q_1, q_2, x)$ are presented as functions of q_1 when $q_2 = 1\,\text{fm}^{-1}$.

in our calculation of the correlation functions are listed in Table 2.1. The functions $\widetilde{C}_{\text{ex},0}(q_1, q_2, x)$ take the following forms:
For ^{4}He,

$$\widetilde{C}_{\text{ex}}(q_1, q_2, x) = 4, \tag{2.76a}$$
$$\widetilde{C}_0(q_1, q_2, x) = 0, \tag{2.76b}$$

for ^{12}C,

$$\widetilde{C}_{\text{ex}}(q_1, q_2, x) = 12 - \frac{4}{3}a^2\left(q_1^2 + q_2^2 + \sqrt{6}q_1 q_2 x\right) + \frac{2}{3}a^4 q_1^2 q_2^2 x^2, \tag{2.77a}$$
$$\widetilde{C}_0(q_1, q_2, x) = -4\sqrt{\frac{2}{3}}a^2 q_1 q_2 x + \frac{4}{27}a^4 q_1^2 q_2^2\left(\frac{9}{2}x^2 - 1\right), \tag{2.77b}$$

for ^{16}O,

$$\widetilde{C}_{\text{ex}}(q_1, q_2, x) = 16 - 2a^2\left(q_1^2 + q_2^2 + 2q_1 q_2 x\right) + a^4 q_1^2 q_2^2 x^2, \tag{2.78a}$$
$$\widetilde{C}_0(q_1, q_2, x) = -4a^2 q_1 q_2 x + a^4 q_1^2 q_2^2\left(x^2 - \frac{1}{4}\right), \tag{2.78b}$$

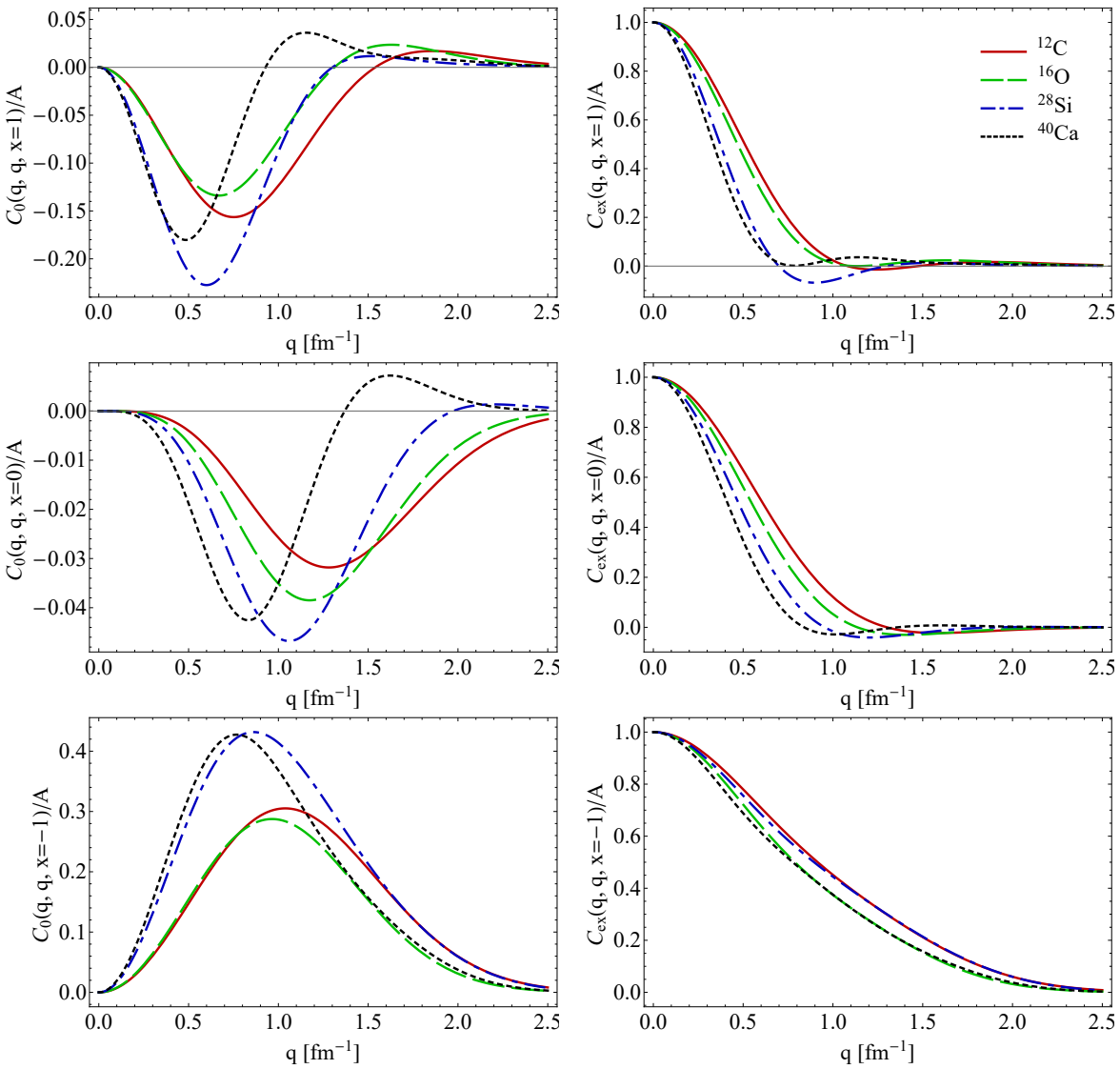

Figure 2.7: The momentum-space HO correlation functions $C_{0,\mathrm{ex}}(q, q, x)$ divided by the atomic mass number A for ^{12}C, ^{16}O, ^{28}Si, and ^{40}Ca.

for ^{28}Si,

$$\widetilde{C}_{\mathrm{ex}}(q_1, q_2, x) = 28 - 6a^2\left(q_1^2 + q_2^2 + \frac{2}{3}\left(1 + 2\sqrt{\frac{5}{3}}\right) q_1 q_2 x\right) + \frac{1}{240}a^8 q_1^4 q_2^4 \left(1 - 3x^2\right)^2$$
$$+ \frac{1}{15}a^4\left(3\left(q_1^4 + q_2^4\right) + 4\sqrt{15}q_1 q_2 x\left(q_1^2 + q_2^2\right) + q_1^2 q_2^2\left(13 - \sqrt{15} + 3(12 + \sqrt{15})x^2\right)\right)$$
$$- \frac{1}{30}a^6 q_1^2 q_2^2\left(\sqrt{15}q_1 q_2 x\left(3x^2 - 1\right) + \left(q_1^2 + q_2^2\right)\left(3x^2 + 1\right)\right), \tag{2.79a}$$

$$\widetilde{C}_0(q_1, q_2, x) = a^2 q_1 q_2\left(-\frac{4}{3}\left(3 + 2\sqrt{15}\right)x + \frac{1}{8400}a^6 q_1^3 q_2^3\left(23 - 210x^2 + 315x^4\right)\right.$$
$$+ \frac{1}{105}a^2\left(28\sqrt{15}\left(q_1^2 + q_2^2\right)x - \left(44 + 7\sqrt{15} - 21\left(12 + \sqrt{15}\right)x^2\right)q_1 q_2\right)$$
$$\left. - \frac{1}{210}a^4 q_1 q_2\left[7\sqrt{15}q_1 q_2 x\left(3x^2 - 1\right) + \left(q_1^2 + q_2^2\right)\left(21x^2 - 2\right)\right]\right), \tag{2.79b}$$

and for ^{40}Ca,

$$\widetilde{C}_{\rm ex}(q_1,q_2,x) = 40 - 10a^2(\boldsymbol{q}_1+\boldsymbol{q}_2)^2 + \frac{1}{2}a^4\left((\boldsymbol{q}_1+\boldsymbol{q}_2)^4 + 10(\boldsymbol{q}_1\cdot\boldsymbol{q}_2)^2\right) - \frac{1}{2}a^6(\boldsymbol{q}_1\cdot\boldsymbol{q}_2)^2\left(q_1^2+q_2^2+\boldsymbol{q}_1\cdot\boldsymbol{q}_2\right) + \frac{1}{16}a^8(\boldsymbol{q}_1\cdot\boldsymbol{q}_2)^4, \tag{2.80a}$$

$$\widetilde{C}_0(q_1,q_2,x) = -20a^2\boldsymbol{q}_1\cdot\boldsymbol{q}_2 + \frac{1}{2}a^4\left(4(\boldsymbol{q}_1+\boldsymbol{q}_2)^2\boldsymbol{q}_1\cdot\boldsymbol{q}_2 + 6(\boldsymbol{q}_1\cdot\boldsymbol{q}_2)^2 - 3q_1^2q_2^2\right) - \frac{1}{8}a^6\left(4(q_1^2+q_2^2+\boldsymbol{q}_1\cdot\boldsymbol{q}_2)(\boldsymbol{q}_1\cdot\boldsymbol{q}_2)^2 - (q_1^2+q_2^2)q_1^2q_2^2\right) + \frac{1}{160}a^8q_1^4q_2^4\left(10x^4-1\right). \tag{2.80b}$$

For obtaining the $C_{0,\rm ex}$ functions in momentum space, we extended the derivation presented in Refs. [187, 189] for ^{12}C, ^{16}O, and ^{40}Ca to the case where $\boldsymbol{q} \neq \boldsymbol{q}'$. By accounting for the difference in normalization conventions, we find that, in the limit $\boldsymbol{q}_1 = -\boldsymbol{q}_2$, the resulting correlation functions $C_{0,\rm ex}(q_1, q_2 = q_1, x = -1)$ for ^{12}C, ^{16}O, and ^{40}Ca are consistent with Ref. [189].[7]

As demonstrated in Figs. 2.5–2.7, the correlation functions $C_{\rm ex}$ and C_0 in momentum space exhibit significantly different behavior at small momenta. The underlying physical nature of this difference will become clear in the next Chapter, where these two types of correlation functions naturally arise from the multiple-scattering formalism.

2.4 Summary

The model-independent FB approach provides accurate and reliable charge form factors directly from measurements of elastic electron scattering. In our treatment of the Coulomb interaction between charged pions and nuclei, we employ the FB form factors from Refs. [185] (for ^{12}C) and [7] (for ^{16}O, ^{28}Si, and ^{40}Ca). Additionally, we use these charge form factors, corrected for the internal charge distribution within nucleons according to Eq. (2.26), to obtain model-independent nucleon density form factors. The electromagnetic form factors of the proton and neutron are taken from the global fits of electron-nucleon scattering data of Ref. [156]. Finally, we utilize the HO nuclear shell model to derive the two-body correlation functions, Eqs. (2.75)–(2.80), with the HO parameters listed in Table 2.1.

Employing the nuclear shell model to incorporate second-order pion rescattering is a more robust approach than using the Fermi-gas assumption or a fully phenomenological treatment. However, the HO shell model still has its limitations. The HO charge form factors demonstrate good agreement with the FB approach up to a momentum transfer of approximately $1.5\,\mathrm{fm}^{-1}$ for light and intermediate-heavy nuclei with closed subshells. The momentum transfer range of $0 \leq q \leq 1.5\,\mathrm{fm}^{-1}$ coincides with the region where other approximations used in our framework for nuclear pion scattering and photoproduction are highly valid. This range also contributes dominantly to the integrated cross sections. For this reason, in the next Chapter, we limit the fitting of differential cross section data for $\pi^{\pm}$-^{12}C scattering to momentum transfers $q \leq 1.5\,\mathrm{fm}^{-1}$. Nevertheless, there

[7] To maintain consistency with Ref. [189], we compare the results at $x = -1$ rather than $x = 1$, due to different definitions of the Fourier transform for the two-body density, Eq. (2.69).

are reasons to expect a satisfactory description of observables even for larger transferred momenta.

Within the $\Delta(1232)$-resonance energy region considered in this work, momentum transfers larger than $1.5\,\mathrm{fm}^{-1}$ are relevant for relatively large scattering angles.[8] Our approach incorporates loop contributions with off-shell momenta going far beyond $1.5\,\mathrm{fm}^{-1}$, yet the corresponding contributions are suppressed in comparison with the on-shell ones. While the HO form factors for ^{28}Si and ^{40}Ca are less pressie than those for ^{12}C and ^{16}O, within our approach the influence of the second-order correction, involving the HO correlation functions, diminishes as the nucleus becomes heavier and as the energy increases (as will be demonstrated in Sec. 3.4.4). Therefore, we expect the HO shell model for the nuclear two-body correlation functions to be sufficient for describing the main properties of scattering and photoproduction in the Δ-resonance energy region, even at large angles. To validate this assumption, we have checked that employing the modified harmonic oscillator shell model[9] results in negligible changes to the observables.

The high-momentum behavior of the nuclear structure characteristics is intricately linked to short-range correlations, a subject of active investigation in recent years [190]. Modern high-energy and large-momentum-transfer electron- and proton-scattering experiments [191–195] together with sophisticated many-body theoretical models [196–201] established that short-range correlated nucleon pairs generate the tail of the nuclear momentum distribution for momenta exceeding the Fermi momentum ($k_F \approx 1.36\,\mathrm{fm}^{-1}$). However, while the mentioned high-energy electron scattering experiments probe nuclei with spacelike high-energy photons to detect the influence short-range correlations, modern pion photoproduction experiments, involving a real photon, predominantly focus on a relatively low-momentum-transfer region. In the context of pion-nucleus interaction, a significant fraction of true pion absorption arises from short-range and high-momentum nucleon pairs [118], becoming sensitive to short-range correlations. However, our approach effectively incorporates true pion absorption by introducing the Δ self-energy, which is determined from a fitting procedure. Consequently, we anticipate that the impact of short-range correlations is encapsulated within the model parameters.

[8] The c.m. momenta of $1\,\mathrm{fm}^{-1}$ and $1.5\,\mathrm{fm}^{-1}$ in $\pi^{\pm}$-^{12}C system correspond to pion laboratory kinetic energies of approximately 106 MeV and 196 MeV, respectively.

[9] The modified harmonic oscillator shell model utilizes the HO shell model densities but treats $\tilde{\alpha}$ in Eqs. (2.62) as an additional free parameter. This adjustment allows for a better description of the charge form factor at larger momenta.

Appendices

2.A Occupation numbers and probabilities

To extend the applicability of Eq. (2.50), derived originally for closed-shell nuclei, we have introduced the concept of occupation probabilities η_{nl}. This extension allows the application of Eq. (2.50) to nuclei where only the highest filled subshell is closed. For deriving the occupation numbers for nuclei with closed subshells, it is essential to consider the addition of the orbital angular momentum and spin in the nlj states within the highest filled shell.

Considering the addition of two angular momenta $\boldsymbol{j}_1$ and $\boldsymbol{j}_2$, which form an uncoupled basis in tensor product space presented as $|j_1, m_1; j_2, m_2\rangle \equiv |j_1, m_1\rangle \otimes |j_2, m_2\rangle$, the total angular momentum coupled state of $\boldsymbol{j} = \boldsymbol{j}_1 + \boldsymbol{j}_2$ can be expanded in the uncoupled basis as

$$|j, m_j\rangle = \sum_{m_1=-j_1}^{j_1} \sum_{m_2=-j_2}^{j_2} |j_1, m_1; j_2, m_2\rangle\langle j_1, m_1; j_2, m_2|j, m_j\rangle, \tag{2.81}$$

where $\langle j_1, m_1; j_2, m_2|j, m_j\rangle$ are the Clebsch-Gordan coefficients. These coefficients can only be nonzero when $|j_1 - j_2| \leq j \leq j_1 + j_2$ and $m = m_1 + m_2$. Thus the squared Clebsch-Gordan coefficient $\langle j_1, m_1; j_2, m_2|j, m_j\rangle^2$ represents the probability of finding the specific uncoupled state $|j_1, m_1; j_2, m_2\rangle$ in the coupled state $|j, m_j\rangle$.

By performing a summation over j, m, and the spin projection m_s in Eq. (2.13a) and using the relation given in Eq. (2.81), the occupation probability of the nlj subshell is obtained as

$$\eta_{nlj} = \frac{1}{2(2l+1)} \sum_{m_j=-j}^{j} \sum_{m_s=-1/2}^{1/2} \langle l, m_j - m_s; 1/2, m_s|j, m_j\rangle^2, \tag{2.82}$$

which gives occupation probabilities of 2/3 for the closed $1p_{3/2}$ subshell of ^{12}C and 3/5 for the closed $1d_{5/2}$ subshell of ^{28}Si. Thus, within the individual particle shell model, the occupation probabilities of closed (sub)shells are given by

$$\eta_{nlj} = \frac{n_{nlj}}{4(2l+1)}, \tag{2.83}$$

where n_{nlj} is the number of nucleons in the nlj shell. Correspondingly, the occupation probabilities are either integers or rational numbers below the Fermi energy and zero above it.

Due to short-range correlations, empirical occupation probabilities as extracted from, e.g., nucleon knockout reactions show smaller values compared to predictions from individual particle shell model calculations [202–204]. In contrast, nlj orbits that are entirely unoccupied in the individual-particle approach exhibit non-zero occupation probabilities. This discrepancy imposes constraints on the maximum momentum transfer applicable in the mean-field approach employed in this study.

Chapter 3

Momentum-space second-order pion-nucleus potential

The study of the pion-nucleus interaction has a long history filled with various theoretical approaches [119] and has seen a renewed interest in very recent years [205–207]. While the earlier works were concentrated on the pion-nucleus scattering and pionic atoms, modern experiments open new perspectives and challenges in applying the pion-nucleus reactions knowledge base. The pion production experiments in photon (electron)- and neutrino-nucleus scattering serve as examples of utmost importance. They are related to the extraction of neutron skin and neutrino oscillation measurements, respectively. The final-state interaction between the outgoing pion and nucleus in these two processes is non-negligible at the energies considered, and it is particularly significant in the $\Delta(1232)$ resonance region [75, 136]. Moreover, the $\Delta(1232)$ excitation is the dominant mechanism of single-pion production, implying the significance of studying modifications of the resonance in the nuclear medium. For the neutrino experiments, a good understanding of the pion final-state interaction is of paramount importance to interpret the measurements to the level of precision required [208, 209].

After the initial studies on pion-nucleus elastic scattering and energy levels of pionic atoms using the simple first-order potential, it became evident that higher-order effects are required for a consistent description of experimental data [101]. There are essentially two types of existing theoretical models. The first is based on multiple-scattering theory and provides terms beyond first order to the pion-nucleus optical potential, treating the pion-nucleon amplitudes phenomenologically. The second approach is the isobar-doorway model, which considers the Δ-resonance as an elementary particle modified by various medium corrections. Our work is inspired by both of these approaches.

The optical potential formalism effectively describes the many-body pion-nucleus scattering process by a one-particle equation for the pion interacting with a complex phenomenological potential. The Kisslinger optical potential [100], built on Watson's theoretical basis [97], was introduced more than half a century ago and has been continuously improved over the years by including various corrections [101, 105–108, 210]. The Kerman-McManus-Thaler formulation of the multiple-scattering theory [98], treatment of the Fermi motion, and relativistic kinematics have been taken into account. The addition of the phenomenological term proportional to the squared nuclear density, which covers beyond-first-order effects and real pion absorption, has resulted in a much-improved agreement between theory and pion-nucleus scattering data for a large set of nuclei.

However, the properties of the $\Delta(1232)$ isobar in the nuclear medium are essential in understanding pion-nucleus interaction and have been the subject of numerous investiga-

tions, especially in the framework of the Δ-hole model [87–90, 93, 211]. This resonance is particularly important for pion-nucleus interaction because its excitation drives the dominant p-wave spin-isospin-$\frac{3}{2}$ (P_{33}) channel in the elementary pion-nucleon scattering. However, strong scalar and vector fields affect the Δ-isobar propagating through the nuclear many-body system. The many-body medium effects are incorporated in the complex effective Δ self-energy Σ_Δ, which shifts the Δ mass and width. The treatment of pion-nuclear reactions within the framework of the Δ-hole model is done by means of a phenomenological spreading potential, the parameters of which are fitted to the data.

The aim of the present work is to develop the second-order pion-nuclear potential in momentum space. In addition to the first-order part of the potential, which has a standard form [106], our second-order part involves more realistic two-body correlation functions than have been used in earlier works. In addition, we account for nuclear medium effects, which affect the resonant P_{33} pion-nucleon scattering amplitude. The pion-bound nucleon amplitude in our approach relies on the relativistic Δ-isobar model [212] with modified Δ-propagator. The effective Δ self-energy is considered as a complex parameter in our model, which is fixed by a multienergy fit to $\pi^{\pm}$-^{12}C scattering data in the energy range 80–180 MeV laboratory kinetic energy. In addition to describing pion-nucleus scattering, our work aims to develop a model that can be applied directly to the processes of pion photoproduction and neutrino-induced pion production on spin-zero nuclei.

The present Chapter is based on Ref. [3] and is organized as follows:

- In Section 3.1, we present the main aspects of the multiple-scattering formalism.
- In Section 3.2, we consider the pion-nucleon elementary amplitudes and the dominant P_{33} channel.
- In Section 3.3, we derive the second-order pion-nucleus potential and introduce in-medium modifications to the scattering amplitudes.
- Next, in Section 3.4, we fit the obtained potential to the data on pion-^{12}C scattering and apply it to the ^{16}O, ^{28}Si, and ^{40}Ca data.
- Finally, in Section 3.5, we provide our conclusions.

3.1 Multiple-scattering formalism

In multiple-scattering theory, the overall pion-nuclear transition amplitude $\hat{T}$ is a symmetric sum of amplitudes over all A individual nucleons,

$$\hat{T}(E) = \sum_{i=1}^{A} \hat{\tau}_i(E) + \sum_{i=1}^{A}\sum_{j\neq i}^{A} \hat{\tau}_i(E)\hat{G}(E)\hat{\tau}_j(E) + \sum_{i=1}^{A}\sum_{j\neq i}^{A}\sum_{k\neq j}^{A} \hat{\tau}_i(E)\hat{G}(E)\hat{\tau}_j(E)\hat{G}(E)\hat{\tau}_k(E) + \cdots , \quad (3.1)$$

where E is the reaction energy and $\hat{G}(E)$ is the Green's function of the noninteracting pion-nuclear system. The pion-nucleon transition amplitude describing scattering to all

orders on a single nucleon bound inside the nucleus is

$$\hat{\tau}_i(E) = \hat{v}_i + \hat{v}_i \hat{G}(E) \hat{\tau}_i(E), \tag{3.2}$$

where $\hat{v}_i$ denotes the pion-single-nucleon potential. Subsequently, we are going to replace the potential $\hat{v}_i$ with the corresponding free-space pion-nucleon amplitude $\hat{t}_i$, which may be more easily parametrized from the experiment (see Sec. 3.2):

$$\hat{t}_i(W) = \hat{v}_i + \hat{v}_i \hat{g}(W) \hat{t}_i(W). \tag{3.3}$$

The scattering series for $\hat{t}_i$ with the pion-nucleon reaction energy W differs from Eq. (3.2) by the Green's function of the pion-free nucleon system $\hat{g}(W)$.

A determination of the transition amplitude $\hat{T}$ from Eq. (3.1) is difficult due to the presence of all possible intermediate nuclear excited states in the series. Moreover, $\hat{T}$, $\hat{G}$ and $\hat{\tau}_i$ are $(A+1)$-particle operators, so nucleon degrees of freedom must be integrated out. Further simplification of the problem is possible by separating the equation involving only the ground state matrix elements from the one containing excited states. For this purpose, we introduce projection operators, which distinguish the ground state from the excited states of the target nucleus:

$$\hat{P}_0 = |\Psi_0\rangle\langle\Psi_0| \qquad \text{and} \qquad \hat{P}_\emptyset = \sum_{\alpha^* \neq 0} |\Psi_{\alpha^*}\rangle\langle\Psi_{\alpha^*}|, \tag{3.4}$$

where $|\Psi_0\rangle$ and $|\Psi_{\alpha^*}\rangle$ correspond to the nuclear ground state and all possible excited states, respectively. Also we assume $\hat{P}_\emptyset = \hat{\mathbb{1}} - \hat{P}_0$. Following the Kerman-McManus-Thaler formulation of the multiple-scattering theory, Eqs. (3.1)–(3.3) are equivalent to the system of integral equations [98]:

$$\hat{T}(E) = \hat{U}(E) + \frac{A-1}{A} \hat{U}(E) \hat{G}(E) \hat{P}_0 \hat{T}(E), \tag{3.5a}$$

$$\hat{U}(E) = A\,\hat{\tau}(E) + (A-1) \hat{\tau}(E) \hat{G}(E) \hat{P}_\emptyset \hat{U}(E), \tag{3.5b}$$

$$\hat{\tau}(E) = \hat{t}(W) + \hat{t}(W) \left[\hat{G}(E) - \hat{g}(W)\right] \hat{\tau}(E). \tag{3.5c}$$

Here and further, we drop the index of $\hat{t}_i$ when there is no need to distinguish nucleons. The above scattering equation on $\hat{T}(E)$ ($\hat{U}(E)$) resembles the Lippmann-Schwinger equation, with the additional factor $(A-1)/A$ and projector $\hat{P}_0$ ($\hat{P}_\emptyset$), which forbids intermediate nuclear excited (ground) states, respectively. The factor $(A-1)/A$ prevents double counting of pion rescattering on the same nucleon since all possible rescatterings on a single nucleon are already included in the pion-nucleon amplitude $\hat{\tau}$.

The many-body process of pion-nucleus elastic scattering is completely determined by the nuclear ground-state expectation value of $\langle\Psi_0|\hat{T}|\Psi_0\rangle$, defined by the scattering equation

$$\langle\Psi_0|\hat{T}(E)|\Psi_0\rangle = \langle\Psi_0|\hat{U}(E)|\Psi_0\rangle + \frac{A-1}{A} \langle\Psi_0|\hat{U}(E)|\Psi_0\rangle \hat{G}_0(E) \langle\Psi_0|\hat{T}(E)|\Psi_0\rangle, \tag{3.6}$$

where we have used the property of $\hat{G}_0(E)$: $\langle\Psi_0|\hat{G}(E)|\Psi_\alpha\rangle = \hat{G}_0(E)\delta_{0\alpha}$. Note, Eq. (3.6) contains only the terms diagonal in the nuclear ground state. As a result, this equation is

not necessarily rapidly convergent. However, it can be solved numerically if the effective potential $\langle\Psi_0|\hat{U}|\Psi_0\rangle$ is known. As follows from Eq. (3.5b), the scattering equation for the potential $\langle\Psi_0|\hat{U}|\Psi_0\rangle$ contains two nondiagonal matrix elements in the second term and is expected to converge rapidly. This is a consequence of the fact that all influence of the excited states is contained in $\hat{U}$. A detailed consideration of the effective potential is presented in Sec. 3.3.

It is convenient to consider the pion-nucleus scattering in the c.m. frame of the pion-nucleus system. The reaction energy is then defined as $E = E(k_0) = \omega(k_0) + E_A(k_0)$, where $\omega(k_0)$ and $E_A(k_0)$ are the energies of the pion and nucleus defined relativistically, and k_0 is the on-shell momentum. As was discussed above, Eq. (3.5a) contains only the diagonal in the nuclear ground-state relativistic propagator of the pion-nucleus system $\hat{G}_0(E) = \langle\Psi_0|\hat{G}(E)|\Psi_0\rangle$. In pion momentum space, it becomes

$$\langle\pi(\boldsymbol{k}')|\hat{G}_0(E)|\pi(\boldsymbol{k})\rangle = (2\pi)^3\delta(\boldsymbol{k}'-\boldsymbol{k})G_0(k) \tag{3.7}$$

where $k = |\boldsymbol{k}|$ and

$$G_0(k) = \frac{1}{E-\omega(k)-E_A(k)+i\,\varepsilon}, \tag{3.8}$$

We can write Eq. (3.8) in the pseudononrelativistic form

$$G_0(k) = \frac{2\mathscr{M}(k)}{k_0^2-k^2+i\,\varepsilon}, \tag{3.9}$$

with an off-shell analog of the relativistic reduced mass,

$$\mathscr{M}(k) \equiv \frac{[E+\omega(k)+E_A(k)][\omega(k_0)E_A(k_0)+\omega(k)E_A(k)]}{2\,(E^2+(\omega(k)+E_A(k))^2)}. \tag{3.10}$$

Taking into account the equality $\mathscr{M}(k_0) = \omega(k_0)E_A(k_0)/(\omega(k_0)+E_A(k_0))$, we introduce the elastic scattering amplitude in the momentum space, defined as

$$F(\boldsymbol{k}',\boldsymbol{k}) = -\frac{\sqrt{\mathscr{M}(k')\mathscr{M}(k)}}{2\pi}\langle\pi(\boldsymbol{k}'),\Psi_0|\hat{T}(E)|\pi(\boldsymbol{k}),\Psi_0\rangle, \tag{3.11}$$

where $\boldsymbol{k}$ and $\boldsymbol{k}'$ are the pion c.m. momenta in the initial and final states, respectively. Then, in accordance with Eq. (3.5a), the elastic scattering amplitude is calculated by solving the integral equation

$$F(\boldsymbol{k}',\boldsymbol{k}) = V(\boldsymbol{k}',\boldsymbol{k}) - \frac{A-1}{A}\int\frac{\mathrm{d}\boldsymbol{k}''}{2\pi^2}\frac{V(\boldsymbol{k}',\boldsymbol{k}'')F(\boldsymbol{k}'',\boldsymbol{k})}{k_0^2-k''^2+i\,\varepsilon}, \tag{3.12}$$

where the momentum space potential of the pion-nuclear interaction is defined as:

$$V(\boldsymbol{k}',\boldsymbol{k}) = -\frac{\sqrt{\mathscr{M}(k')\mathscr{M}(k)}}{2\pi}U(\boldsymbol{k}',\boldsymbol{k}), \tag{3.13}$$

with $U(\boldsymbol{k}',\boldsymbol{k}) = \langle\pi(\boldsymbol{k}'),\Psi_0|\hat{U}(E)|\pi(\boldsymbol{k}),\Psi_0\rangle$.

To solve Eq. (3.12), we use partial wave decomposition and the K-matrix formalism (see Appendix 3.A for details). Note that the formulas given above and developed in the following sections are derived for the case of solely nuclear interaction. The modification that is needed for the inclusion of the Coulomb interaction is discussed in Appendix 3.B.

3.2 Pion-nucleon elementary scattering amplitude

The potential $\hat{U}$ relies on the knowledge of the pion-nucleon scattering amplitude. To describe the scattering on a single bound nucleon, we assume that the contribution from the second term of Eq. (3.5c) can be neglected. In this way, we impose $\hat{\tau}(E) \approx \hat{t}(W)$, which is known as the *impulse approximation*. However, the c.m. energy of the pion-nucleon subsystem W is a dynamical variable [211, 213]. An optimal approach for choosing W would be minimizing the second term of Eq. (3.5c), describing binding correction to $\hat{\tau}$. There are several prescriptions with various motivations for choosing the optimal value for W [105, 106, 214]. We will follow the arguments of Gurvitz [215] and set

$$W(\boldsymbol{k},\boldsymbol{p}) = \sqrt{\left(\omega(k) + E_N(p)\right)^2 - (\boldsymbol{k}+\boldsymbol{p})^2}, \tag{3.14}$$

where $\boldsymbol{k}$ and $\boldsymbol{p}$ are the pion and target nucleon momenta in the pion-nucleus c.m. frame, and $\omega(k = |\boldsymbol{k}|)$ and $E_N(p = |\boldsymbol{p}|)$ are the corresponding relativistic energies. The choice of the effective value of $\boldsymbol{p}$ will be discussed in Sec. 3.3.1. We note that the freedom in choosing W can be absorbed in the model parameters when studying the medium effects (see Sec. 3.3.3).

While we require the pion-nucleon transition amplitude in the pion-nucleus c.m. frame, it is more convenient to consider the pion-single-nucleon interaction in the pion-nucleon c.m. system. All quantities denoted by the subscript "2cm" refer to the pion-nucleon frame in order to distinguish both systems. The pion momenta in both reference frames are related by the Lorentz transformation

$$\begin{aligned} \boldsymbol{k}_{2\mathrm{cm}}(\boldsymbol{k},\boldsymbol{p}) &= \boldsymbol{k} + \alpha\,(\boldsymbol{k}+\boldsymbol{p}), \\ \alpha &= \frac{1}{W(\boldsymbol{k},\boldsymbol{p})}\left(\frac{(\boldsymbol{k}+\boldsymbol{p})\cdot\boldsymbol{k}}{W(\boldsymbol{k},\boldsymbol{p}) + \omega(k) + E_N(p)} - \omega(k)\right), \end{aligned} \tag{3.15}$$

and an analogous relation for $\boldsymbol{k}'_{2\mathrm{cm}}$. Also, we assume that the transformation in Eq. (3.15) is justified for virtual particles, which is the approach of relativistic potential theory [216–218].

The free pion-nucleon scattering matrix in the pion-nucleus and pion-nucleon c.m. frames is then related through

$$\langle \pi(\boldsymbol{k}'), N(\boldsymbol{p}')|\hat{t}|\pi(\boldsymbol{k}), N(\boldsymbol{p})\rangle = (2\pi)^3\delta(\boldsymbol{k}'+\boldsymbol{p}'-\boldsymbol{k}-\boldsymbol{p})\gamma\, t_{2\mathrm{cm}}(\boldsymbol{k}'_{2\mathrm{cm}}, \boldsymbol{k}_{2\mathrm{cm}}), \tag{3.16}$$

with the usual Møller phase-space factor [219]

$$\gamma = \sqrt{\frac{\omega(\boldsymbol{k}_{2\mathrm{cm}})\omega(\boldsymbol{k}'_{2\mathrm{cm}})}{\omega(\boldsymbol{k})\omega(\boldsymbol{k}')}\,\frac{E_N(\boldsymbol{k}_{2\mathrm{cm}})E_N(\boldsymbol{k}'_{2\mathrm{cm}})}{E_N(\boldsymbol{p})E_N(\boldsymbol{p}')}} \tag{3.17}$$

due to the noncovariant normalization convention used to calculate $t_{2\mathrm{cm}}$. In Eq. (3.16) and further, we imply that the transition amplitude is calculated at the pion-nucleon reaction energy calculated according to Eq. (3.14) for the on-shell process. The notation $t(\boldsymbol{k}',\boldsymbol{k})$ indicates that the momentum-conserving δ function was explicitly separated.

The pion-nucleon on-shell T matrix is related to the elastic scattering amplitude f as

$$t_{2\mathrm{cm}}(\boldsymbol{k}'_{0,2\mathrm{cm}}, \boldsymbol{k}_{0,2\mathrm{cm}}) = -\frac{4\pi}{2\bar{\omega}} f(\boldsymbol{k}'_{0,2\mathrm{cm}}, \boldsymbol{k}_{0,2\mathrm{cm}}), \tag{3.18}$$

where $\bar{\omega} = \omega(k_{0,2\mathrm{cm}})E_N(k_{0,2\mathrm{cm}})/W$ is the pion-nucleon relativistic reduced mass, $W = \omega(k_{0,2\mathrm{cm}}) + E_N(k_{0,2\mathrm{cm}})$, and $|\boldsymbol{k}'_{0,2\mathrm{cm}}| = |\boldsymbol{k}_{0,2\mathrm{cm}}| = k_{0,2\mathrm{cm}}$. We consider further in this section only the most relevant properties of the scattering amplitude for the $\pi(\boldsymbol{k}_{2\mathrm{cm}}) + N(-\boldsymbol{k}_{2\mathrm{cm}}) \longrightarrow \pi(\boldsymbol{k}'_{2\mathrm{cm}}) + N(-\boldsymbol{k}'_{2\mathrm{cm}})$ process and refer to Ref. [119] for a more detailed review.

Assuming the isospin conservation, we can explicitly represent the spin-isospin structure of the amplitude as

$$\hat{t} = \hat{t}^{(0)} + \hat{t}^{(1)}\ \hat{\boldsymbol{t}}\cdot\hat{\boldsymbol{\tau}} + \left(\hat{t}^{(2)} + \hat{t}^{(3)}\ \hat{\boldsymbol{t}}\cdot\hat{\boldsymbol{\tau}}\right)\hat{\boldsymbol{\sigma}}\cdot\boldsymbol{n}, \tag{3.19}$$

where $\hat{\boldsymbol{t}}$ and $\hat{\boldsymbol{\tau}}$ are the pion and nucleon isospin operators, $\hat{\boldsymbol{\sigma}}$ is the nucleon Pauli spin operator, and $\boldsymbol{n} = \boldsymbol{k}_{2\mathrm{cm}} \times \boldsymbol{k}'_{2\mathrm{cm}}/|\boldsymbol{k}_{2\mathrm{cm}} \times \boldsymbol{k}'_{2\mathrm{cm}}|$ is the normal to the scattering plane. The same notation also holds for $t_{2\mathrm{cm}}(\boldsymbol{k}'_{2\mathrm{cm}}, \boldsymbol{k}_{2\mathrm{cm}})$ and $f(\boldsymbol{k}'_{2\mathrm{cm}}, \boldsymbol{k}_{2\mathrm{cm}})$.

The P_{33} partial wave is the only resonant one at low and intermediate energies, peaking at about the pion laboratory kinetic energy $T_{\mathrm{lab}} \approx 190\,\mathrm{MeV}$. Correspondingly, within the energy range under our consideration, $T_{\mathrm{lab}} \lesssim 300\,\mathrm{MeV}$, only the s- and p-wave contributions are dominant. As a result, the pion-nucleon scattering amplitude can be written as

$$\begin{aligned} f(\boldsymbol{k}'_{0,2\mathrm{cm}}, \boldsymbol{k}_{0,2\mathrm{cm}}) \approx b_0 + b_1\,\hat{\boldsymbol{t}}\cdot\hat{\boldsymbol{\tau}} + (c_0 + c_1\ \hat{\boldsymbol{t}}\cdot\hat{\boldsymbol{\tau}})\,\boldsymbol{k}'_{0,2\mathrm{cm}}\cdot\boldsymbol{k}_{0,2\mathrm{cm}} \\ + i(s_0 + s_1\ \hat{\boldsymbol{t}}\cdot\hat{\boldsymbol{\tau}})\,\hat{\boldsymbol{\sigma}}\cdot[\boldsymbol{k}'_{0,2\mathrm{cm}} \times \boldsymbol{k}_{0,2\mathrm{cm}}], \end{aligned} \tag{3.20}$$

where $b_{0,1}$, $c_{0,1}$, and $s_{0,1}$ are energy-dependent complex s- and p-wave coefficients.

The multipole expansion (see Appendix 3.C for details) allows us to express the parameters $b_{0,1}$, $c_{0,1}$, and $s_{0,1}$ through the partial wave amplitudes $f^l_{2T\,2J}$ as

$$b_0 = \frac{1}{3}\left[f^0_{1\,1} + 2f^0_{3\,1}\right], \tag{3.21a}$$

$$b_1 = \frac{1}{3}\left[f^0_{3\,1} - f^0_{1\,1}\right], \tag{3.21b}$$

$$c_0 = \frac{1}{3k^2_{0,2\mathrm{cm}}}\left[f^1_{1\,1} + 2f^1_{3\,1} + 2f^1_{1\,3} + 4f^1_{3\,3}\right], \tag{3.21c}$$

$$c_1 = \frac{1}{3k^2_{0,2\mathrm{cm}}}\left[f^1_{3\,1} - f^1_{1\,1} + 2f^1_{3\,3} - 2f^1_{1\,3}\right], \tag{3.21d}$$

$$s_0 = \frac{1}{3k^2_{0,2\mathrm{cm}}}\left[f^1_{1\,1} + 2f^1_{3\,1} - f^1_{1\,3} - 2f^1_{3\,3}\right], \tag{3.21e}$$

$$s_1 = \frac{1}{3k^2_{0,2\mathrm{cm}}}\left[f^1_{3\,1} - f^1_{1\,1} - f^1_{3\,3} + f^1_{1\,3}\right]. \tag{3.21f}$$

Here l, T, and J are, respectively, the orbital angular momentum, isospin, and total angular momentum of the pion-nucleon system. The partial-wave amplitudes are related to the measured pion-nucleon phase shifts as

$$f^l_{2T\,2J} = \frac{1}{2ik_{0,2\mathrm{cm}}}\left(e^{2i\delta^l_{2T\,2J}} - 1\right). \tag{3.22}$$

In this work, we take the complex scattering phase shifts $\delta^l_{2T\,2J}$ as extracted from the state-of-the-art phase shift analysis (WI08) by the SAID Collaboration [220].

As can be seen from Eq. (3.12), explicit knowledge of the off-energy-shell behavior of the potential V is required to solve the scattering equation. Whereas the on-shell behavior is directly defined by the partial wave amplitudes $f^l_{2T\,2J}$, Eq. (3.22), the off-shell extrapolation needs a model specification. We assume that for the on-shell momentum $k_{0,2\mathrm{cm}}$ the dependence of the amplitude $f^l_{2T\,2J}$ on the off-shell momenta $\boldsymbol{k}_{2\mathrm{cm}}$ and $\boldsymbol{k}'_{2\mathrm{cm}}$ is defined by the separable form

$$f^l_{2T\,2J}(k'_{2\mathrm{cm}}, k_{2\mathrm{cm}}) = f^l_{2T\,2J}(k_{0,2\mathrm{cm}}, k_{0,2\mathrm{cm}}) \left(\frac{k'_{2\mathrm{cm}} k_{2\mathrm{cm}}}{k^2_{0,2\mathrm{cm}}} \right)^l v(k'_{2\mathrm{cm}}) v(k_{2\mathrm{cm}}), \tag{3.23}$$

with the off-shell vertex factor for s and p waves

$$v(k) = \frac{\Lambda^2 - m_\pi^2}{\Lambda^2 - (\omega^2(k_{0,2\mathrm{cm}}) - k^2)}, \tag{3.24}$$

where $\Lambda = 1.25$ GeV is taken. Note that including the second-order part of the potential $\hat{U}$ (see Sec. 3.3) reduces the model sensitivity to the off-shell behavior of the pion-nucleon amplitude. The alteration of the off-shell parameter Λ does not significantly impact the model's predictions after fitting. However, the variation of Λ does result in changes to the free parameters, which will be described in the following sections.

An important feature of pion-nucleon scattering is the relative weakness of the s-wave interaction. It makes the p-wave part of the amplitude not only dominant at intermediate energies but also significant at low energies, even close to the threshold. As a result, an accurate description of the p-wave interaction is essential for the pion scattering on both free and bound nucleons. The starting point should be a model which effectively describes the basic dynamical features of the free pion-nucleon process. In our work, we adopt the *relativistic Δ-isobar model* (RΔM) by Oset, Toki and Weise [212], which successfully reproduces the p-wave pion-nucleon phase shifts at low and intermediate energies, especially the resonant P_{33} channel. The model is based on the K-matrix formalism in which we express the elastic-scattering partial amplitudes as

$$f^l_{2T\,2J} = \frac{K^l_{2T\,2J}}{1 - i k_{0,2\mathrm{cm}} K^l_{2T\,2J}}. \tag{3.25}$$

When the K matrix is real, the unitarity is automatically incorporated. In general, the phase shifts and, correspondingly, the K matrix remains real only below the pion production threshold ($\pi N \to \pi\pi N$), which is approximately at 170 MeV pion laboratory kinetic energy. However, even when the inelastic channel is open, the inelasticity parameters for the p wave remain close to 1 with high accuracy. As a result, the p-wave pion-nucleon interaction can be described by the real crossing symmetric K matrix. According to the relativistic Δ-isobar model, the pion-nucleon K matrix is based entirely on the pion-baryon effective Lagrangian and contains direct and crossed contributions from nucleon N, Δ(1232)-isobar, and Roper resonance $N^*(1440)$. The resulting K-matrix in the dominant P_{33} channel is given by

$$K^1_{33} = \frac{1}{3} \frac{k^2_{0,2\mathrm{cm}}}{4\pi m_\pi^2} \frac{m_N}{\sqrt{s}} \left[4 f_N^2 \frac{2m_N}{m_N^2 - \bar{u}} + 4 f_{N^*}^2 \frac{2m_{N^*}}{m_{N^*}^2 - \bar{u}} + f_\Delta^2 \left(\frac{2m_\Delta}{m_\Delta^2 - s} + \frac{1}{9} \frac{2m_\Delta}{m_\Delta^2 - \bar{u}} \right) \right], \tag{3.26}$$

where $s = W^2$, m_π is the pion mass and the approximate u-channel Mandelstam variable is $\bar{u} = u + 2\boldsymbol{k}'_{2\mathrm{cm}} \cdot \boldsymbol{k}_{2\mathrm{cm}} = m_N^2 + m_\pi^2 - 2\omega(k_{0,2\mathrm{cm}})E_N(k_{0,2\mathrm{cm}})$. The masses and coupling constants used are [212]:

$$\begin{aligned} m_N &= 939\,\mathrm{MeV}, & f_N^2/4\pi &= 0.079, \\ m_\Delta &= 1232\,\mathrm{MeV}, & f_\Delta^2/4\pi &= 0.37, \\ m_{N^*} &= 1450\,\mathrm{MeV}, & f_{N^*}^2/4\pi &= 0.015. \end{aligned}$$

The primary role of the Roper resonance $N^*(1440)$ in this model is providing the correct behavior in the P_{11} channel. The contributions of the u-channel $N^*(1440)$ and Δ to the P_{33} channel are on the order of a few percent. In contrast, the nucleon u-channel term is not negligible and becomes particularly significant at lower energies, e.g., making an approximately 50% contribution at the pion laboratory kinetic energy of 50 MeV.

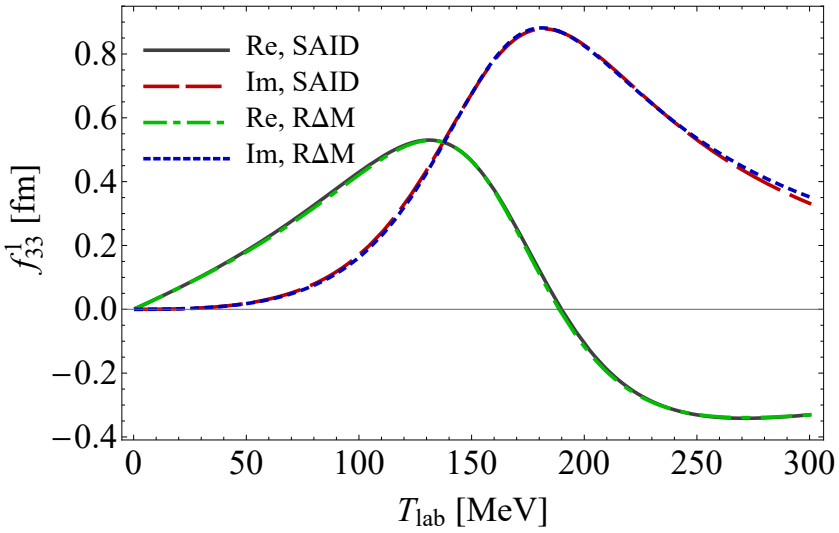

Figure 3.1: The theoretical f_{33}^1 amplitude obtained with the relativistic Δ-isobar model (RΔM) as a function of pion laboratory kinetic energy compared with SAID phase shift analysis [220]. The solid black (long-dashed red) curve represents the real (imaginary) part of the amplitude taken from SAID, while the dot-dashed green (short-dashed blue) curve corresponds to the RΔM calculation.

In Fig. 3.1, we compare the P_{33} partial amplitude taken from the SAID phase shift analysis with the relativistic Δ-isobar model results. The corresponding curves in the plot are almost indistinguishable, showing excellent agreement between the theoretical model and experiment.

The dominant term in Eq. (3.26) comes from the direct (s-channel) Δ-pole contribution. This resonant part of the K_{33}^1 can be written as

$$K_{33}^{1(\Delta)} = \frac{1}{k_{0,2\mathrm{cm}}} \frac{\Gamma_\Delta/2}{m_\Delta - W}, \tag{3.27}$$

where we have introduced the Δ decay width

$$\Gamma_\Delta = \frac{2}{3} \frac{f_\Delta^2}{4\pi} \frac{k_{0,2\mathrm{cm}}^3}{m_\pi^2} \frac{m_N}{W} \frac{2m_\Delta}{W + m_\Delta}. \tag{3.28}$$

The width at resonance ($W = m_\Delta$) is $\Gamma_\Delta \approx 115\,\text{MeV}$. This separation of the s-channel Δ term in the form of Eq. (3.27) will be useful in the following introducing the medium modifications.

3.3 Derivation of the pion-nucleus potential

We are now in the position to construct the effective pion-nucleus potential used in scattering equation (3.12). We assume the potential $\hat{U}(E)$ is approximated by the first two terms of the iterative series for Eq. (3.5b):

$$\hat{U}(E) \approx \hat{U}^{(1)} + \hat{U}^{(2)}, \tag{3.29}$$

where within the impulse approximation, the first-order part has the simple form

$$\hat{U}^{(1)} = A\,\hat{t} \tag{3.30}$$

and the second-order part is given by

$$\hat{U}^{(2)} = A(A-1)\hat{t}\hat{G}(E)\hat{P}_\emptyset\hat{t}. \tag{3.31}$$

In the following, we will express Eqs. (3.30) and (3.31) for the effective potential into more practical forms.

3.3.1 The first-order potential

The first-order potential in momentum space can be written as:

$$U^{(1)}(\boldsymbol{k}', \boldsymbol{k}) = \int \frac{\mathrm{d}\boldsymbol{p}'}{(2\pi)^3}\frac{\mathrm{d}\boldsymbol{p}}{(2\pi)^3}\,\mathrm{Tr}\left[\langle\pi(\boldsymbol{k}'), N(\boldsymbol{p}')|\,\hat{t}\,|\pi(\boldsymbol{k}), N(\boldsymbol{p})\rangle\,\rho(\boldsymbol{p}';\boldsymbol{p})\right], \tag{3.32}$$

where $\boldsymbol{p}$ and $\boldsymbol{p}'$ are the initial and final momenta of the target nucleon under consideration, Tr represents summation over all nucleon spin and isospin projections as:

$$\mathrm{Tr}\left[\hat{t}\,\rho(\boldsymbol{p}';\boldsymbol{p})\right] \equiv \sum_{\sigma,\sigma'}\sum_{\tau,\tau'}\langle\sigma'_{1z}, \tau'_{1z}|\,\hat{t}\,|\sigma_{1z}, \tau_{1z}\rangle\rho(\boldsymbol{p}', \sigma', \tau'; \boldsymbol{p}, \sigma, \tau), \tag{3.33}$$

and the one-body nuclear density matrix in momentum space is given by Eq. (2.7). For simplicity, the spin and isospin variables are omitted in what follows.

As a result, the first-order potential in the impulse approximation including the recoil of the struck nucleon is given by the Fermi motion integral:

$$U^{(1)}(\boldsymbol{k}', \boldsymbol{k}) = \int \frac{\mathrm{d}\boldsymbol{p}}{(2\pi)^3}\gamma\,\mathrm{Tr}\,[\rho(\boldsymbol{p}-\boldsymbol{q}/2;\boldsymbol{p}+\boldsymbol{q}/2) \times t_{2\mathrm{cm}}(\boldsymbol{k}'_{2\mathrm{cm}}(\boldsymbol{k}', \boldsymbol{p}-\boldsymbol{q}/2), \boldsymbol{k}_{2\mathrm{cm}}(\boldsymbol{k}, \boldsymbol{p}+\boldsymbol{q}/2)], \tag{3.34}$$

where $\boldsymbol{q} = \boldsymbol{k}' - \boldsymbol{k}$ and γ is given by Eq. (3.17). The integration over $\boldsymbol{p}$ in Eq. (3.34) requires nondiagonal elements of the one-body density matrix which are model dependent. Moreover, the proper treatment of the Fermi averaging should also take into account the binding effects. To simplify the problem, one can treat the nucleon Fermi motion

approximately by evaluating the pion-nucleon amplitude at the effective initial and final nucleon momenta

$$\boldsymbol{p}_{\rm eff} = \frac{\boldsymbol{q}}{2} - \frac{\boldsymbol{k}' + \boldsymbol{k}}{2A}, \quad \text{and} \quad \boldsymbol{p}'_{\rm eff} = -\frac{\boldsymbol{q}}{2} - \frac{\boldsymbol{k}' + \boldsymbol{k}}{2A}, \tag{3.35}$$

respectively. This result was obtained for elastic nucleon-deuteron scattering (for $A = 2$) in Ref. [221]. The terms proportional to A^{-1} arrive due to the correct treatment of the target recoil employing Eqs. (2.54) and (2.55). In this so-called *optimized factorization approximation* we arrive at

$$U^{(1)}(\boldsymbol{k}', \boldsymbol{k}) = \gamma \, {\rm Tr} \left[\rho(\boldsymbol{q}) t_{\rm 2cm}(\boldsymbol{k}'_{\rm 2cm}(\boldsymbol{k}', \boldsymbol{p}'_{\rm eff}), \boldsymbol{k}_{\rm 2cm}(\boldsymbol{k}, \boldsymbol{p}_{\rm eff})) \right], \tag{3.36}$$

with the nuclear form factor normalized to $\rho(0) = A$ The factorization approximation is justified by the compensation between the binding potential of the nucleon and the Fermi motion kinetic energy [215].

Finally, the pion-nuclear potential, Eq. (3.13), is expressed through the pion-nucleon scattering amplitude as:

$$V^{(1)}(\boldsymbol{k}', \boldsymbol{k}) = \mathscr{W}(\boldsymbol{k}', \boldsymbol{k}) \, {\rm Tr} \left[\rho(\boldsymbol{q}) f \left(\boldsymbol{k}'_{\rm 2cm}, \boldsymbol{k}_{\rm 2cm} \right) \right], \tag{3.37}$$

with the phase space factor

$$\mathscr{W}(\boldsymbol{k}', \boldsymbol{k}) = \sqrt{\frac{\mathscr{M}(k') \mathscr{M}(k)}{\mu(\boldsymbol{k}', \boldsymbol{p}'_{\rm eff}) \mu(\boldsymbol{k}, \boldsymbol{p}_{\rm eff})}}, \tag{3.38}$$

where $\mu(\boldsymbol{k}, \boldsymbol{p}) = \omega(k) E_N(p) / W(\boldsymbol{k}, \boldsymbol{p})$ and we imply $\boldsymbol{k}_{\rm 2cm} = \boldsymbol{k}_{\rm 2cm}(\boldsymbol{k}, \boldsymbol{p}_{\rm eff})$.

For spin- and isospin-zero nuclei, only the spin- and isospin-independent part of the scattering amplitude, Eq. (3.20), contributes to the first-order potential:

$$V^{(1)}(\boldsymbol{k}', \boldsymbol{k}) = \tilde{\mathscr{W}}(\boldsymbol{k}', \boldsymbol{k}) \left[b_0 + c_0 \, \boldsymbol{k}'_{\rm 2cm} \cdot \boldsymbol{k}_{\rm 2cm} \right] \rho(\boldsymbol{q}), \tag{3.39}$$

where $\tilde{\mathscr{W}}(\boldsymbol{k}', \boldsymbol{k}) = \mathscr{W}(\boldsymbol{k}', \boldsymbol{k}) v(k'_{\rm 2cm}) v(k_{\rm 2cm})$. Note that the scattering parameters b_0 and c_0 are derived at the pion-nucleon c.m. energy given by Eq. (3.14) for on-shell momenta and thus depend on the scattering angle.

Note, in our calculation, besides the most important s- and p-wave terms, we also include the d-wave contribution in the same manner.

3.3.2 The second-order correction

The second-order part of the potential, Eq. (3.31), describes scattering to all orders from one nucleon, after which the nucleus makes a transition into an excited state followed by propagation and then scattering to all orders on a second nucleon, summed over all nucleons (see Fig. 3.2). We use the subscripts "1" and "2" in this section to distinguish the initial and final nucleons involved in the second-order scattering process.

In calculating the second-order correction for the kinetic energies larger than around 30 MeV considered in this work, we neglect the nuclear excitation energies in comparison with energies of the pion-nucleus system intermediate states. In this way, the excited

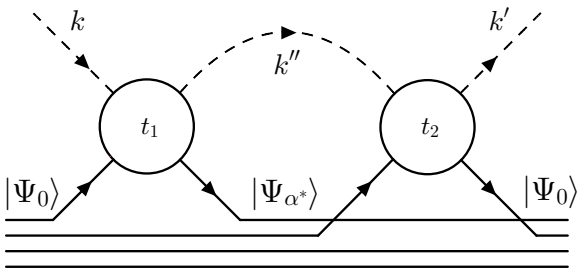

Figure 3.2: Diagrammatic representation of the second-order part of the pion-nuclear potential.

system propagator is approximated by the ground state one, $\hat{G}_{\alpha^*} \approx \hat{G}_0$. Correspondingly, the second-order part of the pion-nucleus becomes

$$\langle\Psi_0|\hat{U}^{(2)}|\Psi_0\rangle = A(A-1)\langle\Psi_0|\hat{t}_2\hat{G}_0\hat{P}_\emptyset\hat{t}_1|\Psi_0\rangle. \tag{3.40}$$

Substituting the projection operator explicitly, we arrive at

$$\langle\Psi_0|\hat{U}^{(2)}|\Psi_0\rangle = A(A-1)\left[\langle\Psi_0|\hat{t}_2\hat{G}_0\hat{t}_1|\Psi_0\rangle - \langle\Psi_0|\hat{t}_2|\Psi_0\rangle\hat{G}_0\langle\Psi_0|\hat{t}_1|\Psi_0\rangle\right]. \tag{3.41}$$

According to Eq. (3.36) for the first-order potential, the second term of Eq. (3.41) in momentum space becomes:

$$\begin{aligned}&\langle\pi(\boldsymbol{k}'),\Psi_0|\hat{t}_2|\Psi_0\rangle\hat{G}_0\langle\Psi_0|\hat{t}_1|\pi(\boldsymbol{k}),\Psi_0\rangle\\ &\quad= \frac{1}{A^2}\int\frac{\mathrm{d}\boldsymbol{k}''}{(2\pi)^3}\,\mathrm{Tr}\left[t_2(\boldsymbol{k}',\boldsymbol{k}'')\rho(\boldsymbol{k}'-\boldsymbol{k}'')\right]G_0(\boldsymbol{k}'')\,\mathrm{Tr}\left[t_1(\boldsymbol{k}'',\boldsymbol{k})\rho(\boldsymbol{k}''-\boldsymbol{k})\right],\end{aligned} \tag{3.42}$$

Similarly, the first term in Eq. (3.41) acquires the form

$$\begin{aligned}\langle\pi(\boldsymbol{k}')\Psi_0|\hat{t}_2\hat{G}_0\hat{t}_1|\pi(\boldsymbol{k})\Psi_0\rangle = \frac{1}{A(A-1)}\int\frac{\mathrm{d}\boldsymbol{k}''}{(2\pi)^3}G_0(\boldsymbol{k}'')\\ \times\,\mathrm{Tr}\left[t_2(\boldsymbol{k}',\boldsymbol{k}'')t_1(\boldsymbol{k}'',\boldsymbol{k})\rho_2(\boldsymbol{k}'-\boldsymbol{k}'',\boldsymbol{k}''-\boldsymbol{k})\right],\end{aligned} \tag{3.43}$$

where $\rho_2(\boldsymbol{q}_1,\boldsymbol{q}_2)$ is the Fourier transform of the two-body density function, Eq. (2.69), normalized to $\rho_2(0,0) = A(A-1)$. In Eqs. (3.42) and (3.43), we imply the same convention as in Eq. (3.33), omitting spin and isospin variables. As can be seen from Eqs. (3.41)–(3.43), the second-order part of the optical potential depends directly on the nuclear two-body correlations function C_{ex} and C_0, defined in coordinate space by Eqs. (2.74). The explicit forms of $C_{\mathrm{ex}}(\boldsymbol{q}_1,\boldsymbol{q}_2)$ and $C_0(\boldsymbol{q}_1,\boldsymbol{q}_2)$ are given by Eqs. (2.77)–(2.80).

Even for a nucleus with zero spin and isospin, the trace operator in Eq. (3.43) yields a nontrivial result containing spin- and isospin-dependent parts of the scattering amplitude, Eq. (3.19). A direct calculation for spin-isospin-zero nuclei yields the following

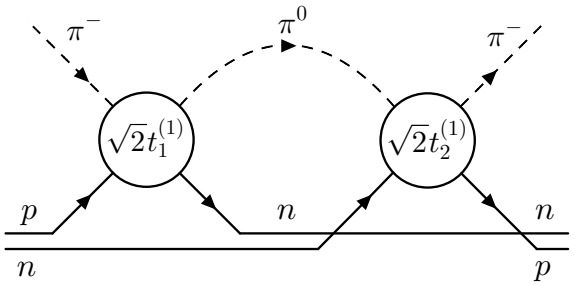

Figure 3.3: Diagrammatic representation of the second-order isospin exchange for negative pion scattering.

spin and isospin sums entering Eq. (3.43):

$$\sum_{s,s',\tau,\tau'=-1/2}^{1/2} \chi_1^\dagger(s)\chi_2^\dagger(s')\eta_1^\dagger(\tau)\eta_2^\dagger(\tau')\left[\hat{t}_2^{(0)} + \hat{t}_2^{(1)}\ \hat{\boldsymbol{t}}\cdot\hat{\boldsymbol{\tau}}_2 + \left(\hat{t}_2^{(2)} + \hat{t}_2^{(3)}\ \hat{\boldsymbol{t}}\cdot\hat{\boldsymbol{\tau}}_2\right)\hat{\boldsymbol{\sigma}}_2\cdot\boldsymbol{n}_2\right]$$
$$\times\left[\hat{t}_1^{(0)} + \hat{t}_1^{(1)}\ \hat{\boldsymbol{t}}\cdot\hat{\boldsymbol{\tau}}_1 + \left(\hat{t}_1^{(2)} + \hat{t}_1^{(3)}\ \hat{\boldsymbol{t}}\cdot\hat{\boldsymbol{\tau}}_1\right)\hat{\boldsymbol{\sigma}}_1\cdot\boldsymbol{n}_1\right]\eta_1(\tau')\eta_2(\tau)\chi_1(s')\chi_2(s)$$
$$= 4\left[\hat{t}_2^{(0)}\hat{t}_1^{(0)} + 2\,\hat{t}_2^{(1)}\hat{t}_1^{(1)} + \left(\hat{t}_2^{(2)}\hat{t}_1^{(2)} + 2\,\hat{t}_2^{(3)}\hat{t}_1^{(3)}\right)\boldsymbol{n}_1\cdot\boldsymbol{n}_2\right], \quad (3.44)$$

where $\chi(s)$ ($\eta(\tau)$) is the nucleon spinor (isospinor). The first term on the right-hand side of Eq. (3.44) consists of the spin-isospin averaged part $\hat{t}^{(0)}$ of the scattering amplitudes. The remaining terms involve the spin- and isospin-dependent parts and describe intermediate spin and isospin exchange. In Fig. 3.3, we show a diagrammatic representation of the isospin exchange for negative pion scattering. In the following, we include the global factor 4, which arises due to spin-isospin summation, in the correlation functions.

Finally, combining the above results, we express the second-order part of the potential for spin- and isospin-zero nuclei in terms of the correlation functions:

$$U^{(2)}(\boldsymbol{k}',\boldsymbol{k}) = -\int\frac{\mathrm{d}\boldsymbol{k}''}{(2\pi)^3}G_0(\boldsymbol{k}'')\left[t^{(0)}(\boldsymbol{k}',\boldsymbol{k}'')t^{(0)}(\boldsymbol{k}'',\boldsymbol{k})C_0(\boldsymbol{k}'-\boldsymbol{k}'',\boldsymbol{k}''-\boldsymbol{k})\right.$$
$$+\left(2t^{(1)}(\boldsymbol{k}',\boldsymbol{k}'')t^{(1)}(\boldsymbol{k}'',\boldsymbol{k}) + \left(t^{(2)}(\boldsymbol{k}',\boldsymbol{k}'')t^{(2)}(\boldsymbol{k}'',\boldsymbol{k}) + 2t^{(3)}(\boldsymbol{k}',\boldsymbol{k}'')t^{(3)}(\boldsymbol{k}'',\boldsymbol{k})\right)\boldsymbol{n}_1\cdot\boldsymbol{n}_2\right)$$
$$\left.\times\, C_{\mathrm{ex}}(\boldsymbol{k}'-\boldsymbol{k}'',\boldsymbol{k}''-\boldsymbol{k})\right] \quad (3.45)$$

or equivalently

$$V^{(2)}(\boldsymbol{k}',\boldsymbol{k}) = \int\frac{\mathrm{d}\boldsymbol{k}''}{2\pi^2}\frac{\mathscr{W}(\boldsymbol{k}',\boldsymbol{k}'')\mathscr{W}(\boldsymbol{k}'',\boldsymbol{k})}{k_0^2 - k''^2 + i\varepsilon}\left[f^{(0)}(\boldsymbol{k}',\boldsymbol{k}'')f^{(0)}(\boldsymbol{k}'',\boldsymbol{k})C_0(\boldsymbol{k}'-\boldsymbol{k}'',\boldsymbol{k}''-\boldsymbol{k})\right.$$
$$+\left(2f^{(1)}(\boldsymbol{k}',\boldsymbol{k}'')f^{(1)}(\boldsymbol{k}'',\boldsymbol{k}) + \left(f^{(2)}(\boldsymbol{k}',\boldsymbol{k}'')f^{(2)}(\boldsymbol{k}'',\boldsymbol{k}) + 2f^{(3)}(\boldsymbol{k}',\boldsymbol{k}'')f^{(3)}(\boldsymbol{k}'',\boldsymbol{k})\right)\boldsymbol{n}_1\cdot\boldsymbol{n}_2\right)$$
$$\left.\times\, C_{\mathrm{ex}}(\boldsymbol{k}'-\boldsymbol{k}'',\boldsymbol{k}''-\boldsymbol{k})\right], \quad (3.46)$$

with

$$f^{(0,1)}(\boldsymbol{k}',\boldsymbol{k}'') = (b_{0,1} + c_{0,1}\,\boldsymbol{k}'_{2\mathrm{cm}'}\cdot\boldsymbol{k}''_{2\mathrm{cm}'})\,v(k')v(k), \quad (3.47a)$$
$$f^{(2,3)}(\boldsymbol{k}',\boldsymbol{k}'') = i\,s_{0,1}\,k'_{2\mathrm{cm}'}k''_{2\mathrm{cm}'}v(k')v(k). \quad (3.47b)$$

The first term in Eq. (3.46) describing spin-isospin averaged individual nucleon scattering on two nucleons is similar to Eq. (6.5) of Foldy and Walecka [153]. The term proportional to $\hat{f}_1^{(2)}\hat{f}_2^{(2)}$ ($\hat{f}_1^{(1)}\hat{f}_2^{(1)}$) corresponds to spin (isospin) exchange between the intermediate pion and two nucleons, keeping the scattered nucleus in the ground state (see Fig. 3.3 for an example). Similarly, the term $\hat{f}_1^{(3)}\hat{f}_2^{(3)}$ describes the simultaneous exchange of both spin and isospin.

At the initial step of our calculation, the Pauli principle was included in the pion-nucleus potential through the antisymmetric nature of the nucleon wave functions. However, for the first-order potential, Eq. (3.36), this property was lost after the integration over nucleon momenta within the factorization approximation [222, 223]. The obtained structure of the second-order correction, Eq. (3.46), explicitly involves two types of two-nucleon correlation functions and arises primarily from the Pauli principle. This can, e.g., be understood by considering the process with zero momentum transfer to each of the nucleons involved in the second-order scattering. As shown in Fig. 2.5, for this situation, $C_0(0,0) = 0$ and $C_{\rm ex}(0,0) = A$. As a result, the first term in Eq. (3.46), describing the process which does not change the nucleon quantum numbers, makes zero contribution to the integral. In contrast, the second term is proportional to the nonzero $C_{\rm ex}$ correlation function. It corresponds to the situation when, after the pion scattering on the first nucleon, this nucleon changes its spin and/or isospin, acquiring quantum numbers already occupied by another nucleon. Similarly, in the case of ^{4}He scattering, where the correlation functions are given by Eqs. (2.76), the influence of the Pauli principle is present only when the target nucleon changes its spin-isospin state. In this way, the second-order part of the potential, Eq. (3.46), introduces the Pauli corrections to the model.

Figure 3.4 demonstrates the first- and second-order parts of the pion-nucleus potential for on-shell forward scattering on ^{12}C. As Pauli blocking limits the phase space available to the struck nucleon, the second-order correction to the potential leads to a reduction of the imaginary part of the potential. Around $T_{\rm lab} = 160$ MeV, the struck nucleon on-shell momentum becomes close to the Fermi momentum, $p_F \approx 1.36\,\text{fm}^{-1}$, and the imaginary part of Eq. (3.46) changes sign. In Appendix 3.D, we further discuss the second-order correction, Eq. (3.46).

3.3.3 Medium modifications

An essential part of the pion-nucleus total cross section for all energies up to 300 MeV comes from pion absorption [114]. In the nuclear medium, the pion can be absorbed by one or more nucleons, which indicates that intermediate states without a pion should also contribute to the pion-nucleus effective potential. This mechanism is usually referred to as "true absorption" to distinguish it from the flux loss due to scattering through many open inelastic channels. However, even zero-energy pion absorption on a single nucleon results in a momentum $\sqrt{2m_N m_\pi} \approx 2.6\,\text{fm}^{-1}$ to be carried off by the nucleon. This value is very large for a nucleon within a nucleus, which means the single-nucleon absorption is significantly suppressed [224]. As a result, the true absorption originates from many-body mechanisms.

Early models of pion absorption hypothesized dominance of two-nucleon pion absorp-

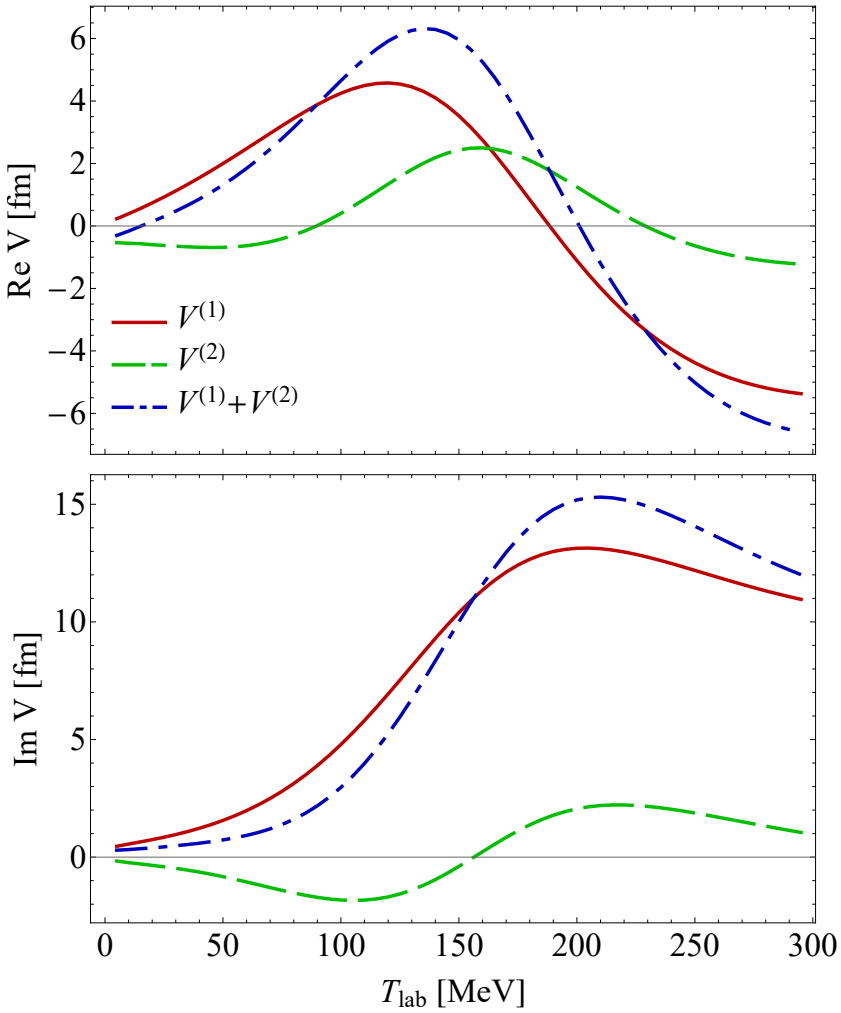

Figure 3.4: The on-shell forward pion-nucleus potential for ^{12}C as a function of pion laboratory kinetic energy for parameters given by fit 1 in Table 3.2. The upper and lower panels are for real and imaginary parts, respectively. The solid red curves represent the first-order part, $V^{(1)}(\boldsymbol{k}_0, \boldsymbol{k}_0)$ given by Eq. (3.39), with the on-shell momentum $\boldsymbol{k}_0$ corresponding to $T_{\rm lab}$. The dashed green curves correspond to the second-order part, $V^{(2)}(\boldsymbol{k}_0, \boldsymbol{k}_0)$ given by Eq. (3.46), and the dash-dotted blue are the sums of these two contributions.

tion [118], where the pion is scattered on one nucleon and then absorbed by another. Following this assumption, the pioneering work of Ref. [101] introduced additional phenomenological terms proportional to the square of the nuclear density in the pion-nucleus potential to allow for true absorption. However, it was shown both experimentally [117] and theoretically [116] that the absorption process is more complicated and the three-nucleon mechanism yields a significant fraction of the total absorption cross section in the resonance region and above.

As a result of the above, the pion-nucleon interaction is significantly modified in the presence of surrounding nucleons. In general, this means that the medium-modified scattering coefficients $b_{0,1}$, $c_{0,1}$, and $s_{0,1}$ are not only functions of the reaction energy

but also acquire a dependence on nuclear density $\rho(r)$. Even if the exact form of this dependence were known, its inclusion in the momentum space approach would not be trivial. To solve this difficulty, we need to use the fact that the pion interacts mainly with a limited part of the nucleus due to strong absorption, which results in the existence of an effective nuclear density. Reference [225] studied the correlations between the $\rho(r)$ and $\rho^2(r)$ terms of the pion-nucleus optical potential from the threshold to $T_{\text{lab}} = 50\,\text{MeV}$. It was proven that an effective density ρ_e could be defined such that the substitution $\rho^2(r) \longleftrightarrow \rho_e\rho(r)$ would result in approximately the same binding energies and scattering amplitudes for various nuclei in the range from ^{12}C to ^{208}Pb.

Even though we only fit in the range 80–180 MeV pion kinetic energy, we still wish to check our model predictions at lower energies. For this reason, the in-medium influence on the s-wave scattering should be considered. Moreover, due to s-p-wave interference in the second-order part of the pion-nucleus potential constructed in Sec. 3.3.2, both isoscalar b_0 and isovector b_1 parts of the s-wave pion-nucleon scattering amplitude are substantial even at high energies (see Appendix 3.D for details). In the following, we subsequently describe modifications of both s- and p-wave pion-nucleon scattering. The primary effect of the Pauli exclusion principle, which reduces the phase space accessible to the struck nucleon, is incorporated by explicitly calculating the second-order correction to the pion-nuclear potential as described in Sec. 3.3.2.

P_{33} modification

In our approach, we assume that for the p-wave interaction, only the resonant P_{33} channel is changed in the nuclear medium, keeping all other small partial-wave amplitudes at their free values taken from SAID.

The interaction of the Δ isobar with the surrounding nucleons significantly modifies the f_{33}^1 partial amplitude. A comparably long lifetime of Δ on the nuclear scale and its mean free path within a nucleus of around 1 fm suggest that the Δ is a nuclear quasiparticle that may still be treated effectively as a separate baryonic species without considering the intrinsic quark dynamics. The open inelastic channels involving many-body interactions, e.g., the two-body absorption ($\pi NN \to \Delta N \to NN$) and three-body absorption [116], considerably affect the Δ-resonance decay width inside nuclear matter. As a result, we consider the in-medium interactions effectively by a renormalization of the intermediate Δ propagator by the complex self-energy Σ_Δ function:

$$K_{33}^{1(\Delta)}(\Sigma_\Delta) = \frac{1}{k_{0,2\text{cm}}} \frac{\Gamma_\Delta/2}{m_\Delta + \Sigma_\Delta - W}. \tag{3.48}$$

In this approach, the dressed resonance leads to a complex K_{33}^1 matrix element in which the effective many-body p-wave absorption is automatically included in the model.

The Δ self-energy Σ_Δ in a finite nucleus is, in general, nonlocal [89]. However, we are looking for a simple phenomenological parametrization of Σ_Δ, which would still provide a reasonable description of the data. Since the real part of Σ_Δ has a weak energy dependence [226], it is often approximated to be constant. In contrast, the imaginary part of Σ_Δ is regularly considered as a function of the pion energy [85]. However, we have found that including the second-order part of the pion-nucleus potential, Eq. (3.46), allows us to neglect the energy dependence of $\text{Im}\,\Sigma_\Delta$. As a result, we treat $\text{Re}\,\Sigma_\Delta$ and

$\mathrm{Im}\,\Sigma_\Delta$ as two energy-independent p-wave model parameters determined by fitting the experimental data for pion-carbon scattering in Sec. 3.4.2.

The pion absorption process by a nucleus, unlike scattering, can occur even at pion energies below its mass. While the Δ width, Eq. (3.28), starts at $\omega = m_\pi$, the imaginary part of the Δ self-energy inside nuclear matter starts at $\omega = 0$ [227]. As a result, we expect the constant $\mathrm{Im}\,\Sigma_\Delta$ assumption to be applicable not only in the Δ-resonance region but also at low energies.

Isoscalar s-wave modification

The s- and p-wave true absorption within the optical potential formalism [101] is typically characterized by two complex parameters denoted as B_0 and C_0, respectively. It is assumed to be based on a two-nucleon mechanism. As was pointed out above, we effectively take into account various inelastic in-medium p-wave channels by introducing the Δ self-energy. Thereby, we expect Σ_Δ to incorporate absorption corrections associated with C_0. Furthermore, we limit our consideration of analyses based on the optical model of Ref. [101] to only the s-wave part of the potential:

$$U^{(s)}(r) \propto b_0\rho(r) + B_0\rho^2(r), \tag{3.49}$$

where phase space factors were omitted for simplicity, and the first term here corresponds to the Fourier-transformed first term in Eq. (3.39). Due to the correlation between b_0 and B_0 pointed out in Ref. [225], the two terms can be lumped together, resulting in an effective modification of the isoscalar parameter b_0:

$$U^{(s)}(r) \propto (b_0 + \Delta b_0)\rho(r), \tag{3.50}$$

where $\Delta b_0 = B_0\rho_e$.

In our model, we assume the following in-medium modification of the isoscalar scattering parameter:

$$b_0^{\mathrm{bound}}(T_{\mathrm{lab}}) = b_0^{\mathrm{free}}(T_{\mathrm{lab}}) + \Delta b_0(T_{\mathrm{lab}}), \tag{3.51}$$

where $b_0^{\mathrm{free}}(T_{\mathrm{lab}})$ is given by Eq. (3.21a), and the complex parameter Δb_0 effectively takes into account not only true absorption but also all possible in-medium modifications.

Comparing Eqs. (3.50) and (3.51), we see that pionic atom analyses with the s-wave part of the potential given by Eq. (3.49) can provide us with information about the threshold value of Δb_0 (see more detailed discussion in Appendix 3.D). Using the value $B_0 = 0.189$ fm^4 from Ref. [228], we arrive at the following result for the imaginary part of the in-medium isoscalar correction:

$$\mathrm{Im}\,\Delta b_0(0) = \frac{1 + m_\pi/2m_N}{1 + m_\pi/m_N}\rho_e\,\mathrm{Im}\,B_0(0) = 0.017\,\mathrm{fm}, \tag{3.52}$$

where we restore the phase space factor and use the s-wave effective density $\rho_e = 0.6\rho_0 \approx 0.1\,\mathrm{fm}^{-3}$ deduced from the overlapping of pion and nucleus densities for pionic atoms [229].

The resulting imaginary part of Δb_0 is assumed to be

$$\mathrm{Im}\,\Delta b_0(T_{\mathrm{lab}}) = \mathrm{Im}\,\Delta b_0(0) + \alpha_{b_0} k_{0,2\mathrm{cm}}(T_{\mathrm{lab}}), \tag{3.53}$$

where α_{b_0} is the effective s-wave isoscalar slope parameter, determined by the fitting procedure, and $k_{0,2\mathrm{cm}}(T_{\mathrm{lab}})$ is the on-shell pion-nucleon c.m. momentum corresponding to T_{lab}.

Performing fitting with various parametrizations of the real part of Δb_0, we conclude that while $\mathrm{Im}\,\Delta b_0$ is an important parameter of our model, the resulting $\mathrm{Re}\,\Delta b_0$ is always close to zero and can be neglected. For this reason, we assume Δb_0 is purely imaginary, given by Eqs. (3.53) and (3.52).

Isovector s-wave modification

Our approach includes the in-medium modification of the s-wave amplitude b_1, as it was successfully applied for the s-wave pionic atom [230, 231] and low-energy pion-nucleus [125, 230] potentials.

To lowest order in the chiral expansion, the parameter b_1 for the scattering of a pion on a free nucleon in the threshold region is given by the Tomozawa-Weinberg expression [232]:

$$b_1^{\mathrm{TW}} = -\frac{1}{8\pi f_\pi^2}\frac{m_\pi m_N}{m_\pi + m_N} \approx -0.11\,\mathrm{fm}, \tag{3.54}$$

where $f_\pi = 92.2\,\mathrm{MeV}$ is the free-space pion decay constant [233, 234]. The value for b_1 obtained in this way is very close to the empirical one not only at low energies but also in the resonance region. According to the suggestion by Weise [235, 236], the medium dependence of the pion decay constant f_π, which is related to the quark condensate, is in the simplest approximation given by a linear function of the nuclear density

$$f_\pi^{*2}(\rho) = f_\pi^2 - \frac{\sigma}{m_\pi^2}\rho, \tag{3.55}$$

where σ is the pion-nucleon sigma term [237]. As a result, the in-medium threshold parameter b_1 is obtained as

$$b_1^{\mathrm{bound}} = \frac{b_1^{\mathrm{free}}}{1 - \sigma\rho/m_\pi^2 f_\pi^2}. \tag{3.56}$$

This simple model successfully described both pionic atoms [229, 238, 239] and low-energy pion-nucleus scattering [240].

For energies above the threshold, b_1 is not constant but a slowly varying function of energy, which is, however, still close to its threshold value even in the Δ-resonance region. In our analysis, we assume the following weak energy dependence of b_1:

$$b_1^{\mathrm{bound}}(T_{\mathrm{lab}}) = b_1^{\mathrm{free}}(T_{\mathrm{lab}}) + \Delta b_1, \tag{3.57}$$

where $b_1^{\mathrm{free}}(T_{\mathrm{lab}})$ is given by Eq. (3.21b) and the energy-independent in-medium correction is taken from the pionic atom

$$\Delta b_1 = b_1^{\mathrm{free}}(0)\frac{\sigma\rho_e/m_\pi^2 f_\pi^2}{1 - \sigma\rho_e/m_\pi^2 f_\pi^2} = -0.044\,\mathrm{fm}, \tag{3.58}$$

where following Ref. [241] $\sigma = 57\,\mathrm{MeV}$ is taken and $b_1^{\mathrm{free}}(0) \approx -0.122\,\mathrm{fm}$ [242]. The resulting value of b_1 at the effective density ρ_e is in quantitative agreement with microscopic [243] and chiral calculations [244], and the recent deeply bound pionic atoms analysis [228]. The effect of double scattering to higher order was shown to be a minor correction [245].

3.4 Results and discussion

In this section, we apply the model developed in Sec. 3.3 to fit $\pi^{\pm}$-^{12}C scattering data. As a result of the fit, we determine our model's three energy-independent real parameters: the real and imaginary parts of the effective Δ-resonance self-energy, $\mathrm{Re}\,\Sigma_\Delta$ and $\mathrm{Im}\,\Sigma_\Delta$ entering Eq. (3.48), and the slope of the imaginary s-wave isoscalar amplitude, α_{b_0} in Eq. (3.53). Subsequently, the same fixed values for three parameters are used to compare our predictions for the pion scattering on ^{16}O, ^{28}Si, and ^{40}Ca with available experimental data.

3.4.1 Observables

The Coulomb interaction significantly influences the charged pion scattering process. The differential elastic cross section is given by

$$\frac{d\sigma}{d\Omega}(\theta) = |F_{C,p}(\theta) + F_{NC}(\theta)|^2\,, \tag{3.59}$$

where we have separated the Coulomb distorted strong-interaction amplitude, F_{NC}, from the singular point-charge Coulomb amplitude

$$F_{C,p}(\theta) = -\frac{\eta_c}{2k_0 \sin^2(\theta/2)} \exp\{2i[\sigma_0 - \eta_c \log\sin(\theta/2)]\}, \tag{3.60}$$

with the Lorentz-invariant Sommerfeld parameter $\eta_c = \alpha Z Z_\pi \omega_{\rm lab}/k_{\rm lab}$, where $Z(Z_\pi)$ is the nucleus (pion) charge. The Coulomb phase shifts σ_l are defined as

$$e^{2i\sigma_l} = \frac{\Gamma(1+l+i\eta_c)}{\Gamma(1+l-i\eta_c)}, \tag{3.61}$$

with Euler's gamma function Γ. The Coulomb-nuclear interference term is split in partial waves as:

$$F_{NC}(\theta) = \sum_l (2l+1) e^{2i\sigma_l} F_l\, P_l(\cos\theta), \tag{3.62}$$

where

$$F_l = \frac{1}{2}\int \mathrm{d}\cos\theta\, F(\boldsymbol{k}', \boldsymbol{k}) P_l(\cos\theta) \tag{3.63}$$

and $\cos\theta = \boldsymbol{k}'\cdot\boldsymbol{k}/(k'k)$. The derivation of F_l is briefly discussed in Appendix 3.A. The full partial-wave amplitudes F_l depend not purely on the hadronic interaction, Eq. (3.12), but also on the short-range part of the Coulomb potential due to the nuclear charge distribution and long-range Coulomb effects. To account for this nuclear-Coulomb interference, we apply the matching method of Vincent and Phatak [246] and an effective Coulomb modification of the reaction energy (see Appendix 3.B for details).

In addition to differential cross sections, experimental measurements also provide Coulomb-subtracted angle-integrated elastic and total cross sections. The direct calculation provides the angle-integrated elastic cross section in the form

$$\sigma^{\rm El} = 4\pi \sum_l (2l+1)\,|F_l|^2\,. \tag{3.64}$$

Table 3.1: Summary of the $\pi^{\pm}$-^{12}C data

Ref.	Facility		T_{lab} [MeV]	Observable
[247]	LAMPF	π^-	30	
[248]	LAMPF	π^+	30, 50	
[249]	LAMPF	$\pi^{\pm}$	30, 50	
[250]	TRIUMF	$\pi^{\pm}$	50	$d\sigma^{\text{El}}/d\Omega$
[251]	LAMPF	$\pi^{\pm}$	50	
[252]	LAMPF	$\pi^{\pm}$	65, 80	
[253]	SIN	$\pi^{\pm}$	100	
[254]	CERN	π^-	120–280	
[254]	CERN	π^-	90–280	$\sigma^{\text{Tot}}, \sigma^{\text{Re}}, \sigma^{\text{El}}$
[110]	RAL	$\pi^{\pm}$	89–855	σ^{Tot}
[114]	SIN	$\pi^{\pm}$	85–245	$\sigma^{\text{Tot}}, \sigma^{\text{Re}}, \sigma^{\text{El}}$
[255]	TRIUMF	$\pi^{\pm}$	42–65	$\sigma^{\text{Tot}}, \sigma^{\text{Re}}$
[256]	TRIUMF	$\pi^{\pm}$	50–80	σ^{Re}
[257]	TRIUMF	$\pi^{\pm}$	20, 30	σ^{Re}

Due to the optical theorem, the total cross section can be derived as

$$\sigma^{\text{Tot}} = \frac{4\pi}{k_0} \sum_l (2l+1)\,\text{Im}[F_l]. \tag{3.65}$$

The pion-nuclear potential is a non-Hermitian operator giving rise to the reaction channel with the corresponding cross section, which can be calculated as

$$\sigma^{\text{R}} = \sigma^{\text{Tot}} - \sigma^{\text{El}}. \tag{3.66}$$

The reaction cross section σ_R includes quasielastic scattering, charge exchange, and true pion absorption.

The total cross section is significant for our analysis since it has a different sensitivity to the imaginary part of the potential as compared with the differential elastic cross section.

3.4.2 Fit to ^{12}C data

Various groups intensively studied pion scattering on carbon from the 1970s through the 1990s. Table 3.1 summarizes the $\pi^{\pm}$-^{12}C scattering data used in our analysis. The dataset includes measurements of the total, angle-integrated elastic, reaction, and differential elastic cross sections done at different facilities: Schweizerisches Institut fur Nuklearforschung (SIN), Canada's particle accelerator center (TRIUMF), Los Alamos Meson Physics Facility (LAMPF), Rutherford Appleton Laboratory (RAL), and the European Organization for Nuclear Research (CERN).

As our aim is the extraction of the effective Δ-resonance self-energy, in the fitting procedure, we only use the data having strong sensitivity to the Δ properties. We choose to fit the data in the energy range of 80–180 MeV pion laboratory kinetic energy, corresponding with the region up to the Δ-resonance excitation energy on a nucleon. Furthermore, our treatment of the Coulomb interaction (the Coulomb energy shift, Eq. (3.79)), as well as the factorization approximation and the HO shell-model correlation functions, relies on the small momentum transfer approximation. Thereby, we limit the fitting of the differential cross section data to momentum transfers $q \leq 1.5\,\mathrm{fm}^{-1}$. Since σ^{Tot}, σ^{R}, and σ^{El} are related through Eq. (3.66), we include in the fit only σ^{Tot} and σ^{El} if all three observables are provided.

The best fit is found by minimizing the χ^2 defined as

$$\chi^2 = \sum_i \sum_j^{n_i} \left[\frac{1}{n_i} \left(\frac{d\sigma_j^{\mathrm{Data}_i} - N_i^{-1} d\sigma_j}{\Delta d\sigma_j^{\mathrm{Data}_i}} \right)^2 + \left(\frac{N_i - 1}{\Delta N_i} \right)^2 \right] + \sum_i \sum_j^{n_i} \left(\frac{\sigma_j^{\mathrm{Data}_i} - \sigma_j}{\Delta \sigma_j^{\mathrm{Data}_i}} \right)^2 , \quad (3.67)$$

where the first (second) term represents a sum over differential (angle-integrated) cross section data sets and n_i is the number of data points in the dataset "i". Every differential cross section dataset $d\sigma^{\mathrm{Data}_i}$ consists of correlated measurements taken at individual energies and is treated as a single uncorrelated point of the fit. Since $\Delta d\sigma_j^{\mathrm{Data}}$ contains only the sum of the statistical and the measured background errors, the normalization parameters N_i are included to account for a fully correlated component between the data points of each differential cross-section data set (instrumental error). The normalization parameters are allowed to vary, keeping the number of degrees of freedom (ndf) the same.

In our formalism, the effective pion-nucleus potential contain only three energy-independent model parameters: the Δ self-energy parameters $\mathrm{Re}\,\Sigma_\Delta$ and $\mathrm{Im}\,\Sigma_\Delta$ in Eq. (3.48), and the s-wave isoscalar slope parameter α_{b_0} in Eq. (3.53). We also tested the possibility of improving our fit by adding model parameters that modify the energy dependence of Σ_Δ and b_0. We found that the resulting χ^2/ndf value can be improved only slightly in this way. However, the strong correlation between the parameters results in large uncertainties, making it impossible to determine the fitted parameters precisely. Moreover, introducing additional parameters does not improve our model predictions beyond the fitting range and for other nuclei.

As was mentioned in Sec. 3.3.1, we also include the d-wave contribution to the first-order potential in addition to the traditional s- and p-wave terms. This small component does not change the overall energy and momentum behavior of observables in a significant way. However, including the d-wave amplitude improves the resulting minimal χ^2 of the fit by about 10%. Note that the observables and fitting parameters are sensitive to the value of the effective bound nucleon mass, which in our calculation is taken as the average of the proton and neutron masses, $m_N = 938.92\,\mathrm{MeV}$.

Tables 3.2–3.4 summarize the fitting results. Two fits were performed: fit 1 with fixed normalization parameters and fit 2 with N_i also being fitted. The obtained model and normalization parameters are collected in Tables 3.2 and 3.3, respectively. The covariance matrix for fit 1 is given in Table 3.4. As can be seen from Table 3.2, letting N_i free improves the resulting χ^2 by about 10%, keeping the fitted parameters almost unchanged. The obtained normalization factors in Table 3.3 are well within the provided

Table 3.2: Model parameters from fits to $\pi^{\pm}$-^{12}C scattering data. For both fits ndf = 32.

fit	$\mathrm{Re}\,\Sigma_\Delta$ [MeV]	$\mathrm{Im}\,\Sigma_\Delta$ [MeV]	α_{b_0} [fm^2]	χ^2	χ^2/ndf
1	12.9 ± 1.3	-33.2 ± 0.8	0.039 ± 0.006	53.4	1.67
2	12.8 ± 1.4	-33.3 ± 0.9	0.040 ± 0.006	47.9	1.50

Table 3.3: Fitted normalization parameters for fit 2. The first column indicates the pion energy, the second (fourth) column – the experimental normalization uncertainties for π^- (π^+) data, and the third (fifth) column – the values of $\Delta N_i^{\mathrm{fit}} = (N_i - 1)\,\%$ for π^- (π^+) data obtained from the fit.

	π^-		π^+	
T_{lab} [MeV]	ΔN_i [%]	$\Delta N_i^{\mathrm{fit}}$ [%]	ΔN_i [%]	$\Delta N_i^{\mathrm{fit}}$ [%]
80	± 5	0.5 ± 4.8	± 7	3.9 ± 4.0
100	± 8	-5.6 ± 4.5	± 8	-1.8 ± 4.5
120	± 5	1.1 ± 3.4		
150	± 4	0.1 ± 2.6		
180	± 3	-1.0 ± 2.2		

Table 3.4: The correlation matrix for fit 1.

	$\mathrm{Re}\,\Sigma_\Delta$	$\mathrm{Im}\,\Sigma_\Delta$	α_{b_0}
$\mathrm{Re}\,\Sigma_\Delta$	1	0.53	0.22
$\mathrm{Im}\,\Sigma_\Delta$	0.53	1	-0.4
α_{b_0}	0.22	-0.4	1

experimental normalization uncertainties. The consistency of the results strengthens the reliability of derived results and the robustness of the method. In the following calculations, we will use the parameter set corresponding to fit 1.

In Fig. 3.5, we show the fitted data compared with the obtained theoretical curves corresponding to fit 1. The resulting agreement is especially good for integrated and differential elastic cross sections for $\theta \leq 60°$. Despite the fact that the data for $q > 1.5\,\mathrm{fm}^{-1}$ were not fitted, our model demonstrates a fairly good description of the data even for large angles, except for the dataset at 100 MeV, which seems to be an outlier. The obtained differential cross section at 100 MeV significantly undershoots the data for $\theta \gtrsim 120°$. The same discrepancy was also reported in the Δ-hole model analysis of Ref. [253] and the phenomenological momentum-space potential approach of Ref. [108] with the $\rho^2(r)$-dependent second-order term.

As seen from the top left panel of Fig. 3.5, the integrated cross sections are well described outside the fitting range denoted by the vertical dashed lines. The predicted

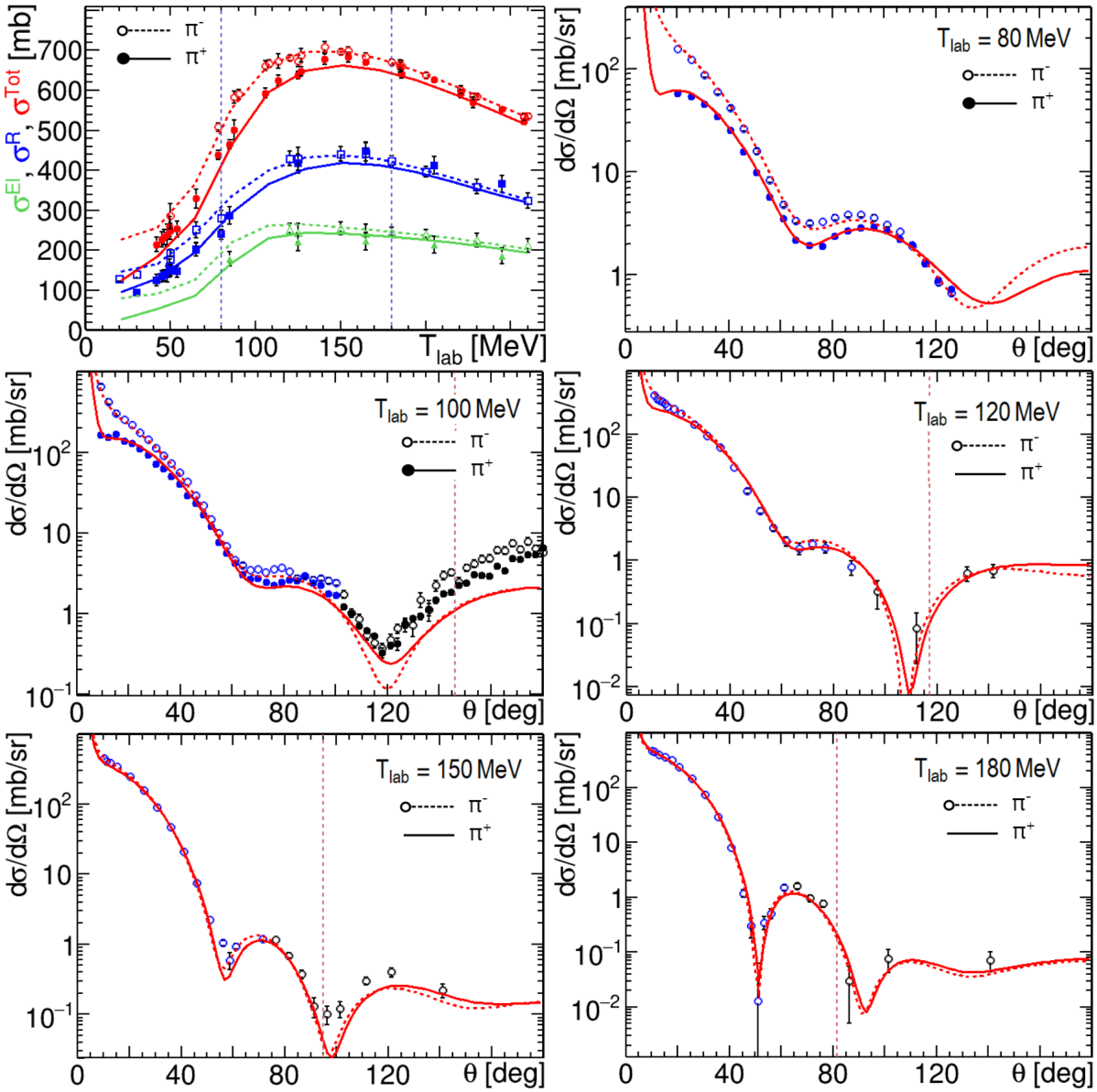

Figure 3.5: Fit to $\pi^{\pm}$-^{12}C scattering data using the full second-order potential. The top left panel demonstrates the total (red curves and circles), integrated reaction (blue curves and squares), and elastic (green curves and triangles) cross sections. Solid curves and closed markers stand for π^+; dashed and open markers for π^-. The vertical dashed lines on the top left panel indicate the fitted energy range. Differential cross sections in the 80–180 MeV range as functions of the scattering angle in the c.m. frame are shown on other panels. The blue circles on the differential cross section plots correspond to the $q < 1.5\,\mathrm{fm}^{-1}$ range, which was fitted; the black circles were not included in χ^2. The dashed vertical lines on $d\sigma/d\Omega$ plots indicate the zero position of the form factor. Table 3.1 lists the experimental data presented in the plots.

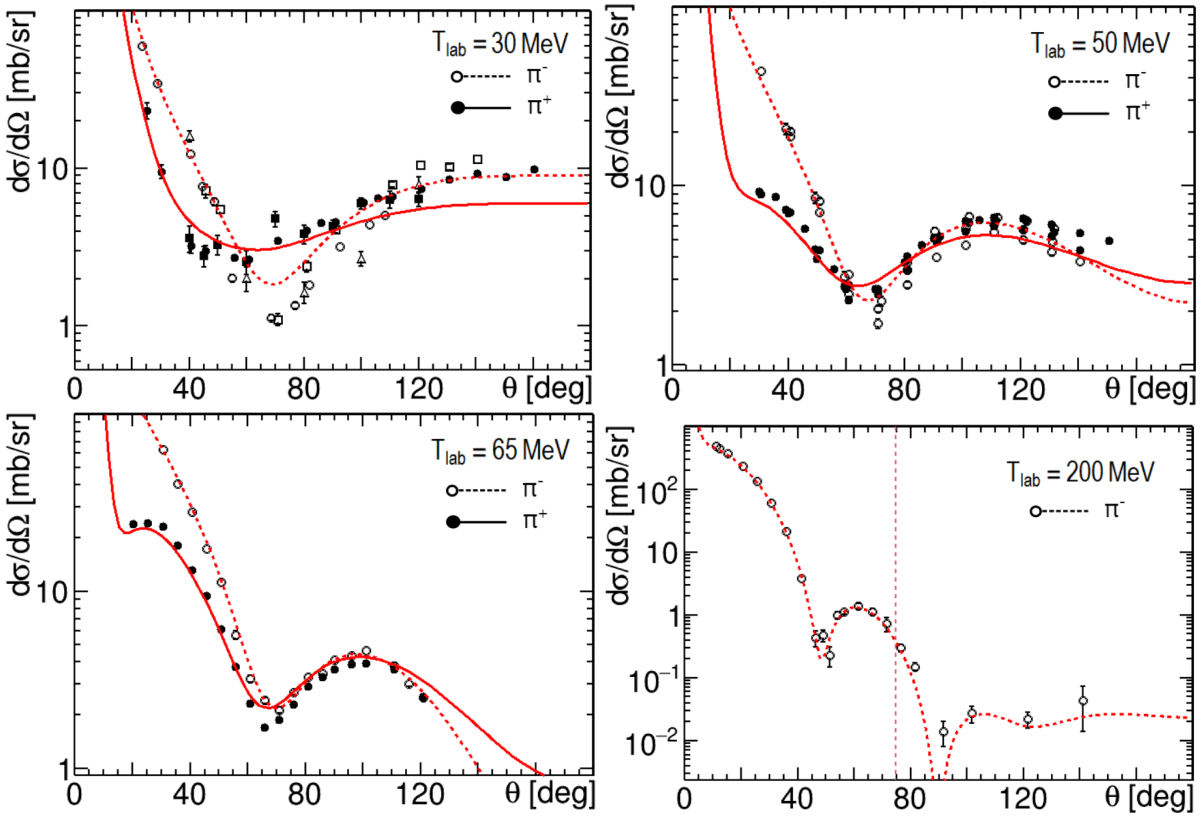

Figure 3.6: Comparison of the theoretical prediction based on fit 1 with the $\pi^{\pm}$-^{12}C scattering data at kinetic energies outside the fitting range. The meaning of the curves is the same as in Fig. 3.5. Table 3.1 lists the experimental data presented in the plots.

differential cross sections based on fit 1 outside the fitting range are plotted in Fig. 3.6. The data measured at 65 and 200 MeV are well reproduced. Some deviations are seen at 30 and 50 MeV, which can be fixed by a more precise treatment of the s-wave medium modifications. This involves a more intricate energy dependence for b_0 with a nonzero real part. Incorporating nuclear excitations in the propagator $\hat{G}_{\alpha^*}$ of Eq. (3.31) also becomes particularly crucial at low energies, where the transition strength to collective states becomes significant.

In Fig. 3.7, we illustrate the impact of the second-order component of the potential on the π^--^{12}C differential cross sections. We compare theoretical curves obtained using the full potential, i.e., the sum of Eqs. (3.39) and (3.46), as presented in Figs. 3.5 and 3.6, with results from calculations using only the first-order potential, Eq. (3.39). First, we disable the second-order part of the potential, resulting in the black dash-dotted curves in Fig. 3.7. Then, we fit the same dataset using the first-order potential, producing the blue long-dashed curves. The minimization process yields $\chi^2/\text{ndf} \approx 10$, indicating a poor fit to the data. The plot at $T_{\text{lab}} = 65$ MeV underscores the substantial significance of the second-order component, $V^{(2)}$, in π-^{12}C scattering at low energies. Although the influence of $V^{(2)}$ diminishes as energy increases, it remains substantial even at $T_{\text{lab}} = 200$ MeV for $\theta > 80°$. For energies $T_{\text{lab}} \lesssim 100$ MeV, within our parametrization, the first-order potential fails to provide sufficient Coulomb splitting between positive and

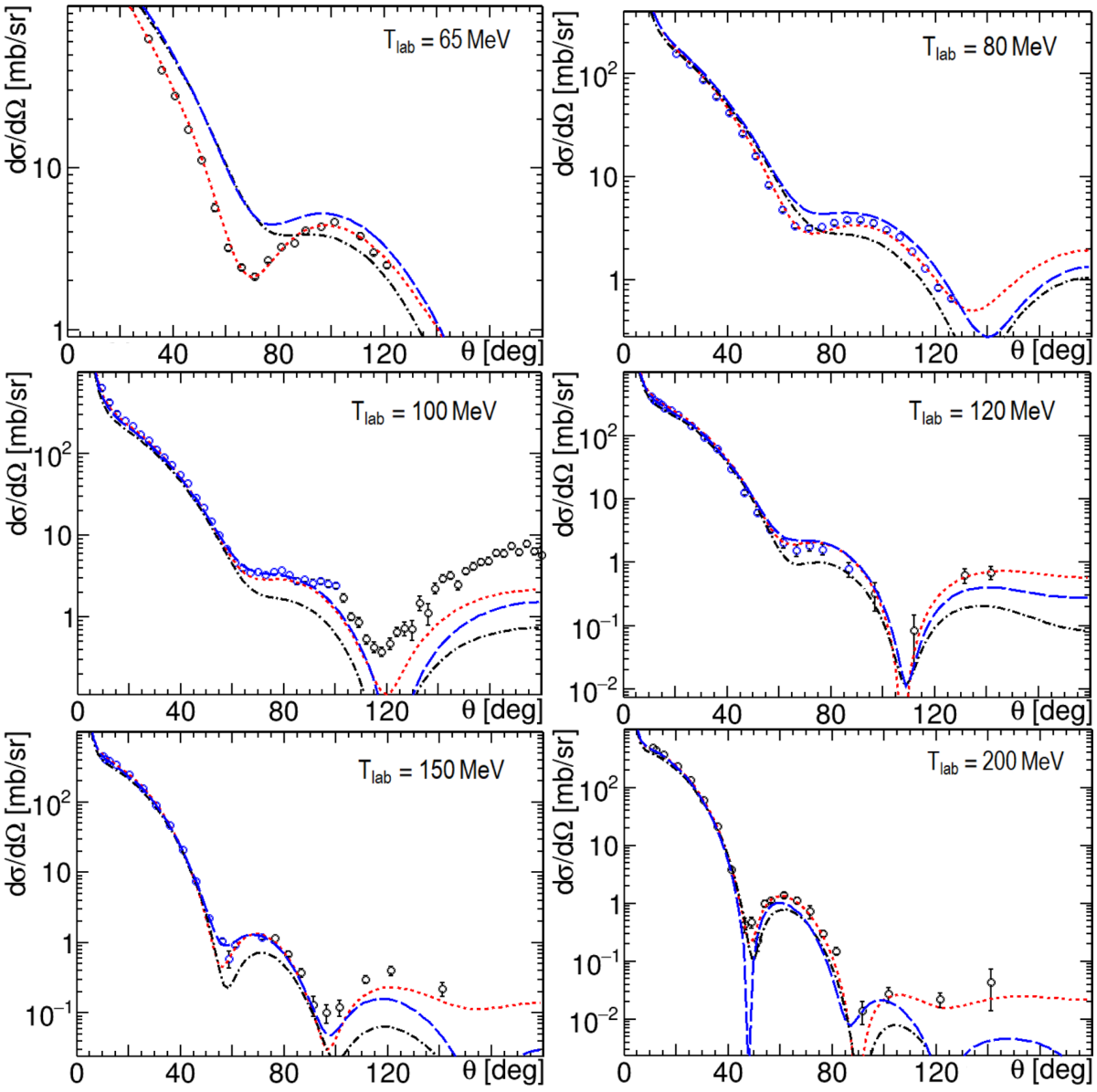

Figure 3.7: Differential cross sections for π^--^{12}C with and without the second-order part of the potential. The red short-dashed curves correspond to fit 1 and are identical to those in Figs. 3.5 and 3.6; the black dash-dotted curves are obtained from fit 1 by switching off the second-order part of the potential, $V^{(2)} = 0$; the blue long-dashed represent the results of fitting $\pi^{\pm}$-^{12}C data using only the first-order potential $V^{(1)}$. Table 3.1 lists the experimental data presented in the plots.

Table 3.5: Summary of the $\pi^{\pm}$-^{16}O data

Ref.	Facility		T_{lab} [MeV]	Observable
[249]	LAMPF	π^-	50	
[248]	LAMPF	π^+	50	$d\sigma^{\text{El}}/d\Omega$
[258]	SIN	π^+	80 - 343	
[259]	SREL	$\pi^{\pm}$	155 - 213	
[260]	SIN	π^+	114 - 240	$\sigma^{\text{Tot}}, \sigma^{\text{El}}$
[110]	RAL	$\pi^{\pm}$	89 - 342	σ^{Tot}

negative pion differential cross sections. Consequently, the differential cross sections for π^+, for which there is less available experimental data, exhibit notably poorer agreement compared to π^-.

3.4.3 Comparison with ^{16}O data

Having the model parameters of the pion-nucleus potential fixed from the $\pi^{\pm}$-^{12}C data fitting, we can further test the predictive power of our model for another p-shell nucleus. We compare our theoretical predictions based on fit 1 with the data on $\pi^{\pm}$-^{16}O scattering. Table 3.5 summarizes the experimental data used for the comparison.

Since ^{12}C and ^{16}O are both spin-isospin-zero closed p-subshell nuclei, in our calculation, we replace only the nuclear form factors and apply the correlation functions given by Eqs. (2.78). The pion-nucleon scattering amplitudes are kept the same. The resulting plots with our predictions are presented in Fig. 3.8, demonstrating a rather good agreement between the model and experimental data. The small deviations between theoretical curves and the differential cross-section data are similar to those present on the plots for ^{12}C. The theoretical curves follow the data even for large angles, except for 114 MeV, where the minimum is shifted by about 5°. The small-angle $\pi^{\pm}$-^{16}O scattering data at 155, 185, and 213 MeV from the Space Radiation Effects Laboratory (SREL) [259] are well reproduced. The comparison supports our expectation of the model's universality and demonstrates its predictive power.

3.4.4 Comparison with ^{28}Si and ^{40}Ca data

The described model copes well with describing both ^{12}C and ^{16}O data using the same set of parameters. In general, it can be applied for any spin- and isospin-zero nucleus if the nuclear form factor and correlation functions C_0 and C_{ex} are known. However, the calculation of the second-order part of the potential, Eq. (3.46), becomes involved even for p-shell nuclei. Moreover, the harmonic oscillator shell model used to calculate the correlation functions for ^{12}C and ^{16}O is much less suitable for describing heavier nuclei like ^{40}Ca, requiring more realistic nucleon wave functions. However, considering that the influence of the second-order correction decreases for heavier nuclei, we can still try applying the harmonic oscillator model to derive C_0 and C_{ex} for closed d-subshell nuclei,

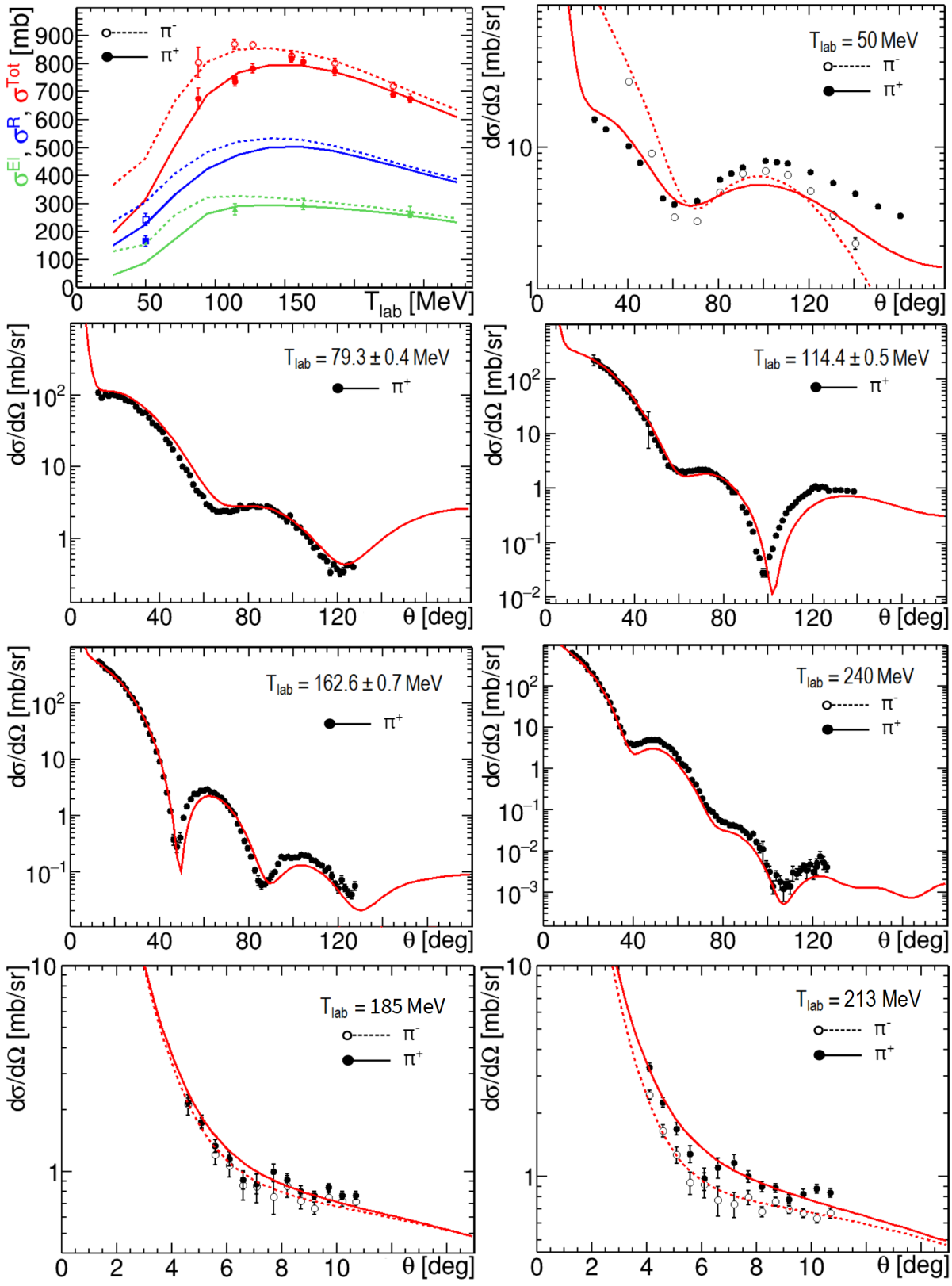

Figure 3.8: Comparison of the theoretical calculation based on fit 1 with the data for $\pi^{\pm}$-^{16}O scattering. The meaning of the curves is the same as in Fig. 3.5. Table 3.5 lists the experimental data presented in the plots.

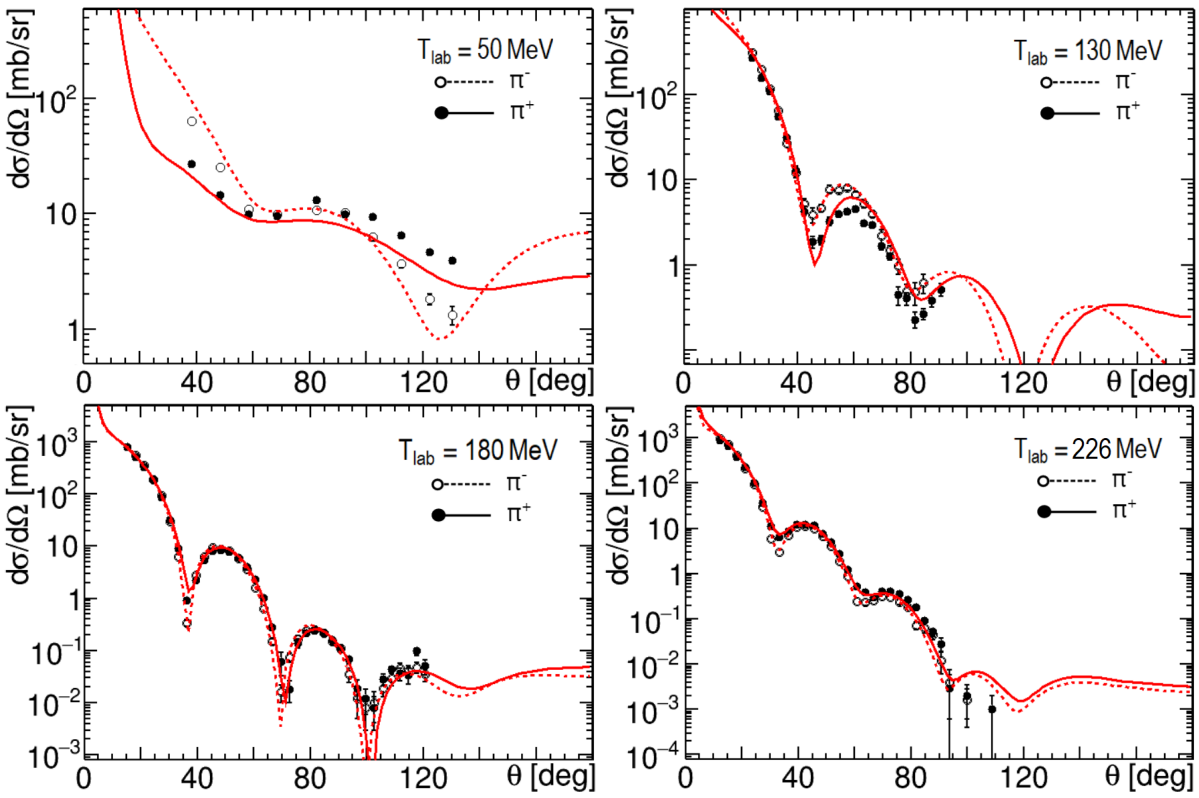

Figure 3.9: Comparison of the theoretical calculation based on fit 1 with the data for $\pi^{\pm}$-^{28}Si scattering. The meaning of the curves is the same as in Fig. 3.5. Table 3.6 lists the experimental data presented in the plots.

Table 3.6: Summary of the $\pi^{\pm}$-^{28}Si and $\pi^{\pm}$-^{40}Ca differential cross section data

Ref.	Facility		T_{lab} [MeV]	Nucleus
[261]	TRIUMF	$\pi^{\pm}$	50	^{28}Si
[262]	SIN	$\pi^{\pm}$	130, 180, 226	
[249]	LAMPF	π^{-}	50	
[248]	LAMPF	π^{+}	50	
[263]	LAMPF	$\pi^{\pm}$	65	^{40}Ca
[264]	LAMPF	$\pi^{\pm}$	80	
[265]	SIN	$\pi^{\pm}$	130, 180, 230	

as given in Eqs. (2.79) and (2.80).

In Figs. 3.9 and 3.10, we demonstrate our prediction for the $\pi^{\pm}$-^{28}Si and $\pi^{\pm}$-^{40}Ca differential cross sections, respectively. The theoretical model is compared with the experimental differential cross section data listed in Table 3.6. Given that no additional adjustments were made, the agreement between our prediction and the data is surprisingly good, especially at larger energies. The observed small discrepancy at low energies can be explained by a more decisive influence in heavier nuclei of the *s*-wave part of the

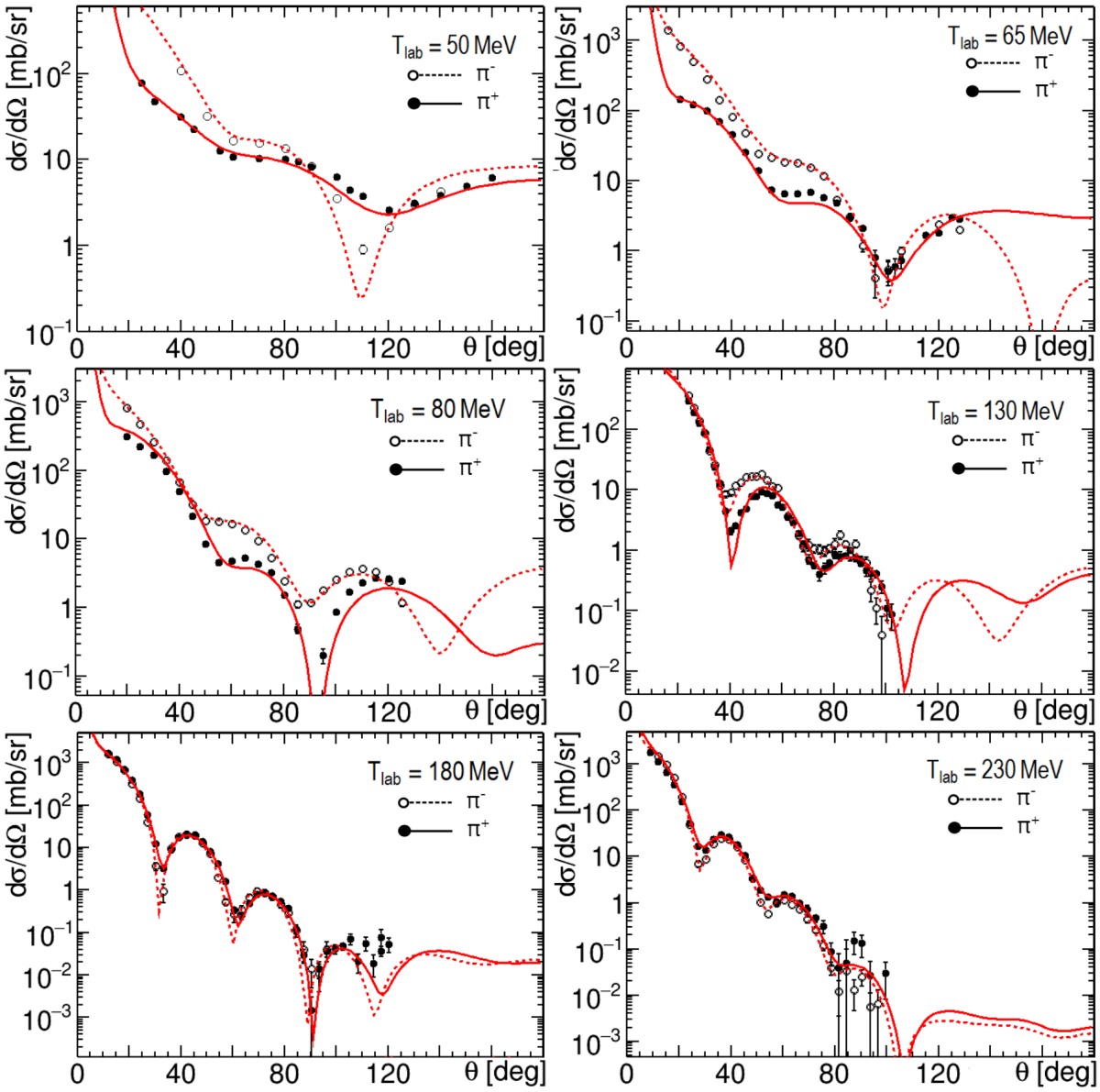

Figure 3.10: Comparison of the theoretical calculation based on fit 1 with the data for $\pi^{\pm}$-^{40}Ca scattering. The meaning of the curves is the same as in Fig. 3.5. Table 3.6 lists the experimental data presented in the plots.

potential and stronger Coulomb-nuclear interference.

In Fig. 3.11, we further investigate the influence of the second-order part of the potential, Eq. (3.46), by comparing the differential cross sections for π^- scattering on ^{12}C, ^{28}Si, and ^{40}Ca at 50 and 180 MeV pion laboratory kinetic energy. We present the results of the full calculation, as displayed in Figs. 3.5, 3.6, 3.9, and 3.10, alongside the theoretical curves obtained after setting $V^{(2)} = 0$. As can be seen from Figs. 3.7 and 3.11, the contribution of $V^{(2)}$ diminishes as the nucleus becomes heavier and as the energy increases. However, the second-order component remains important for achieving a good agreement with the data, particularly for $\theta > 60°$ in the case of π-^{40}Ca scattering at 180 MeV.

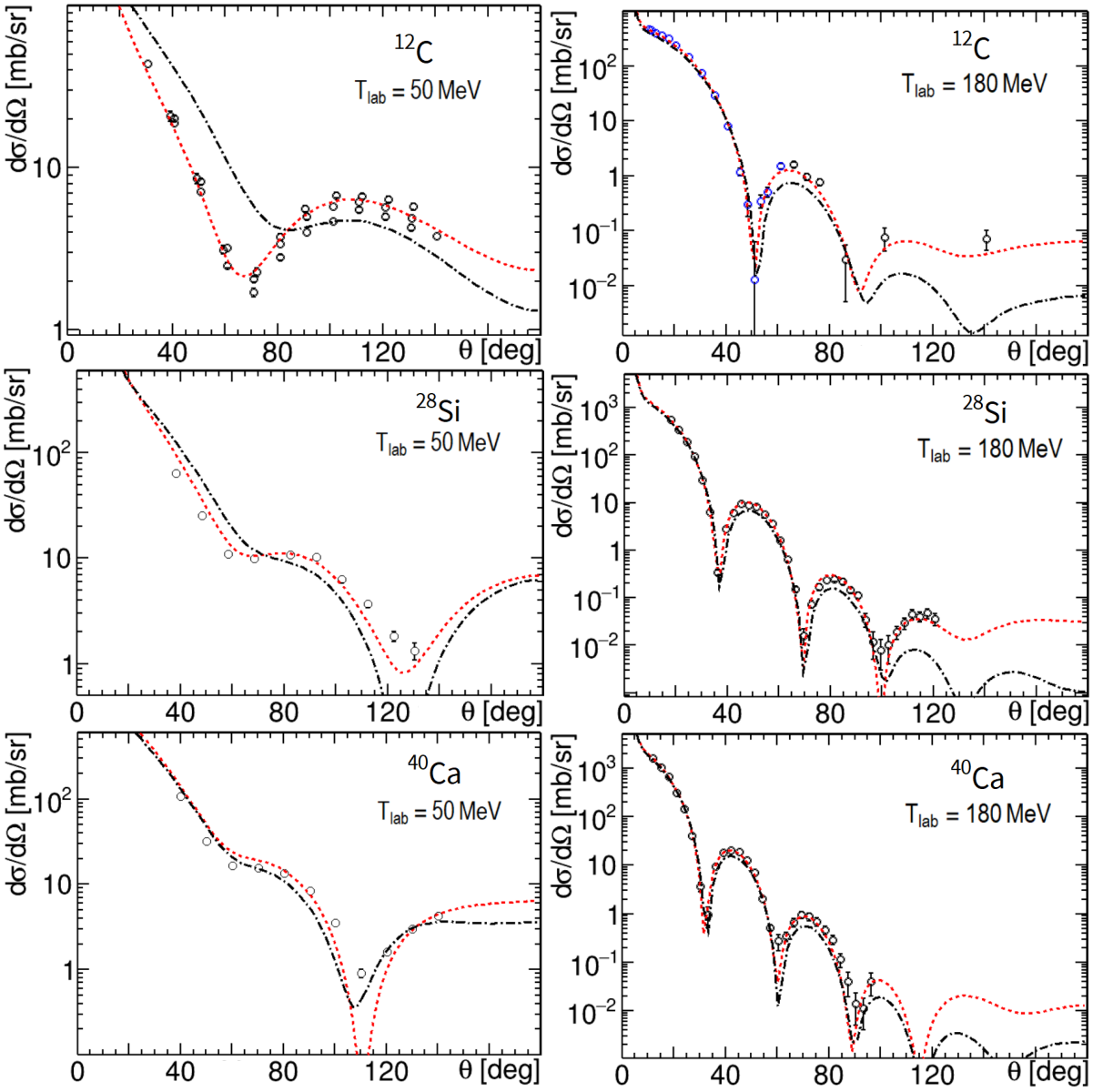

Figure 3.11: Comparison of the theoretical calculation based on fit 1 with the data for π^- scattering on ^{12}C, ^{28}Si and ^{40}Ca at 50 and 180 MeV pion laboratory kinetic energy. The meaning of the curves is the same as in Fig. 3.7. Tables 3.1 and 3.6 list the experimental data presented in the plots.

3.4.5 Comparison with ^{4}He data

To further test the model, we employ it to describe pion scattering on ^{4}He. Although ^{4}He seems to be a straightforward case, the presence of only four nucleons challenges the assumptions regarding the saturation of Σ_Δ and the use of the HO shell model correlation functions, Eqs. (2.76). Table 3.7 summarizes the $\pi^\pm$-^{4}He scattering data used for the comparison. This dataset encompasses measurements of σ^{Tot}, σ^{El}, σ^{Re}, and differential elastic cross sections performed at Lawrence Radiation Laboratory (LRN, now LBNL), Joint Institute for Nuclear Research in Dubna (JINR), and CERN.

Table 3.7: Summary of the $\pi^{\pm}$-^{4}He Data

Ref.	Facility		$T_{\rm lab}$ [MeV]	Observable
[266]	LRN	$\pi^{\pm}$	51 - 75	
[113]	CERN	π^{-}	98 - 260	
[267]	JINR	$\pi^{\pm}$	120, 174	$d\sigma^{\rm El}/d\Omega$
[268]	JINR	$\pi^{\pm}$	68, 154	
[269]	JINR	$\pi^{\pm}$	98 - 208	
[113]	CERN	π^{-}	51 - 260	$\sigma^{\rm Tot}$, $\sigma^{\rm Re}$, $\sigma^{\rm El}$
[269]	JINR	$\pi^{\pm}$	68 - 208	$\sigma^{\rm El}$

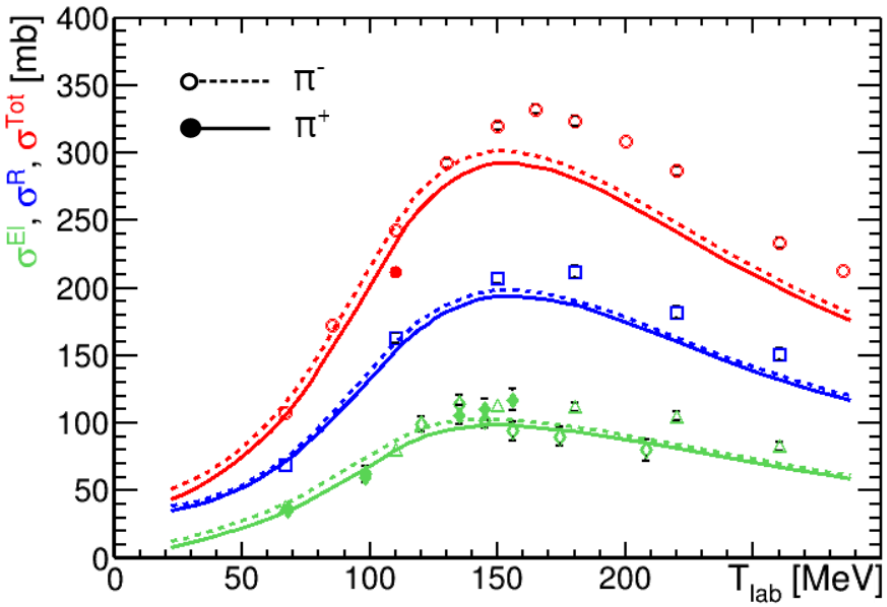

Figure 3.12: Comparison of the theoretical calculation based on fit 1 with the integrated cross-section data for $\pi^{\pm}$-^{4}He scattering. The meaning of the curves is the same as in Fig. 3.5. The green diamonds represent data from JINR, while all other markers denote data from CERN (see Table 3.7).

In Figs. 3.12–3.14, we present our predictions for $\pi^{\pm}$-^{4}He scattering based on fit 1 without additional fitting. As seen from Fig. 3.12, displaying integrated cross sections, the low-energy data of LRN and CERN are well reproduced. The upper four panels of Fig. 3.13 demonstrate a good description of LRN and JINR data, which additionally validates the low-energy regime of our model for ^{4}He. The agreement achieved with the ^{4}He data below the pion laboratory kinetic energy of 80 MeV surpasses that for heavier nuclei. This is attributed to the reduced sensitivity of ^{4}He to the s-wave part of the scattering potential.

Below 120 MeV, a significant disagreement is observed only for the π^+-^{4}He total cross section at $T_{\rm lab} = 110$ MeV (red filled circle in Fig. 3.12). However, the measured splitting between π^+ and π^--^{4}He total cross sections at $T_{\rm lab} = 110$ MeV is about 31 MeV, which

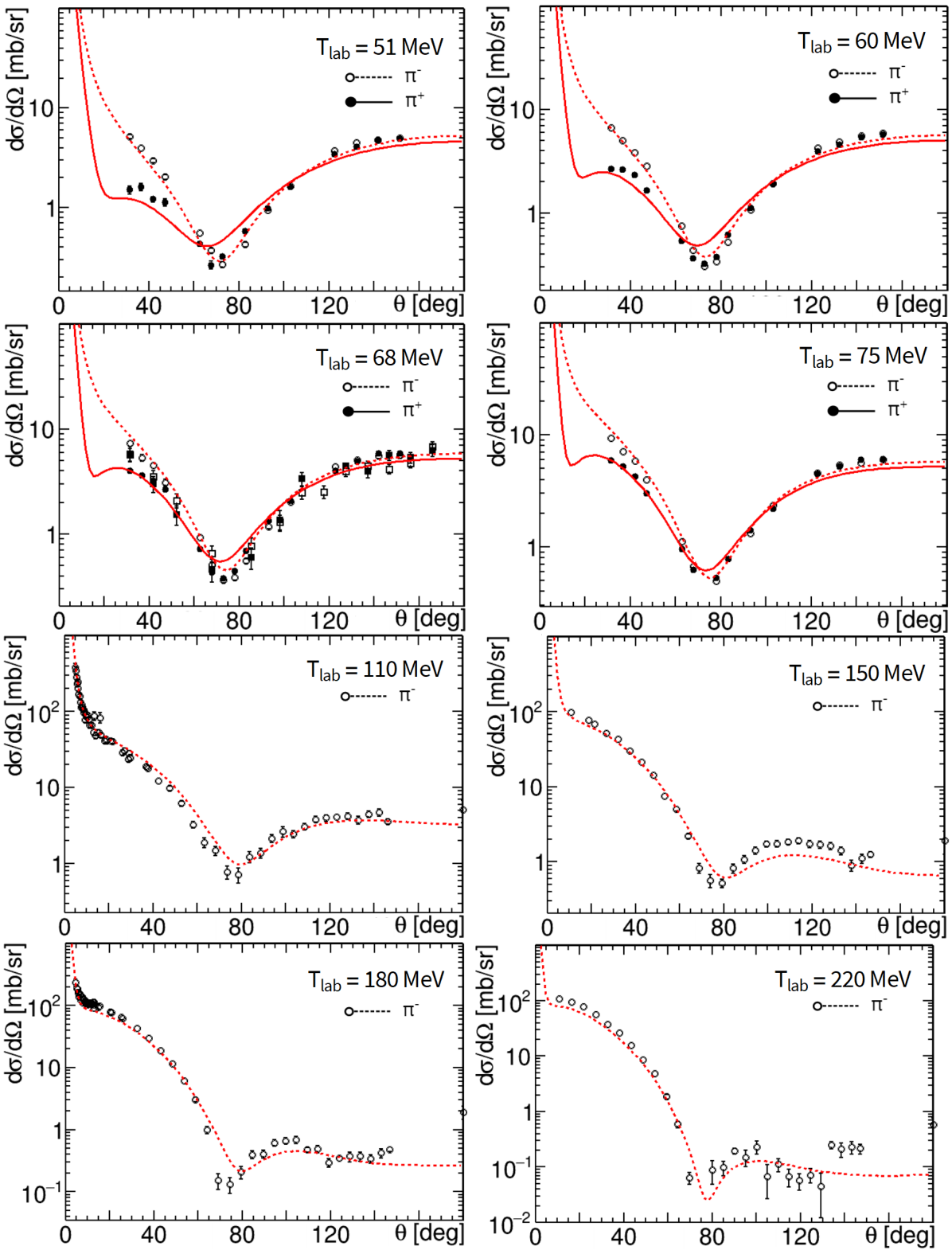

Figure 3.13: Comparison of the theoretical calculation based on fit 1 with LRN (upper 4 panels) and CERN (lower 4 panels) data for $\pi^{\pm}$-^{4}He elastic scattering. The plot for 68 MeV includes JINR data, denoted by square markers. The meaning of the curves is the same as in Fig. 3.5. Table 3.7 lists the experimental data presented in the plots.

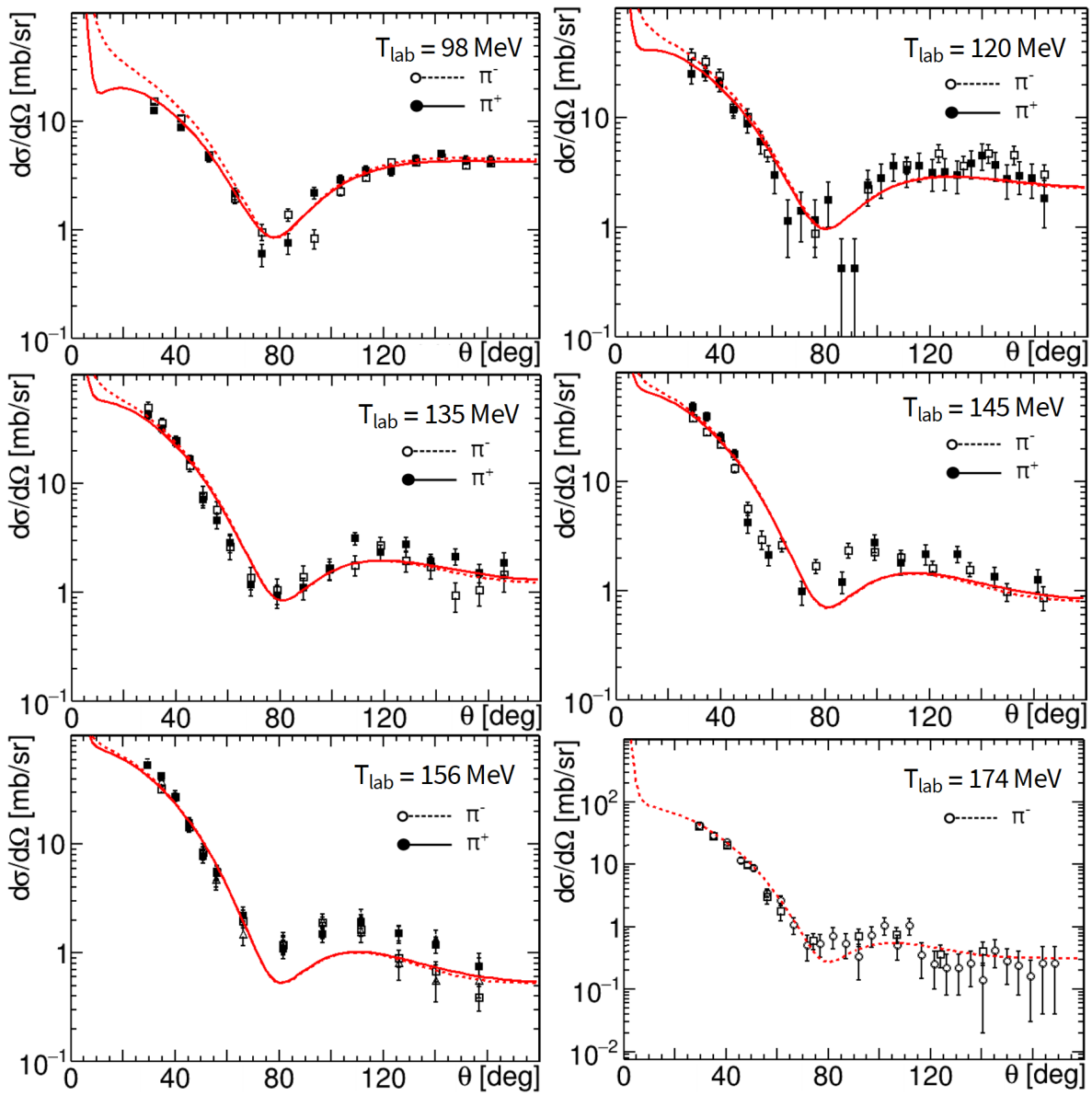

Figure 3.14: Comparison of the theoretical calculation based on fit 1 with JINR data for $\pi^{\pm}$-^{4}He elastic scattering. The meaning of the curves is the same as in Fig. 3.5. Table 3.7 lists the experimental data presented in the plots.

is close to the Coulomb separation observed in ^{12}C. For this reason, we suggest that the π^+ total cross section measurement at 110 MeV underestimates the true value.

As follows from Fig. 3.12, discrepancies emerge for pion laboratory kinetic energies exceeding 130 MeV between CERN and JINR data. While our predictions for integrated elastic cross sections in Fig. 3.12 closely match the green diamonds representing JINR data, the data points from CERN are notably higher. Figure 3.14 and the lower four panels of Fig. 3.13 demonstrate the differential cross section data from JINR and CERN, respectively. Similarly to the integrated cross sections in Fig. 3.12, our predictions underestimate CERN data while providing a satisfactory description of JINR data above 130 MeV. The present disagreement between the data does not allow to properly check

the model at higher energies. However, if the CERN data are correct, the disagreement may be explained by the violation of the assumed saturation of Δ in-medium interaction with surrounding nucleons in ^{4}He.

3.5 Conclusion and outlook

In the present Chapter, we have constructed the second-order pion-nuclear potential in momentum space. The potential is based on the individual pion-nucleon scattering amplitudes extracted from SAID. The second-order correction to the potential depends on two types of correlation functions and, as a result, is consistent with the Pauli principle. The many-body medium effects are incorporated in the complex effective Δ self-energy and the modifications to the s-wave scattering parameters.

In our approach, only three fitting parameters are introduced: the real and imaginary parts of the Δ self-energy and the s-wave isoscalar slope parameter. The free parameters were determined by fitting the $\pi^{\pm}$-^{12}C scattering data in the energy range of 80–180 MeV pion laboratory kinetic energy, which shows a strong sensitivity to the Δ-resonance properties. The developed second-order potential was found to yield a successful description of the total, angle-integrated elastic, reaction, and differential elastic cross-section data, assuming that the model parameters are energy independent.

Furthermore, the model demonstrates that it yields a good description of the $\pi^{\pm}$-^{12}C data not only in the fitting range but also outside of it. To check its predictive power, we have applied the second-order potential to heavier nuclei, using the three parameters which have been fixed by fitting the ^{12}C data. The model predictions for ^{16}O, ^{28}Si, and ^{40}Ca nuclei were found to nicely agree with the experimental data, supporting the model's universality and predictive power.

The present work sets the stage for a more detailed analysis for scattering on heavy nuclei and for the case of nuclei with nonzero isospin. As a next step, the presented model can also be applied to analyze electron- or neutrino-induced pion production processes on nuclei.

Appendices

3.A Partial wave decomposition

The effective potential can be exactly decomposed into a linear combination of Legendre polynomials:

$$V(\boldsymbol{k}', \boldsymbol{k}) = \sum_l (2l+1) V_l(k', k) P_l(x), \tag{3.68}$$

with

$$V_l(k', k) = \frac{1}{2} \int \mathrm{d}x \, V(\boldsymbol{k}', \boldsymbol{k}) P_l(x), \tag{3.69}$$

where $x = \boldsymbol{k}' \cdot \boldsymbol{k}/(k'k)$. A similar decomposition applies to the scattering amplitude $F_l(k', k)$. As a result, the three-dimensional integral equation, Eq.(3.12), can be reduced to a one-dimensional form:

$$F_l(k', k) = V_l(k', k) - \frac{2\alpha}{\pi} \int k''^2 \, \mathrm{d}k'' \frac{V_l(k', k'') F_l(k'', k)}{k_0^2 - k''^2 + i\varepsilon}. \tag{3.70}$$

with $\alpha = (A-1)/A$.

Using the Sokhotski-Plemelj theorem, we can decompose the propagator into its on-shell and off-shell parts:

$$\frac{1}{k_0^2 - k''^2 + i\varepsilon} = \frac{\text{p.v.}}{k_0^2 - k''^2} - \frac{i\pi}{2k_0} \delta(k'' - k_0), \tag{3.71}$$

where "p.v." denotes an integral in the sense of principal value. This decomposition allows us to introduce the K-matrix, which satisfies the scattering equation with the off-shell part of the propagator:

$$K_l(k', k) = V_l(k', k) - \frac{2\alpha}{\pi} \int k''^2 \, \mathrm{d}k'' \frac{V_l(k', k'') K_l(k'', k)}{k_0^2 - k''^2}, \tag{3.72}$$

while the scattering amplitude is given by

$$F_l(k', k) = K_l(k', k) + i\alpha k_0 K_l(k', k_0) F_l(k_0, k). \tag{3.73}$$

Eq. (3.72) can be solved numerically using a matrix inversion method (see a matrix diagonalization technique in momentum space [270]). The on-shell scattering amplitude is related to the on-shell K-matrix as

$$F_l \equiv F_l(k_0, k_0) = \frac{K_l(k_0, k_0)}{1 - i\,\alpha\, k_0 K_l(k_0, k_0)}. \tag{3.74}$$

Outside the range of the potential, the radial wave function of a projectile in the coordinate space can be written as [271]

$$u_l(r) \propto kr \left[j_l(kr) + \tan \delta_l(k) n_l(kr) \right], \tag{3.75}$$

where $j_l(x)$ and $n_l(x)$ are spherical Bessel functions of the first and second kind, respectively. Here $\delta_l(k)$ are the phase shift relative to an undistorted outgoing spherical wave:

$$\lim_{r\to\infty} u_l(r) \propto \sin \left[kr - \frac{1}{2} l\pi + \delta_l(k) \right], \tag{3.76}$$

which are related to the on-shell K-matrix as

$$\tan\delta_l = k_0 K_l(k_0, k_0). \tag{3.77}$$

As result, Eq. (3.75) can be expressed in the form

$$u_l(r) \propto kr\left[j_l(kr) + k_0 F_l h_l^+(kr)\right], \tag{3.78}$$

where $h_l^+(x) = n_l(x) + i\, j_l(x)$ is spherical analogues of the Hankel functions of the first kind.

3.B Scattering by nuclear and Coulomb potentials

The charged pion that approaches the nucleus, π^- (π^+), is accelerated (decelerated) due to the influence of the long-range Coulomb field of the nucleus. This effect occurs before the pion reaches the range of the strong interaction described by the pion-nucleus potential $\hat{U}(E)$. At intermediate energies, the pion-nucleon scattering has a strong energy dependence due to the resonant P_{33} channel and is sensitive to this Coulomb energy shift. As a result, the potential $\hat{U}(E)$ in the scattering equations must be replaced with the nuclear-Coulomb potential $\hat{U}_{NC}(E)$, which can be approximated as

$$\hat{U}_{NC}(E) = \hat{U}(E - \langle\hat{U}_C\rangle) + \hat{U}_C. \tag{3.79}$$

In Eq. (3.79), besides adding the Coulomb potential, $\hat{U}_C$, we shift the reaction energy by the value of the Coulomb potential at the root-mean-squared (rms) radius of the nucleon distribution [272, 273]. The shift in the energy argument of the nuclear potential describes the intermediate Coulomb rescattering and, in general, is given at the operator level, but assuming the commutativity of U_C with the Green's function and neglecting the nucleus excitation by the Coulomb potential, we arrive at Eq. (3.79) (see Ref. [274] for details).

We explicitly separate the momentum transfer dependent nuclear structure characteristics, namely the form factor and correlation functions, from the angle- and energy-dependent single-nucleon scattering amplitudes in the pion-nucleus potential. When dealing with the pion-nuclear potential in coordinate space, applying the Coulomb energy shift in Eq. (3.79) is straightforward and consists in shifting only the argument of the scattering coefficients in Eqs. (3.21). However, the situation is more complicated for the potential in momentum space due to its dependence on the off-shell momentum. To address this, we assume that the entire pion-nucleon on-shell transition and scattering amplitudes are calculated as described in Sec. 3.2 but with the shifted on-shell momentum $k_0(T_{\rm lab} - \langle U_C\rangle)$ in the pion-nucleus c.m. frame, where

$$k_0^2(T_{\rm lab}) = \frac{m_A^2 T_{\rm lab}(2m_\pi + T_{\rm lab})}{(m_A + m_\pi)^2 + 2m_A T_{\rm lab}}. \tag{3.80}$$

For a smooth off-shell extrapolation, we further assume that the Coulomb-affected off-shell momenta involved in calculating the off-shell vertex factor, Eq. (3.24), are replaced by

$$k^2 \longrightarrow k^2 + k_0^2(T_{\rm lab} - \langle U_C\rangle) - k_0^2(T_{\rm lab}). \tag{3.81}$$

A direct solution of the scattering equation (3.12) involving the long-range Coulomb interaction is difficult due to $1/q^2$ singularity in the momentum space representation of the Coulomb potential. To address this issue, we apply Vincent and Phatak's method [246] to treat the Coulomb-nuclear interaction in momentum space. It is assumed that in coordinate space, the nuclear part of the potential vanishes beyond the cutoff radius $R_{\rm cut}$. As a result, at $r \geq R_{\rm cut}$, only the point-charge Coulomb potential exists, and the radial part of the coordinate space wave function can be expressed as

$$u_l(r) \propto \mathscr{F}_l(\eta_c, k_0 r) + k_0 F_l \, \mathscr{H}_l(\eta_c, k_0 r), \tag{3.82}$$

with $\mathscr{H}_l \equiv \mathscr{H}_l^+ = \mathscr{G}_l + i\mathscr{F}_l$, where $\mathscr{F}_l$ and $\mathscr{G}_l$ are the regular and irregular Coulomb functions [275]. The amplitude F_l in Eq. (3.82) represents the correct Coulomb-modified nuclear partial-wave scattering amplitude that describes the observed cross sections and enters Eqs. (3.62)–(3.65). The asymptotic Coulomb wave function, Eq. (3.82), is smoothly matched with the cutoff solution at $r = R_{\rm cut}$, which yields:

$$F_l = \frac{1}{k_0} \frac{\mathscr{F}_l'(\eta_c, \rho) - \xi_l \mathscr{F}_l(\eta_c, \rho)}{\xi_l \mathscr{H}_l(\eta_c, \rho) - \mathscr{H}_l'(\eta_c, \rho)}, \tag{3.83}$$

where $\rho = k_0 R_{\rm cut}$ and

$$\xi_l = \frac{\mathscr{F}_l'(0, \rho) + k_0 F_l^{\rm cut} \mathscr{H}_l'(0, \rho)}{\mathscr{F}_l(0, \rho) + k_0 F_l^{\rm cut} \mathscr{H}_l(0, \rho)}. \tag{3.84}$$

The partial amplitude $F_l^{\rm cut}$ is the solution of the pion-nucleus scattering equation with the short-range potential, which is the sum of the Coulomb potential cut at $R_{\rm cut}$ and the strong pion-nuclear potential described in Sec. 3.3. We derive $F_l^{\rm cut}$ from Eq. (3.12) using the momentum space representation of the cut Coulomb potential given by

$$V_C^{\rm cut}(q) = -2\bar{\omega} \frac{\alpha Z_\pi}{q^2} \left[\rho_{\rm ch}(q) \rho_{\rm ch}^\pi(q) - Z \cos(q R_{\rm cut}) \right], \tag{3.85}$$

where $\rho_{\rm ch}(q)$ and $\rho_{\rm ch}^\pi(q)$ are the charge form factors of the nucleus and pion. We use the value $R_{\rm cut} = 8\,{\rm fm}$.

The original Kerman-McManus-Thaler (KMT) multiple-scattering formalism does not explicitly address the Coulomb interaction. As a result, the KMT scattering Equations (3.6) and (3.12) in the pure Coulomb scattering limit, $\hat{U} \to \hat{U}_C$, fail to provide the correct Coulomb scattering amplitude due to factor $(A-1)/A$. The treatment of the Coulomb interaction in the KMT formalism was examined in detail in Ref. [276]. To recover the Coulomb scattering amplitude effectively, we follow the "KMT No. 3 prescription" of Ref. [276] (Eqs. (48)–(50)) and replace the pure Coulomb KMT T-matrix with the analogous quantity in the Watson approach. Despite being a minor correction, this approach improves the calculated cross sections by a few percent.

3.C Decomposition of the pion-nucleon scattering amplitude

Assuming conservation of both the total (j) and orbital (l) angular momenta, as well as total isospin (T), the π-N scattering amplitude can be expanded as a series of multipole

terms with energy-dependent coefficients $f^l_{2T\,2j}$ [277]:

$$f(\boldsymbol{k}',\boldsymbol{k}) = \sum_{T=\frac{1}{2},\frac{3}{2}} \hat{Q}_T \sum_l (2l+1) \sum_{j=l-\frac{1}{2}}^{l+\frac{1}{2}} \hat{P}_{lj} f^l_{2T\,2j} P_l(\cos\theta), \tag{3.86}$$

where $\hat{Q}_T$ and $\hat{P}_{l,j}$ are the isospin and spin projection operators, respectively, which are expressed as [278]

$$\hat{Q}_{1/2} = \frac{1}{3}(1 - \hat{\boldsymbol{t}}\cdot\hat{\boldsymbol{\tau}}), \qquad \hat{Q}_{3/2} = \frac{1}{3}(2 + \hat{\boldsymbol{t}}\cdot\hat{\boldsymbol{\tau}}), \tag{3.87}$$

and

$$\hat{P}_{l,l-1/2} = \frac{1}{2l+1}(l - \hat{\boldsymbol{\sigma}}\cdot\hat{\boldsymbol{L}}), \qquad \hat{P}_{l,l+1/2} = \frac{1}{2l+1}(l+1 + \hat{\boldsymbol{\sigma}}\cdot\hat{\boldsymbol{L}}). \tag{3.88}$$

Using the relation

$$\hat{\boldsymbol{\sigma}}\cdot\hat{\boldsymbol{L}} P_l(\cos\theta) = -i\hat{\boldsymbol{\sigma}}\cdot\boldsymbol{n} P_l'(\cos\theta)\sin\theta, \tag{3.89}$$

where $P'(x) \equiv dP(x)/dx$, one can explicitly express the spin structure of Eq. (3.86) as

$$f(\boldsymbol{k}',\boldsymbol{k}) = \sum_{T=\frac{1}{2},\frac{3}{2}} \hat{Q}_T \sum_l \Big[\left(l f^l_{2T\,2l-1} + (l+1) f^l_{2T\,2l+1} \right) P_l(\cos\theta) \\ + i\,\hat{\boldsymbol{\sigma}}\cdot\boldsymbol{n} (f^l_{2T\,2l-1} - f^l_{2T\,2l+1}) P_l'(\cos\theta)\sin\theta \Big]. \tag{3.90}$$

Using Eqs. (3.87), an arbitrary function g defined in the π-N isospin space can be expanded with respect to the total isospin quantum number:

$$g = \sum_{T=\frac{1}{2},\frac{3}{2}} \hat{Q}_T g_T = \frac{1}{3}\left[g_{1/2} + 2g_{3/2}\right] + \frac{1}{3}\left[g_{3/2} - g_{1/2}\right]\hat{\boldsymbol{t}}\cdot\hat{\boldsymbol{\tau}}. \tag{3.91}$$

Finally, the scattering amplitude f can be presented in the form given by Eq. (3.19) with the coefficients $f^{(i)}$ decomposed in partial waves as

$$f^{(0)} = \frac{1}{3}\sum_l \left[l\left(f^l_{1\,2l-1} + 2f^l_{3\,2l-1}\right) + (l+1)\left(f^l_{1\,2l+1} + 2f^l_{3\,2l+1}\right)\right] P_l(\cos\theta), \tag{3.92a}$$

$$f^{(1)} = \frac{1}{3}\sum_l \left[l\left(f^l_{3\,2l-1} - f^l_{1\,2l-1}\right) + (l+1)\left(f^l_{3\,2l+1} - f^l_{1\,2l+1}\right)\right] P_l(\cos\theta), \tag{3.92b}$$

$$f^{(2)} = \frac{i}{3}\sum_l \left[(f^l_{1\,2l-1} + 2f^l_{3\,2l-1}) - (f^l_{1\,2l+1} + 2f^l_{3\,2l+1})\right] P_l'(\cos\theta)\sin\theta, \tag{3.92c}$$

$$f^{(3)} = \frac{i}{3}\sum_l \left[f^l_{3\,2l-1} - f^l_{1\,2l-1} - (f^l_{3\,2l+1} - f^l_{1\,2l+1})\right] P_l'(\cos\theta)\sin\theta. \tag{3.92d}$$

The p-wave partial amplitudes, the parameters $b_{0,1}$ and $c_{0,1}$, as well as a comparison between the first thee partial waves of $f^{(0)} = \sum_l f_l^{(0)} P_l(\cos\theta)$ expansion, are presented in Fig. 3.15.

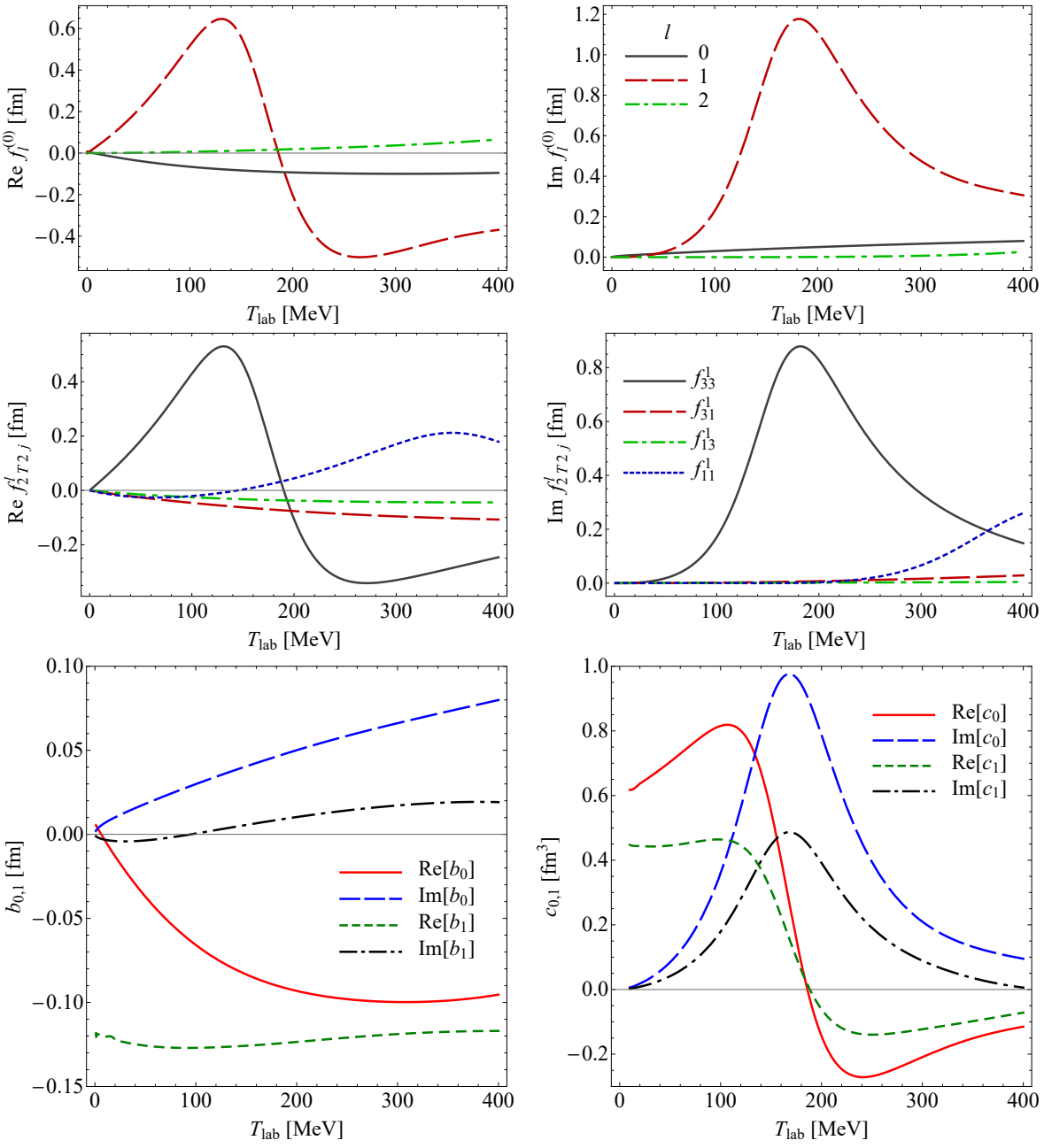

Figure 3.15: The first three partial wave scattering amplitudes $f_l^{(0)}$ (**Upper frames**), p-wave multipoles (**Middle frames**), and s- and p-wave scattering parameters $b_{0,1}$ and $c_{0,1}$ (**Lower frames**) as functions of pion laboratory kinetic energy. The left and right columns show the real and imaginary parts, respectively. The numerical values are taken from MAID2007 [220].

3.D The second-order part of the potential

The pion angular distribution results from the interplay between partial scattering amplitudes and the Coulomb phase shifts, as is described by Eq. (3.63). In Fig. 3.16, we demonstrate the two lowest partial waves for the first- and second-order on-shell potential for pion scattering on ^{12}C. As depicted in the plot, the second-order contribution, Eq. (3.46), substantially affects both s- and p-wave parts of the potential in the low-energy region. This impact allows us to generate enough splitting through the nuclear-Coulomb interference to describe both positive and negative pions accurately. This was impossible to achieve using only the first-order potential and the same minimal number of free parameters, as discussed in Sec. 3.4.2. Note that the second-order contribution to the potential has the most pronounced effect on the s- and p-wave parts, and its influence decreases as the angular momentum increases.

To derive the explicit form of the second-order part of the pion-nucleus potential, we consider the s- and p-wave pion-nucleon scattering amplitude, Eq. (3.20), with the off-shell momentum dependence given by Eq. (3.23). The unit vectors normal to the pion-nucleon scattering planes entering Eqs. (3.44)–(3.46) are $\boldsymbol{n}_1 = (\boldsymbol{k}_{2\mathrm{cm}} \times \boldsymbol{k}''_{2\mathrm{cm}})/|\boldsymbol{k}_{2\mathrm{cm}} \times \boldsymbol{k}''_{2\mathrm{cm}}|$ and $\boldsymbol{n}_2 = (\boldsymbol{k}''_{2\mathrm{cm}'} \times \boldsymbol{k}'_{2\mathrm{cm}'})/|\boldsymbol{k}''_{2\mathrm{cm}'} \times \boldsymbol{k}'_{2\mathrm{cm}'}|$. The subscript "2cm" ("2cm′") corresponds to the c.m. system of the pion and the first (second) nucleon. Collecting all the components, the second-order part of the potential, Eq. (3.46), can be written as a sum of four terms:

$$V^{(2)}(\boldsymbol{k}', \boldsymbol{k}) = V_{ss} + V_{sp} + V_{pp} + V^{(s)}_{pp}, \tag{3.93}$$

where

$$V_{ss} = \int \frac{\mathrm{d}\boldsymbol{k}''}{2\pi^2} \tilde{\mathscr{W}}(\boldsymbol{k}', \boldsymbol{k}'') \tilde{\mathscr{W}}(\boldsymbol{k}'', \boldsymbol{k}) \frac{1}{k_0^2 - k''^2 + i\varepsilon} \times \left[b_0^2 C_0(\boldsymbol{k}' - \boldsymbol{k}'', \boldsymbol{k}'' - \boldsymbol{k}) + 2b_1^2 C_{\mathrm{ex}}(\boldsymbol{k}' - \boldsymbol{k}'', \boldsymbol{k}'' - \boldsymbol{k}) \right], \tag{3.94a}$$

$$V_{sp} = \int \frac{\mathrm{d}\boldsymbol{k}''}{2\pi^2} \tilde{\mathscr{W}}(\boldsymbol{k}', \boldsymbol{k}'') \tilde{\mathscr{W}}(\boldsymbol{k}'', \boldsymbol{k}) \frac{\boldsymbol{k}'_{2\mathrm{cm}'} \cdot \boldsymbol{k}''_{2\mathrm{cm}'} + \boldsymbol{k}_{2\mathrm{cm}} \cdot \boldsymbol{k}''_{2\mathrm{cm}}}{k_0^2 - k''^2 + i\varepsilon} \times \left[b_0 c_0 C_0(\boldsymbol{k}' - \boldsymbol{k}'', \boldsymbol{k}'' - \boldsymbol{k}) + 2b_1 c_1 C_{\mathrm{ex}}(\boldsymbol{k}' - \boldsymbol{k}'', \boldsymbol{k}'' - \boldsymbol{k}) \right], \tag{3.94b}$$

$$V_{pp} = \int \frac{\mathrm{d}\boldsymbol{k}''}{2\pi^2} \tilde{\mathscr{W}}(\boldsymbol{k}', \boldsymbol{k}'') \tilde{\mathscr{W}}(\boldsymbol{k}'', \boldsymbol{k}) \frac{(\boldsymbol{k}'_{2\mathrm{cm}'} \cdot \boldsymbol{k}''_{2\mathrm{cm}'})(\boldsymbol{k}''_{2\mathrm{cm}} \cdot \boldsymbol{k}_{2\mathrm{cm}})}{k_0^2 - k''^2 + i\varepsilon} \times \left[c_0^2 C_0(\boldsymbol{k}' - \boldsymbol{k}'', \boldsymbol{k}'' - \boldsymbol{k}) + 2c_1^2 C_{\mathrm{ex}}(\boldsymbol{k}' - \boldsymbol{k}'', \boldsymbol{k}'' - \boldsymbol{k}) \right], \tag{3.94c}$$

$$V^{(s)}_{pp} = -\int \frac{\mathrm{d}\boldsymbol{k}''}{2\pi^2} \tilde{\mathscr{W}}(\boldsymbol{k}', \boldsymbol{k}'') \tilde{\mathscr{W}}(\boldsymbol{k}'', \boldsymbol{k}) \frac{[\boldsymbol{k}'_{2\mathrm{cm}'} \times \boldsymbol{k}''_{2\mathrm{cm}'}] \cdot [\boldsymbol{k}''_{2\mathrm{cm}} \times \boldsymbol{k}_{2\mathrm{cm}}]}{k_0^2 - k''^2 + i\varepsilon} \times \left[s_0^2 + 2s_1^2 \right] C_{\mathrm{ex}}(\boldsymbol{k}' - \boldsymbol{k}'', \boldsymbol{k}'' - \boldsymbol{k}). \tag{3.94d}$$

Each second-order contribution described in Eqs. (3.94) represents the interference between the s- and p-wave parts of the pion-nucleon amplitude. Figure 3.17 demonstrates the second-order components for on-shell forward scattering on ^{12}C. Generally, the scattering parameters $b_{0,1}$, $c_{0,1}$, and $s_{0,1}$ in Eqs. (3.94) depend modestly on the angle between the corresponding momenta. For the purpose of evaluating the second-order correction, we assume these parameters to be angle independent and fixed at the forward scattering angle.

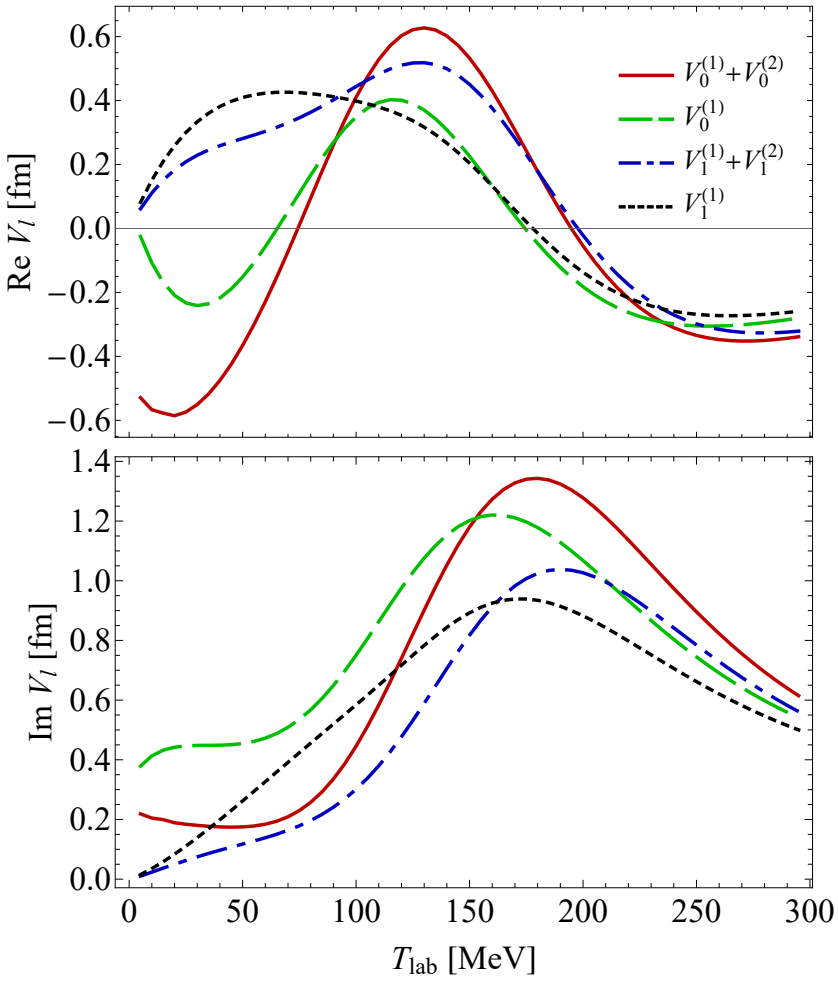

Figure 3.16: The s- and p-wave components of the first- and second-order potential for on-shell pion scattering on ^{12}C as a function of pion laboratory kinetic energy. The potential parameters are given by fit 1 in Table 3.2. The upper and lower panels are for real and imaginary parts, respectively. The solid red (dot-dashed blue) curve represents the s-wave (p-wave) component of the full potential, i.e., the sum of Eqs. (3.39) and (3.46), while the long-dashed green (short-dashed blue) curve corresponds to the first-order potential, Eq. (3.39).

The peculiarity of our approach is the presence of two correlation functions in the second-order potential. However, in the s-s-wave interference term V_{ss}, Eq. (3.94a), the first term with the C_0 correlation function is negligible due to the smallness of b_0 compared to the real part of b_1. This enables us to compare our approach with the s-wave potential originally derived in Ref. [101]. With the second-order correction, the s-wave coordinate space potential given by Eq. (3.49) acquires the form

$$U^{(s)}(r) \propto \left(b_0 - \left(b_0^2 + 2b_1^2\right)\left\langle\frac{1}{r}\right\rangle\right)\rho(r) + B_0\rho^2(r), \tag{3.95}$$

where $\langle 1/r\rangle$ is the so-called inverse nucleon correlation length, which within the Fermi gas model for zero pion kinetic energy becomes $\langle 1/r\rangle = 3p_F/(2\pi) \approx 0.65\,\mathrm{fm}^{-1}$. Perform-

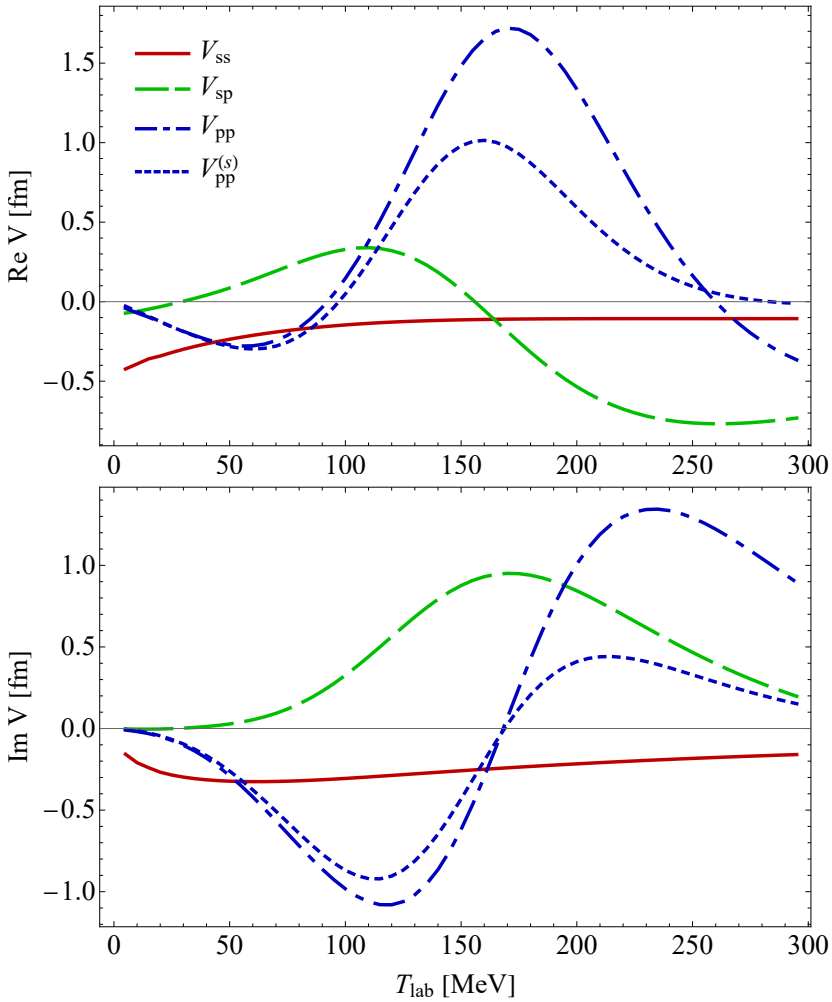

Figure 3.17: The components of the on-shell forward pion-nucleus potential, Eqs. (3.94), for ^{12}C as a function of pion laboratory kinetic energy for parameters given by fit 1 in Table 3.2. The left and right panels are for real and imaginary parts, respectively. The solid red, dashed green, and dash-dotted blue curves correspond to the second-order s-s-, s-p-, and p-p-wave interference of the spin-independent pion scattering, Eqs. (3.94a)–(3.94c). The short-dashed curves represent the contribution from the spin-dependent part of the pion-nucleon amplitude, Eq. (3.94d).

ing the integration in Eq. (3.94a) in the limit $k_0 \to 0$, we obtain $V_{ss}(0,0) = 2b_1^2\langle C_{\rm ex}\rangle$, with $\langle C_{\rm ex}\rangle/A$ acquiring the values $0.61\,{\rm fm}^{-1}$ and $0.56\,{\rm fm}^{-1}$ for ^{12}C and ^{40}Ca, respectively. The approximate agreement between V_{ss} and $U^{(s)}(r)$ at the threshold allows us to directly apply the results of the pionic atom analyses in Secs. 3.3.3 and 3.3.3.

The p-p-wave interference term V_{pp}, Eq. (3.94c), corresponds to the second-order term,

$$U_{pp}(\boldsymbol{r}) \propto -\frac{1}{3}\frac{A-1}{A}\,(4\pi c_0)^2\,\boldsymbol{\nabla}\rho^2(r)\boldsymbol{\nabla}, \tag{3.96}$$

in the coordinate space p-wave potential describing the Lorentz-Lorenz-Ericson-Ericson

effect [101]:

$$U^{(p)}(\boldsymbol{r}) \propto \boldsymbol{\nabla} \frac{c_0 \rho(r)}{1 + \frac{4\pi}{3}\frac{A-1}{A} c_0 \rho(r)} \boldsymbol{\nabla}. \tag{3.97}$$

The kinematic factors are omitted in Eqs. (3.96) and (3.97) for simplicity. While our model does not account for effects beyond second order, unlike Eq. (3.97), we expect V_{pp} to be much more realistic. The reason for this is that Eq. (3.96) is obtained from Eq. (3.94c) in the limit of zero pion kinetic energy by setting $C_{\rm ex}(\boldsymbol{q}_1, \boldsymbol{q}_2) = 0$ and $C_0(\boldsymbol{q}_1, \boldsymbol{q}_2) = \rho(q_1)\rho(q_2)$, which may be a crude approximation in the resonance energy region.

The term V_{sp}, Eq. (3.94b), characterizes the s-p-wave interference. It is nonzero in our approach since we perform the computation within the nuclear shell model without resorting to the Fermi gas model. As seen from Fig. 3.17, this term is not negligible and is important both at high and low energies. Similarly to the case of V_{ss}, the term proportional to C_0 gives a much smaller contribution due to the ratio of b_0 and b_1.

The term V_{pp} describes p-p-wave interference accounting for processes with (term proportional to $C_{\rm ex}$) and without (term proportional to $\propto C_0$) the isospin exchange. Similarly, the term $V_{pp}^{(s)}$, Eq. (3.94d), characterizes the spin exchange. This term has similar energy dependence as V_{pp} (see Fig. 3.17), because both $c_{0,1}$ and $s_{0,1}$ are proportional to the P_{33}^1 partial amplitude. However, V_{pp} and $V_{pp}^{(s)}$ have different angle-dependent structure.

Chapter 4

Nuclear coherent π^0 photoproduction

About a decade after the pion was discovered in the late 1940s, coherent photoproduction of π^0 was first proposed as a valuable tool for studying the distribution of nucleons in nuclei [66, 67]. While this physics motivation remains relevant nowadays [74], the predominant focus has shifted towards extracting the neutron skin of heavy nuclei [65, 279], which is the difference between the root-mean-square radii of the neutron and proton distributions. The neutron skin measurement provides a unique constraint on the symmetry energy of the nuclear Equation Of State, which strongly depends on poorly constrained three-body forces [57, 280]. Consequently, an accurate extraction of the neutron skin in neutron-rich nuclei is motivated for the understanding of neutron star structure. However, Ref. [2] demonstrated low sensitivity of the π^0 coherent photoproduction cross section to variations in the neutron skin thickness, which underscores the importance of a very good understanding of the theoretical model for accurately extracting the neutron skin [20].

Furthermore, nuclear coherent π^0 photoproduction is an effective tool for investigating the properties of the pion-nucleus interaction. For this reason, this process finds relevance in long-baseline neutrino oscillation experiments, e.g., T2K [132] and Hyper-Kamiokande [133], where quasifree single-pion production is a dominant process within the energy region corresponding to the $\Delta(1232)$-resonance excitation. Although the coherent π^0 production in neutrino-nucleus collisions is not a dominant process, it helps to understand the quasifree pion production. Coherent π^0 photoproduction may serve as a reliability test for an approach utilized to describe coherent pion production in neutrino-nucleus scattering [136]. While the coherent pion neutrino-nucleus production amplitude requires the incorporation of the hadronic axial-vector current component in the elementary amplitude, the treatment of the vector part aligns with that of electro- and photoproduction.

Previously, various theoretical approaches have extensively explored the coherent π^0 photoproduction on spin-zero nuclei, each with distinct focuses [75, 281, 282]. As in the case of the pion-nucleus scattering process, we can distinguish two major groups of the existing models. The first group encompasses the distorted wave impulse approximation (DWIA) models, e.g., Refs. [71, 77, 283], which primarily investigate the final state interaction of the pion propagating within the nuclear medium in a momentum-space representation. The DWIA in momentum space was first applied in Ref. [78] for the π^+ photoproduction on ^{16}O. These models dynamically treat the pion-nucleus interaction, taking into account non-locality and off-shell effects. Nevertheless, they typically do not consider the medium-induced shifts of the Δ-resonance's mass and width. The second group of the Δ-hole models, e.g., Refs. [92, 284–287], extensively probes the in-

medium characteristics of the Δ-isobar, mainly focusing on the Δ and pion dynamics but often neglecting non-resonant contributions. However, numerically complex Δ-hole calculations have mainly been limited to light nuclei. Reference [75] effectively merged these two approaches by employing the DWIA calculation alongside the Unitary Isobar Model [288] for the elementary photoproduction amplitude. The in-medium effects were incorporated in the phenomenological Δ self-energy, fitted to experimental data for π^0 photoproduction on ^{4}He from Ref. [80]. Subsequently, this model has been successfully applied to describe coherent π^0 photoproduction data across a diverse range of nuclei [72, 95, 289].

Utilizing the theoretical framework outlined in Ref. [75] to analyze data on the coherent π^0 photoproduction off ^{208}Pb measured with the Crystal Ball at the Mainz Microtron (MAMI), the A2 collaboration derived the neutron skin thickness of ^{208}Pb to be $0.15 \pm 0.03\,(\text{stat.})^{+0.02}_{-0.03}\,(\text{sys.})$ fm [65]. This outcome strongly contrasts with the value of 0.283 ± 0.071 fm obtained from the state-of-the-art parity violation measurement in electron scattering by the PREX-2 collaboration [22], as well as findings from other methods used previously [11, 12, 52]. The discrepancy between these results could be attributed to several contributions ignored in the model of Ref. [75], which was used in the analysis of Ref. [65]. Such neglected contributions include intermediate pion-nucleon charge exchange [69] and nucleon spin-flip. As demonstrated in Ref. [70], incorporating the final-state charge-exchange effects can lead to an additional 5–6% increase in the predicted π^0 photoproduction cross sections, significantly impacting the determination of the neutron skin.

The mechanism of pion rescattering on a nucleon via charge-exchange and/or spin-flip interactions holds significant importance in both nuclear pion photoproduction and scattering processes. The charge-exchange yields an essential contribution for describing the π^0 photoproduction on the deuteron and ^{3}He [120–122]. Reference [123] demonstrated the substantial influence of charge-exchange and spin-flip rescattering effects on the differential cross sections of gamma-induced charged pion production on ^{12}C, ^{13}C, and ^{15}N. Notably, the π^+ photoproduction on ^{12}C was shown to be less affected by the rescattering processes, with the spin-flip effect being much more significant than charge exchange. This distinction from the π^- photoproduction on ^{13}C and ^{15}N underscores the strong sensitivity of spin- and isospin-dependent rescattering processes on the nuclear structure. The second-order charge exchange part of the s-wave pion-nucleus scattering potential initially introduced in Ref. [101] has been proven essential for both pion scattering [125] and pionic atoms [230]. Furthermore, this contribution was shown to be significant also for the p-wave part of the scattering potential [124]. Finally, in the recent work for pion-nucleus scattering [3], described in Chapter 3, the inclusion of charge-exchange and spin-flip second-order rescattering was demonstrated to yield sizable corrections in the Δ-resonance energy region.

This Chapter builds upon our prior research on pion-nucleus scattering presented in Chapter 3. We aim to describe the nuclear π^0 photoproduction within the framework established in Ref. [3], utilizing the common effective description of the Δ self-energy for both processes. For this purpose, we develop the second-order momentum-space potential for nuclear π^0 photoproduction. While the first-order part of the potential, obtained within the framework of the impulse approximation, has a standard form [71, 75], the second-order part is constructed based on our recently developed second-order pion-

nucleus scattering potential [3]. This second-order contribution of both pion scattering and photoproduction potentials describes pion rescattering on intermediate excited nuclear states. It takes into account the explicit spin and isospin structure of the elementary scattering and photoproduction amplitudes involving intermediate nucleon spin-flip and charge-exchange interactions. In the present calculation of coherent π^0 photoproduction on ^{12}C and ^{40}Ca, the in-medium effects are incorporated using the approach of Ref. [75]. However, to determine the numerical value of the effective Δ self-energy, which modifies the elementary photoproduction amplitude, we directly employ the results obtained from the fit of $\pi^{\pm}$-^{12}C scattering data performed in Ref. [3], covering the energy range of 80–180 MeV pion laboratory kinetic energy.

The present chapter is based on Ref. [4] and is organized as follows:

- In Section 4.1, we present the main aspects of the multiple-scattering formalism for nuclear pion photoproduction.
- In Section 4.2, we consider the structure of the elementary amplitude of pion photoproduction and its modification in the nuclear medium.
- In Section 4.3, we derive the second-order potential for coherent nuclear pion photoproduction.
- In Section 4.4, we compare the predictions of our photoproduction model with experimental data for ^{12}C and ^{40}Ca and present our preliminary results for ^{208}Pb.
- Finally, in Section 4.5, we present our conclusions.

4.1 Multiple-scattering formalism

The T-matrix for nuclear pion photoproduction can be presented in terms of a multiple-scattering series:

$$\hat{T}_\gamma = \sum_{i=1}^{A} \hat{\tau}_i^\gamma + \sum_{i=1}^{A}\sum_{j\neq i}^{A} \hat{\tau}_j \hat{G} \hat{\tau}_i^\gamma + \sum_{i=1}^{A}\sum_{j\neq i}^{A}\sum_{k\neq j}^{A} \hat{\tau}_k \hat{G} \hat{\tau}_j \hat{G} \hat{\tau}_i^\gamma + \cdots , \tag{4.1}$$

where A is the nucleon number, $\hat{\tau}_i$ and $\hat{\tau}_i^\gamma$ are transition amplitudes for pion scattering and photoproduction on a single nucleon inside the nucleus, respectively, and $\hat{G}$ is the Green's function of the non-interacting pion-nucleus system.

Due to the structural similarity between Eq. (4.1) and the series describing the pion-nucleus scattering, Eq. (3.1), the Kerman-McManus-Thaler (KMT) multiple scattering approach [98] can be applied to the pion photoproduction process [290]. Consequently, Eq. (4.1) can be subdivided into a system of equations:

$$\hat{T}_\gamma = \hat{U}_\gamma + \frac{A-1}{A} \hat{T} \hat{G} \hat{P}_0 \hat{U}_\gamma, \tag{4.2a}$$

$$\hat{T} = \hat{U} + \frac{A-1}{A} \hat{U} \hat{G} \hat{P}_0 \hat{T}, \tag{4.2b}$$

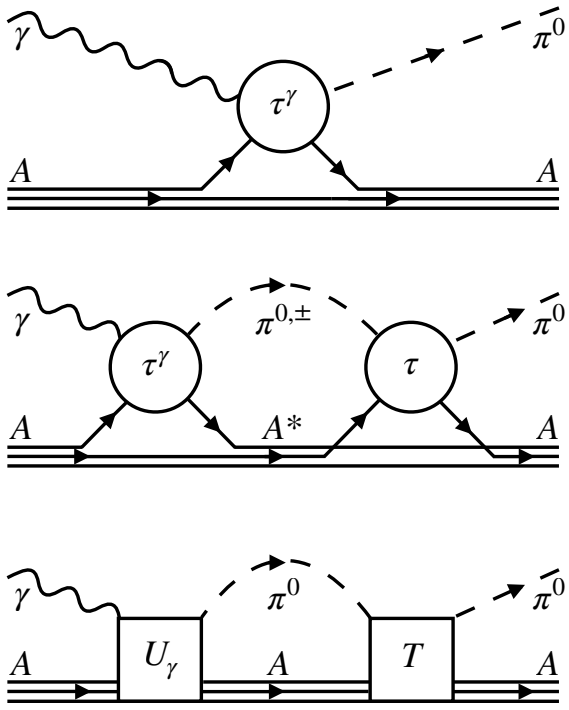

Figure 4.1: Diagrammatic representation of the KMT formalism, Eqs. (4.2) and (4.3), applied to the coherent π^0 photoproduction on the nucleus. The upper and middle panels depict the first and second terms on the right-hand side of Eq. (4.3a), respectively. The lower panel represents the second term on the right-hand side of Eq. (4.2a). In the bottom line of the diagrams, A and A^* denote the nucleus in its ground and excited states.

where T is the transition matrix for pion-nucleus scattering, while $\hat{U}_\gamma$ and $\hat{U}$ are the pion-nuclear photoproduction and scattering potentials, respectively, defined as

$$\hat{U}_\gamma = A\hat{\tau}_1^\gamma + A(A-1)\hat{\tau}_2\hat{G}\hat{P}_\emptyset\hat{\tau}_1^\gamma + A(A-1)^2\hat{\tau}_3\hat{G}\hat{P}_\emptyset\hat{\tau}_2\hat{G}\hat{P}_\emptyset\hat{\tau}_1^\gamma + \cdots , \tag{4.3a}$$

$$\hat{U} = A\hat{\tau}_1 + A(A-1)\hat{\tau}_2\hat{G}\hat{P}_\emptyset\hat{\tau}_1 + A(A-1)^2\hat{\tau}_3\hat{G}\hat{P}_\emptyset\hat{\tau}_2\hat{G}\hat{P}_\emptyset\hat{\tau}_1 + \cdots . \tag{4.3b}$$

In these equations, we have used the fact that the ground state wave function of the target nucleus, $|\Psi_0\rangle$, is completely antisymmetrized, and each term of the same order in the series gives an equal contribution. The operators $\hat{P}_0$ and $\hat{P}_\emptyset$ project on the nuclear ground state and all possible excited states, respectively, as given by Eqs. (3.4). The factor $(A-1)/A$ in the equations above prevents double counting of the rescattering since both $\hat{\tau}_i$ and $\hat{\tau}_i^\gamma$ already include pion scattering to all orders on a single nucleon.

In Eqs. (4.2) and (4.3), we explicitly decoupled the rescattering of photoproduced the pion on the nucleus. The resulting Eqs. (4.2b) and (4.3b) are standard KMT equations for pion-nucleus scattering, which exactly match Eqs. (3.5a) and (3.5b). As can be seen, Eqs. (4.2a) and (4.3a) describing the pion photoproduction are reduced to the corresponding equations for scattering by removing superscript "γ". This convention in the notations will also be valid for all quantities in the following.

For nuclear coherent π^0 photoproduction and elastic pion scattering processes, only the nuclear ground state expectation values of the transition amplitudes ($\hat{T}_\gamma$ and $\hat{T}$) and the potential operators ($\hat{U}_\gamma$ and $\hat{U}$), contribute to Eqs. (4.2). The involvement of excited intermediate nuclear states is excluded by the action of the projector $\hat{P}_0$. All information about nuclear excitation, including intermediate nucleon spin-flip and charge exchange, is encapsulated in the nuclear pion scattering and photoproduction potential operators, given by Eqs. (4.3). Fig. 4.1 illustrates the diagrams corresponding to the nuclear coherent π^0 photoproduction. The upper panel illustrates the pion photoproduction on a nucleon within the nucleus, described by the first term on the right-hand side of Eq. (4.3a). The middle panel corresponds to the second term on the right-hand side of Eq. (4.3a), representing π^0 photoproduction on one nucleon, after which the nucleus undergoes a transition to excited state, followed by propagation and then scattering on a second nucleon. Finally, the second term on the right-hand side of Eq. (4.2a) represents the rescattering of the outgoing π^0 off the nucleus, corresponding to the lower panel in Fig. 4.1. The pion elastic scattering process is described by the same set of diagrams with the photon line replaced with the pion one.

As follows from Eq. (4.2a), the coherent π^0 photoproduction amplitude off nuclei can be presented in momentum space as

$$F_\gamma(\boldsymbol{k}', \boldsymbol{k}) = V_\gamma(\boldsymbol{k}', \boldsymbol{k}) - \frac{A-1}{A} \int \frac{\mathrm{d}\boldsymbol{k}''}{2\pi^2} \frac{F(\boldsymbol{k}', \boldsymbol{k}'') V_\gamma(\boldsymbol{k}'', \boldsymbol{k})}{k_0^2 - k''^2 + i\,\varepsilon}, \tag{4.4}$$

where $\boldsymbol{k}$ ($\boldsymbol{k}'$) is the incident photon (emitted pion) momentum, and k_0 is the pion on-shell momentum. The momentum space coherent photoproduction amplitude F_γ and photoproduction potential V_γ are related to the ground state matrix elements of the corresponding operators via

$$F_\gamma(\boldsymbol{k}', \boldsymbol{k}) = -\frac{\sqrt{\mathscr{M}(k')\mathscr{M}_\gamma(k)}}{2\pi} \langle \pi(\boldsymbol{k}'), \Psi_0 | \hat{T}_\gamma | \gamma(\boldsymbol{k}), \Psi_0 \rangle, \tag{4.5a}$$

$$V_\gamma(\boldsymbol{k}', \boldsymbol{k}) = -\frac{\sqrt{\mathscr{M}(k')\mathscr{M}_\gamma(k)}}{2\pi} \langle \pi(\boldsymbol{k}'), \Psi_0 | \hat{U}_\gamma | \gamma(\boldsymbol{k}), \Psi_0 \rangle. \tag{4.5b}$$

The off-shell analog of the relativistic reduced mass of the pion-nucleus system $\mathscr{M}$ in the pion-nucleus c.m. frame is defined in Eq. (3.10). For the on-shell photon of momentum $|\boldsymbol{k}| = k_0^\gamma$, $\mathscr{M}_\gamma$ is the simple photon-nuclear relativistic reduced mass: $\mathscr{M}_\gamma(k) = k_0^\gamma E_A(k_0^\gamma)/E$.

According to Eq. (4.4), deriving the full photoproduction amplitude requires knowledge of both the photoproduction potential and the elastic scattering amplitude. We employ the scattering amplitude $F(\boldsymbol{k}', \boldsymbol{k})$ obtained in the previous Chapter by solving the integral equation, Eq. (3.12). As follows from Eq. (4.3a), the ground state expectation value of the photoproduction potential operator, $\langle \Psi_0 | \hat{U}_\gamma | \Psi_0 \rangle$, involves an infinite series of terms. All the terms, except the first one, consist of non-diagonal matrix elements of $\hat{\tau}$ and $\hat{\tau}_\gamma$ due to the presence of the projector on excited states, $\hat{P}_\emptyset$. As in the case of the pion-nucleon scattering process, we assume that the photoproduction potential is approximated by the first two terms corresponding to the two top panels of Fig. 4.1:

$$\hat{U}_\gamma \approx A\hat{\tau}_1^\gamma + A(A-1)\hat{\tau}_2 \hat{G} \hat{P}_\emptyset \hat{\tau}_1^\gamma. \tag{4.6}$$

Further development of the nuclear photoproduction potential relies on a comprehensive knowledge of the amplitude for the reaction of photoproduction on a single nucleon,

$$\gamma(\boldsymbol{k}) + N(\boldsymbol{p}) \longrightarrow \pi(\boldsymbol{k}') + N(\boldsymbol{p}'), \tag{4.7}$$

covering its spin-isospin structure, off-shell behavior, and modification in the nuclear medium, which will be discussed next.

4.2 Elementary pion photoproduction amplitude

In general, $\hat{\tau}^\gamma$ is an energy-dependent $(A+1)$-body operator, related to the amplitudes in free space as

$$\hat{\tau}^\gamma = \hat{\tau}^\gamma(E) = \hat{t}^\gamma(W) + \hat{\tau}(E)\left[\hat{G}(E) - \hat{g}(W)\right]\hat{t}^\gamma(W), \tag{4.8}$$

where W is the pion-nucleon reaction energy, $\hat{t}^\gamma$ is the elementary pion photoproduction amplitude on the free nucleon, and $\hat{g}(W)$ is the propagator of the free pion-nucleon system. Here and further, we drop the index "i" when there is no need to distinguish nucleons. As in the case of the pion scattering process, we apply the *impulse approximation*, assuming $\hat{\tau}_i^\gamma(E) \approx \hat{t}^\gamma(W)$. There are various approaches, each motivated by different considerations, to determine the optimal value for W [106, 214, 215, 291]. For consistency with our previous study of pion scattering, we adopt the so-called *two-body choice for the reaction energy*:

$$W = \sqrt{\left(k + E_N(p)\right)^2 - (\boldsymbol{k} + \boldsymbol{p})^2}, \tag{4.9}$$

where $E_N(p)$ is the energy of the struck nucleon. The reaction energy, Eq. (4.9), is evaluated for the on-shell momenta $|\boldsymbol{k}| = k_0^\gamma$ and $|\boldsymbol{k}'| = k_0$.

The momentum space T-matrix for pion photoproduction on free nucleon is related to the free nucleon photoproduction amplitude f^γ in the photon-nucleon c.m. frame as

$$\langle \pi(\boldsymbol{k}'), N(\boldsymbol{p}')|\hat{t}^\gamma|\gamma(\boldsymbol{k}), N(\boldsymbol{p})\rangle = -(2\pi)^3\delta(\boldsymbol{k}' + \boldsymbol{p}' - \boldsymbol{k} - \boldsymbol{p}) \times \frac{2\pi}{\sqrt{\mu(\boldsymbol{k}', \boldsymbol{p}')\mu_\gamma(\boldsymbol{k}, \boldsymbol{p})}}\hat{f}^\gamma(\boldsymbol{k}'_{\text{2cm}}, \boldsymbol{k}_{\text{2cm}}), \tag{4.10}$$

where $\mu_\gamma(\boldsymbol{k}, \boldsymbol{p}) = kE_N(p)/W(\boldsymbol{k}, \boldsymbol{p})$ and $W(\boldsymbol{k}, \boldsymbol{p})$ is the invariant mass of the system with momenta $\boldsymbol{k}$ and $\boldsymbol{p}$. Here, the subscript "2cm" indicates the photon-nucleon c.m. frame. Similarly to how momenta are boosted to the 2cm frame in the pion-nucleon scattering process, Eqs. (3.15), the Lorentz transformation to the photon-nucleon c.m. frame is given by

$$\boldsymbol{k}_{\text{2cm}} = \boldsymbol{k} + \frac{(\boldsymbol{k} + \boldsymbol{p})}{W(\boldsymbol{k}, \boldsymbol{p})}\left(\frac{(\boldsymbol{k} + \boldsymbol{p}) \cdot \boldsymbol{k}}{W(\boldsymbol{k}, \boldsymbol{p}) + k + E_N(p)} - k\right), \tag{4.11a}$$

$$\boldsymbol{k}'_{\text{2cm}} = \boldsymbol{k}' + \frac{(\boldsymbol{k}' + \boldsymbol{p}')}{W(\boldsymbol{k}', \boldsymbol{p}')}\left(\frac{(\boldsymbol{k}' + \boldsymbol{p}') \cdot \boldsymbol{k}'}{W(\boldsymbol{k}', \boldsymbol{p}') + \omega(k') + E_N(p')} - \omega(k')\right). \tag{4.11b}$$

While the Lorentz transformation is originally derived for on-mass-shell objects, we assume Eqs. (4.11) are also applicable to particles off their mass shell [216, 217].

The dependence of the amplitudes on the struck nucleon momenta $\boldsymbol{p}$ and $\boldsymbol{p}'$ (the so-called nucleon Fermi motion) significantly complicates the calculation. In the general case, the procedure implies the integration over nucleon momenta to obtain the matrix element in Eq. (4.5b) and requires knowledge of the model-dependent one-body density matrix [291]. A common approach to simplify this problem is evaluating the elementary amplitudes at the effective nucleon momenta given by Eqs. (3.35). This approximation provides numerical results for cross-sections that closely align with the exact values [292] while conserving energy and momenta. Originally introduced for pion scattering [221, 293], this approach has proven successful in subsequent applications to photoproduction [71, 96, 294].

4.2.1 Decomposition of the pion photoproduction amplitude

The spin structure of the pion photoproduction amplitude in the photon-nucleon c.m. frame is conventionally expressed in terms of the Chew-Goldberger-Low-Nambu (CGLN) amplitudes [295]. For the production process by a real photon, the decomposition has the form

$$\hat{f}^{\gamma}(\boldsymbol{k}',\boldsymbol{k}) = i\,\hat{\boldsymbol{\sigma}}\cdot\boldsymbol{\epsilon}^{\lambda}\hat{F}_1(\boldsymbol{k}',\boldsymbol{k}) + \frac{(\hat{\boldsymbol{\sigma}}\cdot\boldsymbol{k}')\hat{\boldsymbol{\sigma}}\cdot[\boldsymbol{k}\times\boldsymbol{\epsilon}^{\lambda}]}{k'k}\hat{F}_2(\boldsymbol{k}',\boldsymbol{k}) + i\frac{(\hat{\boldsymbol{\sigma}}\cdot\boldsymbol{k})(\boldsymbol{k}'\cdot\boldsymbol{\epsilon}^{\lambda})}{k'k}\hat{F}_3(\boldsymbol{k}',\boldsymbol{k}) + i\frac{(\hat{\boldsymbol{\sigma}}\cdot\boldsymbol{k}')(\boldsymbol{k}'\cdot\boldsymbol{\epsilon}^{\lambda})}{k'^2}\hat{F}_4(\boldsymbol{k}',\boldsymbol{k}), \quad (4.12)$$

where $\boldsymbol{\epsilon}^{\lambda}$ is the photon polarisation vector, and $\hat{\boldsymbol{\sigma}}$ is is the nucleon Pauli spin operator.

For circularly polarized photons with the helicity $\lambda = \pm 1$ moving in the direction $\boldsymbol{k}_{2\mathrm{cm}}/k_{2\mathrm{cm}} = (\sin\theta\cos\phi, \sin\theta\sin\phi, \cos\theta)$, the polarization vector is given by

$$\boldsymbol{\epsilon}^{\lambda} = \frac{e^{i\lambda\phi}}{\sqrt{2}}(-\lambda\cos\theta\cos\phi + i\sin\phi, -\lambda\cos\theta\sin\phi - i\cos\phi,\ \lambda\sin\theta), \quad (4.13)$$

satisfying $\boldsymbol{\epsilon}^{\lambda}\cdot\boldsymbol{k}_{2\mathrm{cm}} = 0$.

For the on-shell process with a given isospin configuration, the CGLN amplitudes are independent complex functions of the reaction energy and the pion scattering angle. The amplitudes $\hat{F}_i$ can be further expanded into a sum of partial-wave contributions from channels with different pion-nucleon final states with angular momentum l. There are four distinct transition types possible for a real photon, classified based on the parity P of the photon and the final-state total angular momentum $J = |l \pm 1/2|$ of the pion-nucleon system. For the transverse photon with the total orbital angular momentum L, the states can either be electric, $\hat{E}_{l\pm}$ with $P = (-1)^L$, or magnetic, $\hat{M}_{l\pm}$ with $P = (-1)^{L+1}$. The explicit form of the multipole expansion for $\hat{F}_i$ is given in Appendix 4.A.

In the computation of the nuclear photoproduction amplitude, as given by Eq. (4.4), it is necessary to specify the behavior of the multipoles in the case of the off-shell pion-nucleon system. To maintain consistency with our calculation of the pion–nucleon scattering amplitude in Ref. [3], we employ the following separable form for the pion

with the off-shell momentum $\boldsymbol{k}'$:

$$\hat{A}_{l\pm}(k', k_0^\gamma) = \hat{A}_{l\pm}(k_0, k_0^\gamma) \left(\frac{k'}{k_0}\right)^l v(k'), \tag{4.14}$$

where $\hat{A}_{l\pm}$ encompasses both $\hat{M}_{l\pm}$ and $\hat{E}_{l\pm}$ and the off-shell vertex factor $v(k)$ is given by Eq. (3.24). For the on-shell process, $\hat{E}_{l\pm} = \hat{E}_{l\pm}(k_0, k_0^\gamma)$ and $\hat{M}_{l\pm} = \hat{M}_{l\pm}(k_0, k_0^\gamma)$ depend solely on the reaction energy.

The amplitudes $\hat{F}_i$, $\hat{E}_{l\pm}$ and $\hat{M}_{l\pm}$ are operators in nucleon isospin space. If isospin conservation in the hadronic system is assumed, the isospin structure of any photoproduction amplitude involving a pion with a Cartesian isospin index b is given by [119]

$$\hat{A} = \delta_{b3} A^+ + \frac{1}{2}[\hat{\boldsymbol{\tau}}_b, \hat{\boldsymbol{\tau}}_3] A^- + \hat{\boldsymbol{\tau}}_b A^0, \tag{4.15}$$

where $\hat{\boldsymbol{\tau}}_b$ represents the nucleon isospin matrices. To facilitate the analysis of resonances in the pion-nucleon system with respect to its total isospin T, it is convenient to introduce the following combinations of the isovector photon amplitudes:

$$A_{l\pm}^{1/2} = A_{l\pm}^+ + 2A_{l\pm}^-, \tag{4.16a}$$
$$A_{l\pm}^{3/2} = A_{l\pm}^+ - A_{l\pm}^-, \tag{4.16b}$$

which correspond to $T = 1/2$ and $3/2$, respectively. The isoscalar amplitudes A^0 correspond to isospin-1/2 states.

The magnetic dipole amplitude $M_{1+}^{3/2}$ holds significant importance as it represents the amplitude for the photoexcitation of the $\Delta(1232)$ resonance [296, 297]. By keeping contributions solely from the s- and p-wave pion-nucleon system and explicitly separating the $\Delta(1232)$ resonance multipole $M_{1+}^{3/2}$, the half-off-shell CGLN amplitudes are expressed as

$$F_1^+(\boldsymbol{k}', \boldsymbol{k}) \approx E_{0+}^+ w(k') + \left(2M_{1+}^{3/2} + M_{1+}^{1/2} + 3E_{1+}^+\right) \frac{\boldsymbol{k}' \cdot \boldsymbol{k}}{k_0 k_0^\gamma} v(k'), \tag{4.17a}$$
$$F_1^-(\boldsymbol{k}', \boldsymbol{k}) \approx E_{0+}^- v(k') + \left(-M_{1+}^{3/2} + M_{1+}^{1/2} + 3E_{1+}^-\right) \frac{\boldsymbol{k}' \cdot \boldsymbol{k}}{k_0 k_0^\gamma} v(k'), \tag{4.17b}$$
$$F_2^+(\boldsymbol{k}', \boldsymbol{k}) \approx \left(\frac{4}{3}M_{1+}^{3/2} + \frac{2}{3}M_{1+}^{1/2} + M_{1-}^+\right) \frac{k'}{k_0} v(k'), \tag{4.17c}$$
$$F_2^-(\boldsymbol{k}', \boldsymbol{k}) \approx \left(-\frac{2}{3}M_{1+}^{3/2} + \frac{2}{3}M_{1+}^{1/2} + M_{1-}^-\right) \frac{k'}{k_0} v(k'), \tag{4.17d}$$
$$F_3^+(\boldsymbol{k}', \boldsymbol{k}) \approx \left(-2M_{1+}^{3/2} - M_{1+}^{1/2} + 3E_{1+}^+\right) \frac{k'}{k_0} v(k'), \tag{4.17e}$$
$$F_3^-(\boldsymbol{k}', \boldsymbol{k}) \approx \left(M_{1+}^{3/2} - M_{1+}^{1/2} + 3E_{1+}^-\right) \frac{k'}{k_0} v(k'), \tag{4.17f}$$
$$F_4^\pm(\boldsymbol{k}', \boldsymbol{k}) \approx 0. \tag{4.17g}$$

A similar expansion is applicable to F_i^0, which, however, does not contribute to nuclear π^0 photoproduction on isospin-zero nuclei. In our computation of the first-order part

of the photoproduction potential, we also include the d-wave contribution in a similar manner, introducing a correction on the order of a few percent at higher energies.

For all multipole amplitudes except $M_{1+}^{3/2}$, we use their free-space values taken from the unitary isobar model MAID2007 [296] based on the dynamical Dubna-Mainz-Taipei model [298]. Note that E_{0+}^{-} is the dominant non-resonant multipole. However, E_{0+}^{-} does not contribute to the first-order potential for spin-zero nuclei. It only appears in the second-order correction (as shown in Sec. 4.3), and for this reason, its in-medium modification has a negligible impact on observables.

Various Δ-hole model calculations for pion scattering [88, 90, 211, 299] and photoproduction [91, 284, 300] indicate significant differences between the properties of the Δ-isobar within the nucleus and in free space. The decay width of the Δ is notably affected by numerous inelastic channels opened in the nuclear medium, such as pion absorption on a few nucleons [116]. Correspondingly, the resonant multipole $M_{1+}^{3/2}$ undergoes significant modifications in the case of the pion photoproduction on a bound nucleon, as will be described next. The modification of the much smaller resonant electric quadrupole amplitude $E_{1+}^{3/2}$ is considered in Appendix 4.B.

4.2.2 In-medium modification of $M_{1+}^{3/2}$

The magnetic dipole amplitude $M_{1+}^{3/2}$ consists of a Δ-resonant term and a non-resonant background contribution [301]:

$$M_{1+}^{3/2} = M_{1+}^{3/2(B)} + M_{1+}^{3/2(\Delta)}. \tag{4.18}$$

In the present calculation, we use the unitary isobar model MAID98 [288], according to which the resonant part of the $M_{1+}^{3/2}$ amplitude can be written as

$$M_{1+}^{3/2(\Delta)} = \sqrt{\frac{3}{2}}\bar{M}_{3/2}\frac{f_{\gamma N\Delta}(W) f_{\pi N\Delta}(W)\Gamma_\Delta(W)/2}{m_\Delta - W - i\,\Gamma_\Delta(W)/2} e^{i\phi(W)}, \tag{4.19}$$

with $\bar{M}_{3/2} = 0.323\,\mathrm{GeV}^{-1/2}$, the Δ-resonance mass m_Δ and decay width $\Gamma_\Delta(W)$. The energy dependence of $\Gamma_\Delta(W)$ in MAID is parametrized as

$$\Gamma_\Delta(W) = \Gamma_R \frac{k_0^3}{k_R^3}\frac{m_\Delta}{W}\frac{2m_\Delta}{W+m_\Delta}\left(\frac{X^2+k_R^2}{X^2+k_0^2}\right)^r. \tag{4.20}$$

The vertex factors are given by

$$f_{\gamma N\Delta}(W) = \left(\frac{k_0^\gamma}{k_R^\gamma}\right)^n \left(\frac{X^2+k_R^{\gamma 2}}{X^2+k_0^{\gamma 2}}\right), \tag{4.21a}$$

$$f_{\pi N\Delta}(W) = \left(\frac{1}{3\pi}\frac{k_0^\gamma}{k_0}\frac{2m_N}{W+m_\Delta}\frac{1}{\Gamma_\Delta(W)}\right)^{1/2}, \tag{4.21b}$$

where Γ_R and k_R^γ (k_R) are the Δ width and photon (pion) momentum at the resonance position, $W = m_\Delta$. In Eqs. (4.21), X is the damping parameter and m_N is the nucleon mass, and $n = 2$ for $M_{1+}^{3/2}$ multipole. Note that RΔM, used in Sections 3.2 and 3.3.3

Table 4.1: Parameters of MAID98 [288] and RΔM [212]

	m_Δ [MeV]	Γ_R [MeV]	r	X [MeV]
MAID98	1235	130	1	500
RΔM	1232	115	0	–

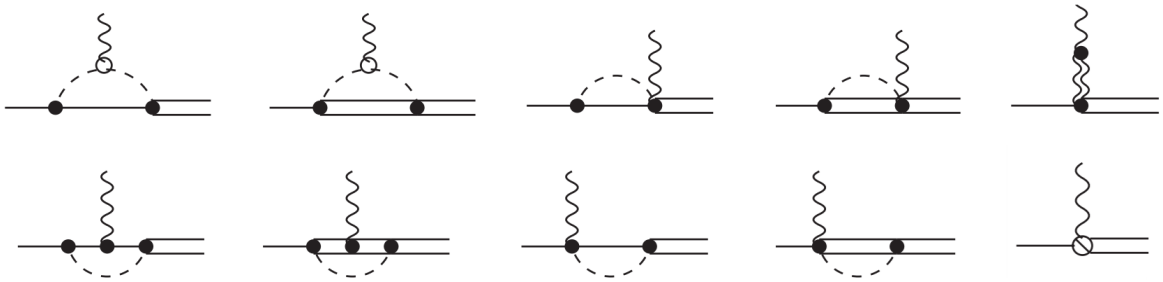

Figure 4.2: The NLO $\gamma N\Delta$ vertex corrections in baryon χEFT in the δ-expansion counting scheme [82]. The solid lines correspond to nucleon propagators; the double lines represent Δ propagators; the wiggly double line corresponds to the vector–meson propagator. The latter process appears as the effective low-energy constant associated with the radius of the g_M form factor at finite photon virtuality. The closed and open circles denote the vertices from the first- and second-order Lagrangian, respectively, the sliced vertex stands for the electric g_E and Coulomb g_C quadrupole couplings.

to describe the pion-nucleon scattering process, employs the resonance mass and width parameters distinct from those of MAID98. The parameters for RΔM and MAID98 are listed Table 4.1.

The phenomenological phase $\phi(W)$ is introduced in Eq. (4.19) to fulfill the Fermi-Watson final state theorem [302], which results from the unitarity of the S-matrix. Following Olson's unitarization procedure [303], the phase of $M_{1+}^{3/2}$ multipole is adjusted to the pion-nucleon scattering phase shift in the spin-isospin-3/2 p-wave channel P_{33}, providing the unitary phase

$$\phi(W) = (22.13\,x - 3.769\,x^2 + 0.184\,x^3)\ [\text{deg}], \tag{4.22}$$

with $x = (W - m_\pi - m_N)/100\,\text{MeV}$.

The separation in Eq. (4.18) is not unique and varies, for example, between dynamical models [298, 304, 305] as well as phenomenological multipole solutions [288, 296, 297]. Specifically addressing the $M_{1+}^{3/2}$ multipole and real photon scenarios, the primary distinction between MAID98 [288] employed in this work (as well as in Ref. [75]) and the later unitary isobar model MAID2007 [296] is their approach to handling the background. The background contribution $M_{1+}^{3/2(B)}$ in MAID98, consisting of Born terms and t-channel vector-meson contributions, is a real monotonic function. Within the framework of MAID2007, the background undergoes unitarization through the K-matrix approach, transforming into a complex function that has zero value at the resonance position. Consequently, this difference leads to distinct unitarization phases $\phi(W)$.

The chiral effective field theory (χEFT) [306] results provide a vigorous framework to understand the role played by the unitary phase. As was shown in Ref. [82] for the pion photoproduction in the Δ-resonance energy region, the Fermi–Watson theorem is fulfilled exactly in the complete next-to-leading-order (NLO) calculation using the δ-expansion power counting scheme [307]. In this approach, the bare resonant part, which defines the LO result, itself satisfies the Fermi–Watson theorem. Going to NLO, the background contribution is purely real. Consequently, their naive summation would result in unitarity breaking. The restoration of unitarity occurs upon including the $\gamma N\Delta$ vertex corrections illustrated in Fig. 4.2 in the calculation.

Comparing the χEFT results with the framework of MAID98 reveals that the multiplicative factor $\exp[i\phi(W)]$ in Eq. (4.19) effectively incorporates the contribution of the additive vertex corrections [308]. The difference between the approaches of MAID98 and MAID2007 can be related to the vertex correction graphs in Fig. 4.2. Depending on whether vertex corrections are associated with the resonant or background contributions, a real or unitary (complex) background term is derived, as implemented in the MAID98 and MAID2007 approaches, respectively.

For the nuclear applications considered in this work, we want to allow for a medium modification of the Δ-resonance. For this purpose, we adopt the approach of MAID98, where all vertex corrections are absorbed in the resonant part of the $M_{1+}^{3/2}$ multipole, offering a more straightforward process of implementing in-medium correction. Notably, various theoretical frameworks for pion photoproduction on the nucleon have been developed in the last decades, categorized into several major groups: dispersive [309, 310], effective Lagrangian [311–313], dynamical models [298, 304, 305, 314, 315], chiral effective field theory [316], and further references therein. However, employing MAID98 enables a direct comparison between the predictions of our model and the results of Ref. [75], avoiding discrepancies due to dependence on the model for the photoproduction of free pions.

Our method of introducing the medium effects is then similar to the approach of Ref. [75]. The non-resonant background $M_{1+}^{3/2(B)}$ is assumed to remain unchanged. The Breit–Wigner denominator and unitary phase in Eq. (4.19) are combined into an effective propagator, which can be presented as

$$\bar{G}(W) = G(W)e^{i\phi} = \frac{1}{\overline{m}_\Delta(W) - W - i\,\overline{\Gamma}_\Delta(W)/2}, \tag{4.23}$$

with

$$\overline{m}_\Delta(W) = m_\Delta \cos\phi + 2W \sin^2\frac{\phi}{2} - \frac{1}{2}\Gamma_\Delta(W)\sin\phi, \tag{4.24a}$$

$$\overline{\Gamma}_\Delta(W) = \Gamma_\Delta(W)\cos\phi - 2(W - m_\Delta)\sin\phi. \tag{4.24b}$$

The effective mass and width of the resonance, Eqs. (4.24), are shifted in the nuclear medium by many-body effects. Correspondingly, for the photoproduction off a bound nucleon, the effective propagator, Eq. (4.23), in Eq. (4.19) is replaced by

$$\bar{G}(\Sigma_\Delta, W) = \frac{1}{\overline{m}_\Delta(W) - W - i\,\overline{\Gamma}_\Delta(W)/2 + \overline{\Sigma}_\Delta}, \tag{4.25}$$

where $\overline{\Sigma}_\Delta$ is the effective Δ self-energy.

In the following subsection, we determine the Δ self-energy $\overline{\Sigma}_\Delta$ consistent with our model for pion-nucleus scattering [3], which was fitted to the experimental data.

4.2.3 The effective Δ self-energy

Despite the nonlocal nature of the Δ self-energy Σ_Δ within a finite nucleus [89], an assumption of locality was successfully applied to both scattering [88, 90, 211] and photoproduction [287] processes within the Δ-hole model framework. The analysis of low-energy pion-nucleus scattering and pionic atom data, conducted in Ref. [225] across a wide range of nuclei, revealed the existence of a nuclear effective density, which determines the parameters of the pion-nucleus potential. The evaluation of the average value of r over the product of the nuclear density and the initial and final pion distorted waves reveals that the pion-nucleus scattering predominantly occurs in the peripheral region. In particular, for the pion-^{12}C elastic scattering at the pion kinetic energy of 100 MeV, the average value of r is 2.52 fm [103]. As demonstrated in Ref. [116], the strong two- and three-body pion absorption mechanisms result in nearly complete absorption of pion flux near the nuclear surface, even at the pion laboratory energy of 165 MeV. Only at high pion energies, about 240 MeV, there is a non-negligible probability that the pions will pass through the nucleus without being absorbed. Due to the strong absorption processes, the outgoing pions primarily interact with a narrow band of the nuclear surface around the effective nuclear density. Consequently, it is reasonable to presume consistency in the Δ self-energy between scattering and photoproduction processes, as only pions produced from the nuclear surface area will likely remain unabsorbed.

The Δ self-energy $\Sigma_\Delta = 12.9 \pm 1.3 - i\,(33.2 \pm 0.8)$ MeV, extracted form the fit to $\pi^\pm$-^{12}C scattering data in the previous Chapter, is not the same as $\overline{\Sigma}_\Delta$ in Eq. (4.25). As was discussed above, the quantities entering Eq. (4.25) incorporate the interference of the bare resonant with the background corrections. Within the RΔM, this interference explicitly arises in the scattering amplitude upon substituting the K-matrix, Eq. (3.26) and (3.48), into Eq. (3.25). The resulting P_{33} channel pion-nucleon scattering amplitude can be expressed in the form

$$f^1_{33} = \frac{1}{k_0}\frac{\Gamma(W)/2}{m_\Delta - W - i\,\Gamma(W)/2 + \overline{\Sigma}_\Delta(W)}, \tag{4.26}$$

where the total elastic width is

$$\Gamma(W) = \Gamma_\Delta(W) + 2(m_\Delta - W)k_0 K^{1(B)}_{33}, \tag{4.27}$$

and we have introduced the effective total Δ self-energy

$$\overline{\Sigma}_\Delta(W) = \Sigma_\Delta \frac{\Gamma_\Delta(W)}{\Gamma(W) + 2\Sigma_\Delta k_0 K^{1(B)}_{33}}. \tag{4.28}$$

Here $K^{1(B)}_{33} = K^1_{33} - K^{1(\Delta)}_{33}$ is the non-resonant background contribution to the K matrix within the RΔM.

In this way, the total elastic width and total Δ self-energy, $\Gamma(W)$ and $\overline{\Sigma}_\Delta(W)$, differ from the corresponding bare-resonance quantities, $\Gamma_\Delta(W)$ and Σ_Δ, due to the inclusion

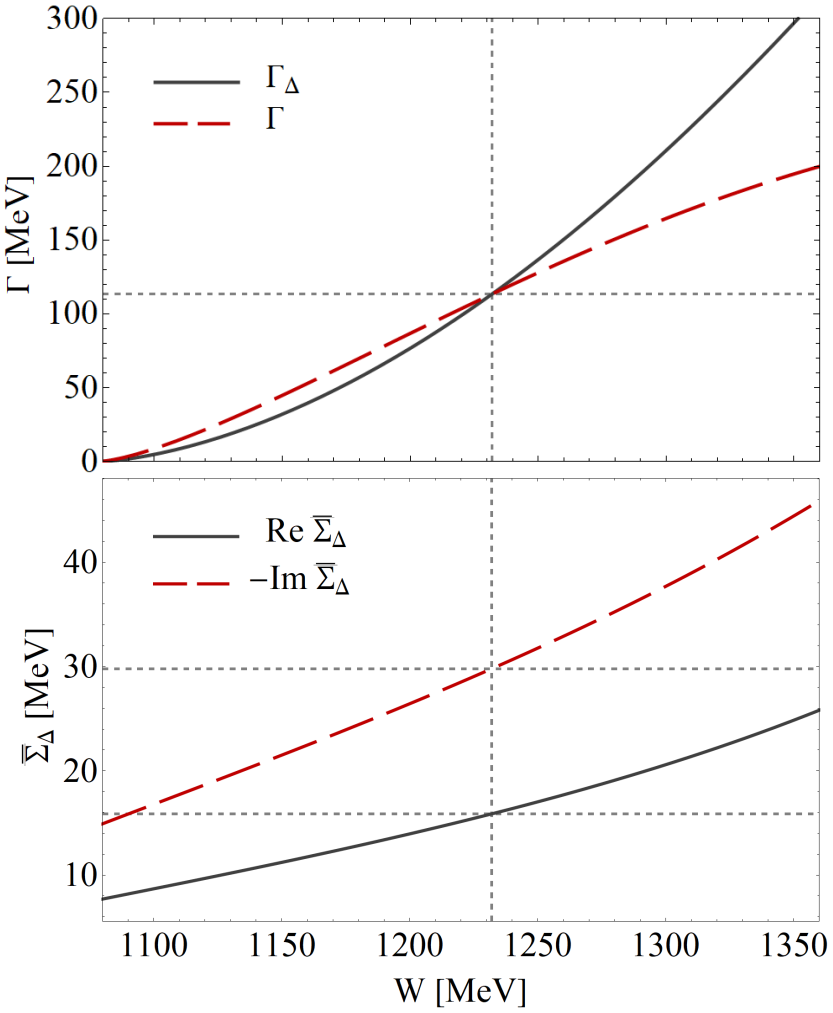

Figure 4.3: Upper panel: the total and bare Δ-resonance elastic decay widths, denoted as Γ and Γ_Δ respectively, as functions of the pion-nucleon reaction energy W obtained within RΔM. Lower panel: the effective total Δ self-energy $\overline{\Sigma}_\Delta$ as a function of W, Eq. (4.28), with $\Sigma_\Delta = (12.9 - i\,33.2)$MeV. The short dashed gray lines represent the resonance position and the magnitude of the corresponding quantities.

of non-resonant contributions. As follows from Eq. (4.28), the influence of the background brings energy dependence to the effective Δ self-energy in Eq. (4.26). The upper and lower panels of Fig. 4.3 illustrate the total and bare-resonance Δ decay widths, as well as the total Δ self-energy provided by the RΔM, respectively.

Finally, we utilize $\overline{\Sigma}_\Delta$ given by Eq. (4.28) to calculate the pion photoproduction amplitude in the nuclear medium using Eq. (4.25). The modified $M_{1+}^{3/2}$ multipole resulting from this process is compared with its free-space counterpart in Fig. 4.4. The plot illustrates that the medium effects significantly modify the magnitude and resonance position of the amplitude. The MAID98 background contribution, $M_{1+}^{3/2(B)}$, also shown in the figure, exhibits a monotonically increasing trend with energy. This behavior mainly arises from vector mesons other than ρ and ω, which are not accounted for in the MAID model and affect the results at higher energies above the Δ(1232) resonance.

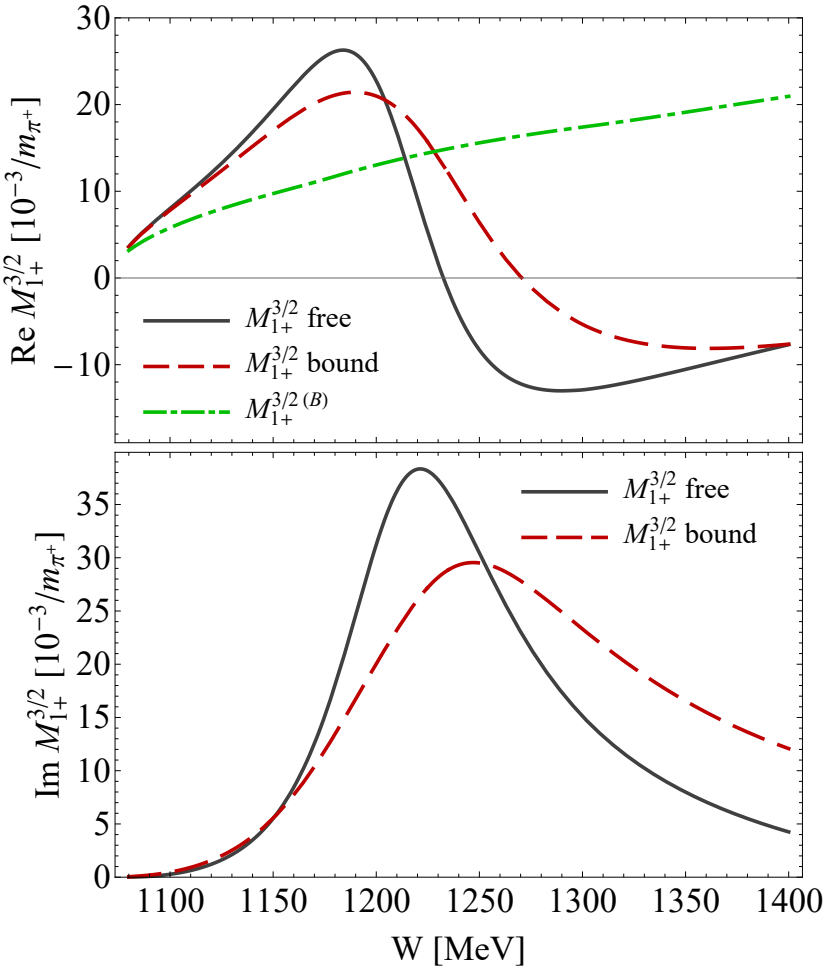

Figure 4.4: The real and imaginary parts of the $M_{1+}^{3/2}$ multipole. The solid black curves correspond to the amplitude in free space given by MAID98 [296]. The dashed red curves represent the modified multipole in the nuclear medium as given by Eq. (4.25) with the effective Δ self-energy illustrated in Fig. 4.3. The dash-dotted green curve is the non-resonant background contribution in MAID98 [288].

In contrast to our model, which assumes that $\overline{\Sigma}_\Delta$ is momentum-independent, Ref. [75] introduces dependence on the momentum transfer q into $\overline{\Sigma}_\Delta$ through the factor $F(q) = \exp(-\beta q^2)$. Here, $F(q)$ is the s-shell harmonic oscillator form factor of ^{4}He with $\beta = 0.54\,\mathrm{fm}^2$. This phenomenological modification is assumed to be universal and applicable to heavier nuclei with the same β. We do not include this factor in $\overline{\Sigma}_\Delta$ to maintain consistency with our model for pion scattering. Incorporating this factor has been observed to spoil the fitting of the scattering data, particularly the differential elastic cross sections at large angles.

4.3 The second-order potential for nuclear pion photoproduction

In this section, we derive the explicit form of the π^0 photoproduction potential in momentum space, as given by Eq. (4.5b), for spin- and isospin-zero nuclei. The derivation

closely aligns with the development of the pion-nucleus scattering potential presented in Sec. 3.3.

According to Eq. (4.6), the potential is approximated as the sum of two terms:

$$V_\gamma(\boldsymbol{k}', \boldsymbol{k}) \approx V_\gamma^{(1)}(\boldsymbol{k}', \boldsymbol{k}) + V_\gamma^{(2)}(\boldsymbol{k}', \boldsymbol{k}), \tag{4.29}$$

where, within the impulse approximation, the first-order part of the potential is

$$V_\gamma^{(1)}(\boldsymbol{k}', \boldsymbol{k}) = -\frac{\sqrt{\mathscr{M}(k')\mathscr{M}_\gamma(k)}}{2\pi} A \langle \pi(\boldsymbol{k}'), \Psi_0 | \hat{t}^\gamma | \gamma(\boldsymbol{k}), \Psi_0 \rangle \tag{4.30}$$

and the second-order part is given by

$$V_\gamma^{(2)}(\boldsymbol{k}', \boldsymbol{k}) = -\frac{\sqrt{\mathscr{M}(k')\mathscr{M}_\gamma(k)}}{2\pi} A(A-1) \langle \pi(\boldsymbol{k}'), \Psi_0 | \hat{t}_2 \hat{G} \hat{P}_\emptyset \hat{t}_1^\gamma | \gamma(\boldsymbol{k}), \Psi_0 \rangle. \tag{4.31}$$

Using the matrix element given by Eq. (4.10) and following similar steps as in the derivation of Eq. (3.37), we obtain the first-order momentum-space spin-isospin-averaged photoproduction potential:

$$V_\gamma^{(1)}(\boldsymbol{k}', \boldsymbol{k}) = \mathscr{W}_\gamma(\boldsymbol{k}', \boldsymbol{k}) \frac{[\boldsymbol{k}'_{\rm 2cm} \times \boldsymbol{k}_{\rm 2cm}] \cdot \boldsymbol{\epsilon}^\lambda}{k'_{\rm 2cm} k_{\rm 2cm}} F_2^+(\boldsymbol{k}'_{\rm 2cm}, \boldsymbol{k}_{\rm 2cm}) \rho(\boldsymbol{k}' - \boldsymbol{k}), \tag{4.32}$$

with the phase space factor

$$\mathscr{W}_\gamma(\boldsymbol{k}', \boldsymbol{k}) = \sqrt{\frac{\mathscr{M}(k')\mathscr{M}_\gamma(k)}{\mu(\boldsymbol{k}', \boldsymbol{p}'_N)\mu_\gamma(\boldsymbol{k}, \boldsymbol{p}_N)}}. \tag{4.33}$$

The second-order component of the potential characterizes the subsequent rescattering of the generated pion on a second nucleon, occurring concurrently with the excitation and de-excitation processes within the nucleus. To calculate the matrix element in Eq. (4.31), we need to account for the spin-isospin structure of both $\hat{t}^\gamma$ and $\hat{t}$. While the photoproduction amplitude is decomposed according to Eqs. (4.12) and (4.15), the scattering amplitude is commonly presented as given by Eq. (3.19).

The spin and isospin dependence in Eq. (4.31) can be explicitly factored out. For spin-zero nuclei, the direct summation over spin components yields:

$$\begin{aligned}
\sum_{s,s'=-1/2}^{1/2} \chi_1^\dagger(s)\chi_2^\dagger(s') \left(\hat{t}^{(0,1)} + \hat{t}^{(2,3)} \hat{\boldsymbol{\sigma}}_2 \cdot \boldsymbol{n}_2\right) \hat{f}_1^\gamma(\boldsymbol{k}''_{\rm 2cm}, \boldsymbol{k}_{\rm 2cm}) \chi_1(s')\chi_2(s) = \\
2 \Bigg(\boldsymbol{\epsilon}^\lambda \cdot \boldsymbol{n}_1 \hat{F}_2(\boldsymbol{k}''_{\rm 2cm}, \boldsymbol{k}_{\rm 2cm}) \hat{t}^{(0,1)} + i \boldsymbol{\epsilon}^\lambda \cdot \boldsymbol{n}_2 \hat{\mathscr{F}}_1(\boldsymbol{k}''_{\rm 2cm}, \boldsymbol{k}_{\rm 2cm}) \hat{t}^{(2,3)} \\
+ i \frac{(\boldsymbol{k}_{\rm 2cm} \cdot \boldsymbol{n}_2)(\boldsymbol{k}''_{\rm 2cm} \cdot \boldsymbol{\epsilon}^\lambda)}{k_{\rm 2cm} k''_{\rm 2cm}} \hat{\mathscr{F}}_3(\boldsymbol{k}''_{\rm 2cm}, \boldsymbol{k}_{\rm 2cm}) \hat{t}^{(2,3)} \Bigg),
\end{aligned} \tag{4.34}$$

where $\chi_i(s)$ is the nucleon spinor, $\boldsymbol{n}_1 = [\boldsymbol{k}''_{\rm 2cm} \times \boldsymbol{k}_{\rm 2cm}]/(k''_{\rm 2cm} k_{\rm 2cm})$ and $\boldsymbol{n}_2 = [\boldsymbol{k}'_{\rm 2cm'} \times \boldsymbol{k}''_{\rm 2cm'}]/(k'_{\rm 2cm'} k''_{\rm 2cm'})$. The subscript "2cm′" corresponds to the c.m. frame of the pion and

the second nucleon. The spin-flip pion photoproduction amplitudes $\hat{\mathscr{F}}_{1,3}$ amplitudes are related to the CGLN amplitudes as

$$\hat{\mathscr{F}}_1(\boldsymbol{k}',\boldsymbol{k}) = \hat{F}_1(\boldsymbol{k}',\boldsymbol{k}) - \frac{\boldsymbol{k}'\cdot\boldsymbol{k}}{k'k}\hat{F}_2(\boldsymbol{k}',\boldsymbol{k}), \tag{4.35a}$$

$$\hat{\mathscr{F}}_3(\boldsymbol{k}',\boldsymbol{k}) = \hat{F}_2(\boldsymbol{k}',\boldsymbol{k}) + \hat{F}_3(\boldsymbol{k}',\boldsymbol{k}). \tag{4.35b}$$

Note that contributions proportional to $\hat{F}_4\hat{t}^{(2)}$ exactly cancel. This cancellation arises from the fact that the operator $(\boldsymbol{n}\cdot\hat{\boldsymbol{\sigma}})$ serves as a spin projector onto the $\boldsymbol{n}$ axis. Consequently, operators $(\boldsymbol{n}_2\cdot\hat{\boldsymbol{\sigma}})$ and $(\boldsymbol{k}'\cdot\hat{\boldsymbol{\sigma}})$ project onto perpendicular directions. Although these operators correspond to different nucleons, the summation over spin makes the final result proportional to $\boldsymbol{n}_2\cdot\boldsymbol{k}' = 0$.

It is convenient to use the relation

$$\langle\pi_b|\hat{\boldsymbol{t}}\cdot\hat{\boldsymbol{\tau}}|\pi_a\rangle = i\varepsilon_{abc}\hat{\boldsymbol{\tau}}_c = -\frac{1}{2}[\hat{\boldsymbol{\tau}}_b,\hat{\boldsymbol{\tau}}_a] \tag{4.36}$$

to write the isospin decomposition of Eq. (4.15) in the form similar to Eq. (**??**). Taking the sum over the isospin in Eq. (4.31) for nuclei with zero isospin, one obtains

$$\begin{aligned}\sum_{\tau,\tau'=-1/2}^{1/2}\eta_1^\dagger(\tau)\eta_2^\dagger(\tau')\left[\delta_{ba}\hat{t}^{(0,2)} - \frac{1}{2}[\hat{\boldsymbol{\tau}}_a,\hat{\boldsymbol{\tau}}_b]\hat{t}^{(1,3)}\right]_2 \\ \times\left[\delta_{b3}A^+_{l\pm} + \frac{1}{2}[\hat{\boldsymbol{\tau}}_b,\hat{\boldsymbol{\tau}}_3]A^-_{l\pm} + \hat{\boldsymbol{\tau}}_bA^0_{l\pm}\right]_1\eta_1(\tau')\eta_2(\tau) = 2\left(\hat{t}^{(0,2)}\hat{A}^+ - 2\,\hat{t}^{(1,3)}\hat{A}^-\right),\end{aligned} \tag{4.37}$$

where $\eta_i(\tau)$ is the nucleon isospinor and the subscript $i = 1,2$ in $[\cdots]_i$ refers to the nucleon index as in Eq. (4.31).

Finally, neglecting the nuclear excitation energies in $\hat{G}$ and combining Eqs. (4.34) and (4.37), the second-order part of the potential in momentum space for spin- and isospin-zero nuclei can be written as

$$\begin{aligned}V^{(2)}_\gamma(\boldsymbol{k}',\boldsymbol{k}) = \int\frac{\mathrm{d}\boldsymbol{k}''}{2\pi^2}\frac{\mathscr{W}(\boldsymbol{k}',\boldsymbol{k}'')\mathscr{W}_\gamma(\boldsymbol{k}'',\boldsymbol{k})}{k_0^2 - k''^2 + i\varepsilon}\Big[f^{(0)}(\boldsymbol{k}',\boldsymbol{k}'')f^{(0)}_\gamma(\boldsymbol{k}'',\boldsymbol{k})C_0(\boldsymbol{k}'-\boldsymbol{k}'',\boldsymbol{k}''-\boldsymbol{k}) \\ + \Big(2f^{(1)}(\boldsymbol{k}',\boldsymbol{k}'')f^{(1)}_\gamma(\boldsymbol{k}'',\boldsymbol{k}) + f^{(2)}(\boldsymbol{k}',\boldsymbol{k}'')f^{(2)}_\gamma(\boldsymbol{k}'',\boldsymbol{k}) + 2f^{(3)}(\boldsymbol{k}',\boldsymbol{k}'')f^{(3)}_\gamma(\boldsymbol{k}'',\boldsymbol{k})\Big) \\ \times C_{\mathrm{ex}}(\boldsymbol{k}'-\boldsymbol{k}'',\boldsymbol{k}''-\boldsymbol{k})\Big],\end{aligned} \tag{4.38}$$

where

$$f^{(0,1)}_\gamma(\boldsymbol{k}'',\boldsymbol{k}) = \pm\boldsymbol{\epsilon}^\lambda\cdot\boldsymbol{n}_1F_2^\pm(\boldsymbol{k}''_{2\mathrm{cm}},\boldsymbol{k}_{2\mathrm{cm}}), \tag{4.39a}$$

$$f^{(2,3)}_\gamma(\boldsymbol{k}'',\boldsymbol{k}) = \pm i\boldsymbol{\epsilon}^\lambda\cdot\boldsymbol{n}_2\mathscr{F}_1^\pm(\boldsymbol{k}''_{2\mathrm{cm}},\boldsymbol{k}_{2\mathrm{cm}}) \pm i\frac{(\boldsymbol{k}_{2\mathrm{cm}}\cdot\boldsymbol{n}_2)(\boldsymbol{k}''_{2\mathrm{cm}}\cdot\boldsymbol{\epsilon}^\lambda)}{k_{2\mathrm{cm}}k''_{2\mathrm{cm}}}\mathscr{F}_3^\pm(\boldsymbol{k}''_{2\mathrm{cm}},\boldsymbol{k}_{2\mathrm{cm}}). \tag{4.39b}$$

with $\mathscr{F}^\pm_{1,3}$ holding the same meaning as defined in Eq. (4.15). The scattering amplitudes $f^{(i)}$ are given by Eqs. (3.47). The contribution of the P_{33} channel to p-wave parameters $c_{0,1}$ and $s_{0,1}$ is modified in nuclear medium as described in Sec. 3.3.3. The properties

of the nucleon distribution contribute to the second-order potential via the correlation functions C_0 and $C_{\rm ex}$, which are discussed in Sec. 2.3.

The second-order part of the photoproduction potential, as expressed in Eq. (4.31), shares a similar form with the scattering potential, and the four terms on the right-hand side carry the same physical meaning. The first term describes spin-isospin averaged individual nucleon scattering on two nucleons. The term proportional to $f^{(1)}f^{(1)}_\gamma$ ($\hat{f}^{(2)}\hat{f}^{(2)}_\gamma$) describes the contribution of the intermediate charge exchange (nucleon spin-flip) on two nucleons, keeping the scattered nucleus in the ground state. Similarly, the term $\hat{f}^{(3)}\hat{f}^{(3)}_\gamma$ represents the simultaneous exchange of both spin and isospin.

4.4 Results and discussion

4.4.1 Comparison with ^{12}C and ^{40}Ca data

In this section, we compare the predictions of the described model for the coherent nuclear pion photoproduction on ^{12}C and ^{40}Ca with experimental data and theoretical model calculations derived from Ref. [75]. Note that no fitting of the Δ self-energy was done, and the obtained results are based on the parameters from the multi-energy fit to $\pi^{\pm}$-^{12}C scattering data in the energy range of 80–180 MeV pion laboratory kinetic energy.

The comparison data are sourced from Refs. [72] and [95]. These experiments were performed with the TAPS [317, 318] and Crystal Ball [319] detectors, respectively, at the electron microtron in Mainz (MAMI) [320], combining it with the Glasgow tagged photon beam [321, 322].

The unpolarized differential cross section for the nuclear pion photoproduction on a spin-zero target is expressed in terms of the nuclear photoproduction amplitude, Eq. (4.4), as

$$\frac{d\sigma}{d\Omega}(\theta) = \frac{k_0}{k_0^\gamma}\frac{1}{2}\sum_{\lambda=\pm}|F_\gamma|^2\,. \tag{4.40}$$

The computation of the amplitude F_γ involves several sequential steps, each depicted in the upper panel of Fig. 4.5, showing the integrated cross section for the π^0 photoproduction on ^{12}C in the energy range from threshold to photon laboratory kinetic energy of $\omega^\gamma_{\rm lab} \approx 400$ MeV. Initially, we calculate the first-order momentum space photoproduction potential, Eq. (4.32), with the free-space CGLN amplitude F_2. This initial step is depicted by the dotted black curve in the plot assuming $F_\gamma \approx V^{(1)}_\gamma(\boldsymbol{k}', \boldsymbol{k})$, which is known as the plane-wave impulse approximation (PWIA). Subsequently, we incorporate the pion-nucleus rescattering as given by Eq. (4.4) with $V_\gamma(\boldsymbol{k}', \boldsymbol{k}) \approx V^{(1)}_\gamma(\boldsymbol{k}', \boldsymbol{k})$ and utilize the pion-^{12}C scattering amplitude $F(\boldsymbol{k}', \boldsymbol{k})$ from Ref. [3]. This corresponds to the distorted wave impulse approximation (DWIA), represented by the dot-dashed green curve in Fig. 4.5. The next step, illustrated by the blue dashed curve in the plot, involves modification of the resonant $M^{3/2}_{1+}$ multipole in the nuclear medium, as given by Eq. (4.25), using the effective Δ self-energy $\bar{\Sigma}_\Delta$, Eq. (4.28). Finally, the solid red curve represents the complete model incorporating the second-order photoproduction potential, $V_\gamma(\boldsymbol{k}', \boldsymbol{k}) \approx V^{(1)}_\gamma(\boldsymbol{k}', \boldsymbol{k}) + V^{(2)}_\gamma(\boldsymbol{k}', \boldsymbol{k})$, utilizing the second-order part described by Eq. (4.38). This last component accounts for the second-order rescattering on excited

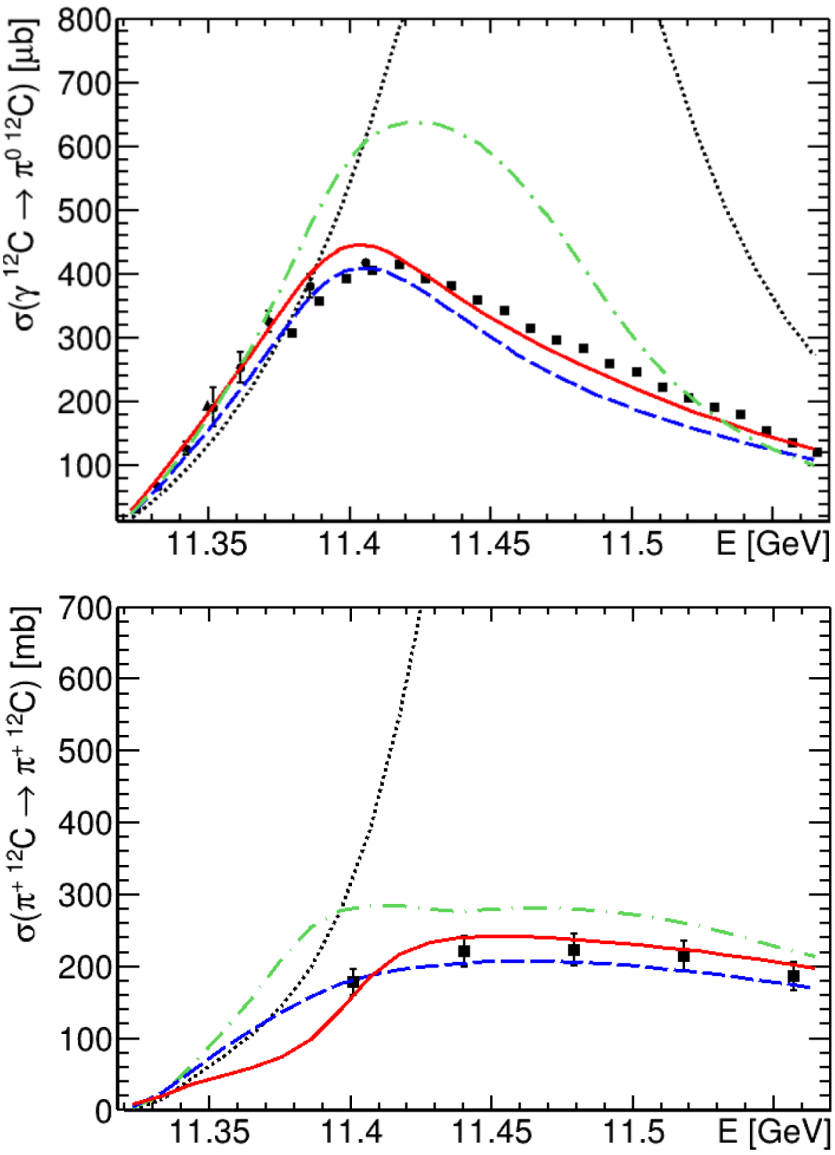

Figure 4.5: The integrated cross sections for coherent π^0 photoproduction (upper panel) and π^+ elastic scattering (lower panel) on ^{12}C as functions of the total c.m. energy E of the system. The black dotted curves depict results under the PWIA. The green dot-dashed curves incorporate pion rescattering on the nucleus in its ground state (DWIA). The blue dashed curves are obtained when the in-medium modification of the elementary amplitudes is introduced to the DWIA. The red solid curves represent the complete calculation in which the second-order rescattering on excited nuclear states (middle diagram in Fig. 4.1) is included. The data on the upper panel are taken from Refs. [95] (●) [72] (■), and [323] (▲); while data on the lower panel are from Ref. [114].

nuclear continuum states, involving intermediate nucleon spin-flip and charge exchange, corresponding with the middle diagram in Fig. 4.1.

As seen from the upper panel of Fig. 4.5, the DWIA prediction incorporating the effective Δ self-energy correction (the blue dashed curve) fails to match the magnitude of the data, although it captures the overall shape adequately. Discrepancies between PWIA, DWIA, and the modification of the elementary photoproduction amplitude are minor at low incident photon energies but become significant in the Δ-resonance region. Incorporating the second-order component of the photoproduction potential, $V_\gamma^{(2)}$, results in an upward shift of the predicted integrated cross section, increasing it by approximately 7% at $\omega_{\text{lab}}^\gamma \approx 250\,\text{MeV}$ to 17% at $\omega_{\text{lab}}^\gamma \approx 330\,\text{MeV}$. In the Δ-resonance energy region, the inclusion of $V_\gamma^{(2)}$ into the calculation yields a relatively smaller effect compared to the influence of the final state interaction and the modification of the Δ-resonance characteristics inside the nucleus. However, the impact of $V_\gamma^{(2)}$ remains sizeable both at low energies and in the Δ-resonance region, providing the necessary correction for a satisfactory description of the data.

The resemblance between nuclear pion scattering and photoproduction allowed us to employ a unified approach, yielding a satisfactory description of experimental data. However, it is important to consider the differences between the two processes when applying the same computational steps. In the lower panel of Fig. 4.5, we show the effects of corrections similar to those illustrated in the upper panel, this time focusing on π^+-^{12}C elastic scattering in the energy range from threshold to pion laboratory kinetic energy of 260 MeV.

Figure 4.5 demonstrates the importance of the final state interaction and modification of the single-nucleon amplitudes in the nuclear medium for both processes. However, while the scattering amplitude is determined from the Lippmann–Schwinger equation, which is self-consistent, the DWIA photoproduction amplitude, as given by Eq. (4.5), is defined as the difference between two terms, each of which in the Δ-resonance energy region is noticeably larger than the total. For this reason, the photoproduction amplitude in the Δ-resonance energy region can become sensitive to effects only slightly influencing the scattering process, as, for example, a modification of the s-wave part of the pion-nucleus scattering potential. Consequently, obtaining the correct photoproduction amplitude requires precise and consistent computation of both the photoproduction potential and the scattering amplitude.

As can be seen from Fig. 4.5, the energy dependence of the shift in integrated cross sections for photoproduction and scattering, induced by the second-order parts of the potentials $V_\gamma^{(2)}$ and $V^{(2)}$, respectively, displays distinct behaviors. Although the improvement in the description of the integrated elastic scattering cross section may not be apparent from the lower panel due to scarce data points, significant enhancements become evident when considering the differential elastic scattering cross section [3]. The second-order photoproduction potential $V_\gamma^{(2)}$ consistently increases the cross section across the energy range. In contrast, the influence of $V^{(2)}$ exhibits a different behavior, providing a larger effect at lower energies and undergoing a change in sign. This different energy behavior is explained by the distinct spin structure of the pion scattering and photoproduction amplitudes for individual nucleons, Eqs. (3.19) and (4.12). While the isospin structure of the elementary amplitudes, and consequently the impact on observ-

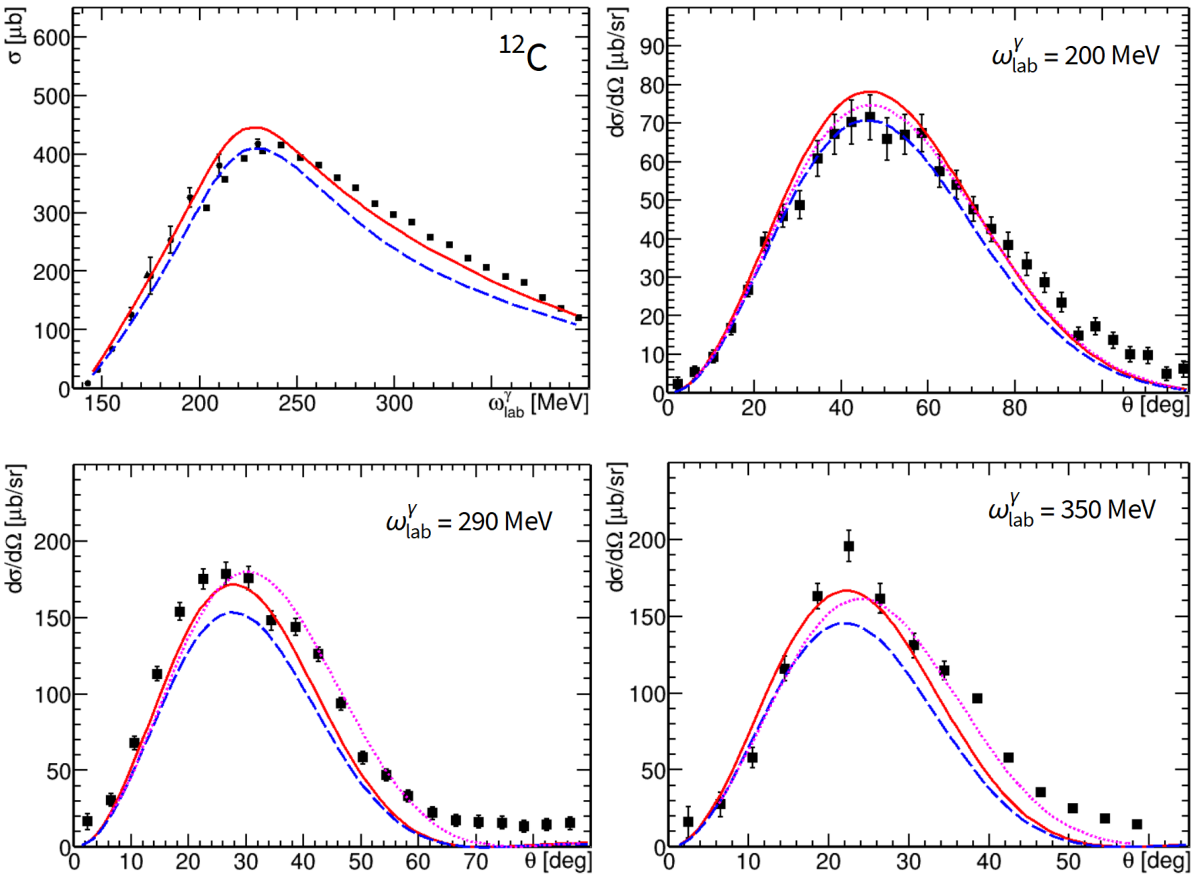

Figure 4.6: Comparison of theoretical predictions for the coherent π^0 photoproduction on ^{12}C with the data from Ref. [72]. The top left panel demonstrates the integrated cross section as a function of the photon laboratory energy $\omega^{\gamma}_{\rm lab}$; the differential cross sections as functions of the scattering angle in the c.m. frame are shown in the other panels. The solid red curves are the predictions of our model; the blue dashed curves are obtained by switching off the second-order part of the photoproduction potential, $V^{(2)}_{\gamma}$; the dotted magenta curves are results obtained with the theoretical model of Ref. [75] according to Ref. [72]. In addition to the data from Ref. [72] (■), the top left panel also includes data from Refs. [95] (●) and [323] (▲).

ables from intermediate charge exchange, remains similar for both processes, the photon vertex introduces a larger number of channels involving intermediate nucleon spin-flip.

In Figures 4.6–4.9, we demonstrate a comparison of the integrated and differential cross sections for the coherent π^0 photoproduction on ^{12}C and ^{40}Ca, respectively, with the experimental data from Refs. [72, 95, 323]. The measurements in Ref. [95] were performed starting from near-threshold photon laboratory energy $\omega^{\gamma}_{\rm lab} = 140\,\text{MeV}$. However, for the present analysis, we omit the consideration of the differential cross-section data corresponding to emitted pion laboratory energies below 30 MeV, as their comprehensive analysis requires the inclusion of nuclear excitations in the propagator $\hat{G}$ of Eq. (4.31). To examine the impact of the second-order corrections, we provide both the predictions of the complete model and the results obtained after setting $V^{(2)}_{\gamma} = 0$. The

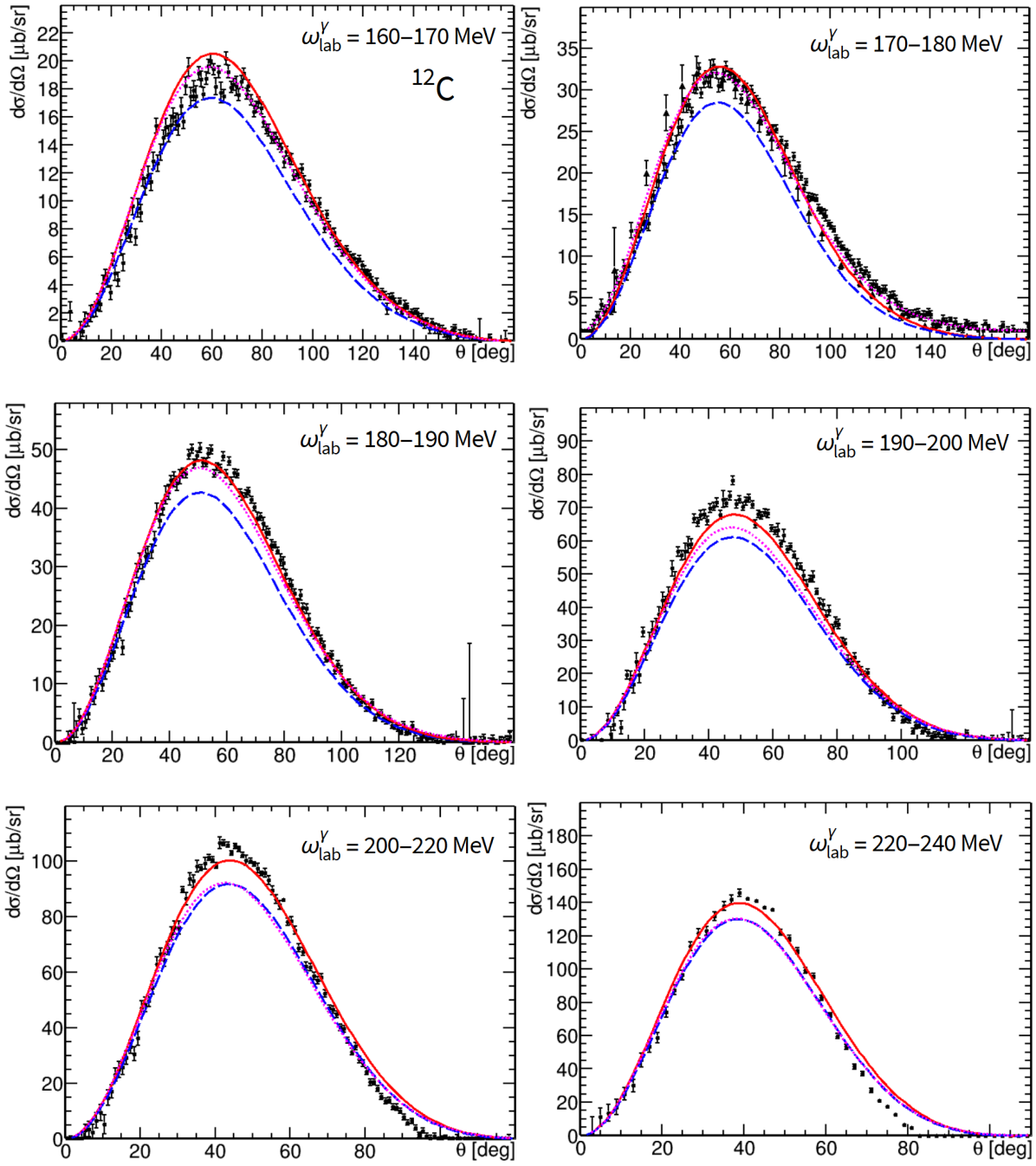

Figure 4.7: Comparison of theoretical predictions for the coherent π^0 photoproduction on ^{12}C with the differential cross section data from Ref. [95]. The meaning of the curves is the same as in Fig. 4.6. The dotted magenta curves are results obtained with the theoretical model of Ref. [75] according to Ref. [95]. The top left panel also includes data from Ref. [323], measured at $\omega^{\gamma}_{lab} = 170 - 177$ MeV and presented by triangular markers.

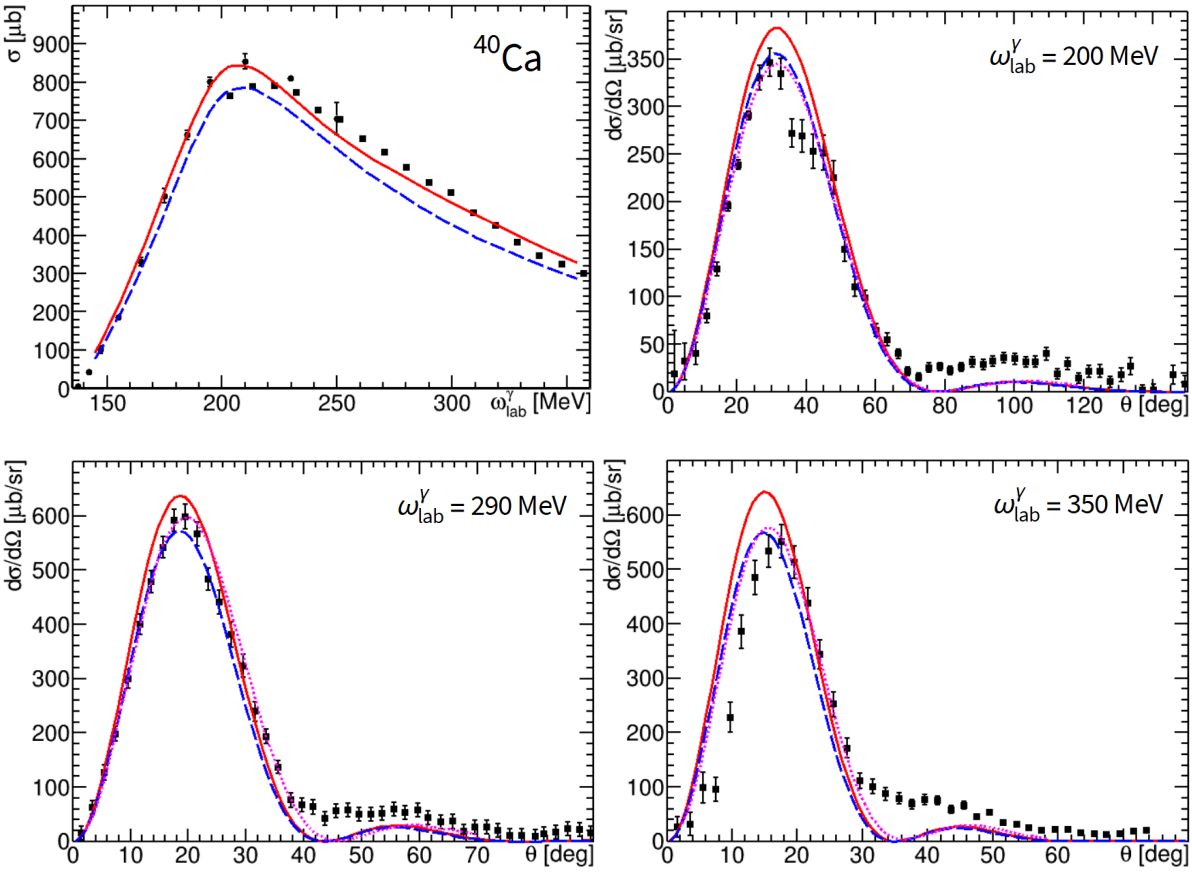

Figure 4.8: Comparison of theoretical predictions for the coherent π^0 photoproduction on ^{40}Ca with the data from Ref. [72]. The top left panel demonstrates the integrated cross section as a function of the photon laboratory energy $\omega^{\gamma}_{\text{lab}}$; the differential cross sections as functions of the scattering angle in the c.m. frame are shown in the other panels. The top left panel also includes data from Refs. [95]. The meaning of the curves and markers is the same as in Fig. 4.6.

solid red and dashed blue curves in Fig. 4.6 match the corresponding curves in Fig. 4.5. For comparison, we also display the theoretical predictions given in Refs. [95] and [72], which are based on the model of Ref. [75]. In Ref. [75], only the first-order photoproduction potential was taken into account, and the effective Δ self-energy was fitted to experimental data for ^{4}He [80]. Due to the mentioned sensitivity of the theoretical results to the scattering amplitude, for the current computation, we have improved the s-wave part of the scattering potential for ^{40}Ca (see Appendix 4.C for details).

The observed reasonable agreement between the predictions of our model and the experimental data demonstrated in Figs. 4.5–4.9 supports the universality of both our approach, initially applied to pion-nucleus scattering, and the parameter Σ_Δ derived from fitting to the scattering data. As noted in Ref. [72], the TAPS data at larger angles possess contamination from incoherent excitations of nuclear levels, which explains the observed disagreement at 200, 290, and 350 MeV photon laboratory energy between the data and all theoretical predictions. The overall discrepancy at 350 MeV can be at least partially attributed to the overestimated background contribution in MAID98 at the

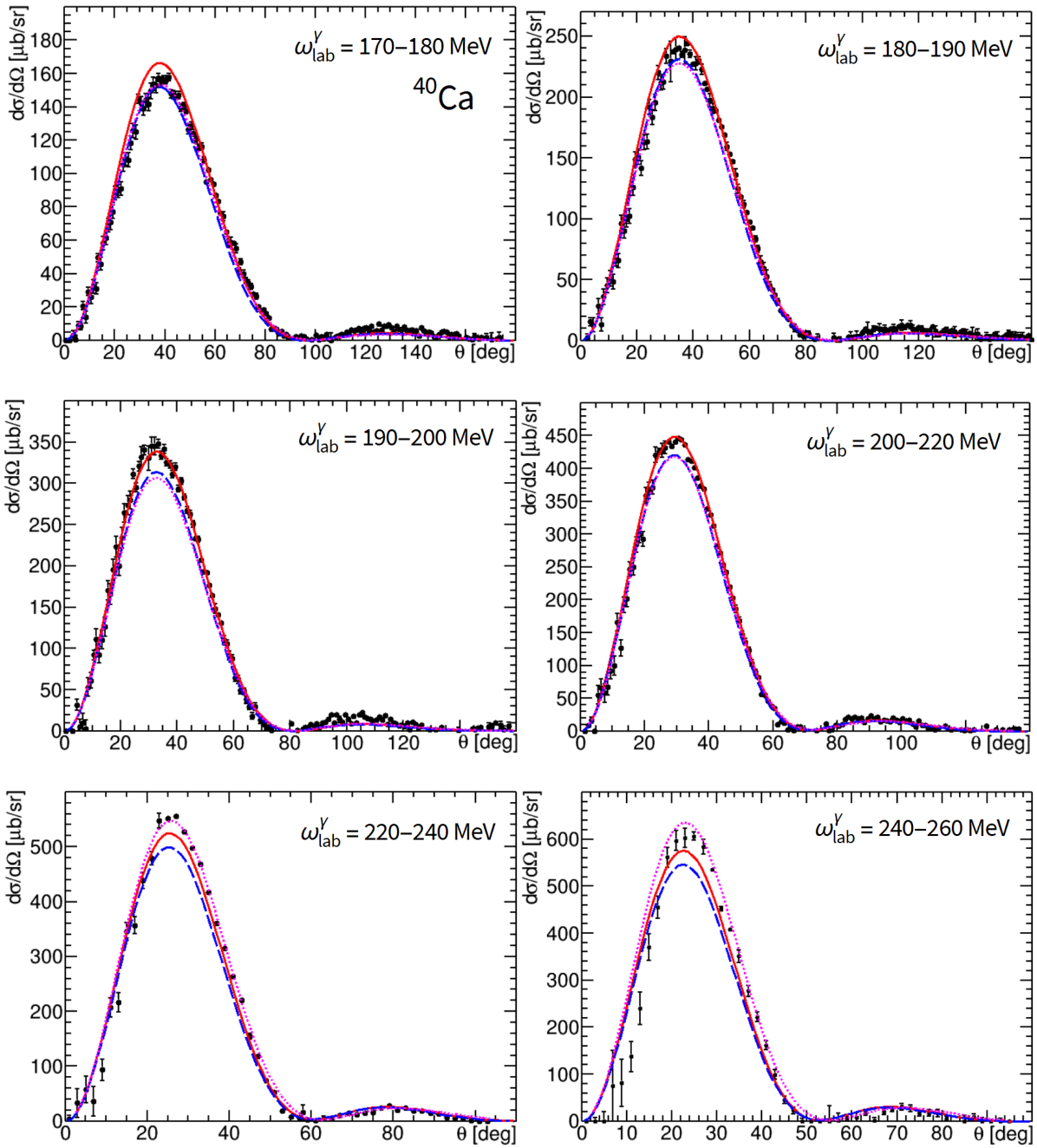

Figure 4.9: Comparison of theoretical predictions for the coherent π^0 photoproduction on ^{40}Ca with the differential cross section data from Ref. [95]. The dotted magenta curves are results obtained with the theoretical model of Ref. [75] according to Ref. [95]. The meaning of the curves is the same as in Fig. 4.6.

higher-energy side of the Δ-resonance, as discussed in Sec. 4.2. As seen from Figs. 4.5–4.8, there is a disagreement between the data of Refs. [95] and [72] within the energy range of 200–240 MeV photon laboratory energy for both ^{12}C and ^{40}Ca. In this energy region, our model better agrees with the more recent Crystal Ball measurements [95].

The data for ^{16}O from Ref. [95] are not taken for the current comparison due to their significant discrepancy with the prior measurements conducted by the Glasgow group using TAPS [324] and the theoretical predictions based on Ref. [75]. This disagreement may stem from the fact that the measurements on ^{16}O were done using a liquid water target, requiring precise treatment for background from Hydrogen, which results in additional systematic uncertainties. However, our predictions for ^{16}O are found to be in quantitative agreement with the data from Ref. [324] and the model of Ref. [75]

4.4.2 Preliminary results for ^{208}Pb

The presented model has shown good agreement with experimental data for both light and medium-heavy nuclei, utilizing the same Δ self-energy. Testing the applicability of the described approach to heavy nuclei is a compelling next step, for which we have selected ^{208}Pb as a test case.

The key components for constructing the scattering and photoproduction potentials are nucleon density form factor and correlation functions. The nucleon distribution of nuclei with nonzero isospin cannot be extracted directly from the FB charge densities provided in Ref. [7]. To address this issue, we utilize the phenomenological model of Ref. [325] to obtain the difference between proton and neutron density distributions (see Fig. 4.10). The neutron skin thickness obtained with this model is approximately 0.356 fm for ^{208}Pb, significantly larger than the PREX-2 analysis result of 0.283 ± 0.071 fm [22] This difference will impact our preliminary predictions and should be further investigated in future analyses. As the first approximation for the correlation functions of ^{208}Pb, we adopt the modified HO shell-model correlation functions for ^{40}Ca, scale them by 208/40, and fit them to the form factor of ^{208}Pb as discussed in Sec. 2.2.4.

In Figure 4.11, we illustrate the prediction of our model for $\pi^{\pm}$-^{208}Pb scattering, utilizing parameters extracted from fitting $\pi^{\pm}$-^{12}C scattering data. The high-energy differential cross sections depicted in the lower panels are well described within the 80° range, reflecting the universality of the Δ self-energy as discussed. At lower energies, as shown in the upper plot, deviations between theoretical curves and experimental data appear due to the significant influence of the poorly constrained s-wave part of the scattering potential and the Coulomb interference. The strong Coulomb field of ^{208}Pb complicates the direct refinement of the s-wave component and requires a more precise treatment for further detailed analysis of low-energy data.

Achieving a reasonable description of the high-energy scattering data motivates testing our model for coherent π^0 photoproduction in this energy range without further adjustments. In Figure 4.12, we compare the prediction of our model with TAPS [72] and Crystal Ball [95] data at a photon laboratory energy of 290 MeV, corresponding to a pion laboratory kinetic energy of 155 MeV. The plot illustrates a rather satisfactory description of the data, highlighting the non-negligible influence of second-order rescattering involving excited intermediate nuclear states in this energy region. Additionally, the figure includes dotted curves representing theoretical predictions given in Refs. [72]

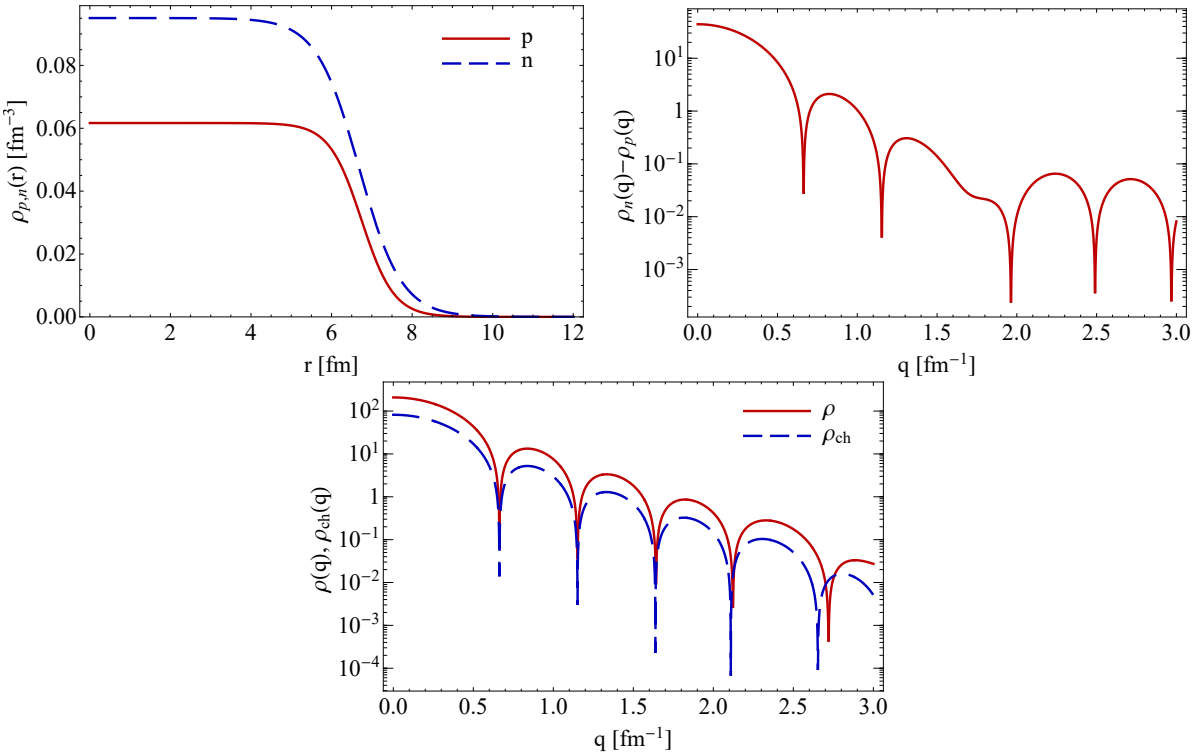

Figure 4.10: **Upper panels**: Neutron and proton density distributions in ^{208}Pb (left) as provided by the phenomenological model of Ref. [325], and the corresponding neutron-proton density difference in momentum space (right). **Lower panel**: Charge form factor of ^{208}Pb from the model-independent FB analysis[7] (solid red curve) and the extracted nucleon density form factor (dashed blue curve).

.

and [95] based on the approach described in Ref. [75]. The significant difference between these curves is attributed to the distinct parameter fits of the model [75] used in Refs. [72] and [95], highlighting a substantial theoretical uncertainty that affects the accuracy of extracting the neutron skin. Our predictions, represented by the red solid curve in Fig. 4.12, are based on the fit of $\pi^{\pm}$-^{12}C scattering data without any additional adjustment.

Despite significant influence from pion rescattering in the Δ resonance energy region, coherent pion photoproduction at 200 MeV photon energy (corresponding to the pion energy of 65 MeV) allows for an approximate treatment within the DWIA. As shown in Ref. [2], the effect of pion-nucleus final state interaction at this energy on coherent photoproduction is approximately 10%, as consistent with Fig. 4.5. To roughly refine the s-wave part of the potential, we fit the s-wave scattering parameter b_0 to $\pi^{\pm}$-^{208}Pb scattering data at 80 MeV within the $\theta \leq 50°$ range. Using the corrected s-wave part of the potential, we obtained results for coherent π^0 photoproduction as illustrated in Fig. 4.13.

The results for ^{208}Pb confirm the assumed universality of the Δ self-energy Σ_Δ in scattering and photoproduction across different nuclei. However, the s-wave part of the potential, which is yet poorly established, compromises the scattering amplitude at

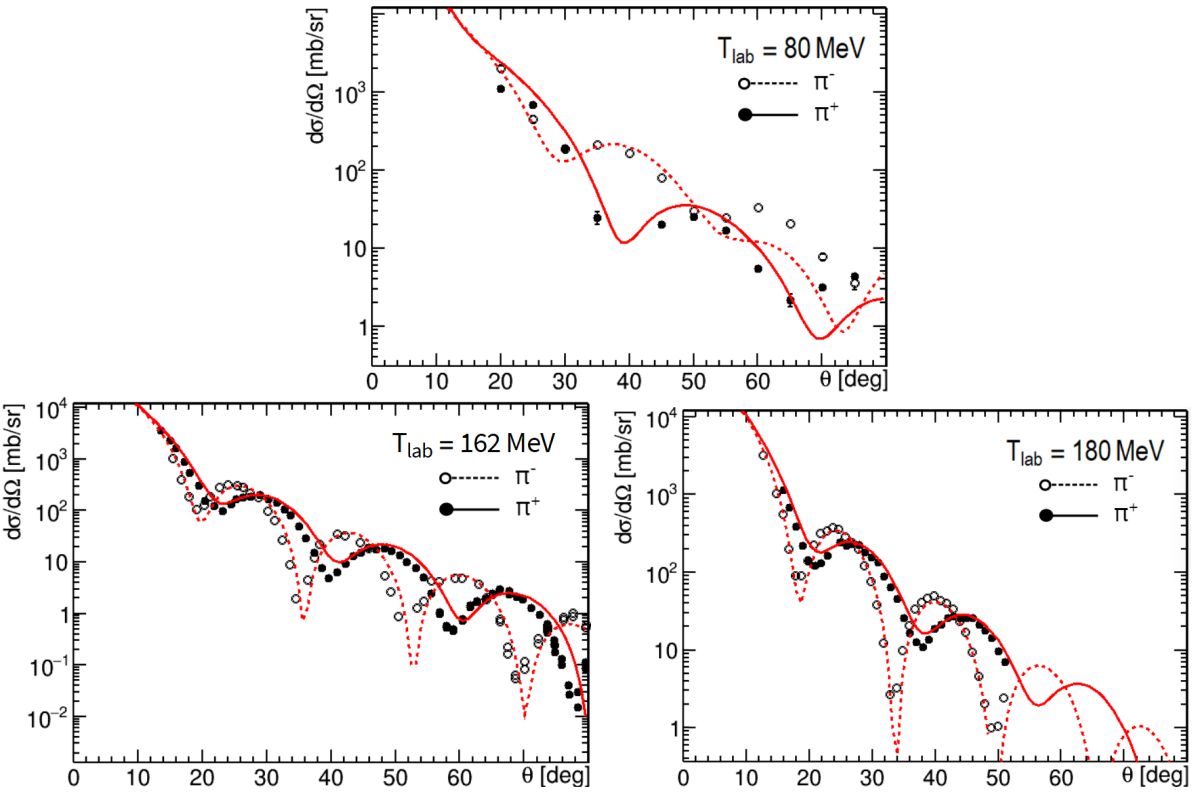

Figure 4.11: The differential cross section for $\pi^{\pm}$-^{208}Pb elastic scattering. Solid curves and closed markers stand for π^+; dashed and open markers for π^-. The theoretical calculation are based on fit 1 to $\pi^{\pm}$-^{12}C scattering data. The experimental data are from Refs. [264] (80 MeV), [326] (162 MeV), and [327] (180 MeV)

.

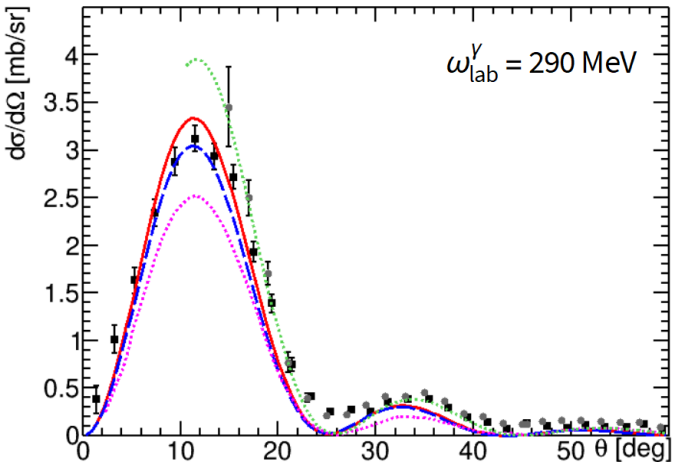

Figure 4.12: The differential cross section for coherent π^0 photoproduction on ^{208}Pb at photon laboratory energy of 290 MeV. The solid red curves are the predictions of our model; the blue dashed curves are obtained by switching off the second-order part of the photoproduction potential, $V^{(2)}_{\gamma}$. The experimental data are taken from Refs. [72] (black squares) and [95] (gray circles). The dotted magenta (green) curve represents theoretical predictions based on the model described in Ref. [75] as reported in Ref. [72] ([95]).

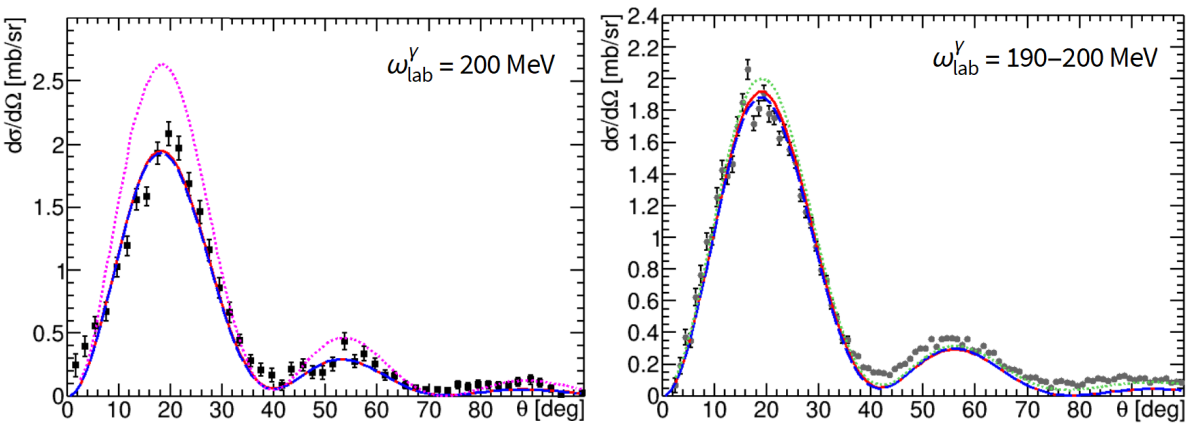

Figure 4.13: The differential cross section for coherent π^0 photoproduction on ^{208}Pb at photon laboratory energy of 200 MeV (left panel) and within the 190–200 MeV energy bin (right panel). The meaning of the curves and markers is the same as in Fig. 4.12.
.

lower energies. Also, heavy nuclei necessitate a more precise approach to manage strong Coulomb interference for an accurate description of $\pi^{\pm}$ scattering. Despite these challenges, a satisfactory description of coherent pion photoproduction data can be achieved without adjusting Σ_Δ in the energy region where the impact of s-wave rescattering diminishes or is better established.

We anticipate that a more detailed treatment of the second-order components of the scattering and photoproduction potentials, which were simplified for deriving the presented preliminary results for ^{208}Pb, will lead to further improvements in accuracy.

4.5 Conclusion and outlook

In this Chapter, we have developed the second-order momentum space potential for nuclear pion photoproduction on spin-isospin-zero nuclei. Our approach to photoproduction builds upon our established model for pion-nucleus scattering [3]. The incorporation of many-body medium effects is achieved through the utilization of the complex effective Δ self-energy Σ_Δ, previously determined by fitting $\pi^{\pm}$-^{12}C scattering data within the energy range of 80 to 180 MeV of pion laboratory kinetic energy. Since the model parameters originate from the scattering process, the achieved agreement with the experimental data for coherent π^0 photoproduction on ^{12}C and ^{40}Ca, along with the preliminary results for ^{208}Pb, obtained without any adjustments of Σ_Δ, underscores the universality and predictive power of our approach.

The rescattering, involving intermediate excited nuclear states and encompassing intermediate nucleon spin-flip and charge exchange, was incorporated by the second-order part of the photoproduction potential. This correction yields a non-negligible contribution across the considered energy range, proving essential for describing the experimental data without requiring the additional fitting of the model parameters. The associated upward shift of the predicted cross section for the coherent π^0 photoproduction was found to be about 10%.

Within the Δ-resonance energy region, the accuracy of the obtained results relies on the precise determination of the pion-nucleus scattering amplitude and is sensitive to the model for the pion photoproduction on a free nucleon. Moreover, the inclusion of higher-order effects on the effective total Δ self-energy for both pion scattering and photoproduction may lead to minor discrepancies between both processes. In principle, one can fit the total Δ self-energy $\overline{\Sigma}_\Delta$ for photoproduction to achieve a better agreement with the data. However, more high-quality data for both scattering and photoproduction are required for such a more refined analysis.

In future work, our intention is to efficiently extend the model to heavy nuclei with nonzero isospin. The achieved agreement with the photoproduction data also indicates the potential applicability of our demonstrated approach to neutrino-induced pion production on nuclei.

Appendices

4.A Pion production on a nucleon

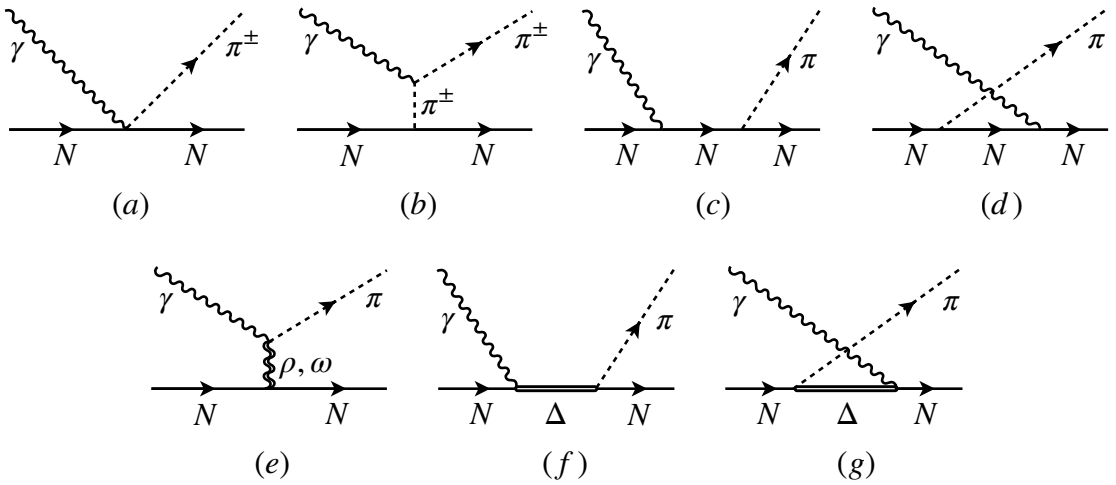

Figure 4.14: Diagrams contributing to pion production on a nucleon: (a) Kroll-Ruderman contribution, (b) pion pole, (c) s-channel nucleon pole, (d) u-channel nucleon pole, (e) heavier meson exchange, (f) s-channel Δ excitation, (g) u-channel Δ excitation.

Figure 4.14 illustrates the lowest-order Feynman diagrams for pion photoproduction on a nucleon as they appear. e.g., in the phenomenological MAID approach. The Kroll-Ruderman (a) and pion pole (b) diagrams contribute only to charged pion production. The resonant contribution to the photoproduction multipoles $M_{1+}^{3/2}$ and $E_{1+}^{3/2}$ arises from the direct Δ production (f).

The expansion of the CGNL amplitudes in therms of electric and magnetic multipoles is given by [295]

$$\hat{F}_1 = \sum_{l\geq 0} \left[\left(l\hat{M}_{l+} + \hat{E}_{l+} \right) P'_{l+1} + \left((l+1)\hat{M}_{l-} + \hat{E}_{l-} \right) P'_{l-1} \right], \tag{4.41a}$$

$$\hat{F}_2 = \sum_{l\geq 1} \left[(l+1)\hat{M}_{l+} + l\hat{M}_{l-} \right] P'_l, \tag{4.41b}$$

$$\hat{F}_3 = \sum_{l\geq 1} \left[\left(\hat{E}_{l+} - \hat{M}_{l+} \right) P''_{l+1} + \left(\hat{E}_{l-} + \hat{M}_{l-} \right) P''_{l-1} \right], \tag{4.41c}$$

$$\hat{F}_4 = \sum_{l\geq 2} \left[\hat{M}_{l+} - \hat{E}_{l+} - \hat{M}_{l-} - \hat{E}_{l-} \right] P''_l, \tag{4.41d}$$

where P'_l is the derivatives of the Legendre polynomials of the argument $x = \boldsymbol{k}'_{2\mathrm{cm}} \cdot \boldsymbol{k}_{2\mathrm{cm}}/(k'_{2\mathrm{cm}} k_{2\mathrm{cm}})$. The photoproduction multipoles with the corresponding angular momentum configurations are listed in Table 4.2.

Applying the isospin decomposition of the photoproduction amplitude given by Eq. (4.15)

Table 4.2: Multipole components of the pion photoproduction amplitude. The columns j and P indicate the total angular moment and parity of the initial and final states of the system.

Photon J	Photon Multipole	Total j	Total P	Pion l	Multipole amplitude
1	$E1$	1/2	−	0	E_{0+}
		3/2	−	2	E_{2-}
	$M1$	1/2	+	1	M_{1-}
		3/2	+	1	M_{1+}
2	$E2$	3/2	+	1	E_{1+}
		5/2	+	3	E_{3-}
	$M2$	3/2	−	2	M_{2-}
		5/2	−	2	M_{2+}
3	$E3$	5/2	−	2	E_{2+}
		7/2	−	4	E_{4-}
	$M3$	5/2	+	3	M_{3-}
		7/2	+	3	M_{3+}
...	...	...	...	...	...

to the four physical photoproduction processes results in the following relations

$$A(\gamma p \to \pi^0 p) = +A^0 + \frac{1}{3}A^{1/2} + \frac{2}{3}A^{3/2} = A^+ + A^0, \tag{4.42a}$$

$$A(\gamma n \to \pi^0 n) = -A^0 + \frac{1}{3}A^{1/2} + \frac{2}{3}A^{3/2} = A^+ - A^0, \tag{4.42b}$$

$$A(\gamma p \to \pi^+ n) = \sqrt{2}(A^0 + \frac{1}{3}A^{1/2} - \frac{1}{3}A^{3/2}) = +\sqrt{2}(A^- + A^0), \tag{4.42c}$$

$$A(\gamma n \to \pi^- p) = \sqrt{2}(A^0 - \frac{1}{3}A^{1/2} + \frac{1}{3}A^{3/2}) = -\sqrt{2}(A^- - A^0). \tag{4.42d}$$

As a result of the isospin decomposition, the four photoproduction multipoles per pion partial wave ($E_{l\pm}$ and $M_{l\pm}$) are split in twelve amplitudes for each pion angular momentum l: $E^0_{l\pm}$, $E^{1/2}_{l\pm}$, $E^{3/2}_{l\pm}$, $M^0_{l\pm}$, $M^{1/2}_{l\pm}$, $M^{3/2}_{l\pm}$. For each value of the total angular momentum j, these twelve amplitudes can be categorized based on their isospin T and orbital angular momentum l values:

$$\begin{aligned}
&l = j - 1/2,\ T = 1/2: && E^0_{l+},\ E^{1/2}_{l+},\ M^0_{l+},\ M^{1/2}_{l+}\\
&l = j - 1/2,\ T = 3/2: && E^{3/2}_{l+},\ M^{3/2}_{l+}\\
&l = j + 1/2,\ T = 1/2: && E^0_{l-},\ E^{1/2}_{l-},\ M^0_{l-},\ M^{1/2}_{l-}\\
&l = j + 1/2,\ T = 3/2: && E^{3/2}_{l-},\ M^{3/2}_{l-},
\end{aligned}$$

where each group has the same final pion-nucleon state and consistently the same phase.

4.B In-medium modification of $E_{1+}^{3/2}$

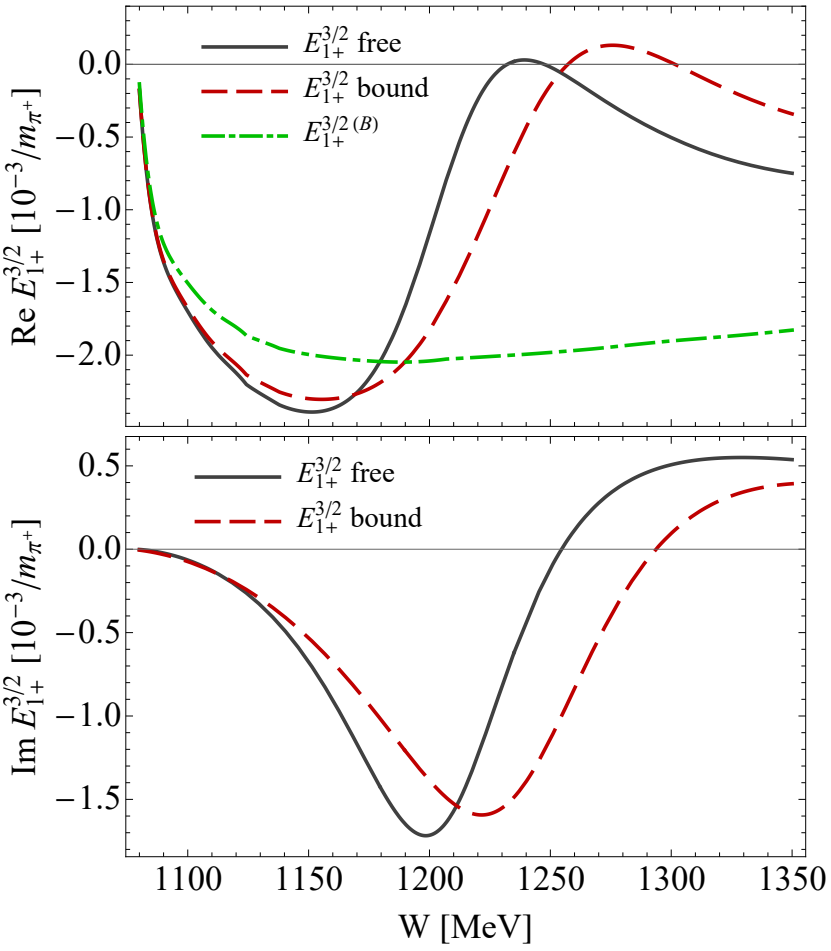

Figure 4.15: The real and imaginary parts of the $E_{1+}^{3/2}$ multipole. The meaning of the curves and markers is the same as in Fig. 4.4.

The formalism outlined in Sections 4.2.2 and 4.2.3 can also be directly applied to the $\Delta(1232)$ electric quadrupole $E_{1+}^{3/2}$, which is numerically in the percent range as compared to the dominant magnetic dipole. By utilizing parameter $\bar{E}_{3/2} \approx -0.017\,\mathrm{GeV}^{-1/2}$ (in place of $\bar{M}_{3/2}$) and setting $n = 1$ in Eqs. (4.19) and (4.21a), respectively, we reproduce the free-space resonant part of $E_{1+}^{3/2}$ as given by the MAID98 model. Employing identical procedures as those for $M_{1+}^{3/2}$, we obtain the in-medium modification for $E_{1+}^{3/2}$. Finally, in Fig. 4.15, we demonstrate the resulting $E_{1+}^{3/2}$ in the nuclear medium along with its free-space counterpart.

Despite the significant change in the amplitude depicted in the plot, its in-medium modification has a negligible effect on the observables. For coherent photoproduction, the contribution of $E_{1+}^{3/2}$ is confined to a second-order correction, Eq. (4.38), resulting in a shift of less than 1% in the cross sections. For the same reason, the in-medium modification of $E_{0+}^{\pm}$ can also be neglected, which we have also verified by computations.

4.C The s-wave part of the pion-^{40}Ca scattering potential

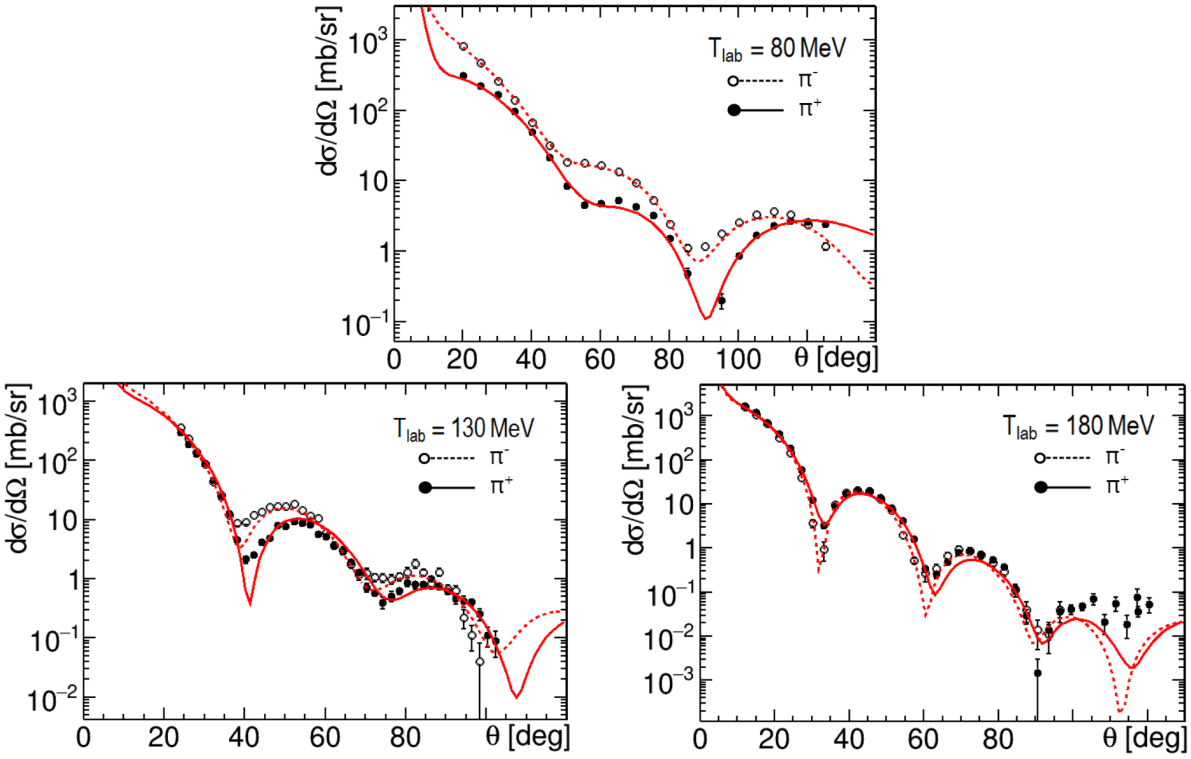

Figure 4.16: The differential cross section for $\pi^{\pm}$-^{40}Ca elastic scattering. Solid curves and closed markers stand for π^+; dashed and open markers for π^-. The experimental data are from Refs. [264] (80 MeV) and [265] (130, 180 MeV).

In this Appendix, we aim to further improve upon the accuracy and reliability of the pion-^{40}Ca scattering amplitude. This is motivated by the well-established sensitivity of the photoproduction process within the Δ-resonance energy region to the nuclear scattering amplitude. To achieve this improvement, we slightly modify the s-wave part of the potential and fit it to the measured differential cross sections for $\pi^{\pm}$-^{40}Ca elastic scattering. In the present calculation for ^{40}Ca, we minimally extend the s-wave part of the potential by assuming

$$\Delta b_0(k) = \beta + i(\mathrm{Im}\,\Delta b_0(0) + \alpha\, k). \tag{4.43}$$

The parameters α and β are fitted to the $\pi^{\pm}$-^{40}Ca scattering data from Refs. [264, 265] within the 80–180 MeV energy range. The resulting values of the parameters are $\alpha = 0.004(9)\,\mathrm{fm}^2$ and $\beta = -0.048(4)\,\mathrm{fm}$.

In Fig. 4.16, we compare the data with the obtained theoretical fitted curves. As a result of the fit, we obtained better agreement at 80 MeV pion laboratory kinetic energy, while the plots for 130 and 180 MeV show almost identical behavior to our previous results. This reconfirms the low sensitivity to the s-wave part of the potential within the considered energy range. For the same reason, introducing additional s-wave parameters does not improve our model agreement with the data within the Δ-resonance energy region.

Chapter 5

Summary and outlook

In this thesis, we presented a novel unified theoretical framework for nuclear pion scattering and photoproduction processes, consistently incorporating in-medium effects and final-state interaction. By constructing the second-order momentum-space potentials for $\pi^{\pm}$ scattering and π^0 photoproduction on spin-isospin-zero nuclei, we have achieved a comprehensive description of intermediate pion-nucleon charge exchange and nucleon spin flip.

The nuclear pion scattering and photoproduction potentials are based on the elementary amplitudes extracted from SAID and MAID, respectively. Nuclear-medium effects were incorporated in the complex effective Δ self-energy Σ_Δ modifying the resonant spin-isospin-3/2 p-wave channel. The value of Σ_Δ was determined from the best fit to $\pi^{\pm}$-^{12}C scattering data within the energy range of 80–180 MeV pion laboratory kinetic energy. Utilizing this fixed value of Σ_Δ without further adjustment, our model successfully reproduced experimental data for $\pi^{\pm}$ scattering on ^{16}O, ^{28}Si, and ^{40}Ca, as well as data for coherent π^0 photoproduction on ^{12}C and ^{40}Ca. The achieved agreement between our predictions and the data underscores the robustness and universality of the proposed approach, suggesting its broad applicability.

The cornerstone of the presented approach lies in our treatment of the second-order rescattering dynamics. Specifically, the second-order parts of the developed scattering and photoproduction potentials describe pion rescattering on a nucleon with an excited intermediate nuclear state. In particular, the final-state charge exchange and nucleon spin-flip are encompassed in strict accordance with the Pauli exclusion principle.

Using the developed potential, we successfully described pion-nucleus scattering with only three energy-independent model parameters determined by the fitting procedure. The presented approach successfully describes the total, angle-integrated elastic, reaction, and differential elastic cross-section for pion scattering data on light and medium-heavy nuclei. Reasonable agreement with experimental data was achieved not only within the fitted energy range but also beyond it.

The considered second-order pion rescattering was demonstrated to provide a significant contribution of approximately 10% to the predicted cross sections for nuclear coherent pion photoproduction in the Δ-resonance energy region. This underscores the importance of second-order rescattering dynamics in achieving a precise alignment between theoretical predictions and experimental data for nuclear pion photoproduction while maintaining a minimal number of model parameters.

In summary, the presented work represents an advancement in our understanding of of nuclear pion coherent photoproduction and scattering, offering a comprehensive theoretical framework and clearing the way for further understanding of complex nuclear

reactions. Next we offer insights into promising directions for future research.

Effect of short-range correlations

In the present study, the second-order parts of the potentials were computed using two-body correlation functions derived from the harmonic oscillator nuclear shell model. While the shell model provides a reasonable description of nucleon long-range correlations, it falls short in correctly capturing short-range correlations. However, the obtained good agreement with the experimental data suggests that either the effect of short-range correlations is minimal or it is effectively absorbed in fitted model parameters. Notably, the developed framework does not rely on any specific form of the correlation function, thus offering flexibility in incorporating more realistic ones. To comprehensively explore the influence of short-range correlations, we work on an analysis of pion scattering on ^{4}He and ^{12}C, employing the two-body densities derived from a chiral effective field theory perspective via variational Monte Carlo calculations [200, 201]. This analysis will help to understand the role of the short-range correlations in pion rescattering, further improving the accuracy of our model.

Neutron skin of heavy nuclei

The preliminary results obtained for ^{208}Pb illustrate the potential for expanding the application of our approach. In future research, we aim to further improve our model for pion scattering and photoproduction on heavy nuclei. The equations outlined in this thesis for isospin-zero nuclei can be readily adapted to accommodate nuclei with non-zero isospin. The analysis of photoproduction presented here has been limited due to the existing disagreement between available data. However, forthcoming high-precision data for coherent π^0 photoproduction on ^{40}Ca and ^{48}Ca by the A2 collaboration [328, 329] offer significant promise. These measurements will allow for a more precise determination of model parameters and estimation of realistic theoretical uncertainties. In perspective, the presented model can be applied to tin isotopes ^{116,120,124}Sn, for which coherent photoproduction has been measured at MAMI [279], and to scrutinize the result obtained for ^{208}Pb [65].

Pion production in neutrino-nucleus scattering

The described approach is promising for analyzing neutrino-induced nuclear pion production. Accurate accounting for the pion-nucleus final-state interaction is crucial for the accurate reconstruction of the neutrino energy. Thus, our scattering model has the potential to contribute to the long-baseline neutrino scattering program, which aims at a better extraction of neutrino oscillation parameters. Additionally, upon incorporating the axial-vector current component, our framework can be extended to encompass coherent pion production in neutrino-nucleus collisions. This process is particularly relevant to long-baseline neutrino projects, generating a significant background contribution with large uncertainty.

True pion absorption

Nuclear pion absorption holds particular importance for T2K [132] and future Hyper-Kamiokande [133] neutrino oscillation analyses that select events with no pion in the final state. In our approach, the rescattering involving excited nuclear states is explicitly separated into the second-order part of the potential. As a result, the imaginary part of Σ_Δ directly characterizes true pion absorption by the nucleus. Our forthcoming research plans to delve into investigating pion absorption. Comparing our predictions with available experimental data, including recent measurements on ^{12}C by the DUET collaboration at TRIUMF [205, 330], could serve as a reliability test of our approach. This analysis will not only provide meaningful constraints on the strongly correlated model parameters, $\mathrm{Re}\,\Sigma_\Delta$ and $\mathrm{Im}\,\Sigma_\Delta$, but will also provide the theoretical error estimate associated with the absorption process.

Low-energy pion scattering and pionic atoms

Another possible extension of the presented model lies in the domain of low energies, which is notably sensitive to final-state charge exchange [101, 125, 230]. In this work, our primal focus was on the Δ-resonance energy region. In this regard, the s-wave pion scattering has been treated using simplified approximations utilizing the results of pionic atom analyses [228]. To accurately describe pion-nucleus interaction at lower energies, more sophisticated modeling is necessary to account for in-medium modifications of s-wave scattering parameters. Additionally, the inclusion of excited states in the nuclear propagator is required. Subsequently, the updated model, covering low-energy interactions, could find an application in modern pionic atom experiments, which investigate chiral symmetry restoration at higher matter density.

Bibliography

[1] V. Tsaran, "Coherent pion photoproduction on spin-zero nuclei", EPJ Web Conf. **274**, 07005 (2022).

[2] F. Colomer, P. Capel, M. Ferretti, J. Piekarewicz, C. Sfienti, M. Thiel, V. Tsaran, and M. Vanderhaeghen, "Theoretical analysis of the extraction of neutron skin thickness from coherent π^0 photoproduction off nuclei", Phys. Rev. C **106**, 044318 (2022), arXiv:2204.13395 [nucl-th].

[3] V. Tsaran and M. Vanderhaeghen, "Momentum-space second-order pion-nucleus potential including medium effects in the $\Delta(1232)$ region", Phys. Rev. C **108**, 044608 (2023), arXiv:2306.04913 [nucl-th].

[4] V. Tsaran and M. Vanderhaeghen, "Nuclear coherent π^0 photoproduction with charge-exchange and spin-flip rescattering", (2024), arXiv:2403.08608 [nucl-th].

[5] R. L. Workman et al., "Review of Particle Physics", PTEP **2022**, 083C01 (2022).

[6] R. Hofstadter, "Electron scattering and nuclear structure", Rev. Mod. Phys. **28**, 214–254 (1956).

[7] H. De Vries, C. De Jager, and C. De Vries, "Nuclear charge and magnetization density distribution parameters from elastic electron scattering", Atom. Data Nucl. Data Tabl. **36**, 495–536 (1987).

[8] G. Fricke, C. Bernhardt, K. Heilig, L. A. Schaller, L. Schellenberg, E. B. Shera, and C. W. de Jager, "Nuclear Ground State Charge Radii from Electromagnetic Interactions", Atom. Data Nucl. Data Tabl. **60**, 177–285 (1995).

[9] I. Angeli and K. Marinova, "Table of experimental nuclear ground state charge radii: An update", Atom. Data Nucl. Data Tabl. **99**, 69–95 (2013).

[10] G. Giacalone, G. Nijs, and W. van der Schee, "Determination of the Neutron Skin of ^{208}Pb from Ultrarelativistic Nuclear Collisions", Phys. Rev. Lett. **131**, 202302 (2023), arXiv:2305.00015 [nucl-th].

[11] B. Klos et al., "Neutron density distributions from antiprotonic ^{208}Pb and ^{209}Bi atoms", Phys. Rev. C **76**, 014311 (2007), arXiv:nucl-ex/0702016.

[12] J. Zenihiro et al., "Neutron density distributions of ^{204,206,208}Pb deduced via proton elastic scattering at E_p=295 MeV", Phys. Rev. C **82**, 044611 (2010).

[13] J. Piekarewicz and S. P Weppner, "Insensitivity of the elastic proton-nucleus reaction to the neutron radius of ^{208}Pb", Nucl. Phys. A **778**, 10–21 (2006), arXiv:nucl-th/0509019.

[14] F. J. Fattoyev, C. J. Horowitz, J. Piekarewicz, and G. Shen, "Relativistic effective interaction for nuclei, giant resonances, and neutron stars", Phys. Rev. C **82**, 055803 (2010), arXiv:1008.3030 [nucl-th].

[15] G. A. Lalazissis, J. Konig, and P. Ring, "A New parametrization for the Lagrangian density of relativistic mean field theory", Phys. Rev. C **55**, 540–543 (1997), arXiv:nucl-th/9607039.

[16] B. G. Todd-Rutel and J. Piekarewicz, "Neutron-Rich Nuclei and Neutron Stars: A New Accurately Calibrated Interaction for the Study of Neutron-Rich Matter", Phys. Rev. Lett. **95**, 122501 (2005), arXiv:nucl-th/0504034.

[17] H. Mueller and B. D. Serot, "Relativistic mean field theory and the high density nuclear equation of state", Nucl. Phys. A **606**, 508–537 (1996), arXiv:nucl-th/9603037.

[18] C. J. Horowitz and J. Piekarewicz, "Neutron star structure and the neutron radius of ^{208}Pb", Phys. Rev. Lett. **86**, 5647 (2001), arXiv:astro-ph/0010227.

[19] X. Roca-Maza, M. Centelles, X. Vinas, and M. Warda, "Neutron skin of ^{208}Pb, nuclear symmetry energy, and the parity radius experiment", Phys. Rev. Lett. **106**, 252501 (2011), arXiv:1103.1762 [nucl-th].

[20] M. Thiel, C. Sfienti, J. Piekarewicz, C. J. Horowitz, and M. Vanderhaeghen, "Neutron skins of atomic nuclei: per aspera ad astra", J. Phys. G **46**, 093003 (2019), arXiv:1904.12269 [nucl-ex].

[21] D. Adhikari et al., "Precision Determination of the Neutral Weak Form Factor of ^{48}Ca", Phys. Rev. Lett. **129**, 042501 (2022), arXiv:2205.11593 [nucl-ex].

[22] D. Adhikari et al., "Accurate Determination of the Neutron Skin Thickness of ^{208}Pb through Parity-Violation in Electron Scattering", Phys. Rev. Lett. **126**, 172502 (2021), arXiv:2102.10767 [nucl-ex].

[23] T. W. Donnelly, J. Dubach, and I. Sick, "Isospin Dependences in Parity Violating Electron Scattering", Nucl. Phys. A **503**, 589–631 (1989).

[24] C. J. Horowitz, S. J. Pollock, P. A. Souder, and R. Michaels, "Parity violating measurements of neutron densities", Phys. Rev. C **63**, 025501 (2001), arXiv:nucl-th/9912038.

[25] C. J. Horowitz et al., "Weak charge form factor and radius of 208Pb through parity violation in electron scattering", Phys. Rev. C **85**, 032501 (2012), arXiv:1202.1468 [nucl-ex].

[26] B. Hu et al., "Ab initio predictions link the neutron skin of ^{208}Pb to nuclear forces", Nature Phys. **18**, 1196–1200 (2022), arXiv:2112.01125 [nucl-th].

[27] M. C. Atkinson, M. H. Mahzoon, M. A. Keim, B. A. Bordelon, C. D. Pruitt, R. J. Charity, and W. H. Dickhoff, "Dispersive optical model analysis of ^{208}Pb generating a neutron-skin prediction beyond the mean field", Phys. Rev. C **101**, 044303 (2020), arXiv:1911.09020 [nucl-th].

[28] J. Piekarewicz and M. Centelles, "Incompressibility of neutron-rich matter", Phys. Rev. C **79**, 054311 (2009), arXiv:0812.4499 [nucl-th].

[29] G. Gamow, "Mass defect curve and nuclear constitution", Proceedings of the Royal Society of London. Series A, Containing Papers of a Mathematical and Physical Character **126**, 632–644 (1930).

[30] H. A. Bethe and R. F. Bacher, "Nuclear Physics A. Stationary States of Nuclei", Rev. Mod. Phys. **8**, 82–229 (1936).

[31] C. F. V. Weizsacker, "Zur Theorie der Kernmassen", Z. Phys. **96**, 431–458 (1935).

[32] B. A. Brown, "Neutron radii in nuclei and the neutron equation of state", Phys. Rev. Lett. **85**, 5296–5299 (2000).

[33] M. Centelles, X. Roca-Maza, X. Vinas, and M. Warda, "Nuclear symmetry energy probed by neutron skin thickness of nuclei", Phys. Rev. Lett. **102**, 122502 (2009), arXiv:0806.2886 [nucl-th].

[34] J. M. Lattimer, "Constraints on Nuclear Symmetry Energy Parameters", Particles **6**, 30–56 (2023), arXiv:2301.03666 [nucl-th].

[35] S. Tagami, T. Wakasa, M. Takechi, J. Matsui, and M. Yahiro, "Neutron skin in ^{48}Ca determined from p+^{48}Ca and ^{48}Ca+^{12}C scattering", 10.48550/arXiv.2201.08541 (2022), arXiv:2201.08541 [nucl-th].

[36] B. A. Brown, "Mirror Charge Radii and the Neutron Equation of State", Phys. Rev. Lett. **119**, 122502 (2017).

[37] C. J. Horowitz, K. S. Kumar, and R. Michaels, "Electroweak Measurements of Neutron Densities in CREX and PREX at JLab, USA", Eur. Phys. J. A **50**, 48 (2014), arXiv:1307.3572 [nucl-ex].

[38] J. Piekarewicz, B. K. Agrawal, G. Colo, W. Nazarewicz, N. Paar, P. G. Reinhard, X. Roca-Maza, and D. Vretenar, "Electric dipole polarizability and the neutron skin", Phys. Rev. C **85**, 041302 (2012), arXiv:1201.3807 [nucl-th].

[39] G. Raaijmakers, S. K. Greif, K. Hebeler, T. Hinderer, S. Nissanke, A. Schwenk, T. E. Riley, A. L. Watts, J. M. Lattimer, and W. C. G. Ho, "Constraints on the Dense Matter Equation of State and Neutron Star Properties from NICER's Mass–Radius Estimate of PSR J0740+6620 and Multimessenger Observations", Astrophys. J. Lett. **918**, L29 (2021), arXiv:2105.06981 [astro-ph.HE].

[40] M. C. Miller et al., "PSR J0030+0451 Mass and Radius from *NICER* Data and Implications for the Properties of Neutron Star Matter", Astrophys. J. Lett. **887**, L24 (2019), arXiv:1912.05705 [astro-ph.HE].

[41] T. E. Riley et al., "A *NICER* View of PSR J0030+0451: Millisecond Pulsar Parameter Estimation", Astrophys. J. Lett. **887**, L21 (2019), arXiv:1912.05702 [astro-ph.HE].

[42] M. C. Miller et al., "The Radius of PSR J0740+6620 from NICER and XMM-Newton Data", Astrophys. J. Lett. **918**, L28 (2021), arXiv:2105.06979 [astro-ph.HE].

[43] J. M. Lattimer and M. Prakash, "Neutron Star Observations: Prognosis for Equation of State Constraints", Phys. Rept. **442**, 109–165 (2007), arXiv:astro-ph/0612440.

[44] J. Carriere, C. J. Horowitz, and J. Piekarewicz, "Low mass neutron stars and the equation of state of dense matter", Astrophys. J. **593**, 463–471 (2003), arXiv:nucl-th/0211015.

[45] W.-C. Chen and J. Piekarewicz, "Building relativistic mean field models for finite nuclei and neutron stars", Phys. Rev. C **90**, 044305 (2014), arXiv:1408.4159 [nucl-th].

[46] C. J. Horowitz and J. Piekarewicz, "The Neutron radii of ^{208}Pb and neutron stars", Phys. Rev. C **64**, 062802 (2001), arXiv:nucl-th/0108036.

[47] F. J. Fattoyev, J. Piekarewicz, and C. J. Horowitz, "Neutron Skins and Neutron Stars in the Multimessenger Era", Phys. Rev. Lett. **120**, 172702 (2018), arXiv:1711.06615 [nucl-th].

[48] B. T. Reed, F. J. Fattoyev, C. J. Horowitz, and J. Piekarewicz, "Implications of PREX-2 on the Equation of State of Neutron-Rich Matter", Phys. Rev. Lett. **126**, 172503 (2021), arXiv:2101.03193 [nucl-th].

[49] P.-G. Reinhard, X. Roca-Maza, and W. Nazarewicz, "Information Content of the Parity-Violating Asymmetry in ^{208}Pb", Phys. Rev. Lett. **127**, 232501 (2021), arXiv:2105.15050 [nucl-th].

[50] B. P. Abbott et al., "GW170817: Observation of Gravitational Waves from a Binary Neutron Star Inspiral", Phys. Rev. Lett. **119**, 161101 (2017), arXiv:1710.05832 [gr-qc].

[51] X. Roca-Maza, X. Viñas, M. Centelles, B. K. Agrawal, G. Colo', N. Paar, J. Piekarewicz, and D. Vretenar, "The neutron skin thickness from the measured electric dipole polarizability in ^{68}Ni, ^{120}Sn, and ^{208}Pb", Phys. Rev. C **92**, 064304 (2015), arXiv:1510.01874 [nucl-th].

[52] A. Tamii et al., "Complete electric dipole response and the neutron skin in ^{208}Pb", Phys. Rev. Lett. **107**, 062502 (2011), arXiv:1104.5431 [nucl-ex].

[53] A. W. Steiner, M. Prakash, J. M. Lattimer, and P. J. Ellis, "Isospin asymmetry in nuclei and neutron stars", Phys. Rept. **411**, 325–375 (2005), arXiv:nucl-th/0410066.

[54] J. Xu, L.-W. Chen, B.-A. Li, and H.-R. Ma, "Nuclear constraints on properties of neutron star crusts", Astrophys. J. **697**, 1549–1568 (2009), arXiv:0901.2309 [astro-ph.SR].

[55] A. W. Steiner, J. M. Lattimer, and E. F. Brown, "The Equation of State from Observed Masses and Radii of Neutron Stars", Astrophys. J. **722**, 33–54 (2010), arXiv:1005.0811 [astro-ph.HE].

[56] G. Hagen et al., "Neutron and weak-charge distributions of the ^{48}Ca nucleus", Nature Phys. **12**, 186–190 (2015), arXiv:1509.07169 [nucl-th].

[57] M. B. Tsang et al., "Constraints on the symmetry energy and neutron skins from experiments and theory", Phys. Rev. C **86**, 015803 (2012), arXiv:1204.0466 [nucl-ex].

[58] C. Drischler, R. J. Furnstahl, J. A. Melendez, and D. R. Phillips, "How Well Do We Know the Neutron-Matter Equation of State at the Densities Inside Neutron Stars? A Bayesian Approach with Correlated Uncertainties", Phys. Rev. Lett. **125**, 202702 (2020), arXiv:2004.07232 [nucl-th].

[59] D.-H. Wen, B.-A. Li, and L.-W. Chen, "Super-soft symmetry energy encountering non-Newtonian gravity in neutron stars", Phys. Rev. Lett. **103**, 211102 (2009), arXiv:0908.1922 [nucl-th].

[60] S. J. Pollock and M. C. Welliver, "Effects of neutron spatial distributions on atomic parity nonconservation in cesium", Phys. Lett. B **464**, 177–182 (1999), arXiv:nucl-th/9904062.

[61] A. Carbone, G. Colo, A. Bracco, L.-G. Cao, P. F. Bortignon, F. Camera, and O. Wieland, "Constraints on the symmetry energy and on neutron skins from the pygmy resonances in ^{68}Ni and ^{132}Sn", Phys. Rev. C **81**, 041301 (2010), arXiv:1003.3580 [nucl-th].

[62] L.-W. Chen, C. M. Ko, B.-A. Li, and J. Xu, "Density slope of the nuclear symmetry energy from the neutron skin thickness of heavy nuclei", Phys. Rev. C **82**, 024321 (2010), arXiv:1004.4672 [nucl-th].

[63] B.-A. Li, L.-W. Chen, and C. M. Ko, "Recent Progress and New Challenges in Isospin Physics with Heavy-Ion Reactions", Phys. Rept. **464**, 113–281 (2008), arXiv:0804.3580 [nucl-th].

[64] M. B. Tsang, Y. Zhang, P. Danielewicz, M. Famiano, Z. Li, W. G. Lynch, and A. W. Steiner, "Constraints on the density dependence of the symmetry energy", Phys. Rev. Lett. **102**, 122701 (2009), arXiv:0811.3107 [nucl-ex].

[65] C. M. Tarbert et al., "Neutron skin of ^{208}Pb from Coherent Pion Photoproduction", Phys. Rev. Lett. **112**, 242502 (2014), arXiv:1311.0168 [nucl-ex].

[66] J. E. Leiss and R. A. Schrack, "Nuclear matter distributions from coherent neutral pion production", Rev. Mod. Phys., 10.1103/RevModPhys.30.456.

[67] R. A. Schrack, J. E. Leiss, and S. Penner, "Neutral Meson Photoproduction from Complex Nuclei", Phys. Rev. **127**, 1772–1783 (1962).

[68] P. Adlarson et al., "Measurement of π^0 photoproduction on the proton at MAMI C", Phys. Rev. C **92**, 024617 (2015), arXiv:1506.08849 [hep-ex].

[69] A. Gardestig, C. J. Horowitz, and G. A. Miller, "Comment on "Neutron Skin of ^{208}Pb from Coherent Pion Photoproduction"", (2015), arXiv:1504.08347 [nucl-th].

[70] G. A. Miller, "Coherent-Nuclear Pion Photoproduction and Neutron Radii", Phys. Rev. C **100**, 044608 (2019), arXiv:1907.11764 [nucl-th].

[71] A. A. Chumbalov, R. A. Eramzhian, and S. S. Kamalov, "Dwia in the Momentum Space for (γ, π^0) Reaction Near Threshold", Z. Phys. A **328**, 195 (1987).

[72] B. Krusche, J. Ahrens, R. Beck, S. Kamalov, V. Metag, R. O. Owens, and H. Stroher, "Coherent π^0 photoproduction from atomic nuclei", Phys. Lett. B **526**, 287–294 (2002), arXiv:nucl-ex/0304006.

[73] D Drechsel, S. Kamalov, and L Tiator, "Unitary isobar model–MAID2007", The European Physical Journal A **34**, 69 (2007).

[74] B. Krusche, "Nuclear mass form-factors from coherent photoproduction of π^0 mesons", Eur. Phys. J. A **26**, 7–18 (2005), arXiv:nucl-ex/0509003.

[75] D. Drechsel, L. Tiator, S. S. Kamalov, and S. N. Yang, "Medium effects in coherent pion photoproduction and electroproduction on ^{4}He and ^{12}C", Nucl. Phys. A **660**, 423–438 (1999), arXiv:nucl-th/9906019.

[76] L. M. Saunders, "Electromagnetic production of pions from nuclei", Nucl. Phys. B **7**, 293–310 (1968).

[77] V. Girija, V. Devanathan, A. Nagl, and H. Uberall, "Coherent pion photoproduction", Phys. Rev. C **27**, 1169–1174 (1983).

[78] R. A. Eramzhian, M. Gmitro, S. S. Kamalov, and R. Mach, "Nuclear pion photoproduction: a theory and the ^{16}O $(\gamma,\pi^+)^{16}$N (bound) example", J. Phys. G **9**, 605–619 (1983).

[79] S. S. Kamalov and T. D. Kaipov, "On the contradictory situation in coherent ^{12}C(γ,π^0) and ^{4}He(γ,π^0) reactions", Phys. Lett. B **162**, 260–264 (1985).

[80] F. Rambo et al., "Coherent π^0 photoproduction from ^{4}He", Nucl. Phys. A **660**, 69–83 (1999), arXiv:nucl-ex/9907020.

[81] G. Cattapan and L. S. Ferreira, "The role of the Δ in nuclear physics", Phys. Rept. **362**, 303–407 (2002).

[82] V. Pascalutsa, M. Vanderhaeghen, and S. N. Yang, "Electromagnetic excitation of the $\Delta(1232)$-resonance", Phys. Rept. **437**, 125–232 (2007), arXiv:hep-ph/0609004.

[83] G. Brown and W. Weise, "Pion Scattering and Isobars in Nuclei", Phys. Rept. **22**, 279–337 (1975).

[84] S. Boffi, L. Bracci, and P. Christillin, "Coherent $(\gamma,\ \pi^0)$ on nuclei", Nuovo Cim. A **104**, 843–854 (1991).

[85] J. Nieves, E. Oset, and C. Garcia-Recio, "Many body approach to low-energy pion nucleus scattering", Nucl. Phys. A **554**, 554–579 (1993).

[86] M. Hjorth-Jensen, H. Muther, and A. Polls, "Width of the Δ resonance in nuclei", Phys. Rev. C **50**, 501–504 (1994), arXiv:nucl-th/9309019.

[87] M. Hirata, F. Lenz, and K. Yazaki, "Excitation of Δ Nuclear States in π-^{4}He Scattering", Annals Phys. **108**, 116–164 (1977).

[88] Y. Horikawa, M. Thies, and F. Lenz, "The Δ-nucleus spin-orbit interaction in π-nucleus scattering", Nucl. Phys. A **345**, 386–408 (1980).

[89] E. Oset and W. Weise, "Isobar hole description of pion elastic scattering and the pion-nuclear many body problem", Nucl. Phys. A **319**, 477–517 (1979).

[90] E. Oset and L. L. Salcedo, "Δ Selfenergy in Nuclear Matter", Nucl. Phys. A **468**, 631–652 (1987).

[91] J. H. Koch and E. J. Moniz, "Coherent π^0 photoproduction in the isobar-hole formalism", Phys. Rev. C **20**, 235–241 (1979).

[92] J. H. Koch and E. J. Moniz, "Ccoherent π^0 photoproduction at intermediate-energy", Phys. Rev. C **27**, 751–764 (1983).

[93] R. C. Carrasco and E. Oset, "Interaction of Real Photons With Nuclei From 100 to 500 MeV", Nucl. Phys. A **536**, 445–508 (1992).

[94] T. Takaki, T. Suzuki, and J. H. Koch, "Photoproduction of neutral pions to discrete nuclear states", Nucl. Phys. A **443**, 570–588 (1985).

[95] C. M. Tarbert, "Coherent π^0 photoproduction on nuclei", PhD thesis (Edinburgh U., 2007).

[96] L. Tiator and L. E. Wright, "Delta resonance and nonlocal effects in pion photoproduction from nuclei", Phys. Rev. C **30**, 989 (1984).

[97] K. M. Watson, "Multiple Scattering and the Many-Body Problem-Applications to Photomeson Production in Complex Nuclei", Phys. Rev. **89**, 575–587 (1953).

[98] A. K. Kerman, H. McManus, and R. M. Thaler, "The Scattering of fast nucleons from nuclei", Annals Phys. **8**, 551–635 (1959).

[99] B. Lippmann and J. Schwinger, "Variational Principles for Scattering Processes. I", Phys. Rev. **79**, 469–480 (1950).

[100] L. Kisslinger, "Scattering of Mesons by Light Nuclei", Phys. Rev. **98**, 761–765 (1955).

[101] M. Ericson and T. E. O. Ericson, "Optical properties of low-energy pions in nuclei", Annals Phys. **36**, 323–362 (1966).

[102] J. Eisenberg, "Beyond Lowest Order Results in Pion-Nucleus Reactions", NATO Sci. Ser. B **45**, 551–594 (1979).

[103] M. B. Johnson and D. J. Ernst, "Meson nucleus dynamics", Annals Phys. **219**, 266–327 (1992).

[104] R. H. Landau, S. C. Phatak, and F. Tabakin, "Improved theoretical pion-nucleus optical potentials", Annals Phys. **78**, 299–339 (1973).

[105] R. Landau and A. W. Thomas, "A Theory of Low-Energy Pion-Nucleus Scattering", Nucl. Phys. A **302**, 461–492 (1978).

[106] M. Gmitro, J. Kvasil, and R. Mach, "Pion elastic and inelastic scattering on s d shell nuclei in the $\Delta(33)$ resonance region. coupled channel analysis", Phys. Rev. C **31**, 1349–1359 (1985).

[107] J. A. Carr, H. McManus, and K. Stricker-Bauer, "Nuclear absorption of low energy pions and the pion-nucleus optical potential", Phys. Rev. C **25**, 952–961 (1982).

[108] M. Gmitro, S. S. Kamalov, and R. Mach, "Momentum Space Second Order Optical Potential for Pion Nucleus Elastic Scattering", Phys. Rev. C **36**, 1105–1117 (1987).

[109] C. Wilkin, C. R. Cox, J. J. Domingo, K. Gabathuler, E. Pedroni, J. Rohlin, P. Schwaller, and N. W. Tanner, "A comparison of π^+ and π^- total cross-sections of light nuclei near the 3-3 resonance", Nucl. Phys. B **62**, 61–85 (1973).

[110] A. S. Clough et al., "Pion-Nucleus Total Cross-Sections from 88 MeV to 860 MeV", Nucl. Phys. B **76**, 15–28 (1974).

[111] R. Jackle, H. Pilkuhn, and H. G. Schlaile, "Amplitude analysis of elastic pion-nucleus scattering", Phys. Lett. B **76**, 177–181 (1978).

[112] R. h. Jeppesen et al., "Pion nucleus forward scattering amplitudes from total cross-section measurements", Phys. Rev. C **27**, 697–708 (1983).

[113] F. G. Binon, P. Duteil, M. Gouanere, L. Hugon, J. Jansen, J. P. Lagnaux, H. Palevsky, J. P. Peigneux, M. Spighel, and J. P. Stroot, "Scattering of Negative Pions on Helium", Nucl. Phys. A **298**, 499 (1978).

[114] D. Ashery, I. Navon, G. Azuelos, H. K. Walter, H. J. Pfeiffer, and F. W. Schleputz, "True Absorption and Scattering of Pions on Nuclei", Phys. Rev. C **23**, 2173–2185 (1981).

[115] S. Ciulli, H. Pilkuhn, and H. G. Schlaile, "Phase shift analysis of elastic π-^{16}O scattering between 0 MeV and 340 MeV", Z. Phys. A **302**, 45–50 (1981).

[116] E. Oset, Y. Futami, and H. Toki, "Pion Absorption in the Resonance Region", Nucl. Phys. A **448**, 597–636 (1986).

[117] H. J. Weyer, "Pion absorption in light nuclei", Phys. Rept. **195**, 295–367 (1990).

[118] D. Ashery and J. P. Schiffer, "Pion Absorption in Nuclei", Ann. Rev. Nucl. Part. Sci. **36**, 207–252 (1986).

[119] T. E. O. Ericson and W. Weise, *Pions and Nuclei*, Vol. 74 (Clarendon Press, Oxford, UK, 1988).

[120] P. Argan et al., "π^0 photoproduction near threshold on hydrogen, deuterium, ^{3}He, and ^{3}He", Phys. Rev. C **21**, 1416–1425 (1980).

[121] J. M. Laget, "Pion Photoproduction on Few Body Systems", Phys. Rept. **69**, 1–84 (1981).

[122] P. Wilhelm and H. Arenhovel, "Rescattering effects in coherent pion photoproduction on the deuteron in the Δ resonance region", Nucl. Phys. A **609**, 469–487 (1996), arXiv:nucl-th/9606008.

[123] N. Odagawa, T. Sato, and H. Ohtsubo, "Charged pion photoproduction on the p shell nuclei at low-energy and rescattering effect of a pion", Prog. Theor. Phys. **86**, 1277 (1991).

[124] K. Stricker-Bauer, "A study of the pion-nucleus optical potential", PhD thesis (Michigan State University, 1980).

[125] E. Friedman et al., "The In-medium isovector πN amplitude from low energy pion scattering", Phys. Rev. Lett. **93**, 122302 (2004), arXiv:nucl-ex/0404031.

[126] L. Alvarez-Ruso, Y. Hayato, and J. Nieves, "Progress and open questions in the physics of neutrino cross sections at intermediate energies", New J. Phys. **16**, 075015 (2014), arXiv:1403.2673 [hep-ph].

[127] U. Mosel, "Neutrino Interactions with Nucleons and Nuclei: Importance for Long-Baseline Experiments", Ann. Rev. Nucl. Part. Sci. **66**, 171–195 (2016), arXiv:1602.00696 [nucl-th].

[128] T. Katori and M. Martini, "Neutrino–nucleus cross sections for oscillation experiments", J. Phys. G **45**, 013001 (2018), arXiv:1611.07770 [hep-ph].

[129] L. Alvarez-Ruso et al., "NuSTEC White Paper: Status and challenges of neutrino–nucleus scattering", Prog. Part. Nucl. Phys. **100**, 1–68 (2018), arXiv:1706.03621 [hep-ph].

[130] K. Mahn, C. Marshall, and C. Wilkinson, "Progress in Measurements of 0.1–10 GeV Neutrino–Nucleus Scattering and Anticipated Results from Future Experiments", Ann. Rev. Nucl. Part. Sci. **68**, 105–129 (2018), arXiv:1803.08848 [hep-ex].

[131] M. B. Avanzini et al., "Comparisons and challenges of modern neutrino-scattering experiments", Phys. Rev. D **105**, 092004 (2022), arXiv:2112.09194 [hep-ex].

[132] K. Abe et al., "The T2K Experiment", Nucl. Instrum. Meth. A **659**, 106–135 (2011), arXiv:1106.1238 [physics.ins-det].

[133] K. Abe et al., "Hyper-Kamiokande Design Report", (2018), arXiv:1805.04163 [physics.ins-det].

[134] J. A. Formaggio and G. P. Zeller, "From eV to EeV: Neutrino Cross Sections Across Energy Scales", Rev. Mod. Phys. **84**, 1307–1341 (2012), arXiv:1305.7513 [hep-ex].

[135] *Fundamental Physics at the Intensity Frontier* (May 2012), arXiv:1205.2671 [hep-ex].

[136] S. X. Nakamura, T. Sato, T. S. H. Lee, B. Szczerbinska, and K. Kubodera, "Dynamical Model of Coherent Pion Production in Neutrino-Nucleus Scattering", Phys. Rev. C **81**, 035502 (2010), arXiv:0910.1057 [nucl-th].

[137] R. Acciarri et al., "Design and Construction of the MicroBooNE Detector", JINST **12**, P02017 (2017), arXiv:1612.05824 [physics.ins-det].

[138] K. Abe et al., "Physics potential of a long-baseline neutrino oscillation experiment using a J-PARC neutrino beam and Hyper-Kamiokande", PTEP **2015**, 053C02 (2015), arXiv:1502.05199 [hep-ex].

[139] R. Acciarri et al., "Long-Baseline Neutrino Facility (LBNF) and Deep Underground Neutrino Experiment (DUNE): Conceptual Design Report, Volume 1: The LBNF and DUNE Projects", (2016), arXiv:1601.05471 [physics.ins-det].

[140] M. Hasegawa et al., "Search for coherent charged pion production in neutrino-carbon interactions", Phys. Rev. Lett. **95**, 252301 (2005), arXiv:hep-ex/0506008.

[141] K. Hiraide et al., "Search for Charged Current Coherent Pion Production on Carbon in a Few-GeV Neutrino Beam", Phys. Rev. D **78**, 112004 (2008), arXiv:0811.0369 [hep-ex].

[142] A. Higuera et al., "Measurement of Coherent Production of $\pi^{\pm}$ in Neutrino and Antineutrino Beams on Carbon from E_{ν} of 1.5 to 20 GeV", Phys. Rev. Lett. **113**, 261802 (2014), arXiv:1409.3835 [hep-ex].

[143] A. Mislivec et al., "Measurement of total and differential cross sections of neutrino and antineutrino coherent $\pi^{\pm}$ production on carbon", Phys. Rev. D **97**, 032014 (2018), arXiv:1711.01178 [hep-ex].

[144] K. Abe et al., "Measurement of Coherent π^+ Production in Low Energy Neutrino-Carbon Scattering", Phys. Rev. Lett. **117**, 192501 (2016), arXiv:1604.04406 [hep-ex].

[145] K. Abe et al., "Measurements of the $\nu\mu$ and $\nu^{-}\mu$-induced coherent charged pion production cross sections on C12 by the T2K experiment", Phys. Rev. D **108**, 092009 (2023), arXiv:2308.16606 [hep-ex].

[146] P. Adamson et al., "Measurement of single π^0 production by coherent neutral-current ν Fe interactions in the MINOS Near Detector", Phys. Rev. D **94**, 072006 (2016), arXiv:1608.05702 [hep-ex].

[147] M. A. Acero et al., "Measurement of neutrino-induced neutral-current coherent π^0 production in the NOvA near detector", Phys. Rev. D **102**, 012004 (2020), arXiv:1902.00558 [hep-ex].

[148] U. Mosel, "Pion Production in High-Energy Neutrino Reactions with Nuclei", Phys. Rev. C **91**, 065501 (2015), arXiv:1502.08032 [nucl-th].

[149] S. L. Adler, "Tests of the Conserved Vector Current and Partially Conserved Axial-Vector Current Hypotheses in High-Energy Neutrino Reactions", Phys. Rev. **135**, B963–B966 (1964).

[150] S. L. Adler, "Photoproduction, electroproduction and weak single pion production in the (3,3) resonance region", Annals Phys. **50**, 189–311 (1968).

[151] C. Berger and L. M. Sehgal, "PCAC and coherent pion production by low energy neutrinos", Phys. Rev. D **79**, 053003 (2009), arXiv:0812.2653 [hep-ph].

[152] T. Sato, D. Uno, and T. S. H. Lee, "Dynamical model of weak pion production reactions", Phys. Rev. C **67**, 065201 (2003), arXiv:nucl-th/0303050.

[153] L. L. Foldy and J. D. Walecka, "On the theory of the optical potential", Annals Phys. **54**, 447–504 (1969).

[154] H. Feshbach, A. Gal, and J. Huefner, "On high-energy scattering by nuclei – II.", Annals Phys. **66**, 20–59 (1971).

[155] T.-S. H. Lee and S. Chakravarti, "Second Order Pion-Nucleus Optical Potential", Phys. Rev. C **16**, 273–283 (1977).

[156] Z. Ye, J. Arrington, R. J. Hill, and G. Lee, "Proton and Neutron Electromagnetic Form Factors and Uncertainties", Phys. Lett. B **777**, 8–15 (2018), arXiv:1707.09063 [nucl-ex].

[157] P.-O. Lowdin, "Quantum Theory of Many-Particle Systems. 1. Physical Interpretations by Means of Density Matrices, Natural Spin-Orbitals, and Convergence Problems in the Method of Configurational Interaction", Phys. Rev. **97**, 1474–1489 (1955).

[158] R. Jastrow, "Many-Body Problem with Strong Forces", Phys. Rev. **98**, 1479–1484 (1955).

[159] S. S. Dimitrova, D. N. Kadrev, A. N. Antonov, and M. V. Stoitsov, "Two-body density matrix for closed s - d shell nuclei", Eur. Phys. J. A **7**, 335–345 (2000), arXiv:nucl-th/9904071.

[160] R. F. Frosch, R. Hofstadter, J. S. McCarthy, G. K. Noldeke, K. J. van Oostrum, M. R. Yearian, B. C. Clark, R. Herman, and D. G. Ravenhall, "Electron Scattering Studies of Calcium and Titanium Isotopes", Phys. Rev. **174**, 1380–1399 (1968).

[161] R. D. Ehrlich, D. Fryberger, D. A. Jensen, C. Nissim-Sabat, R. J. Powers, V. L. Telegdi, and C. K. Hargrove, "Precise measurements of muonic isotope shifts for 29 nuclides, in particular, for the ca isotopes 40, 42, 44, and 48", Phys. Rev. Lett. **18**, 959–962 (1967).

[162] W. Bertozzi, J. Friar, J. Heisenberg, and J. Negele, "Contributions of neutrons to elastic electron scattering from nuclei", Phys. Lett. B **41**, 408–414 (1972).

[163] J. Borysowicz and J. H. Hetherington, "Errors on Charge Densities Determined from Electron Scattering", Phys. Rev. C **7**, 2293–2303 (1973).

[164] B. Dreher, J. Friedrich, K. Merle, H. Rothhaas, and G. Lührs, "The determination of the nuclear ground state and transition charge density from measured electron scattering data", Nucl. Phys. A **235**, 219–248 (1974).

[165] I. Sick, "Model-independent nuclear charge densities from elastic electron scattering", Nucl. Phys. A **218**, 509–541 (1974).

[166] R. Anni, G. Co, and P. Pellegrino, "Nuclear charge density distributions from elastic electron scattering data", Nucl. Phys. A **584**, 35–59 (1995), arXiv:nucl-th/9410023.

[167] J. L. Friar and J. W. Negele, "The determination of the nuclear charge distribution of ^{208}Pb from elastic electron scattering and muonic x-rays", Nucl. Phys. A **212**, 93–137 (1973).

[168] J. Heisenberg and H. P. Blok, "Inelastic electron scattering from nuclei", Ann. Rev. Nucl. Part. Sci. **33**, 569–609 (1983).

[169] G. Duda, A. Kemper, and P. Gondolo, "Model Independent Form Factors for Spin Independent Neutralino-Nucleon Scattering from Elastic Electron Scattering Data", JCAP **04**, 012 (2007), arXiv:hep-ph/0608035.

[170] A. Antonov, V. Nikolaev, and I. Z. Petkov, "Nucleon momentum and density distributions of nuclei", Z Physik A **297**, 257–260 (1980).

[171] A. N. Antonov, P. E. Hodgson, and I. Z. Petkov, *Nucleon correlations in nuclei* (Springer Science & Business Media, 2012).

[172] A. DeShalit and H. Feshbach, "Theoretical nuclear physics", (1990).

[173] P. Cappellaro, *Introduction to Applied Nuclear Physics* (MIT Course Number 22.02, MIT OpenCourseWare, 2012).

[174] K. L. G. Heyde, "The nuclear shell model", in *The nuclear shell model* (Springer Berlin Heidelberg, Berlin, Heidelberg, 1990), pp. 54–135.

[175] A. Unsöld, "Beiträge zur quantenmechanik der atome", Annalen der Physik **387**, 355–393 (1927).

[176] R. Mach, "The inclusion of the fermi motion in elastic pion-nucleus scattering calculations", Nucl. Phys. A **205**, 56–72 (1973).

[177] D. Weiss and D. Ernst, "Kinematic aspects of pion nucleus elastic scattering", Phys. Rev. C **26**, 605–615 (1982).

[178] R. Mach, "Galileo Invariant Theory of Low-energy Pion - Nucleus Scattering. Part 1.", Czech. J. Phys. B **33**, 549 (1983).

[179] J. Elliott and T. Skyrme, "Centre-of-mass effects in the nuclear shell-model", Proceedings of the Royal Society of London. Series A. Mathematical and Physical Sciences **232**, 561–566 (1955).

[180] L. Tassie and F. Barker, "Application to Electron Scattering of Center-of-Mass Effects in the Nuclear Shell Model", Phys. Rev. **111**, 940–940 (1958).

[181] H. Lipkin, "Center-of-Mass Motion in the Nuclear Shell Model", Phys. Rev. **110**, 1395–1397 (1958).

[182] D. R. Bes and O. Civitarese, "Removal of spurious center-of-mass effects in nuclear many body systems", Phys. Rev. C **63**, 044323 (2001).

[183] S. Gamba, G. Ricco, and G. Rottigni, "A phenomenological woods-saxon potential for p-shell nuclei", Nucl. Phys. A **213**, 383–396 (1973).

[184] F Malaguti, A Uguzzoni, E Verondini, and P. Hodgson, "Nuclear charge distributions", La Rivista del Nuovo Cimento (1978-1999) **5**, 1–67 (1982).

[185] L. Cardman, J. Lightbody, S. Penner, S. Fivozinsky, X. Maruyama, W. Trower, and S. Williamson, "The charge distribution of 12 C", Phys. Lett. B **91**, 203–206 (1980).

[186] C. De Jager, H. De Vries, and C. De Vries, "Nuclear charge and magnetization density distribution parameters from elastic electron scattering", Atom. Data Nucl. Data Tabl. **14**, [Erratum: Atom.Data Nucl.Data Tabl. 16, 580–580 (1975)], 479–508 (1974).

[187] D. F. Jackson and S. Murugesu, "Two nucleon density functions and correlation functions with realistic single particle wavefunctions", Nucl. Phys. A **149**, 261–272 (1970).

[188] K. Gottfried, "The determination of the nuclear pair correlation function and momentum distribution", Annals Phys. **21**, 29–46 (1963).

[189] S. Murugesu, "Optical model potential for pion-nucleus scattering", PhD thesis (University of Surrey, 1971).

[190] O. Hen, G. A. Miller, E. Piasetzky, and L. B. Weinstein, "Nucleon-Nucleon Correlations, Short-lived Excitations, and the Quarks Within", Rev. Mod. Phys. **89**, 045002 (2017), arXiv:1611.09748 [nucl-ex].

[191] A. Tang et al., "n-p short range correlations from $(p, 2p + n)$ measurements", Phys. Rev. Lett. **90**, 042301 (2003), arXiv:nucl-ex/0206003.

[192] E. Piasetzky, M. Sargsian, L. Frankfurt, M. Strikman, and J. W. Watson, "Evidence for the strong dominance of proton-neutron correlations in nuclei", Phys. Rev. Lett. **97**, 162504 (2006), arXiv:nucl-th/0604012.

[193] I. Korover et al., "Probing the Repulsive Core of the Nucleon-Nucleon Interaction via the ^{4}He$(e, e'pN)$ Triple-Coincidence Reaction", Phys. Rev. Lett. **113**, 022501 (2014), arXiv:1401.6138 [nucl-ex].

[194] O. Hen et al., "Momentum sharing in imbalanced Fermi systems", Science **346**, 614–617 (2014), arXiv:1412.0138 [nucl-ex].

[195] M. Duer et al., "Direct Observation of Proton-Neutron Short-Range Correlation Dominance in Heavy Nuclei", Phys. Rev. Lett. **122**, 172502 (2019), arXiv:1810.05343 [nucl-ex].

[196] R. Schiavilla, R. B. Wiringa, S. C. Pieper, and J. Carlson, "Tensor Forces and the Ground-State Structure of Nuclei", Phys. Rev. Lett. **98**, 132501 (2007), arXiv:nucl-th/0611037.

[197] M. Alvioli, C. Ciofi degli Atti, and H. Morita, "Proton-neutron and proton-proton correlations in medium-weight nuclei and the role of the tensor force", Phys. Rev. Lett. **100**, 162503 (2008).

[198] M. Alvioli, C. Ciofi degli Atti, L. P. Kaptari, C. B. Mezzetti, and H. Morita, "Nucleon momentum distributions, their spin-isospin dependence and short-range correlations", Phys. Rev. C **87**, 034603 (2013), arXiv:1211.0134 [nucl-th].

[199] C. Ciofi degli Atti and H. Morita, "Universality of many-body two-nucleon momentum distributions: Correlated nucleon spectral function of complex nuclei", Phys. Rev. C **96**, 064317 (2017), arXiv:1708.05168 [nucl-th].

[200] R. B. Wiringa, R. Schiavilla, S. C. Pieper, and J. Carlson, "Nucleon and nucleon-pair momentum distributions in $A \leq 12$ nuclei", Phys. Rev. C **89**, 024305 (2014), arXiv:1309.3794 [nucl-th].

[201] M. Piarulli, S. Pastore, R. B. Wiringa, S. Brusilow, and R. Lim, "Densities and momentum distributions in A≤12 nuclei from chiral effective field theory interactions", Phys. Rev. C **107**, 014314 (2023), arXiv:2210.02421 [nucl-th].

[202] G. J. Kramer, "The proton spectral function of ^{40}Ca and ^{48}Ca studied with the $(e, e'p)$ reaction", (1990).

[203] M. V. Stoitsov, A. N. Antonov, and S. S. Dimitrova, "Natural orbital representation and short-range correlations in nuclei", Phys. Rev. C **48**, 74–86 (1993).

[204] N. Fomin, D. Higinbotham, M. Sargsian, and P. Solvignon, "New Results on Short-Range Correlations in Nuclei", Ann. Rev. Nucl. Part. Sci. **67**, 129–159 (2017), arXiv:1708.08581 [nucl-th].

[205] E. S. Pinzon Guerra et al., "Measurement of σ_{ABS} and σ_{CX} of π^+ on carbon by the Dual Use Experiment at TRIUMF (DUET)", Phys. Rev. C **95**, 045203 (2017), arXiv:1611.05612 [hep-ex].

[206] E. S. Pinzon Guerra et al., "Using world charged $\pi^{\pm}$−nucleus scattering data to constrain an intranuclear cascade model", Phys. Rev. D **99**, 052007 (2019), arXiv:1812.06912 [hep-ex].

[207] E. Gramellini et al., "Measurement of the π–Ar total hadronic cross section at the LArIAT experiment", Phys. Rev. D **106**, 052009 (2022), arXiv:2108.00040 [hep-ex].

[208] A. B. Balantekin et al., "Snowmass Neutrino Frontier: Neutrino Interaction Cross Sections (NF06) Topical Group Report", (2022), arXiv:2209.06872 [hep-ex].

[209] A. M. Ankowski et al., "Electron scattering and neutrino physics", J. Phys. G **50**, 120501 (2023), arXiv:2203.06853 [hep-ex].

[210] K. Stricker, H. Mcmanus, and J. Carr, "Nuclear scattering of low-energy pions", Phys. Rev. C **19**, 929–947 (1979).

[211] M. Hirata, J. H. Koch, E. J. Moniz, and F. Lenz, "Isobar Hole Doorway States and π-^{16}O Scattering", Annals Phys. **120**, 205–248 (1979).

[212] E. Oset, H. Toki, and W. Weise, "Pionic modes of excitation in nuclei", Phys. Rept. **83**, 281–380 (1982).

[213] L. D. Faddeev, "Scattering theory for a three particle system", Sov. Phys. JETP **12**, 1014–1019 (1961).

[214] R Mach, "Galileo-invariant theory of low energy pion-nucleus scattering", Czech. J. Phys. B **33**, 772–786 (1983).

[215] S. Gurvitz, "Optimal approximation to elastic and inelastic scattering on a bound nucleon system", Phys. Rev. C **33**, 422–438 (1986).

[216] D. Ernst and G. Miller, "Relativistic kinematics for elastic pion nucleus scattering", Phys. Rev. C **21**, 1472–1479 (1980).

[217] L. Heller, G. Bohannon, and F. Tabakin, "Dependence of the Off Energy Shell T Matrix on the Total Three Momentum", Phys. Rev. C **13**, 742–748 (1976).

[218] B. Bakamjian and L. Thomas, "Relativistic particle dynamics. II", Phys. Rev. **92**, 1300–1310 (1953).

[219] C Møller, "General properties of the characteristic matrix in the theory of elementary particles i", K. Danske Vidensk. Selsk. Mat. Fys. Medd **23**, 1 (1945).

[220] R. Workman, R. Arndt, W. Briscoe, M. Paris, and I. Strakovsky, "Parameterization dependence of T matrix poles and eigenphases from a fit to πN elastic scattering data", Phys. Rev. C **86**, 035202 (2012), arXiv:1204.2277 [hep-ph].

[221] K. Kowalski and D Feldman, "Elastic nucleon-deuteron scattering", Physical Review **130**, 276 (1963).

[222] M. L. Goldberger, "The interaction of high energy neutrons and heavy nuclei", Physical Review **74**, 1269 (1948).

[223] R. Landau and M. Mcmillan, "Pauli-principle effects in pion-nucleus scattering", Phys. Rev. C **8**, 2094–2100 (1973).

[224] B. Bassalleck, H. D. Engelhardt, W. D. Klotz, F. Takeutchi, H. Ullrich, and M. Furic, "Single Neutron Emission Induced by Stopped π^- in 1p Shell Nuclei", Nucl. Phys. A **319**, 397–408 (1979).

[225] R. Seki and K. Masutani, "Unified analysis of pionic atoms and low-energy pion nucleus scattering: phenomenological analysis", Phys. Rev. C **27**, 2799–2816 (1983).

[226] C. Garcia-Recio, E. Oset, L. L. Salcedo, D. Strottman, and M. J. Lopez, "Pion Nucleus Elastic Scattering in the Microscopic Local Δ Hole Model", Nucl. Phys. A **526**, 685–702 (1991).

[227] M. Hjorth-Jensen, H. Muther, and A. Polls, "Width of the Δ resonance in nuclei", Phys. Rev. C **50**, 501–504 (1994), arXiv:nucl-th/9309019.

[228] T. Nishi et al., "Chiral symmetry restoration at high matter density observed in pionic atoms", Nature Phys. **19**, 788–793 (2023), arXiv:2204.05568 [nucl-ex].

[229] P. Kienle and T. Yamazaki, "Pions in nuclei, a probe of chiral symmetry restoration", Prog. Part. Nucl. Phys. **52**, 85–132 (2004).

[230] E. Friedman, "Indications of partial chiral symmetry restoration from pionic atoms", Phys. Lett. B **524**, 87–92 (2002), arXiv:nucl-th/0107050.

[231] K. Suzuki et al., "Precision spectroscopy of pionic 1s states of Sn nuclei and evidence for partial restoration of chiral symmetry in the nuclear medium", Phys. Rev. Lett. **92**, 072302 (2004), arXiv:nucl-ex/0211023.

[232] S. Weinberg, "Pion scattering lengths", Phys. Rev. Lett. **17**, 616–621 (1966).

[233] B. R. Holstein, "How large is F_π?", Phys. Lett. B **244**, 83–87 (1990).

[234] S. Descotes-Genon and B. Moussallam, "Radiative corrections in weak semi-leptonic processes at low energy: A Two-step matching determination", Eur. Phys. J. C **42**, 403–417 (2005), arXiv:hep-ph/0505077.

[235] W. Weise, "Hadronic excitations and chiral symmetry in nuclear systems", Nucl. Phys. A **690**, edited by P. Braun-Munzinger and A. Zilges, 98–109 (2001).

[236] W. Weise, "Pionic excitations and chiral symmetry in dense matter", Acta Phys. Polon. B **31**, edited by L. Jarczyk, C. Guaraldo, H. Machner, and A. Magiera, 2715–2726 (2000).

[237] J. Gasser, H. Leutwyler, and M. E. Sainio, "Sigma term update", Phys. Lett. B **253**, 252–259 (1991).

[238] E. Friedman, "Indications of partial chiral symmetry restoration from pionic atoms", Phys. Lett. B **524**, 87–92 (2002), arXiv:nucl-th/0107050.

[239] E. Friedman, "Density dependence of the s wave repulsion in pionic atoms", Nucl. Phys. A **710**, 117–130 (2002), arXiv:nucl-th/0205054.

[240] E. Friedman et al., "Elastic scattering of low energy pions by nuclei and the in-medium isovector πN amplitude", Phys. Rev. C **72**, 034609 (2005), arXiv:nucl-ex/0507008.

[241] E. Friedman and A. Gal, "The pion-nucleon σ term from pionic atoms", Phys. Lett. B **792**, 340–344 (2019), arXiv:1901.03130 [nucl-th].

[242] V. Baru, C. Hanhart, M. Hoferichter, B. Kubis, A. Nogga, and D. R. Phillips, "Precision calculation of the π^- deuteron scattering length and its impact on threshold π N scattering", Phys. Lett. B **694**, 473–477 (2011), arXiv:1003.4444 [nucl-th].

[243] M. Doring and E. Oset, "The s-wave pion-nucleus optical potential", Phys. Rev. C **77**, 024602 (2008), arXiv:0705.3027 [nucl-th].

[244] U. G. Meissner, J. A. Oller, and A. Wirzba, "In-medium chiral perturbation theory beyond the mean field approximation", Annals Phys. **297**, 27–66 (2002), arXiv:nucl-th/0109026.

[245] N. Kaiser and W. Weise, "Systematic calculation of s-wave pion and kaon self-energies in asymmetric nuclear matter", Phys. Lett. B **512**, 283–289 (2001), arXiv:nucl-th/0102062.

[246] C. Vincent and S. Phatak, "Accurate momentum-space method for scattering by nuclear and Coulomb potentials", Phys. Rev. C **10**, 391–394 (1974).

[247] D. H. Wright et al., "Elastic Scattering of 19.5 MeV and 30 MeV Negative Pions From ^{12}C", Phys. Rev. C **36**, 2139–2142 (1987).

[248] B. M. Preedom et al., "Positive pion-nucleus elastic scattering at 30 and 50 MeV", Phys. Rev. C **23**, 1134–1140 (1981).

[249] K. K. Seth et al., "Negative pion nucleus elastic scattering at 30 MeV and 50 MeV", Phys. Rev. C **41**, 2800–2808 (1990).

[250] R. J. Sobie et al., "Elastic and Inelastic Scattering of 50 MeV Pions From ^{32}S and ^{34}S", Phys. Rev. C **30**, 1612 (1984).

[251] B. G. Ritchie et al., "50 MeV π^+ and π^- scattering from ^{12}C", Phys. Rev. C **41**, 1668–1673 (1990).

[252] M. Blecher et al., "Isospin effects in $\pi^\pm$ elastic scattering from ^{12}C, ^{12}C, and ^{14}C at 65 MeV and 80 MeV", Phys. Rev. C **28**, 2033–2041 (1983).

[253] L. E. Antonuk et al., "Elastic and Inelastic Pion Scattering on ^{12}C and ^{13}C at 100 MeV", Nucl. Phys. A **420**, 435 (1984).

[254] F. G. Binon, P. Duteil, J. P. Garron, J. Gorres, L. Hugon, J. P. Peigneux, C. Schmit, M. Spighel, and J. P. Stroot, "Scattering of negative pions on carbon", Nucl. Phys. B **17**, 168–188 (1970).

[255] A. Saunders, S. Hoeibraten, J. J. Kraushaar, B. J. Kriss, R. J. Peterson, R. A. Ristinen, J. T. Brack, G. Hofman, E. F. Gibson, and C. L. Morris, "Reaction and total cross-sections for low-energy π^+ and π^- on isospin zero nuclei", Phys. Rev. C **53**, 1745–1752 (1996).

[256] O. Meirav, E. Friedman, R. R. Johnson, R. Olszewski, and P. Weber, "Low-energy Pion - Nucleus Potentials From Differential and Integral Data", Phys. Rev. C **40**, 843–849 (1989).

[257] E. Friedman, A. Goldring, R. R. Johnson, O. Meirav, D. Vetterli, P. Weber, and A. Altman, "Total reaction cross-sections for 20–30 MeV pions and the anomaly of pionic atoms", Phys. Lett. B **257**, 17–20 (1991).

[258] J. P. Albanese, J. Arvieux, J. Bolger, E. Boschitz, C. H. Q. Ingram, J. Jansen, and J. Zichy, "Elastic scattering of positive pions by ^{16}O between 80 MeV and 340 MeV", Nucl. Phys. A **350**, 301–331 (1980).

[259] G. S. Mutchler et al., "Nuclear Coulomb Interference in $\pi^{\pm}$ ^{16}O Scattering", Phys. Rev. C **11**, 1873–1879 (1975).

[260] C. H. Q. Ingram, P. A. M. Gram, J. Jansen, R. E. Mischke, J. Zichy, J. Bolger, E. T. Boschitz, G. Probstle, and J. Arvieux, "Measurement of quasielastic scattering of pions from ^{16}O at energies around the $\Delta(1232)$ resonance", Phys. Rev. C **27**, 1578–1601 (1983).

[261] U. Wienands et al., "Elastic and Inelastic Scattering of 50 MeV Pions From ^{28}Si and ^{30}Si", Phys. Rev. C **35**, 708–717 (1987).

[262] B. M. Preedom, R. Corfu, J. P. Egger, P. Gretillat, C. Lunke, J. Piffaretti, E. Schwarz, J. Jansen, and C. Perrin, "A systematic study of π^+ and π^+ inelastic scattering from ^{28}Si in the region of the $\pi N(3,3)$ resonance", Nucl. Phys. A **326**, 385–400 (1979).

[263] S. H. Dam et al., "Elastic scattering of π^+ and π^- from ^{40}Ca at 64.8 MeV", Phys. Rev. C **25**, 2574–2582 (1982).

[264] M. J. Leitch et al., "Pion nucleus elastic scattering at 80 MeV", Phys. Rev. C **29**, 561–568 (1984).

[265] P. Gretillat, J. P. Egger, J. F. Germond, C. Lunke, E. Schwarz, C. Perrin, and B. M. Preedom, "Study of π^+ and π^- Elastic Scattering From ^{40}Ca and ^{48}Ca in the Region of the πN (3,3) Resonance", Nucl. Phys. A **364**, 270–284 (1981).

[266] K. M. Crowe, A. Fainberg, J. Miller, and A. S. L. Parsons, "Measurement of $\pi^{\pm}$-He scattering and its relation to the pion form-factor", Phys. Rev. **180**, 1349–1358 (1969).

[267] F. Balestra et al., "Elastic and Inelastic Scattering of $\pi^{\pm}$ Mesons on ^{4}He and ^{3}He", Nuovo Cim. A **43**, 219–229 (1978).

[268] I. V. Falomkin et al., "Elastic scattering of π^+ and π^- on ^{4}He at 68 and 154 MeV", Nuovo Cim. A **21**, 168–178 (1974).

[269] Y. A. Shcherbakov et al., "Scattering of Charged Pions on ^{4}He Nuclei in the Energy Range of 68–208 MeV", Nuovo Cim. A **31**, 249 (1976).

[270] M. I. Haftel and F. Tabakin, "Nuclear saturation and the smoothness of nucleon-nucleon potentials", Nuclear Physics A **158**, 1–42 (1970).

[271] C. J. Joachain, "Quantum collision theory", in (North-Holland, Amsterdam, 1975).

[272] J. Huefner, "Non-overlapping potentials and the ericson-ericson renormalization in the pion-nucleus optical potential", Nucl. Phys. B **58**, 55–76 (1973).

[273] J. Dedonder, J. Maillet, and C Schmit, "Comparison of π^+ and π^- elastic scattering on the isotopic pair ^{16}O ^{18}O in the resonance region", Annals Phys. **127**, 1–48 (1980).

[274] F. Cannata, J. P. Dedonder, and W. R. Gibbs, "Optical potentials for charged hadron nucleus scattering: Role of Coulomb excitations", Phys. Rev. C **41**, 1637–1650 (1990).

[275] N. Michel, "Precise coulomb wave functions for a wide range of complex l, η and z", Comput. Phys. Commun. **176**, 232–249 (2007).

[276] L. Ray, G. W. Hoffmann, and R. M. Thaler, "Coulomb interaction in multiple scattering theory", Phys. Rev. C **22**, 1454–1467 (1980).

[277] D. S. Koltun, "The interaction of pions with nuclei", in *Advances in nuclear physics* (Springer, 1969), pp. 71–191.

[278] S. Gasiorowicz, *Elementary particle physics* (Wiley New York, 1966), pp. 369–370.

[279] M. I. F. Bondy, "Neutron skin studies in heavy nuclei with coherent π^0 photoproduction", PoS **Bormio2015**, 008 (2015).

[280] C. J. Horowitz, E. F. Brown, Y. Kim, W. G. Lynch, R. Michaels, A. Ono, J. Piekarewicz, M. B. Tsang, and H. H. Wolter, "A way forward in the study of the symmetry energy: experiment, theory, and observation", J. Phys. G **41**, 093001 (2014), arXiv:1401.5839 [nucl-th].

[281] W. Peters, H. Lenske, and U. Mosel, "Coherent photoproduction of pions on nuclei in a relativistic, nonlocal model", Nucl. Phys. A **640**, 89–113 (1998), arXiv:nucl-th/9803009.

[282] L. J. Abu-Raddad, J. Piekarewicz, A. J. Sarty, and R. A. Rego, "Lessons to be learned from the coherent photoproduction of pseudoscalar mesons", Phys. Rev. C **60**, 054606 (1999), arXiv:nucl-th/9812061.

[283] S. Boffi and R. Mirando, "Coherent π^0 photoproduction near threshold on closed shell nuclei", Nucl. Phys. A **448**, 637–651 (1986).

[284] A. N. Saharia and R. M. Woloshyn, "Isobar Doorway Model for Coherent π^0 Photoproduction", Phys. Rev. C **23**, 351 (1981).

[285] E. Oset and W. Weise, "Photon Nucleus Scattering and Coherent π^0 Photoproduction in the Δ Hole Model", Nucl. Phys. A **368**, [Erratum: Nucl.Phys.A 402, 612–612 (1983)], 375–393 (1981).

[286] B. Koerfgen, F. Osterfeld, and T. Udagawa, "Longitudinal and transverse spin response of ^{12}C in the Δ resonance region", Phys. Rev. C **50**, 1637–1647 (1994).

[287] R. C. Carrasco, J. Nieves, and E. Oset, "Coherent (γ, π^0) photoproduction in a local approximation to the delta-hole model", Nucl. Phys. A **565**, 797–817 (1993).

[288] D. Drechsel, O. Hanstein, S. S. Kamalov, and L. Tiator, "A Unitary isobar model for pion photoproduction and electroproduction on the proton up to 1 GeV", Nucl. Phys. A **645**, 145–174 (1999), arXiv:nucl-th/9807001.

[289] V. Bellini et al., "Coherent π^0 photo-production on ^{4}He at intermediate-energies with polarized photons", Nucl. Phys. A **646**, 55–66 (1999).

[290] S. S. Kamalov, L. Tiator, and C. Bennhold, "Coherent π^0 and η photoproduction on the deuteron", Phys. Rev. C **55**, 98–110 (1997), arXiv:nucl-th/9602023.

[291] A. A. Chumbalov and S. S. Kamalov, "Off-shell Effects in the Coherent π^0 Photoproduction Off Nuclei", Phys. Lett. B **196**, 23 (1987).

[292] L. Tiator, A. K. Rej, and D. Drechsel, "Fermi motion and off-shell effects in the reaction ^{3}He$(\gamma, \pi^+)^3$H", Nucl. Phys. A **333**, 343–356 (1980).

[293] R. H. Landau, "Scattering of Pions from ^{3}He and ^{4}He Calculated with Realistic Form-Factors", Annals Phys. **92**, 205 (1975).

[294] R. A. Eramzhian, M. Gmitro, and S. S. Kamalov, "Momentum-space analysis of the nuclear partial transitions in the charged pion photoproduction", Phys. Rev. C **41**, 2865–2877 (1990).

[295] G. Chew, M. Goldberger, F. Low, and Y. Nambu, "Application of Dispersion Relations to Low-Energy Meson-Nucleon Scattering", Phys. Rev. **106**, 1337–1344 (1957).

[296] D. Drechsel, S. S. Kamalov, and L. Tiator, "Unitary Isobar Model – MAID2007", Eur. Phys. J. A **34**, 69–97 (2007), arXiv:0710.0306 [nucl-th].

[297] R. L. Workman, M. W. Paris, W. J. Briscoe, and I. I. Strakovsky, "Unified Chew-Mandelstam SAID analysis of pion photoproduction data", Phys. Rev. C **86**, 015202 (2012), arXiv:1202.0845 [hep-ph].

[298] S. S. Kamalov, S. N. Yang, D. Drechsel, O. Hanstein, and L. Tiator, "$\gamma^* N \to \Delta$ transition form-factors: A New analysis of the JLab data on $p(e, e'p)\pi^0$ at $Q^2 = 2.8$ and 4.0 $(\mathrm{GeV/c})^2$)", Phys. Rev. C **64**, 032201 (2001), arXiv:nucl-th/0006068.

[299] R. A. Freedman, G. A. Miller, and E. M. Henley, "Isobar dynamics and pion nucleus elastic scattering", Nucl. Phys. A **389**, 457–491 (1982).

[300] I. Laktineh, W. M. Alberico, J. Delorme, and M. Ericson, "Coherent photoproduction of neutral pions in nuclei as a detector of nuclear pionic modes", Nucl. Phys. A **555**, 237–248 (1993).

[301] H. Tanabe and K. Ohta, "Dynamical model for pion photoproduction in the Δ region", Phys. Rev. C **31**, 1876–1884 (1985).

[302] K. M. Watson, "Some general relations between the photoproduction and scattering of π mesons", Phys. Rev. **95**, 228–236 (1954).

[303] M. Olsson, "Solutions of the Multichannel Unitarity Equations Describing the Addition of a Resonance and Background: Application to a Pole Model of Photoproduction", Nucl. Phys. B **78**, 55–76 (1974).

[304] T. Sato and T.-. S. H. Lee, "Meson exchange model for πN scattering and $\gamma N \to \pi N$ reaction", Phys. Rev. C **54**, 2660–2684 (1996), arXiv:nucl-th/9606009.

[305] V. Pascalutsa and J. A. Tjon, "Pion photoproduction on nucleons in a covariant hadron-exchange model", Phys. Rev. C **70**, 035209 (2004), arXiv:nucl-th/0407068.

[306] V. Bernard, N. Kaiser, and U.-G. Meissner, "Chiral dynamics in nucleons and nuclei", Int. J. Mod. Phys. E **4**, 193–346 (1995), arXiv:hep-ph/9501384.

[307] V. Pascalutsa and D. R. Phillips, "Effective theory of the $\Delta(1232)$ in Compton scattering off the nucleon", Phys. Rev. C **67**, 055202 (2003), arXiv:nucl-th/0212024.

[308] A. M. Bernstein, S. Nozawa, and M. A. Moinester, "Quadrupole amplitude in the $\gamma N \rightleftarrows \Delta$ transition", Phys. Rev. C **47**, 1274–1281 (1993).

[309] O. Hanstein, D. Drechsel, and L. Tiator, "Multipole analysis of pion photoproduction based on fixed t dispersion relations and unitarity", Nucl. Phys. A **632**, 561–606 (1998), arXiv:nucl-th/9709067.

[310] I. G. Aznauryan, "Multipole amplitudes of pion photoproduction on nucleons up to 2 GeV within dispersion relations and unitary isobar model", Phys. Rev. C **67**, 015209 (2003), arXiv:nucl-th/0206033.

[311] R. M. Davidson, N. C. Mukhopadhyay, and R. S. Wittman, "Effective Lagrangian approach to the theory of pion photoproduction in the $\Delta(1232)$ region", Phys. Rev. D **43**, 71–94 (1991).

[312] C. Fernandez-Ramirez, E. Moya de Guerra, and J. M. Udias, "Effective Lagrangian approach to pion photoproduction from the nucleon", Annals Phys. **321**, 1408–1456 (2006), arXiv:nucl-th/0509020.

[313] A. Mariano, "πN scattering and $\gamma N \to N\pi$ photoproduction within the unitary improved Born approximation", J. Phys. G **34**, 1627–1651 (2007).

[314] S. Nozawa and T. S. H. Lee, "Electroproduction of Pions on the Nucleon", Nucl. Phys. A **513**, 511–542 (1990).

[315] G. L. Caia, V. Pascalutsa, J. A. Tjon, and L. E. Wright, "$\gamma^* N\Delta$ form-factors from a relativistic dynamical model of pion electroproduction", Phys. Rev. C **70**, 032201 (2004), arXiv:nucl-th/0407069.

[316] V. Pascalutsa and M. Vanderhaeghen, "Chiral effective-field theory in the $\Delta(1232)$ region: I. Pion electroproduction on the nucleon", Phys. Rev. D **73**, 034003 (2006), arXiv:hep-ph/0512244.

[317] R. Novotny, "The BaF-2 photon spectrometer TAPS", in International Workshop on Heavy Scintillators for Scientific and Industrial Applications: Crystal 2000 (Sept. 1992), pp. 267–272.

[318] A. R. Gabler et al., "Response of TAPS to monochromatic photons with energies between 45 MeV and 790 MeV", Nucl. Instrum. Meth. A **346**, 168–176 (1994).

[319] A. Starostin et al., "Measurement of $K\vec{p}\eta\Lambda$ near threshold", Phys. Rev. C **64**, 055205 (2001).

[320] K. H. Kaiser et al., "The 1.5 GeV harmonic double-sided microtron at Mainz University", Nucl. Instrum. Meth. A **593**, 159–170 (2008).

[321] I. Anthony, J. D. Kellie, S. J. Hall, G. J. Miller, and J. Ahrens, "Design of a tagged photon spectrometer for use with the Mainz 840 MeV microtron", Nucl. Instrum. Meth. A **301**, 230–240 (1991).

[322] S. J. Hall, G. J. Miller, R. Beck, and P. Jennewein, "A focal plane system for the 855 MeV tagged photon spectrometer at MAMI-B", Nucl. Instrum. Meth. A **368**, 698–708 (1996).

[323] R. W. Gothe, W. Lang, S. Klein, B. Schoch, V. Metag, H. Stroeher, S. J. Hall, and R. O. Owens, "Measurement of the elastic π^0 photoproduction cross-sections on ^{12}C and ^{13}C", Phys. Lett. B **355**, 59–64 (1995).

[324] R. Sanderson, "Coherent neutral pion photoproduction on sup ^{16}O and sup ^{208}Pb", PhD thesis (Glasgow U., 2002).

[325] L. C. Chamon, B. V. Carlson, L. R. Gasques, D. Pereira, C. De Conti, M. A. G. Alvarez, M. S. Hussein, M. A. Candido Ribeiro, E. S. Rossi Jr., and C. P. Silva, "Toward a global description of the nucleus-nucleus interaction", Phys. Rev. C **66**, 014610 (2002), arXiv:nucl-th/0202015.

[326] C. Olmer et al., "Elastic and inelastic scattering of 162 MeV pions by ^{28}Si, ^{58}Ni, and ^{208}Pb", Phys. Rev. C **21**, 254–271 (1980).

[327] N. M. Hintz et al., "Determination of neutron and proton multipole matrix elements in ^{208}Pb from π^- and π^+ scattering at 180 MeV", Phys. Rev. C **45**, 601–612 (1992).

[328] P. Pedroni and A. Thomas, "Proposal for an Experiment "Isospin asymmetry dependence of neutron skins with Coherent pion photoproduction"", A2 Collaboration at MAMI (2016).

[329] M. Mocanu, "Exploring Neutron stars EoS with coherent π^0 π^0 photoproduction at A2@MAMI", talk presented at MENU 2023.

[330] K. Ieki et al., "Measurement of absorption and charge exchange of π^+ on carbon", Phys. Rev. C **92**, 035205 (2015), arXiv:1506.07783 [hep-ex].